Long Term Project

2005-2008

FINAL EXPERIMENTAL REPORT

KINETICS AND MECHANISM OF HYDROGEN STORAGE IN ADVANCED INTERMETALLIC HYDRIDES

Experiments 01-02-735 and 01-01-709

Institute for Energy Technology

Kjeller, Norway

August 2008

Main proposer:	Prof. Volodymyr A. YARTYS, IFE E-mail: volodymyr.yartys@ife.no Tel. +47 63 80 64 53 Fax +47 63 81 29 05
Principal investigators:	Volodymyr A. YARTYS, IFE
	Jan Petter MÆHLEN, IFE
	Roman V. DENYS, IFE
Beam Line Scientists:	Yaroslav FILINCHUK, SNBL, BM1A
	Dmitry CHERNYSHOV, SNBL, BM1A
	Phil PATTISON, SNBL, BM1A
	Hermann EMERICH, SNBL, BM1B
	Wouter VAN BEEK, SNBL, BM1B

Content

1. Summary

This report presents results of the Long Term Project KINETICS AND MECHANISM OF HYDROGEN STORAGE IN ADVANCED INTERMETALLIC HYDRIDES performed by Institute for Energy Technology, Norway in collaboration with staff of the Swiss Norwegian Beam Lines at ESRF, Grenoble, in the period 2005-2008.

Hydrogen storage materials are characterized by amazingly fast rates of H exchange with H_2 gas. *In situ* Synchrotron X-ray Powder Diffraction (SR-XRD) is a very valuable tool in probing mechanism of H uptake and release and allows to study kinetics, mechanism of the transformations and structure of the metal and hydrogen sublattices. This work was aimed on studies of the hydrogenation and dehydrogenation processes in different metal hydride systems by *in situ* SR-XRD at H_2 pressures 0 - 15 bar and temperatures from ÷100 to 800 °C. A specially designed cell for *in situ* studies in H_2-atmosphere was utilised. The cell is attached to a metal hydride hydrogen storage unit developed at IFE providing hydrogen gas at convenient pressures. The work benefits form a possibility to control hydrogen content in the nonstable at ambient conditions materials by settling increased H_2 pressures and/or decreased temperatures (see the chapter below).

The *in situ* SR-XRD experiments were performed at the Swiss-Norwegian Beam Line (SNBL) at the European Synchrotron Radiation Facility (ESRF), Grenoble, France, in collaboration with the research staff from SNBL and resulted in numerous publications [1-8]. The work was focused on three groups of materials:

- Hydrides of the light elements, Al and Mg, with high gravimetric and volumetric densities of H, 10 and 7.6 wt.% H, correspondingly. These are considered as prospective for transport applications solid H storage materials.
- Intermetallic hydrides with strong anisotropic hydrogen induced expansion.
- Intermetallic hydrides where a combination of nanostructuring and thermal management approaches allows to effectively compress and store hydrogen gas. Here, Ti and Zr-based Laves phase compounds and modified AB_5-type of materials were in focus.

Particular focus was on:

- Structure of alanes, α-AlH_3 and γ-AlH_3, and mechanism of thermal decomposition of the alanes;
- Catalytic hydrogenation and H desorption in the system Mg-Mg_2Ni-$LaMg_{12}$;
- Hydrogen absorption and desorption at subzero temperatures.

The studies also included investigations of the hexagonal-monoclinic low temperature order-disorder transition in $ErMn_2D_2$ Laves phase deuteride. A list of materials investigated is presented in Table 1, while related presentations and main publications are presented in Tables 2 and 3, respectively.

2. List of materials studied.

Table 1: List of materials studied

Beam line	Exp. No	Type of materials studied
BM01B	01-01-660	α-AlH_3, $ErMn_2H_x$, VaTiZr, $MmLaNi_5$--H,Ce_2Ni_7D4, $Ce_3Ni_2AlD_4$, Fe (reference), $LaNi_3D_3$
BM01B		γ-AlH_3 High-Res.
BM01A		γ-AlH_3 decomposition
BM01B	01-01-709	$CeMgNi_3$,LaNiIn,Mg-Mg_2Ni, MmMgNi, $TiCrMn_x$, YMgNi, Zr_4Fe_2O
BM01A	01-02-735	AB_2(FRN121)-H, YMgIn-H, MmMgNi-AB_5-H, MgMmNi-H, La_3MgNi_{14}-H, γ-AlD_3
BM01A	01-02-735	γ-AlD_3, α-AlH_3-BNL, Al(GaIn)H_x, Mg-V-H, Mg-H MgMmNi-V-H, MgMmNi-H (RS), La_3MgNi_{14}, $LaCeNi_5$, V-H
BM01A	01-02-735	α-AlH_3-BNL (BM, oxides), Sodium Alanate, $LaCeNi_5$-H, AB_2(FRN118)-H, La_2Ni_7-H, Mg-BM, Mg-V-BM
BM01B	01-01-709	Surface treated AB_5–H, VTiZrH, VZrH
BM01A	01-02-735	α-AlH_3-BNL (BM, oxides)+ Raman, γ-AlD_3 + Raman, La_2Ni_7-H, AB_5(JSV139)-H, AB_2(FRN117)-H

3. Presentations

Table 2: List of the most important presentations involving work performed during this LTP

In situ SR diffraction studies of the phase-structural transformations in hydrogen storage materials. V.A.Yartys and J.P.Maehlen. Workshop on Nanoscience and SR XRD at ESRF / SNBL. 22-23.06.2006.
International Symposium Hydrogen Power Theoretical and Engineering Solutions HYPOTHESIS VII. El Castellano, Merida, Mexico. March 27-30, 2007. Book of Abstracts. V.A.Yartys, J.K.Solberg, R.V.Denys, J.P.Mæhlen, A.B.Riabov, M.V.Lototsky, Ying Wu, S.Løken, B.P.Tarasov, D.N.Borisov. Nanostructured hydrides of light metals for hydrogen storage. P.40.
V.A.Yartys. NORSTORE 2002-2007: 5 Years of Nordic and Regional Collaboration on Hydrogen Storage. NORSTORE 2007 Conference. Sigulda, Latvia, May 31-June 2, 2007). (Oral presentation).

V.A.Yartys and J.P.Mæhlen. Nanostructured hydrides of light elements for hydrogen storage and H storage units. NANOMAT conference. Bergen, June 2007. (Oral presentation).
V.A.Yartys, J.P.Mæhlen, A.Vik, A.Strand, R.V.Denys, M.V.Lototsky. Nano Science for New Advanced Metal-Hydrogen Systems Towards Applications. NANOMAT conference. Bergen, June 2007. (POSTER).
Proceedings of the 2nd International Hydrogen Energy Congress and Exhibition IHEC 2007 Istanbul, Turkey, 13-15 July 2007. Nanostructured Hydrides of Light Metals for Hydrogen Storage V.A.Yartys, J.K.Solberg, J.P. Maehlen, R.V.Denys, A.B.Riabov, M.V.Lototsky, Ying Wu, B.P.Tarasov. Collected abstracts. (Invited keynote lecture).
V.A. Yartys , A.B. Riabov , R.V. Denys . CRYSTAL CHEMISTRY OF ANISOTROPIC HYDRIDES: NOVEL MATERIALS WITH UNUSUAL STRUCTURAL BEHAVIOURS. X International Conference on Crystal Chemistry of Intermetallic Compounds. Lviv, Ukraine, September 2007. (Invited Talk).
V.A.Yartys, J.P.Mæhlen, P.Pattison, T.Blach, E.Gray. In situ SR X-Ray and Neutron Diffraction Studies of Phase-Structural Transformations in Hydrogen Storage Materials. Swiss-Norwegian Seminar "In situ experiments at SNBL using high gas pressures". GRENOBLE, November 2007 (Oral presentation).

4. Main publications

Table 3: List of the main publications involving work from current LTP

V.A.Yartys, A.B.Riabov, R.V.Denys, M.Sato, R.G.Delaplane. Novel Intermetallic Hydrides.// J.Alloys and Compounds, 408-412 (2006) 273-279.
J. P. Maehlen, V. A.Yartys.// Aluminum Trihydride Studied By Powder Synchrotron X-Ray Diffraction: Crystal Structure and Thermal Decomposition.// Advanced Materials for Energy Conversion III. Symposium held during the TMS 2006 Annual Meeting in San Antonio, Texas, USA, March 12-16, Edited by D.Chandra, J.Petrovic, R.G.Bautista, A.Imam (2006) 77-85.
V.A.Yartys, R.V.Denys, J.P.Maehlen, Ch.Frommen, M.Fichtner, B.M.Bulychev, H.Emerich.// Double bridge bonding of aluminium and hydrogen in the crystal stucture of γ-AlH3.// Inorganic Chemistry, 46 (4) (2007) 1051-1055. DOI: 10.1021/ic0617487.
J.P.Maehlen, V.A.Yartys, A.B.Riabov, A.Budziak, H.Figiel, J.Żukrowski.// Synchrotron X-ray diffraction study of ErMn2D2.// J.Alloys and Compounds, 437 (2007) 140-145. doi:10.1016/j.jallcom.2006.07.088.
J. P. Maehlen, V.A.Yartys, R.V.Denys, M.Fichtner, Ch.Frommen, B.M.Bulychev, P.Pattison, H.Emerich, Y.E. Filinchuk, D.Chernyshov.. Thermal Decomposition of

AlH3 Studied by in situ Synchrotron X-ray Diffraction and Thermal Desorption Spectroscopy.// Journal of Alloys and Compounds, Volumes 446-447, 31 October 2007, Pages 280-289

R. V.Denys, A. B. Riabov, V. A. Yartys, R. G. Delaplane, M. Sato. Hydrogen storage properties and structure of La1–xMgx(Ni1–yMny)3 intermetallics and their hydrides.// Journal of Alloys and Compounds, Volumes 446-447, 31 October 2007, Pages 166-172

R.V. Denys, V.A. Yartys, Masashi Sato, A.B. Riabov, R.G. Delaplane. Crystal chemistry and thermodynamic properties of anisotropic Ce2Ni7H4.7 hydride// Journal of Solid State Chemistry, Volume 180, Issue 9, September 2007, Pages 2566-2576

R.V. Denys, A.B. Riabov, V.A. Yartys, Masashi Sato, R.G. Delaplane. Mg substitution effect on the hydrogenation behaviour, thermodynamic and structural properties of the La2Ni7–H(D)2 system//Journal of Solid State Chemistry, Volume 181, Issue 4, April 2008, Pages 812-821

5. In situ Experimental Setup

A setup designed for in situ studies of the chemical processes in hydrogen gas/vacuum [9-11] was used. A scheme of the setup used is shown in Figure 1. A small amount of the sample is contained in a quartz glass capillary (with inner diameter of 0.3, 0.5 or 0.7 mm) and fills approximately 1–2 mm in its bottom part. The capillary is hermetically connected to the gaseous system using a carbon ferrule mounted in a T-piece (Figure 1 b), which, in turn, is attached to the goniometer head. A two-stringed flow system makes it possible to switch between hydrogen gas and vacuum during the experiment. The fixed connection of the microreaction cell to the goniometer head makes a full rotation of the sample difficult. However, the averaging over the different orientations of the crystallites, resulting in the elimination of the preferred orientation effects in the collected diffraction data is achieved by applying wobbling of the setup around the axis of the capillary using a flexible PEEK (Polyetheretherketon) tubing connection between the microreaction cell and the flow system. During the experiments, hydrogen gas is supplied from a portable metal hydride storage unit developed at IFE, Kjeller ($La_{1-x}Mm_xNi_5$ hydrogen storage alloy). Vacuum is created using a turbo molecular vacuum pump. Except for the PEEK tubing allowing the wobbling of the sample cell, stainless steel tubes are used for the connections to prevent oxygen diffusion through the tubes during the experiments.

a) b)

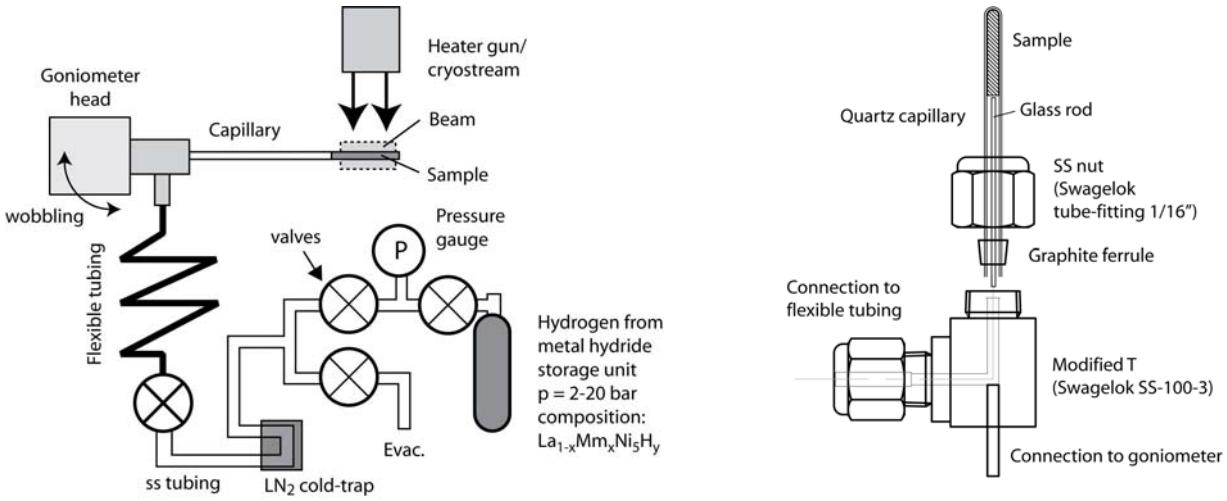

Figure 1: Scheme of the experimental set-up used for in situ SR-XRD experiments; (a) layout of the setup; the hydrogen and vacuum lines can be operated remotely; (b) the individual parts and assembly of the microreaction cell.

Experiments at the BM01A station were collected using a MAR2300 image plate detector. Wavelength and sample-to-detector distance were calibrated from individual runs of LaB_6. Typical, a time resolution of ~1 minute was used (10 seconds for data collection and about 50 seconds for processing/reading of the image plate) with 2θ range of about 1-30°. To obtain data suitable for whole-profile refinements, the 2D patterns were integrated to 1D using the Fit2D program [12].

The diffractometer at BM01B is equipped with six counting chains (Si(111) chanell-cut monochromator, scintillation detectors), with an angular offset in 2θ of 1.1°. For *in situ* measurements, in order to keep the counting time per scan as low as possible, the detector bank was moved by 1.2 º during one measurement and the data from the six different detectors were added using a data-binning program. Typically, one dataset was collected within 3 minutes. The wavelengths selected for the measurements were accurately determined from separate calibration measurements of a standard Si sample. In addition, patterns of LaB_6 were collected for correction of the instrumental contribution to profile parameters.

All powder diffraction data were analysed by the Rietveld whole-profile refinement method [13] using the General Structure Analysis System (GSAS) software [13]. Peak shapes were described by a multi-term Simpson's rule integration of the pseudo-Voigt function [15-16], which includes the asymmetry correction according to Finger *et al*. [17]

6. Selected Highlights

6.1. Aluminium hydride

Aluminium trihydride (alane) is considered as a prospective solid H storage material, having high gravimetric (10 wt.% H) and volumetric density of H (2 times higher compared to LH_2) and, also, because of its convenient range of thermal stability. AlH_3 forms several polymorphic modifications, which are often polymers $(AlH_3)_n$ [18]. α-Alane AlH_3 was first synthesized in 1947 by an exchange reaction between $AlCl_3$ and lithium hydride in ether solution [18]. This binary hydride has a covalent Al-H bonding and exhibits dielectric properties. α-AlH_3, the most stable modification of alane, has a rhombohedral unit cell (space group $R\bar{3}c$) [20]. Metastable alane does not release hydrogen at normal conditions and is stable in air. At atmospheric pressure AlH_3 desorbs hydrogen at rather moderate temperatures (350 – 400 K, depending on its preparation history). Achieving sufficiently rapid and controllable decomposition of AlH_3 and proposal of the efficient synthesis routes to make the system Al-AlH_3 reversible are focused in ongoing research (see, e.g., [21]). We have studied two different alane polymorphs, α-AlH_3 and γ-AlH_3.

High-resolution scan at room temperature of α-AlH_3 (station BM01B)

Refinements of the high-resolution SR-XRD pattern of α-AlH_3 yielded unit cell parameters: a = 4.44994(5) Å, c = 11.8200(2) Å, and V = 202.701(4) $Å^3$ which agree well with the reference data: a = 4.449 Å; c = 11.804Å; V = 202.34 $Å^3$ [20]. Since Al has a relative low atomic number, it was possible to locate the hydrogen sublattice during the refinements, starting with Al placed in a special position 6*a* [0,0,0] and performing differential Fourier analysis. Performing the refinements without including the H position gave the following best goodness-of-fit parameters: R_{wp} =14.2%, R_p = 11.7 %, and χ^2 = 6.0. Including the hydrogen atom (at site 18*e* [0.625(2), 0, ¼]), the quality of the fit significantly improved, giving goodness-of-fit parameters of R_{wp} = 12.1%, R_p = 10.6 %, and χ^2 = 4.9. Figure 2a shows the Rietveld-type plots of the high-resolution data. The refinements yielded an Al-H bonding distance of 1.712(3) Å and an octahedral coordination of Al into AlH_6 units where bridge bonds Al-H-Al are formed with a bond angle of 141°. Furthermore, they indicated a small charge transfer from Al to H corresponding to the formation of $Al^{+0.15}$ and $H^{-0.05}$. This charge distribution can be observed in the Fourier transform of the observed XRD pattern as shown in Figure 2b. We note a good correspondence between the data of the present powder XRD work and the results of the powder neutron diffraction study of AlD_3 [20], where an Al-D bond distance of 1.715 Å in the AlD_6 octahedra was reported. This experiment shows that hydrides with light metal atoms can be successfully characterised, also including hydrogen positions, using the synchrotron XRD technique.

A B

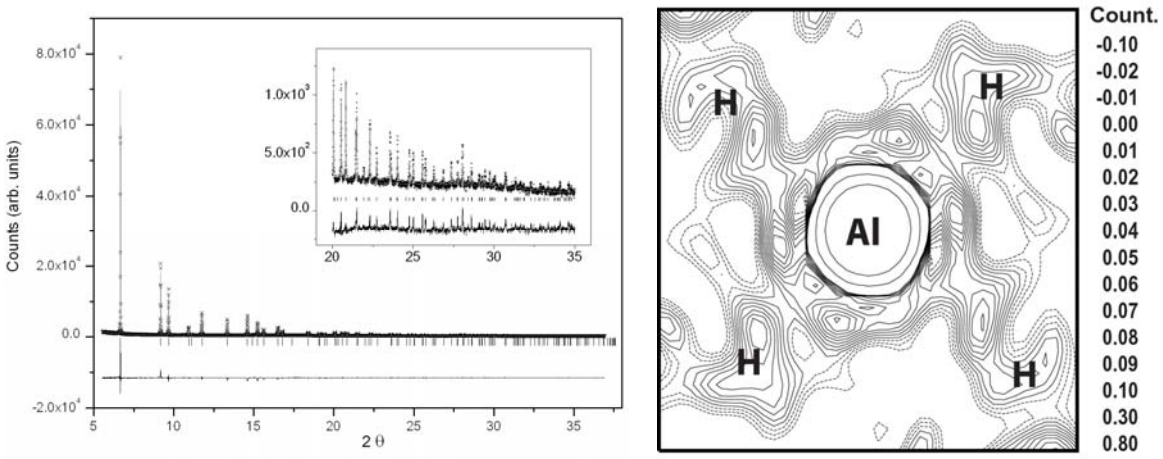

Figure 2: (A) Rietveld-type plots of AlH3 (λ = 0.37504 Å) collected at room temperature showing observed (crosses), calculated (upper line) and difference (bottom line) plots. The positions of the Bragg peaks are shown as ticks. An enlargement of the high-angle part is shown in the inse; and (B) Fourier transform of the observed SR-XRD pattern (GSAS Rietveld refinements) showing the Al-H bonds (equatorial plane of the octahedron containing 4 H atoms is selected)

In situ scan of the aged α-AlH_3 sample (station BM01B), heating rate 1 K/min

The *in situ* diffraction patterns of the decomposition of the hydride (aged sample) were collected in the temperature range 25 – 150 °C. Rietveld type refinements of the data were performed (goodness-of-fit parameters for the refinements were all rather large, with wRp in the range 13-28%.) and showed that on heating a linear increase of the unit cell dimensions of AlH_3 takes place in an interval from RT to ~125 °C (a = 4.46; c = 11.83 Å for T = 135 °C; see Figure 3 a and b). The volume expansion is pronouncedly anisotropic, as can be seen from Figure 3b. Indeed, the c-axis is almost constant in the temperature interval 25-125 °C (Δc/c ~ -0.02 %). This contrasts to a significant expansion along [100]: Δa/a ~0.28 %. The latter expansion can mainly be attributed to the elongations of the bridge bonds Al-H-Al aligned along [1 ½], which are expanding from 3.243 to 3.248 Å (Δd/d ~ 0.17 %).

During the heating, a continuous decrease of the intensities of the pattern of AlH3 was observed indicating a gradual decomposition of the crystalline hydride phase, probably forming amorphous aluminium. This decrease was not accompanied by any significant broadening of the peaks. The intensities of the diffraction peaks from Al firstly appeared at ~135 °C and then gradually increased with raising temperature. At T~145 °C, the hydride peaks completely vanished indicating completeness of the transformation $AlH_3 \rightarrow$ Al. The fraction of the hydride observed in the SR-XRD patterns as a function of the temperature is given in Figure 3c.

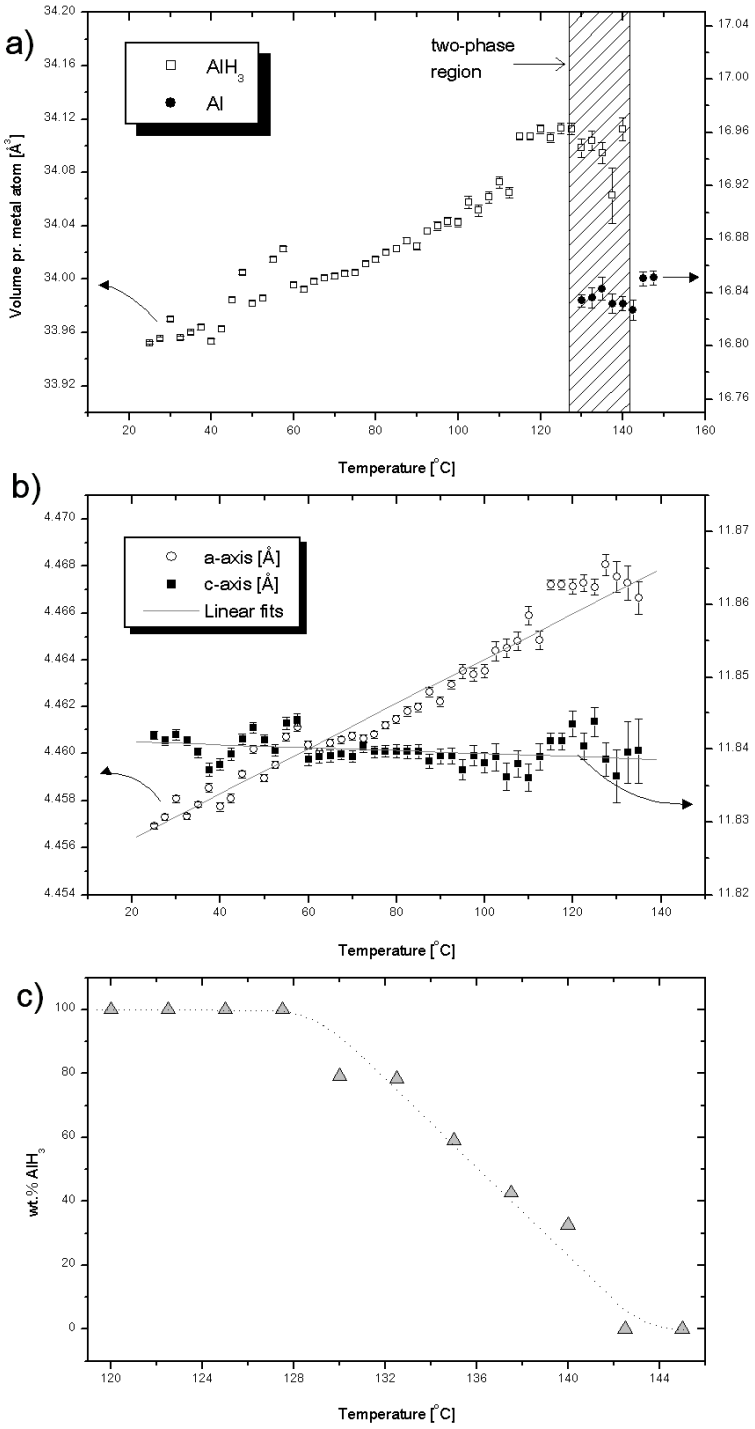

Figure 3: Results from the refinements of the in situ SR-XRD patterns of the aged α-AlH_3 thermal decomposition vs temperature; a) volumes of the unit cells of the crystal structures of alane and Al metal (per one aluminium atom), b) evolution of the unit cell parameters of the hydride during the heating, and c) temperature-dependent fraction of crystalline aluminium hydride (by mass) in the system (the refinements included crystalline aluminium and crystalline aluminium hydride).

Crystal structure of γ-AlH_3 (station BM01B)

The γ-AlH_3 polymorph was for the first time successfully characterised using synchtrotron powder XRD where hydrogen atoms in the structure were located from the difference Fourier synthesis maps. The pattern was indexed as an orthorhombic cell with the unit cell parameters *a* = 5.3806(1); *b* = 7.3555(2), *c* = 5.77509(5) Å and volume *V* of the unit cell of 228.561(7) $Å^3$. An interesting feature of the Al sublattice is the formation of very short Al-Al distances of 2.606 Å between atoms Al2 and Al2. Hydrogen atoms occupy 4 different crystallographic sites occupied by 18 H atoms / unit cell. These included H1 (2*d*: 0, ½ , ½), H2 (4*g*: *x*, *y*, 0), H3 (4*g*: *x*, *y*, 0) and H4 (8*h*: *x*, *y*, 0). In γ-AlH_3 hydrogen atoms form octahedra around Al. Al1 is bonded with 2 H2 and 4 H4 while Al2 is surrounded by H1, H2, 2 H3 and 2 H4. The bonding distances Al-H in the structure are in the range 1.66 -1.79 Å. Despite showing quite a big variation, they all are rather close to the only available binding distance Al-H in α-AlH_3 of 1.712 Å *(8)*. The structure of γ–AlH_3 is composed of AlH_6 octahedra as the building blocks (Figure 4), similar to α-AlH_3. However, these octahedra are differently connected resulting in formation of hydrogen bridge bonds Al-H-Al in α-AlH_3 (Al-H = 1.712 Å; Al-Al = 3.24 Å; $\angle$ 142°) or two different types of bridges in γ-AlH_3, where AlH_6 octahedra of two kinds share vertices and edges. In addition to a normal bridge bond (γ; Al-H = 1.65-1.80 Å; Al-Al = 3.17 Å; $\angle$ 124.9°), a bifurcated bridge bond between two aluminum and two hydrogen atoms is formed. The geometry of this bond (Al-H = 1.68 and 1.70 Å; $\angle$ 100.7°) allows for a close proximity between aluminum atoms Al-Al = 2.606 Å. This appears to be even shorter compared to the Al-Al distances in Al metal (2.86 Å).

The formation of the bifurcated *double bridge* bond Al-2H-Al is a prominent feature of the crystal structure of γ-AlH_3. This feature is unique for the Al-containing hydrides and has not been previously reported for its hydrides.

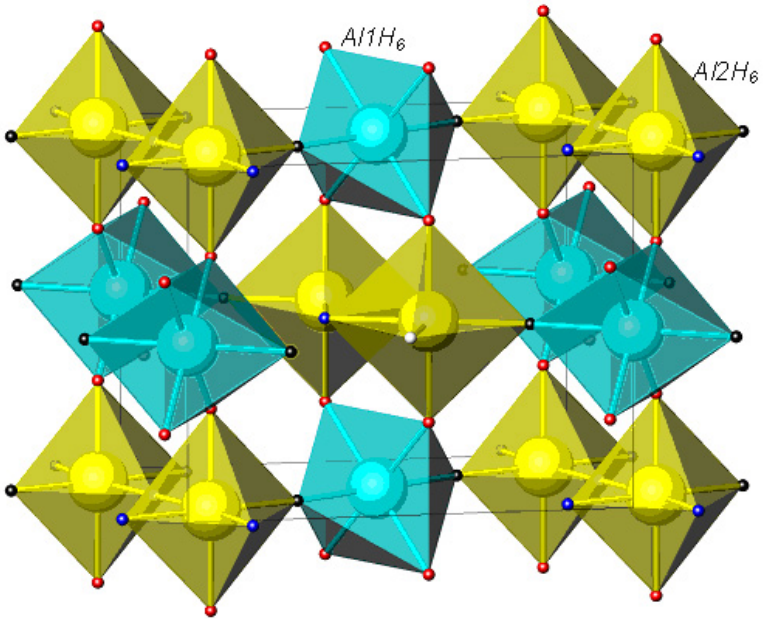

Figure 4: Framework of the AlH_6 octahedra in the crystal structure of γ-AlH_3 showing interconnection between two types of the available AlH_6 units, $Al1H_6$ and $Al2H_6$. Octahedra are connected by vertices ($Al1H_6$-$Al2H_6$) or by edges ($Al2H_6$-$Al2H_6$). This results in formation of normal bridge bonds H-Al-H or double bridge bonds Al-2H-Al (latter case).

In situ scan of the γ-AlH_3 sample (station BM01A), heating rate ½ K/min

The initial sample used in the *in situ* SR-XRD experiment contained mainly γ-AlH_3 with smaller additions of α-AlH_3 and aluminium. A surface plot of a selected range of the experimental data is presented in Figure 5. The γ-AlH_3 starts to decompose at T~80 °C and the content of aluminium and α-AlH_3 starts to increase. As this happens, the anisotropic expansion of the α-AlH_3 unit cell gets more pronounced. The unit cell axes expand almost linearly within limited temperature regions. To get a more detailed view of how the phase transformations proceed, the changes of hydrogen concentrations in the hydride phases were calculated based on the weight fractions of the crystalline phases as obtained from the Rietveld refinements. The assumption that both the α- and the γ-polymorph contain 3 H atoms pr. formula unit was used, an assumption well justified by literature and chemical consideration**.** The result is presented in Figure 6 in the form of 'hydrogen desorption traces'. Formation of the α-phase ('absorption traces' γ to α) consumes less hydrogen than the number of moles hydrogen liberated by the decomposition of γ-AlH_3. It is then natural to assume that this excess of hydrogen is desorbed directly from the γ-AlH_3 *i.e.* due to direct transformation of γ-AlH_3 to aluminium. By this type of argument, two decomposition paths are observed: γ-$AlH_3 \rightarrow$ Aluminium, and γ-$AlH_3 \rightarrow \alpha$-$AlH_3 \rightarrow$ Aluminium. From integrating the 'desorption traces', we find that about 60% of the hydrogen is released in the first process.

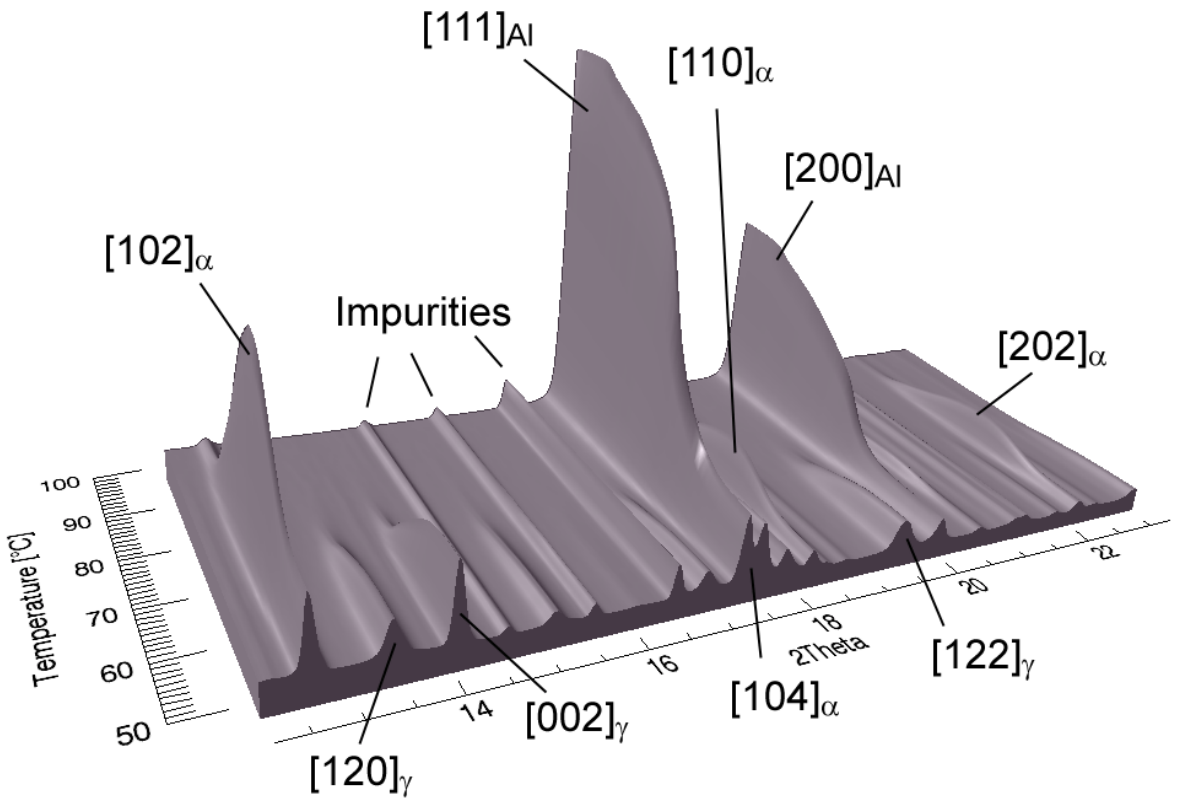

Figure 5: In situ SR-XRD pattern of γ-AlH_3 thermal decomposition (in the temperature range 50-100 °C). The γ-AlH_3 peaks observed in the low temperature region diminish as α-AlH_3 starts to form. At even higher temperatures, a relative fast growth of the aluminium peaks is observed.

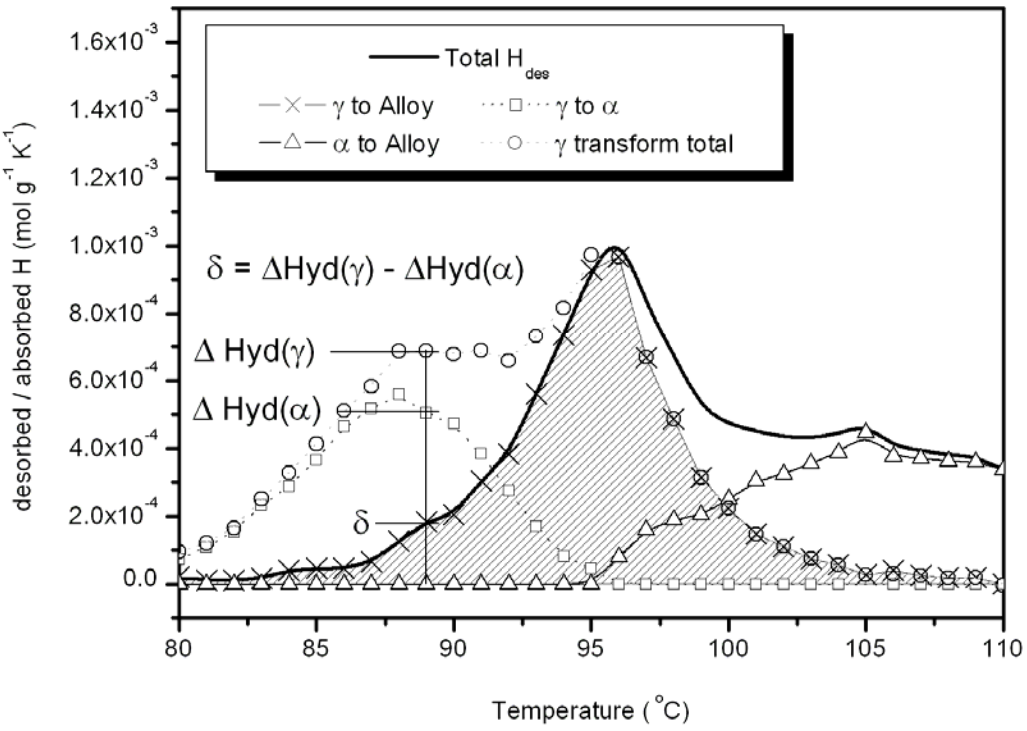

Figure 6: Calculated hydrogen desorption and absorption traces from the in situ SR-XRD patterns of the γ-AlH_3 thermal decomposition. Subtracting the amount of hydrogen used during the formation of α-AlH_3 from the amount of hydrogen released by the decomposition of γ-AlH_3, a net hydrogen desorption trace is found (shaded are) attributed to direct γ-AlH_3 to Alloy phase transformation.

Effect of reactive ball-milling and doping by TiO_2 (BM01A)

By reactive high-energy ball-milling of alane with small additives of TiO_2, the hydrogen desorption temperature is decreased. This effect was studied by *in situ* SR-XRD where samples with different amount of additives and different processing parameters were tested. Example of a multi-pattern is shown in Figure 7. For all samples, at the final stage of the alane-to-aluminium transformation, a negative temperature expansion of the alane unit cell was observed (see Figure 8, alane ball-milled with 2 wt.% TiO_2). For samples without TiO_2 additives, we found that larger grains only decompose at rather high temperatures, while with TiO_2 additives large grains can also decompose at moderately low temperatures (Figure 9). Raman spectra was also obtained during decomposition of several of the samples (also including thermal decomposition of γ-AlH_3). Example of a Raman spectrum obtained during thermal decomposition of α-AlH3 ball-milled with 1 wt.% TiO_2 (anatase) compared with calculated spectra (averaged over direction) by response function method in the DFT scheme (the ab-initio calculations were performed using the ABINIT code [22] based on the planewave pseudopotential method under the local density approximation using Hartwigsen–Goedecker–Hutter pseudopotential) is presented in Figure 10.

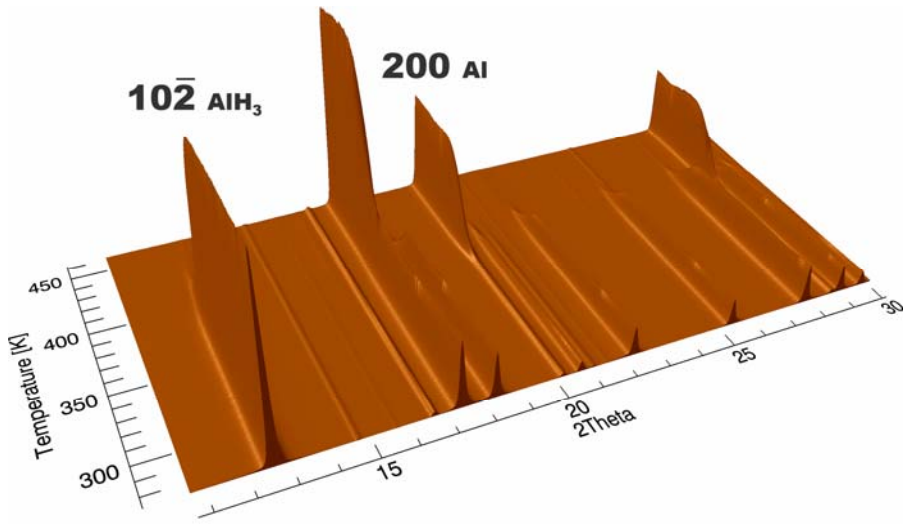

Figure 7 Example of in situ SR-XRD patterns (decomposition of ball-milled alane)

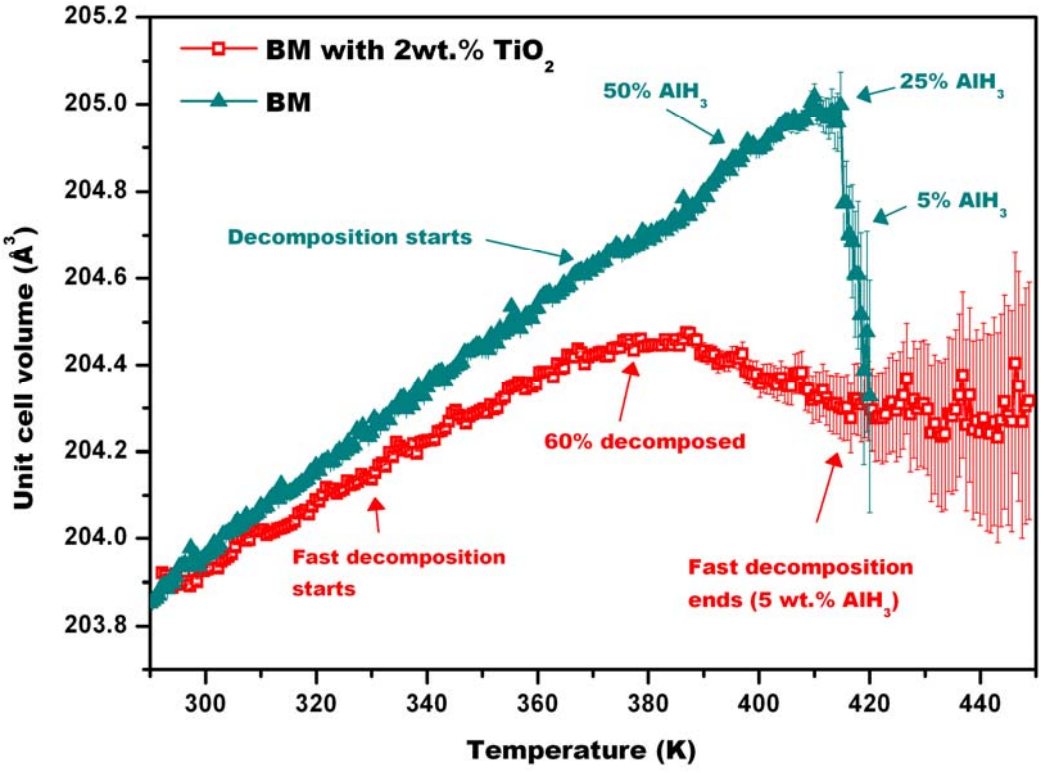

Figure 8: Change of unit cell volume for alane during decomposition (constant heating rate 0.5 K/min; secondary vacuum conditions)

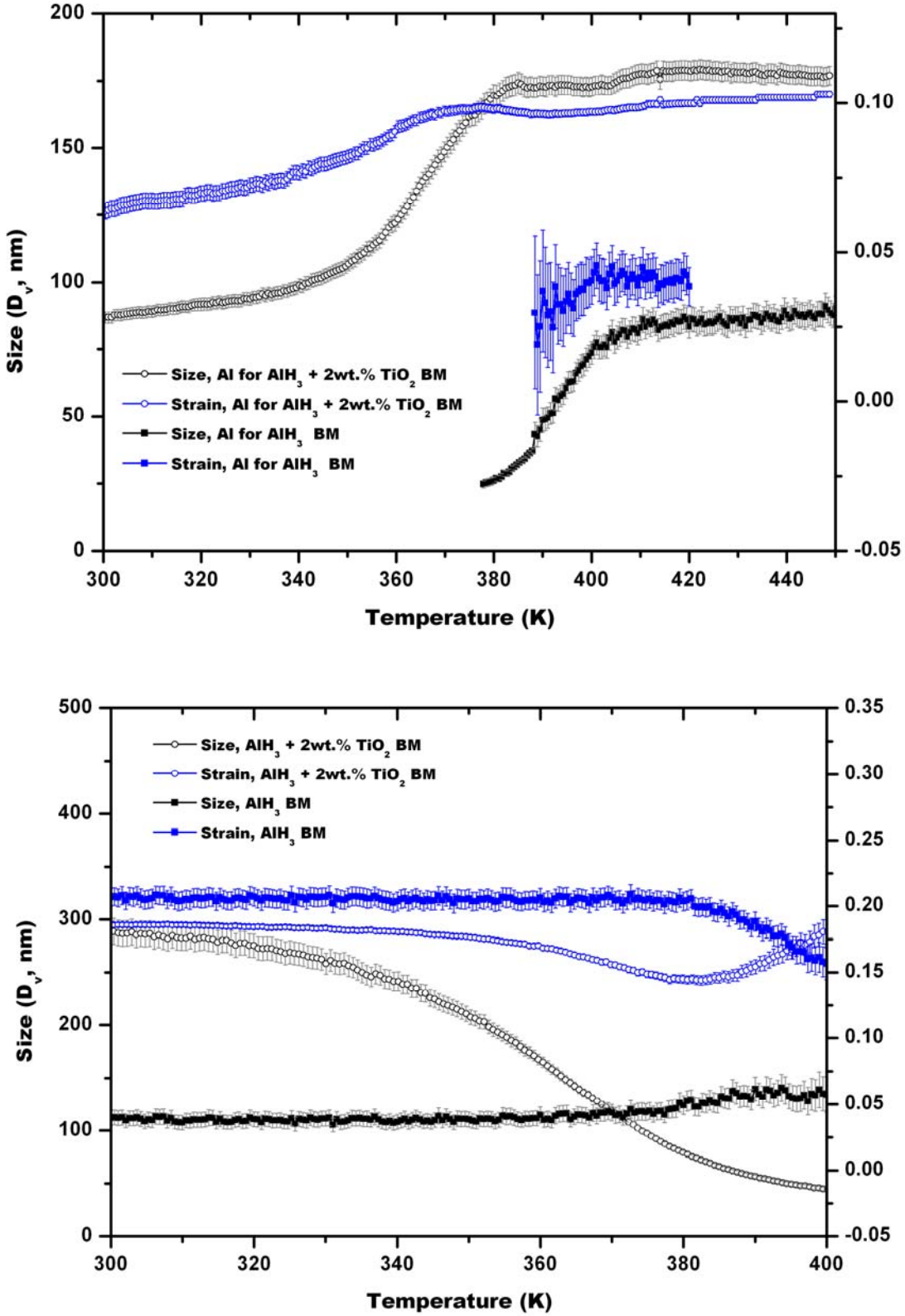

Figure 9: Size and strain in Al (top) and AlH_3 (bottom) vs T during the decomposition (constant heating rate 0.5 K/min; secondary vacuum conditions). Average AlH_3 grain size increase for only-BM sample. Large grains decompose last. For BM with TiO_2, larger particles decompose also at lower T. Aluminium particles grow gradually during decomposition for both BM and BM with TiO_2.

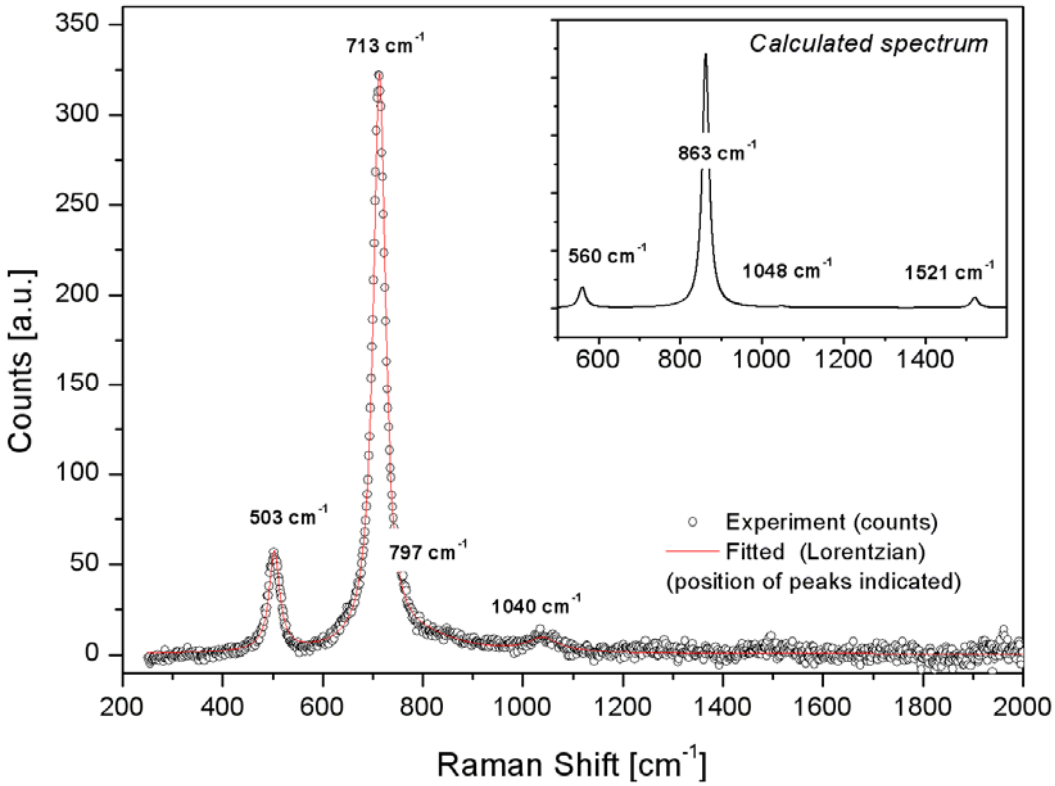

Figure 10: Raman spectrum of α-AlH_3 BM with 1 wt.% TiO2 (first scan) during thermal decomposition including peak fits (Lorenzian peaks). Also shown is calculated spectrum (DFT + RF, using the Abinit DFT package, LDA approx., HGH plane wave pseudo potentials; relaxed UC and atomic pos.); averaged over directions (powder).

6.2. Mg-hydrogen compounds

Low price, abundance and high hydrogenation capacity (up to 7.6 wt.%) put magnesium and its alloys into the row of the most promising materials for hydrogen storage. At the same time, the implementation of these materials into hydrogen storage applications is hampered by kinetic obstacles, caused by: hydrogen impenetrable layers of MgO on the surface of Mg metal; high energy barrier for dissociation of hydrogen molecules on the surface of magnesium metal; and low diffusion parameters of hydrogen in the formed MgH_2. Substantial improvement of hydrogenation kinetics can be reached by the use of ball-milling of MgH_2 in inert atmosphere or Mg in hydrogen gas. The thus created fine powders absorb hydrogen within several minutes, an order of magnitude faster than for non-milled material [23]. Another method to improve kinetics of hydrogenation of Mg-based materials is by doping by catalytic additions of metals or active hydrogen absorbing materials. Time-resolved *in situ* synchrotron X-ray diffraction studies of Mg-H_2 and Mg8Mm20Ni-H_2 (88 at. % Mg + 2 at. % Mm + 10 at. % Ni) systems during absorption and desorption of hydrogen was performed. As was shown in [24] the time-resolved XRD allows determining kinetic characteristics of processes. The use of SR XRD, in its turn, provides much better time resolution and higher precision of

determination of crystallographic parameters of available phases. For example, basing on XRD and SR XRD studies of MgH_2–Nb [25] Huot *et al* established the mechanism of hydride decomposition the interactions with determining the crystallite sizes of available phases and activation energies of constituent processes. Selected results obtained by *in situ* SR-XRD studies of reactive ball-milled (RBM) Mg and Mg8Mm20Ni-H_2 is presented below.

Effect of reactive ball-milling of Mg (BM01A)

Evolution of the diffraction pattern during time-resolved SR XRD studies of the hydrogen desorption from the RBM magnesium hydride into dynamic vacuum and consequent re-hydrogenation at 300 °C under 9.5 bar H_2 gas are shown in Figure 11 *a* and *b*, respectively.

Refinement of the SR XRD data show formation of two allotropic modifications of magnesium hydride – α-MgH_2 with rutile type of structure and an orthorhombic γ-MgH_2 (α-PbO_2 type) [26] high pressure form. Impurities of Fe (originated from wearing out of the milling balls and the vial during the RBM) and MgO (which is present in the initial Mg powder), where detected in addition. The ratio γ-MgH_2/α-MgH_2, 30:70, is close to the maximum reached for the ball-milled MgH_2, 40:60 [27]. Presence of the high-pressure γ-modification of magnesium hydride indicates that the local high-energy collisions between the milling balls and the particles of magnesium create conditions required for the formation of γ-MgH_2, which is formed in MgH_2 under applied static pressures exceeding 0.387 GPa [28].

The observed lattice parameters well agree with the reference data (α-MgH_2: *a*=4.5198, *c*=3.0250 Å [29]; γ-MgH_2: *a*=4.5213, *b*=5.4382, *c*=4.9337 Å [30]). As can be seen from Figure 12, increase of temperature above 100°C during thermal desorption leads to the rise of the crystallite sizes for both modification of MgH_2 from 7 nm at 100°C to 10 nm at 300°C and further to 20 nm in the end of decomposition process at 360 °C. For the Mg metal, formed during desorption, the *crystallites* growth is much more pronounced; from the initial ~20 nm at the beginning of the Mg formation (*ca.* 250°C) to ~150 nm at temperatures above 310°C. This difference between sizes of crystallites can be easily seen in Figure 12b, in which peaks from Mg metal are much narrower than those from both modifications of MgH_2 (e.g. half-width (in 2Θ) of *101* α-MgH_2 is 0.26°, *111* α-MgH_2 is 0.27°, *101* Mg is 0.12°). Further accurate estimation of crystallite sizes for Mg at higher temperatures becomes impossible since contribution of size broadening into the profile parameters of the diffraction pattern became too small compared to the instrumental peak-broadening. The micro-strain parameters obtained from the Rietveld refinement of SR XRD data are rather small, around 0.08(3)%, which are substantially lower than reported by Huot for MgH_2 ball-milled in argon, >1% [31] indicating possible relaxation of the stresses influenced by hydrogen atmosphere preserving decomposition of the hydride during the milling. During subsequent re-hydrogenation the formed α-MgH_2 has average crystallite sizes of 161(13) nm, manifesting the loss in nanocrystallinity.

The decomposed material was rehydrogenated in the SR XRD setup, the evolution of the SR XRD diffraction pattern during 20 minutes of hydrogen absorption is presented in Figure 11*b*. As can be seen, no traces of γ-MgH_2 were observed in this experiment, confirming that this phase can be formed only under high applied static pressures or when subjected to high energy mechanical stresses during milling.

A few seconds after injection of hydrogen into the system, a small isotropic volume expansion (0.1%) of Mg phase occurs (in Figure 13 such changes are presented depending on the amount of MgH_2 formed; in the corresponding SR XRD patterns (not shown) slight yet visible shifts of Mg diffraction peaks are clearly seen). Since crystallographic parameters of other available phases at this stage of hydrogenation remain constant, we reject volume expansion due to heating, and interpret this observation as a formation of hydrogen solid solution in Mg. The quick formation of MgH_x solid solution is supported by fast diffusion of hydrogen in Mg metal [32]. From the isothermal increase of the unit cell volume the hydrogen content in the MgH_x solid solution can be estimated as $x \sim 0.007$.

As the fraction of α-MgH_2 phase is growing, a continuous decrease of the volume of the MgH_x solid solution occurs until it reaches a constant value -0.09% compared to the initial Mg metal. Simultaneously, the unit cell of α-MgH_2 during this stage of hydrogenation decreases as well. Such a decrease can be caused by the mutual contraction between MgH_x and α-MgH_2 during formation of the latter. Such contraction can be observed during contracting envelope or grain boundary attack topochemical forms of hydride phase progression.

A

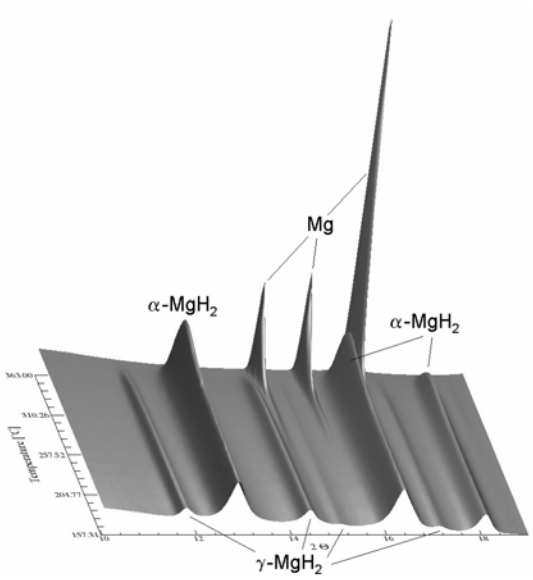

B

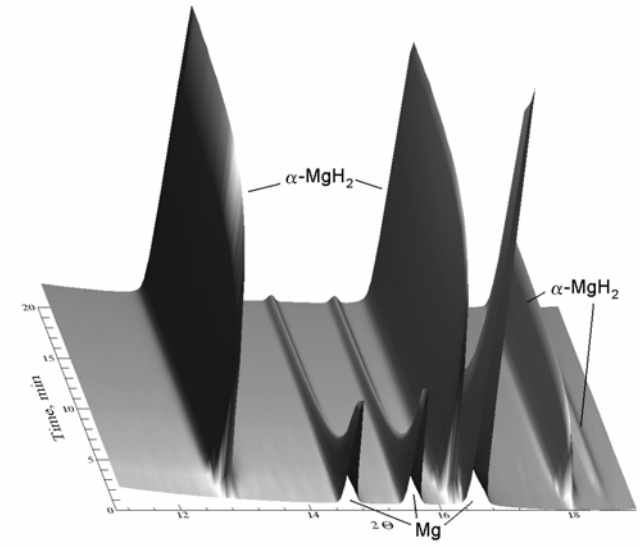

Figure 11: Evolution of in situ SR-XRD pattern of the reactive ball-milled Mg hydride during its (a) thermal decomposition in dynamic vacuum, and (b) re-hydrogenation at 300°C; 9.5 bar H_2

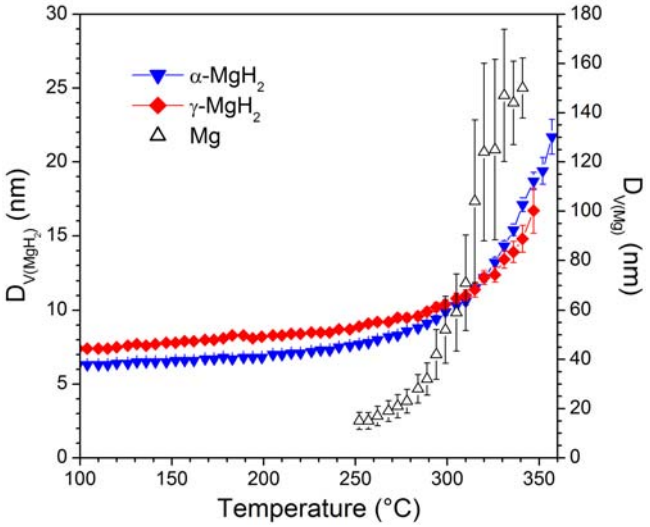

Figure 12: Change in crystallite sizes (D_v, volume weighted average) during thermal decomposition of MgH_2 prepared by RBM. Left Y axis gives sizes for MgH_2 and right Y-axis for Mg.

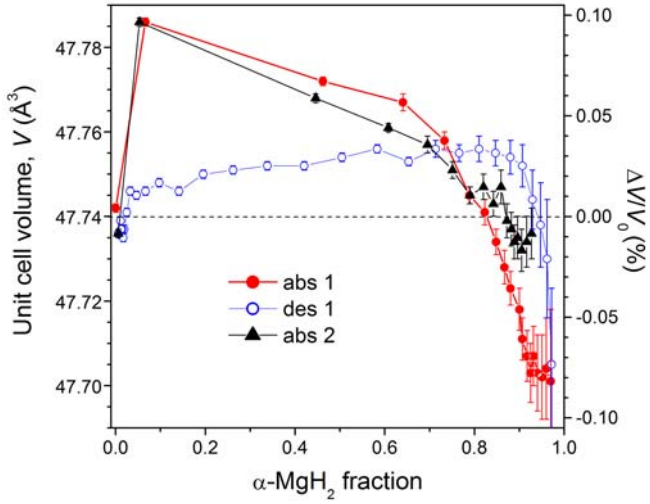

Figure 13: Evolution of Mg-phase unit cell volume vs the conversion during hydrogen absorption-desorption cycling of the RBM Mg after TDS.

Eutectic Mg-Mm-Ni hydrogen system (BM01B)

The as-cast Mg8Mm20Ni alloy of eutectic type contains three phases, Mg, Mg_2Ni and $MmMg_{12}$ [33]. After RBM hydrogenation the *ex situ* SR XRD analysis of the as-milled material revealed the presence of three phases – MgH_2, $Mg_2NiH_{0.3}$ and small amount of Mg_2NiH_4. No traces of $MmMg_{12}$, and, moreover, of any Mm-containing phases have been identified. Such an observation can be explained by complete amorphisation of $MmMg_{12}$ or its disproportionation by the reaction $MmMg_{12} + 13\ ½\ H_2 \rightarrow MmH_3 + 12\ MgH_2$, with amorphous MmH_3 formed where the latter scenario is the most reasonable. In contrast to RBM of pure magnesium in hydrogen described above, no formation of γ-MgH_2 takes place.

For the in situ experiments, the material was put inside the *in situ* SR XRD setup and heated in vacuum in a stepwise mode with patterns measured at several temperatures – 25, 100, 150 °C, then up to 250 °C with a step of 20° and finally at 300 °C.

The following changes in phase-structural composition of the material were observed:

At 100 °C the Mg_2NiH_4 hydride disappeared, completely transforming into $Mg_2NiH_{0.3}$.

At 230 °C the partial recrystallisation of MmH_{3-x} started, the further rise in temperature is accompanied by the growth of the detected amount of MmH_2 from <1 wt. % to ~5 wt.% with a simultaneous growth of crystallite size of MmH_2 up to 8 nm, preserved almost unchanged over all further experiments.

Above 250 °C the α-$Mg_2NiH_{0.3}$ decomposes into Mg_2Ni phase, which is monitored by a sharp drop of the unit cell volume from 322 Å^3 at 250 °C to ~317.5 Å^3 at 300 °C.

MgH_2 starts desorbing hydrogen at 230 °C, at 300 °C the process is finished completely. Note that the temperature of complete decomposition of Mg in the presence of $Mg_2NiH_{0.3}$ and MmH_x is lower by 75° than that for RBM magnesium.

At 300°C there exist three phases in the alloy – Mg metal, Mg_2Ni intermetallic compound and MmH_2 hydride.

The evolution of patterns of the Mg8Mm20Mg alloy during hydrogenation and dehydrogenation at 250 °C is presented in Figure 14, the changes of lattice parameters of $Mg_2NiH_{0...0.3}$ and $MmH_{2...3}$ hydrides during these processes are provided in Figure 15.

The re-hydrogenation of Mg8Mm20Mg alloy starts from the instantaneous formation of α-$Mg_2NiH_{0.3}$ hydride with a sharp rise in its unit cell volume by 6 Å^3. The hydrogenation $MmH_2 \rightarrow MmH_3$, monitored by the decrease of its unit cell (Figure 15), finishes within 15 minutes. Hydrogen desorption at 250 °C from Mg_2NiH_4 finished during 20 minutes; 90% MgH_2 decomposed during 25 min. The hydrogen desorption from the two other constituents of the alloy, $Mg_2NiH_{0.3}$ and MmH_3, is a continuous process lasting for 90 minutes, when the unit cells volumes returned to values before hydrogenation. Finally, a short-run hydrogenation of the Mg8Mm20Ni alloy at 300 °C was performed. The rise in temperature by 50 °C gave the expected acceleration of all processes, the hydrogenation of $Mg_2NiH_{0.4}$ was two times, and $Mg \rightarrow MgH_2$ reaction – three times quicker that at 250°C.

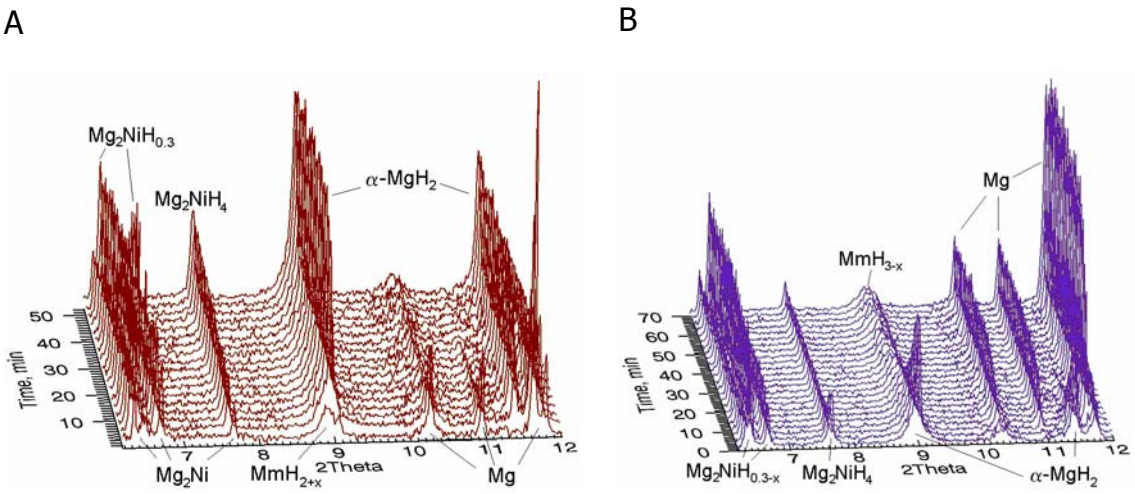

Figure 14: Evolution of SR XRD patterns of the Mg8Mm20Ni alloy during its (a) hydrogenation and (b) dehydrogenation at 250 °C.

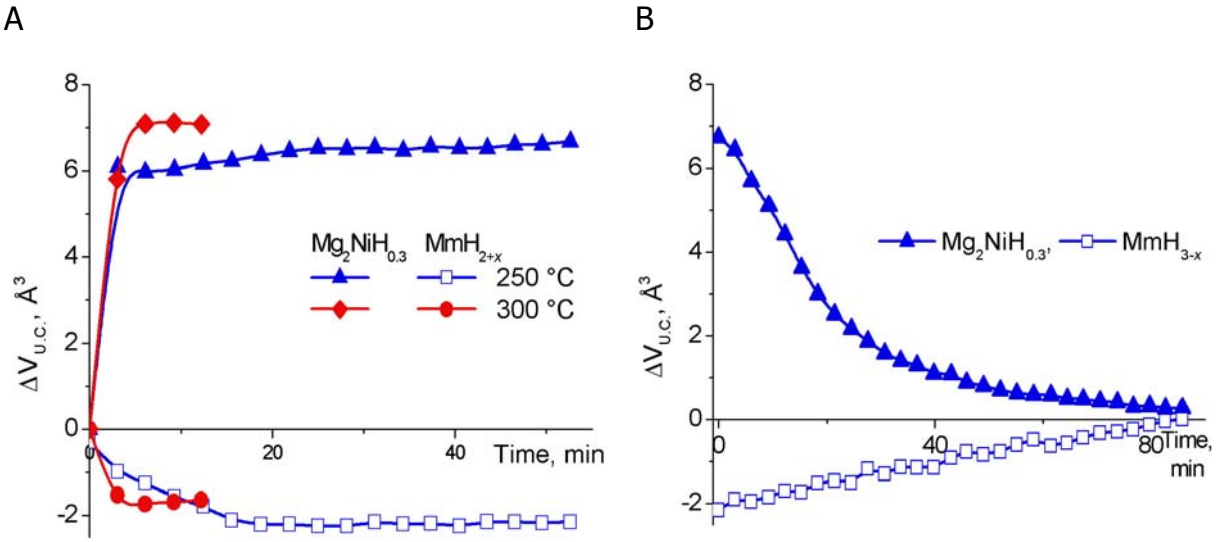

Figure 15: Changes of lattice parameters of MmH_{3-x} and $Mg_2NiH_{0.3-x}$ during hydrogen (a) absorption and (b) desorption.

7. Conclusions

In the present work, we have established the importance of *in situ* Synchrotron X-ray Powder Diffraction in probing mechanism of H uptake and release in metal-hydrogen systems. The current work was aimed on studies of the hydrogenation and dehydrogenation processes in different metal hydride systems at relatively low H_2 pressures 0 - 15 bar and temperatures from ÷100 to 800 °C where a specially designed cell for *in situ* studies in H_2-atmosphere was utilised. Based on the experience obtained during the current work, the setup was also upgraded, e.g. by integrating a cold-trap for additional purification of the hydrogen gas. The scientific outcome of this work was very successful, with seven publications in international journals with referees (including a paper on the structure of γ-AlH_3, awarded the

cover page in the issue of Inorganic Chemistry), about 10 papers in preparation, and numerous presentations, both nationally and at international conferences and workshops.

8. Acknowledgements

We have a pleasure to express our sincere appreciation to the members of the scientific staff at the Swiss-Norwegian Beam Lines for the fruitful collaboration and friendly support.

9. References

1. V.A.Yartys, A.B.Riabov, R.V.Denys, M.Sato, R.G.Delaplane. Novel Intermetallic Hydrides.// *J.Alloys and Compounds,* **408-412** (2006) 273-279.

2. J. P. Maehlen, V. A.Yartys.// Aluminum Trihydride Studied By Powder Synchrotron X-Ray Diffraction: Crystal Structure and Thermal Decomposition.// *Advanced Materials for Energy Conversion III.* Symposium held during the TMS 2006 Annual Meeting in San Antonio, Texas, USA, March 12-16, Edited by D.Chandra, J.Petrovic, R.G.Bautista, A.Imam (2006) 77-85.

3. V.A.Yartys, R.V.Denys, J.P.Maehlen, Ch.Frommen, M.Fichtner, B.M.Bulychev, H.Emerich.// Double bridge bonding of aluminium and hydrogen in the crystal stucture of γ-AlH_3.// *Inorganic Chemistry*, **46** (4) (2007) 1051-1055.

4. J.P.Maehlen, V.A.Yartys, A.B.Riabov, A.Budziak, H.Figiel, J.Żukrowski.// Synchrotron X-ray diffraction study of $ErMn_2D_2$.// *J.Alloys and Compounds*, **437** (2007) 140-145.

5. J. P. Maehlen, V.A.Yartys, R.V.Denys, M.Fichtner, Ch.Frommen, B.M.Bulychev, P.Pattison, H.Emerich, Y.E. Filinchuk, D.Chernyshov. Thermal Decomposition of AlH_3 Studied by *in situ* Synchrotron X-ray Diffraction and Thermal Desorption Spectroscopy.// *J.Alloys and Compounds* **446-447**, 31 October 2007, Pages 280-289.

6. R. V.Denys, A. B. Riabov, V. A. Yartys, R. G. Delaplane, M. Sato. Hydrogen storage properties and structure of $La_{1-x}Mg_x(Ni_{1-y}Mn_y)_3$ intermetallics and their hydrides.// *J. Alloys and Compounds*, **446-447**, 31 October 2007, Pages 166-172. PII: S0925-8388(07)00030-8.

7. R.V. Denys, V.A. Yartys, Masashi Sato, A.B. Riabov, R.G. Delaplane. Crystal chemistry and thermodynamic properties of anisotropic Ce2Ni7H4.7 hydride// Journal of Solid State Chemistry, Volume **180**, Issue 9, September 2007, Pages 2566-2576.

8. R.V. Denys, A.B. Riabov, V.A. Yartys, Masashi Sato, R.G. Delaplane. Mg substitution effect on the hydrogenation behaviour, thermodynamic and structural properties of the La2Ni7–H(D)2 system//Journal of Solid State Chemistry, Volume **181**, Issue 4, April 2008, Pages 812-821.

9. M. Stange, J. P. Maehlen, V. A. Yartys, P. Norby, W. van Beek & H. Emerich. *J Alloy Compd* **404** (2005) 604-608.

10. P. Norby. Journal of the American Chemical Society **119** (1997) 5215-5221.

11. E. K. Andersen, I. G. K. Andersen, P. Norby & J. C. Hanson. *J Solid State Chem* **141** (1998) 235-240.

12. Fit2D (http://www.esrf.eu/computing/scientific/FIT2D/)

13. H. M. Rietveld. *J Appl Crystallogr* **2** (1969) 65-71.

14. C. Larson & R. B. v. Dreele. (LANL, Los Alamos, 1994).

15. P. Thompson, D. E. Cox & J. B. Hastings. *J Appl Crystallogr* **20** (1987) 79-83.

16. C. J. Howard. *J Appl Crystallogr* **15** (1982) 615-620.

17. L. W. Finger, D. E. Cox & A. P. Jephcoat. *J Appl Crystallogr* **27** (1994) 892-900.

18. F. M. Brower, N. E. Matzek, P. F. Reigler, H. W. Rinn, C. B. Roberts, D. L. Schmidt, J. A. Snover & K. Terada. *Journal of the American Chemical Society* **98** (1976) 2450-2453.

19. E. Finholt, A. C. Bond & H. I. Schlesinger. *Journal of the American Chemical Society* **69** (1947) 1199-1203.

20. J. W. Turley & H. W. Rinn. *Inorg Chem* **8** (1969) 18-&.

21. G. Sandrock, J. Reilly, J. Graetz, W. M. Zhou, J. Johnson & J. Wegrzyn. *Applied Physics a-Materials Science & Processing* **80** (2005) 687-690.

22. X. Gonze, J.-M. Beuken, R. Caracas, F. Detraux, M. Fuchs, G.-M. Rignanese, L. Sindic, M. Verstraete, G. Zerah, F. Jollet, M. Torrent, A. Roy, M. Mikami, Ph. Ghosez, J.-Y. Raty and D.C. Allan, Computat. Mater. Sci. **25** (2002), p. 478; http://www.abinit.org

23. Huot J, Liang G, Boily S, Van Neste A, Schulz R. J Alloys Compd 1999;293-295:495

24. Jensen TR, Andreasen A, Vegge T, Andreasen JW, Ståhl K, Pedersen AS, Nielsen MM, Molenbroek AM, Besenbacher F. Int J Hydrogen Energy 2006;31:2052

25. Huot J, Pelletier JF, Lurio LB, Sutton M, Schulz R. *J Alloys Compd* 2003;348:319

26. Bastide J-P, Bonnetot B, Létoffé J-M, Claudy P. *Mat Res Bull* 1980;15:1215

27. K.-F. Aguey-Zinsou, J.R. Ares Fernandez, T. Klassen, R. Bormann. Using MgO to improve the (de)hydriding properties of magnesium. *Mat. Res. Bull.* **41** (6) (2006) 1118-1126.

28. Vajeeston P, Ravindran P, Hauback BC, Fjellvåg H, Kjekshus A, Furuseth S, Hanfland M. *Phys Rev B* 2006;73:#224102

29. S. Ono, Y. Ishido, K. Imanari, T. Tabata, Y. K. Cho, R. Yamamoto and, M. Doyama Phase transformation and thermal expansion of Mg---Ni alloys in a hydrogen atmosphere. *J. Less-Common Met.* **88** (1982) 57-61.

30. M. Bortz, B. Bertheville, G. Böttger, K. Yvon. Structure of the high pressure phase γ-MgH_2 by neutron powder diffraction. *J. Alloys Compd*. **287** (1999) L4–L6.

31. Zaluska A, Zaluski L, Ström-Olsen JO. *J Alloys Compd* 1999;289:197

32. C. Nishimura, M. Komaki, M. Amano. Hydrogen permeation through magnesium. *J. Alloys Compd.* **293–295** (1999) 329–333.

33. Løken S, Solberg JK, Maehlen JP, Denys RV, Lototsky MV, Tarasov BP, Yartys VA*. J Alloys Compd* 2007;446–447:114

10. Appendix. Copies of published papers.

V.A.Yartys, A.B.Riabov, R.V.Denys, M.Sato, R.G.Delaplane. Novel Intermetallic Hydrides.// *J.Alloys and Compounds,* **408-412** (2006) 273-279.

J. P. Maehlen, V. A.Yartys.// Aluminum Trihydride Studied By Powder Synchrotron X-Ray Diffraction: Crystal Structure and Thermal Decomposition.// *Advanced Materials for Energy Conversion III.* Symposium held during the TMS 2006 Annual Meeting in San Antonio, Texas, USA, March 12-16, Edited by D.Chandra, J.Petrovic, R.G.Bautista, A.Imam (2006) 77-85.

V.A.Yartys, R.V.Denys, J.P.Maehlen, Ch.Frommen, M.Fichtner, B.M.Bulychev, H.Emerich.// Double bridge bonding of aluminium and hydrogen in the crystal stucture of γ-AlH_3.// *Inorganic Chemistry*, **46** (4) (2007) 1051-1055.

J.P.Maehlen, V.A.Yartys, A.B.Riabov, A.Budziak, H.Figiel, J.Żukrowski.// Synchrotron X-ray diffraction study of $ErMn_2D_2$.// *J.Alloys and Compounds*, **437** (2007) 140-145.

J. P. Maehlen, V.A.Yartys, R.V.Denys, M.Fichtner, Ch.Frommen, B.M.Bulychev, P.Pattison, H.Emerich, Y.E. Filinchuk, D.Chernyshov. Thermal Decomposition of AlH_3 Studied by *in situ* Synchrotron X-ray Diffraction and Thermal Desorption Spectroscopy.// *J.Alloys and Compounds* **446-447**, 31 October 2007, Pages 280-289.

R. V.Denys, A. B. Riabov, V. A. Yartys, R. G. Delaplane, M. Sato. Hydrogen storage properties and structure of $La_{1-x}Mg_x(Ni_{1-y}Mn_y)_3$ intermetallics and their hydrides.// *J. Alloys and Compounds*, **446-447**, 31 October 2007, Pages 166-172. PII: S0925-8388(07)00030-8.

R.V. Denys, V.A. Yartys, Masashi Sato, A.B. Riabov, R.G. Delaplane. Crystal chemistry and thermodynamic properties of anisotropic Ce2Ni7H4.7 hydride// Journal of Solid State Chemistry, Volume **180**, Issue 9, September 2007, Pages 2566-2576.

R.V. Denys, A.B. Riabov, V.A. Yartys, Masashi Sato, R.G. Delaplane. Mg substitution effect on the hydrogenation behaviour, thermodynamic and structural properties of the La2Ni7–H(D)2 system//Journal of Solid State Chemistry, Volume **181**, Issue 4, April 2008, Pages 812-821.

ELSEVIER

Journal of Alloys and Compounds 408–412 (2006) 273–279

Journal of ALLOYS AND COMPOUNDS

www.elsevier.com/locate/jallcom

Novel intermetallic hydrides

V.A. Yartys [a,*], A.B. Riabov [b], R.V. Denys [b,c], Masashi Sato [a], R.G. Delaplane [c]

[a] *Institute for Energy Technology, P.O. Box 40, Kjeller, NO 2027, Norway*
[b] *Physico-Mechanical Institute of the National Academy of Sciences of Ukraine, 29601 Lviv, Ukraine*
[c] *Studsvik Neutron Research Laboratory, Uppsala University, Sweden*

Available online 2 August 2005

Abstract

The paper focuses on structural chemistry of novel intermetallic hydrides with unusual structural properties. In such "anisotropic" hydrides, a huge expansion proceeds in a sole crystallographic direction and leads to a dramatic differentiation of the properties of the hydrides along the direction of the expansion and normal to it. The behaviour of the "anisotropic" hydrides is dominated by the metal–hydrogen and hydrogen–hydrogen interactions in contrast to the "conventional" intermetallic hydrides where the metal–metal interactions are the most important ones. In sharp contrast to the known crystal structures of intermetallic hydrides, in "anisotropic" hydrides deuterium atoms do not fill *initially existing* interstices but, instead, attract rare earth atoms into their surrounding and form *new D-occupied sites*. This paper will summarise our recent research on the "anisotropic" hydrides with a particular focus on two groups of materials: (a) RENiIn-based deuterides (RE = rare earth metal) containing the shortest known separation of hydrogen atoms in the structures of metal hydrides and (b) $RENi_3$–($CeNi_3$) and RE_2Ni_7–(La_2Ni_7)-based deuterides which develop unusually large (59–63%) expansion of the constituent $RENi_2$ layers.

Keywords: Hydrogen storage materials; Intermetallics; Neutron diffraction; Crystal structure and symmetry

1. Introduction

Hydrogenation of intermetallic compounds (IMC), from gas or electrochemically, leads to a storage of atomic, interstitial hydrogen in the metal lattice providing a high ratio of H/M (>1) and a high volume density of the stored hydrogen compared to liquid hydrogen. Intermetallic hydrides exhibit a close interrelation between crystal chemistry and hydrogen sorption properties allowing alteration and optimisation of their H storage performance. Hydrogen accommodation by the metal lattice is typically accompanied by modest (few percent) changes of the interatomic metal–metal distances. Consequently, H atoms enter the interstices, which are originally available in the virgin intermetallics. However, this "typical" case does not cover a large group of very interesting and so far insufficiently studied compounds, the so-called "anisotropic" hydrides. In such hydrides, a huge expansion proceeds in a sole crystallographic direction and leads to a dramatic differentiation of the properties of the hydrides along the direction of the expansion and normal to it. This paper will summarise our recent research on the "anisotropic" hydrides with a particular focus on two groups of materials.

(a) RENiIn-based deuterides (RE = rare earth metal) containing the shortest known separation of hydrogen atoms in the structures of metal hydrides, 1.56–1.60 Å and, consequently, providing the highest local volume content of H [1]. The effect of substitution of the constituent elements, RE, Ni and In, on the crystal structure and thermodynamics of the IMC–H_2 systems, will be presented and discussed.
(b) $RENi_3$–($CeNi_3$) and RE_2Ni_7–(La_2Ni_7)-based deuterides are built from the two kinds of metal slabs, $RENi_5$ and $RENi_2$. They stack along $[0\,0\,1]_{hex}$, the direction of anisotropic expansion of the lattice. Such an expansion (20–31%) proceeds within the $RENi_2$ slabs only and leads to an incredible (59–63%) expansion of these layers. In sharp contrast to the known crystal structures of intermetallic hydrides, in $CeNi_3D_{2.8}$ [2] and $La_2Ni_7D_{6.5}$

* Corresponding author. Tel.: +47 63 80 64 53; fax: +47 63 81 29 05.
E-mail address: volodymyr.yartys@ife.no (V.A. Yartys).

0925-8388/$ – see front matter © 2005 Elsevier B.V. All rights reserved.
doi:10.1016/j.jallcom.2005.04.190

(present study) deuterium atoms do not fill *initially existing* interstices but, instead, attract rare earth atoms into their surrounding and form *new D-occupied sites*, RE_3Ni and RE_3Ni_3.

The behaviour of the "anisotropic" hydrides is dominated by the metal–hydrogen and hydrogen–hydrogen interactions in contrast to the "conventional" intermetallic hydrides where the metal–metal interactions are the most important ones.

2. Experimental

The alloys were prepared by arc melting of mixtures of high purity constituent metals. A slight excess of rare earth metals, 1 at.%, was used to compensate their evaporation during the melting. As cast alloys were sealed into the evacuated quartz tubes and homogenised by high-temperature annealing, followed by quenching into the mixture of ice and water.

Phase-structural composition of the alloy and their corresponding hydrides was characterised by powder X-ray diffraction (Siemens D5000 diffractometer; Cu $K\alpha_1$ radiation; Bragg–Brentano geometry; position sensitive detector).

The prepared alloys were first activated by heating for 1 h at 400 °C in secondary vacuum ($\sim 10^{-5}$ mbar) and then saturated with deuterium gas (99.8% purity) under pressures of 1–10 bar D_2.

The deuterides were studied either ex situ (in *V* cans filled by Ar) or in situ under the pressure of deuterium gas. In the latter case, they were placed into the quartz tube ($CeNi_3D_{2.8}$) or into the stainless steel autoclave ($NdNi_{1-x}Cu_xIn_{1-y}Al_yD_z$).

Powder neutron diffraction (PND) data were collected at the R2 reactor at Studsvik Neutron Research Laboratory using SLAD instrument ($\lambda = 1.117$ Å) and the high-resolution diffractometer NPD ($\lambda = 1.470$ Å). The NPD instrument uses 35 ^{3}He counters to measure the intensities in 2θ steps of 0.08° to cover a 2θ range of 4.0–137°. The SLAD instrument uses a position sensitive detector system. The data were fully corrected for scattering due to the absorption and then normalised to the vanadium standard. During the refinements of the in situ experiments peaks from the stainless steel tube were excluded from the refinements.

The PND studies of the $CeNi_3D_{2.8}$ were performed on the D1B diffractometer, Institute Laue Langevin, Grenoble.

Crystal structure data were derived by Rietveld profile refinements using the GSAS software [3].

3. RENiIn-based hydrides

NdNiIn intermetallic crystallises with the ZrNiAl-type hexagonal structure (space group $P\bar{6}2m$; $a = 7.5202$; $c = 3.9278$ Å). Two different deuterides, β (0.4–0.67 at.H/f.u.) and γ (1.2–1.6 at.H/f.u.) formed by NdNiIn were structurally characterised by PND [1]. Structural properties of the higher, γ-deuteride $NdNiInD_{1.2}$ are very unusual. It is formed via anisotropic expansion of the hexagonal unit cell along [0 0 1] ($\Delta c/c = 16.5\%$) leading to the *double* occupancy of the trigonal bypiramidal (TB) sites Nd_3Ni1_2 and a formation of the D···D pairs with D–D distance of 1.56 Å (Fig. 1). At lower D content, in the β-deuteride $NdNiInD_{0.6}$, half of hydrogen is removed from the bypiramidal sites and deuterium atoms randomly occupy every second Nd_3Ni1 tetrahedron. Volume expansion in this case is relatively small, 3.6%, and isotropic.

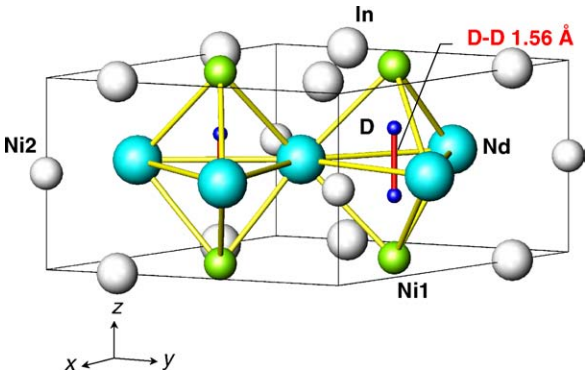

Fig. 1. Crystal structure of $NdNiInD_{1.2}$ containing short D–D distances of 1.56 Å. 3 Nd in 3*g* (0.6440, 0, 1/2); 2 Ni1 in 2*c* (1/3, 2/3, 0); 1 Ni2 in 1*b* (0, 0, 1/2); 3 In in 3*f* (0.2473, 0, 0); 3.6 D in 4*h* (1/3, 2/3, 0.6707).

The most important feature of the $NdNiInD_{1.2}$ is that it does not obey the "rule of 2 Å", empirically known for the metal hydrides, the shortest found separation between hydrogen atoms which has been considered as a lowest possible value for the distance between H atoms thus imposing limits on the maximum volume hydrogen storage capacity of the metal hydrides. Naturally, a decrease in this limiting distance down from 2 Å leads to a corresponding rise in the volume content of hydrogen in the metal hydrides.

In order to understand better the reasons for the H···H pairing in the NdNiIn-based hydrides, we have studied the effect of the replacement of the constituent elements by chemically related substitutes on the structural and thermodynamic behaviours. Ni substitution by Cu and In substitution by Al have been tried. Two related to NdNiIn equiatomic ABC intermetallics, NdCuIn ($a = 7.480$; $c = 4.219$ Å) and NdNiAl ($a = 7.016$; $c = 4.062$ Å) are isostructural to NdNiIn and crystallise with the ZrNiAl type structures. Opposite volume effects are observed on substitution: unit cell volume for the Cu compound is 6.2% higher compared to NdNiIn, while Al-based intermetallic has a significantly contracted unit cell ($\Delta V/V = -10\%$).

A complete range of solid solutions is formed between NdNiIn and NdCuIn; a gradual increase of c_{hex} and *V* accompanies an increase of Cu content. In contrast, in case of Al, only a limited solubility takes place between compositions NdNiIn and $NdNiIn_{0.75}Al_{0.25}$. The substitution significantly decreases both *a* and *V* leaving *c* practically constant. Three types of interstices most favourable for the insertion of hydrogen atoms, which exist in the structures of the Nd(Ni,Cu)(In,Al) intermetallic alloys are shown in Fig. 2: TB

Table 1
Ni/Cu distribution in the 2*c* and 1*b* sites of the $NdNi_{1-x}Cu_xIn$-based materials

	Ni/Cu stoichiometry	Ni/Cu 2*c* (PND)	Ni/Cu 1*b* (PND)	$d_{Ni(Cu)–D}$ (Å, PND)
$NdNi_{0.75}Cu_{0.25}In$	3/1	7/1	1/1	1.667
$NdNi_{0.50}Cu_{0.50}In$	1/1	7/4	1/3	1.84

Table 2
Types of hydrides formed in the $NdNi_{1-x}Cu_xIn_{1-y}Al_y$–$D_2$ systems

	Structure type of hydride	*x*	*y*	Expansion	Filled interstices (as in Fig. 2)
I	γ-$LaNiInD_{1.63}$ [3]	≤0.05	≤0.05	A	
II	β-$RNiInD_{0.67}$ [1]	≥0.25	0	I	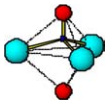
III	$NdNiIn_{0.875}Al_{0.125}D_{0.7}$	0	0.125	I	
IV	$NdNiIn_{0.75}Al_{0.25}D_{1.3}$	0	0.25	A	

A, anisotropic; I, isotropic.
Type II hydrides are present as secondary phases in all the Type I hydrides-based samples. (I) D–D pair in Nd_3Ni1_2 (D1) + D in Nd_3Ni2In_2 (D2); (II) single occupancy of the Nd_3Ni1; (III) single occupancy of the Nd_3Ni1 (D1) + D in Nd_3Ni2In_2 (D2); (IV) single occupancy of the Nd_3Ni1 (D1) + D in Nd_2Ni1In (D2).

$Nd_3[(Ni,Cu)1]_2$; O octahedron $Nd_3[(Ni,Cu)2](In,Al)_2$ and T tetrahedron $Nd_2(In,Al)[(Ni,Cu)1]$.

Analysis of the PND data concludes that Cu substitution for Ni proceeds with a strong preference for the 1*b* site (Table 1); the level of Ni substitution in the 2*c* site is much lower. In the 1*b* site, transition element is surrounded by a trigonal prism of In. Possibly, In–Cu bonds are stronger compared to the Ni–In ones.

Substitutions significantly affect the mechanism of the formation of the hydrides. Four different types of the hydrides were identified in the studied systems and are characterised in Table 2.

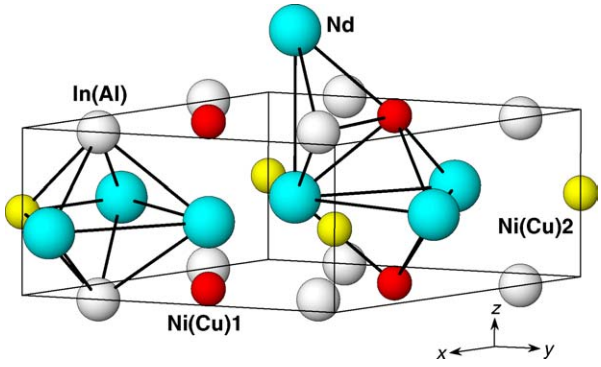

Fig. 2. Hexagonal ZrNiAl-type structure formed in the Nd(Ni,Cu)(In,Al) alloys. Three most favourable for the insertion of hydrogen atoms types of interstices, TB $Nd_3[(Ni,Cu)1]_2$, O $Nd_3[(Ni,Cu)2](In,Al)_2$ and T $Nd_2(In,Al)[(Ni,Cu)1]$ are shown.

Hydride I containing the D···D pair was formed in the samples with low copper and aluminium contents ($x \leq 0.05$) only. In addition to the double-occupied Nd_3Ni1_2 trigonal bipyramids, the octahedral $Nd_3Ni(Cu)2In_2$ sites are simultaneously filled by D atoms. It seems that the filling of these sites becomes possible only as associated with the formation of short D–D distances in the trigonal bipyramid. The probable reason for that is an isotropic expansion of the unit cell which makes In–D2 distances sufficiently large (In–D ≈2.28 Å) thus lifting the blocking effect of In on hydrogen insertion into the site.

4. $RENi_3$–D_2 and RE_2Ni_7–D_2 systems

From structural point of view, in $NdNiInD_{1.2}$, the appearance of short H–H distances correlates with an anisotropic uniaxial lattice expansion on hydrogenation (16%). Thus, we have extended our studies to the hydrides where this feature is even more pronounced.

One important example of “anisotropic” structures represents hexagonal (trigonal) hydrides formed on the basis of $RENi_3$ and RE_2Ni_7 intermetallics in the binary systems of rare earth metals with nickel. Their crystal structures are closely related, and can be presented as a stacking of the

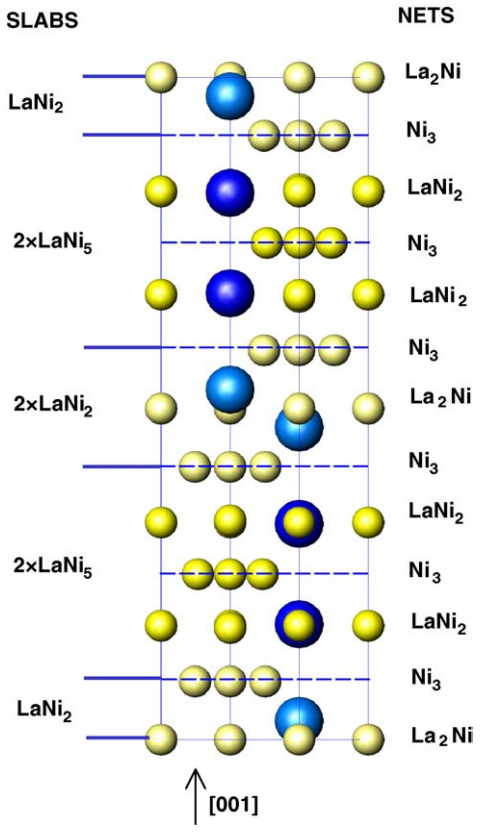

Fig. 3. The crystal structure of La_2Ni_7 shown as composed of the slabs $LaNi_2$ and $LaNi_5$ and the nets $LaNi_2$, Ni_3 and La_2Ni.

$CaCu_5$- and $MgZn_2$-type slabs along [0 0 1]. Combination $1 \times RENi_5 + 2 \times RENi_2$ provides the overall stoichiometry $3 \times RENi_3$. For the RE_2Ni_7 compounds the ratio of the $RENi_5$ and $RENi_2$ slabs is 1:1. $CeNi_3$ structure contains 12 types of tetrahedral sites with three kinds of surrounding, Ce_2Ni_2, $CeNi_3$ and Ni_4. The same type of the surrounding of the tetrahedral sites, RE_2Ni_2, $RENi_3$ and Ni_4, can be found for the RE_2Ni_7 crystal structures. Stacking of the $LaNi_2$ and $LaNi_5$ slabs and containing the plain (Ni_3 and $LaNi_2$) and "buckled" (La_2Ni) nets in the structure of La_2Ni_7 is shown in Fig. 3.

5. $CeNi_3D_{2.8}$

During the hydrogenation, the hexagonal $CeNi_3$ transforms into an orthorhombic $CeNi_3D_{2.8}$ and an extremely pronounced expansion along the [0 0 1] direction, 30.7%, occurs [2]. PND of this deuteride has shown that in the $CeNi_3D_{2.8}$ the lattice elongation does not touch the $CeNi_5$ parts which even "shrink" along [0 0 1] (−2.8%). This contrasts to the behaviour of the $CeNi_2$ slabs where the expansion is uniquely high (63.1%). Thus, the metal sublattice is completely rebuilt. Especially pronounced changes are observed for the chains of the Ni_4 and $CeNi_3$ tetrahedra, which are aligned along [0 0 1]. In the $CeNi_3$ intermetallic compound the Ni_4 tetrahedra are nearly regular. In contrast, after the expansion to form $CeNi_3D_{2.8}$ some of these tetrahedra become so expanded that they do not exist any more (see Table 3). The same conclusion is valid for the aligned along [0 0 1] $CeNi_3$ sites: Ce–Ni bonding is broken in the 0 0 z direction.

Occupancy/vacancy of the $CeNi_2$ and $CeNi_5$ parts by deuterium is in agreement with the observed values of volume expansion. All D atoms are located inside the $CeNi_2$ part and on the border of $CeNi_2$ and $CeNi_5$ leaving $CaCu_5$-type part empty. Deuterium atoms occupy eight different sites. The limiting stoichiometric composition is $D/CeNi_3 = 3.0$.

6. $La_2Ni_7D_{6.5}$

Studies of the crystallographically similar to $CeNi_3D_{2.8}$ anisotropic hydrides are necessary to understand general features governing their formation. A related new example is the $La_2Ni_7D_{6.5}$ deuteride. The hexagonal crystal structure of the original La_2Ni_7 intermetallic alloy (Ce_2Ni_7 type of structure; space group $P6_3/mmc$; $a = 5.059(3)$; $c = 24.68(2)$ Å) similarly to $CeNi_3$ expands exclusively along [0 0 1] ($La_2Ni_7D_{6.5}$: $a = 4.9534(6)$; $c = 29.579(5)$ Å; $\Delta a/a = -2.1\%$; $\Delta c/c = 19.8\%$; $\Delta V/V = 14.9\%$). The expansion is less pronounced compared to $CeNi_3D_{2.8}$. The observed in present study volume expansion of the unit cell of La_2Ni_7 on hydrogenation is less pronounced compared to the data published in [4] for $La_2Ni_7H_x$ ($a = 5.01$; $c = 31.0$ Å; $\Delta V/V = 23.1\%$). This difference indicates that further hydrogen absorption takes place during an increase of the synthesis pressure from 10 bar used in current work to 80 bar H_2 applied in [4].

For the two types of the constituent slabs, the hydrogenation behaviour is opposite: the $MgZn_2$-type slab expands along c by 58.7% while the $CaCu_5$-type slab remains unaffected by hydrogen absorption and even slightly shrinks ($\Delta c/c = -0.5\%$). These features of the crystal structure of $La_2Ni_7D_{6.5}$ completely resemble the behaviour of $CeNi_3D_{2.8}$.

Furthermore, PND study revealed that hydrogen does not enter the $LaNi_5$ layers at all residing only at the borders of the $LaNi_5$ and $LaNi_2$ slabs (within the Kagome Ni-nets) and inside the $LaNi_2$ slabs. In total, four different sites are filled with D. All three interstitial sites occupied by D inside the $LaNi_2$ layers do not exist in the initial crystal structures and are formed during a modification of the crystal structure of La_2Ni_7 on hydrogenation. These sites include two types of the La_3Ni_3 octahedra and one type of the La_3Ni tetrahedron. In addition, deuterium atoms fill the La_2Ni_2 tetrahedra, which are present in the original structure of La_2Ni_7 and equally belong to $LaNi_2$ and $LaNi_5$ slabs. Deuterium content of the $LaNi_2$ slabs is rather high, 5 at.D/f.u. in maximum. Approximately 1/4 of the overall deuterium content is associated with the $LaNi_5$ slab (1.5 at.D/f.u.; $La_2Ni_7D_{6.5} = LaNi_2D_{5.0} + LaNi_5D_{1.5}$). The Rietveld plot of the NPD data for $La_2Ni_7D_{6.5}$ is shown in Fig. 4. The crystal structure data for $La_2Ni_7D_{6.5}$ are given in Table 4.

Table 3
Coordination of the D atoms in the structures of $CeNi_3D_{2.8}$ and $La_2Ni_7D_{6.5}$ as related to the interstices available in the crystal structures of intermetallic compounds

Intermetallic alloy	Deuteride	$CeNi_3D_{2.8}$	$La_2Ni_7D_{6.5}$
New coordination of D is achieved via deformation of the metal sublattice			
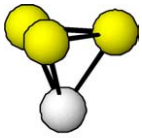 Ni_4	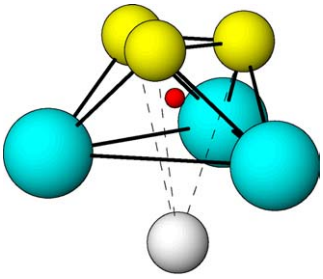 RE_3Ni_3	D1 D6	D1
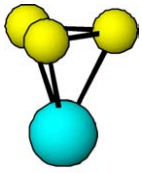 RNi_3	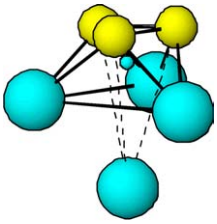 RE_3Ni_3	D2 D7	D2
Formation of a new type of interstice due to the strong expansion of the $MgZn_2$-type layer			
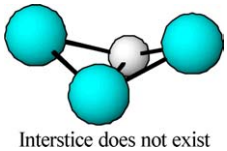 Interstice does not exist	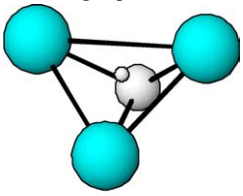 RE_3Ni	D3 D5	D3
Filling of the available RE_2Ni_2 tetrahedra at the boundary between the $CaCu_5$- and $MgZn_2$-type layers			
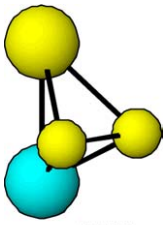 RE_2Ni_2	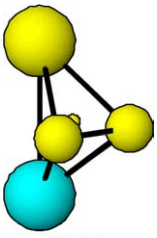 RE_2Ni_2	D4 D8	D4

All D–D distances in the structure are high and exceed 1.8 Å. Maximum stoichiometric composition, which can be reached by increasing the occupancy of the 50% filled D3 site to 100%, is $La_2Ni_7D_{8.0}$. This will not require any extra deformation of the structure. The shortest Ni–D and La–D distances are 1.515(5) and 2.385(18) Å, respectively.

Further D uptake inside the $LaNi_5$ layers is anticipated at higher D_2 pressures with D entering the La_2Ni_2 sites inside the $LaNi_5$ layers and, in addition, the $LaNi_3$ (12*n* in the $LaNi_5$ structure) sites.

An ordered hydrogen sublattice in the structure of $La_2Ni_7D_{6.5}$ can be described as a stacking of the 15-vertex coordination polyhedra formed by D around the La atoms belonging to the $LaNi_2$ slabs (see Fig. 5).

Analysis shows that Ni-hydrogen interaction in $La_2Ni_7D_{6.5}$ does not result in a formation of the NiH_4 units observed for the complex Ni-containing hydrides.

The most important common features of the formation of the crystal structures of $CeNi_3D_{2.8}$ and $La_2Ni_7D_{6.5}$ related to the coordination of H atoms in their structures are summarized in Table 3. As can be seen from this table, “traditional” mechanism of hydrogenation when H atoms enter the available in the crystal lattice interstitial sites (tetrahedra RE_2Ni_2), the other occupied by D sites are formed via a pronounced

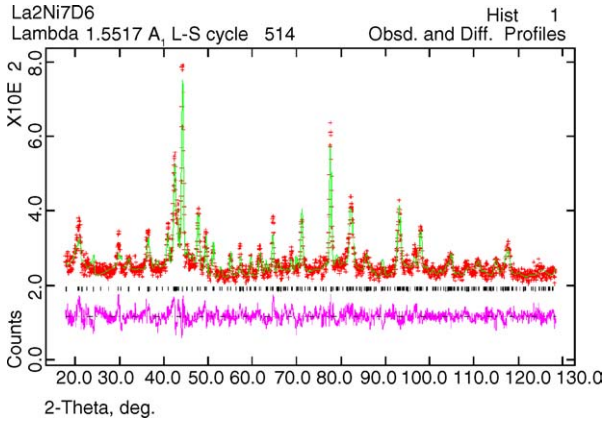

Fig. 4. Powder neutron diffraction pattern for $La_2Ni_7D_{6.5}$ (NPD instrument, $\lambda = 1.5517$ Å) showing observed (dots), calculated (line) and difference (line in bottom) pattern. Positions of the peaks are marked. $R_p = 4.41\%$; $R_{wp} = 5.57\%$.

deformation of the structures. This deformation significantly increases amount of rare earth atoms in the surrounding of H (RE_3Ni_3 octahedra) or even creates new tetrahedral sites RE_3Ni.

Comparison of the structural features of two different anisotropic hydrides, $CeNi_3D_{2.8}$ and $La_2Ni_7D_{6.5}$, allows drawing the following conclusions.

(a) Both types of the initial structures, $RENi_3$ and RE_2Ni_7, are composed of the slabs with a compositions $RENi_5$ ($CaCu_5$-type) and $RENi_2$ (Laves phase type), which stack in different sequence (1:2 and 1:1, respectively) along the *c*-axis of the hexagonal (trigonal) unit cells. At low applied hydrogenation pressures, all expansion of the "composite" unit cells proceeds within the $RENi_2$ layers only and is very anisotropic confined to the [0 0 1] direction. Within the layers with the compositions $LaNi_2$ and $CeNi_2$, the expansion is very similar being close to 60%.

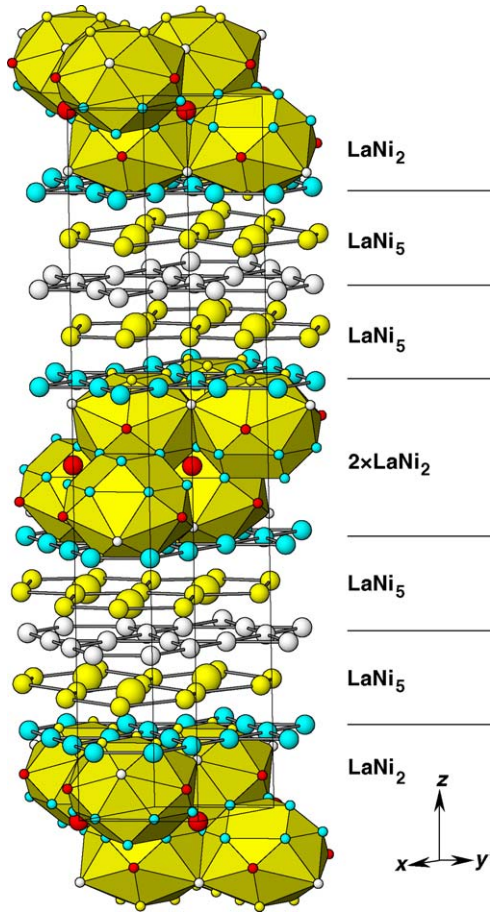

Fig. 5. Deuterium sublattice in the crystal structure of $La_2Ni_7D_{6.5}$ built as a stacking of the LaD_{15} polyhedra.

(b) The absorbed hydrogen does not enter the $RENi_5$ layers and is accumulated exclusively inside the $RENi_2$ slabs and on their borders.

(c) A deformation of the $RENi_2$ layers occupied by H is so significant that the stacking and coordination characteristics of the metal atoms in these layers are significantly

Table 4
Crystal structure data for $La_2Ni_7D_{6.5}$

Atoms	Site	*x*	*y*	*z*	Uiso ($\times 10^{-2}$ Å^2)	D surrounding
La1	4*f*	1/3	2/3	0.4514(8)	3.3(8)	
La2	4*f*	1/3	2/3	0.3124(7)	1.4(5)	
Ni1	2*a*	0	0	0	1.6(5)	
Ni2	4*e*	0	0	0.3188(8)	3.7(7)	
Ni3	4*f*	1/3	2/3	0.6854(7)	3.3(4)	
Ni4	6*h*	0.840(2)	0.679(4)	1/4	1.0(3)	
Ni5	12*k*	0.834(1)	0.668(3)	0.3868(2)	0.6(2)	
D1	4*e*	0	0	0.0864(8)	3.5	O $La1_3Ni5_3$
D2	4*f*	1/3	2/3	0.5586(11)	3.5	O $La1_3Ni5_3$
D3	12*k*	0.330(6)	0.165(3)	0.020(5)	3.5	T $La1_3Ni1$
D4	12*k*	0.485(3)	0.970(6)	0.120(1)	3.5	T $La1La2Ni5_2$

Space group $P6_3/mmc$; $a = 4.9534(6)$; $c = 29.579(5)$ Å.
Occupancy $n = 0.5$ for D3. For all other D atoms, it was constrained to $n = 1$.
Actual deuterium content in the deuteride will be refined further using the data of the PCT studies, which are in progress. The latter studies indicate (R.V. Denys, unpublished results) that it could be close to 5 at./f.u.La_2Ni_7 slightly reducing the occupancy of the completely filled D sites to approximately 77%.

modified creating new types of positions (octahedra RE_3Ni_3, tetrahedra RE_3Ni) which do not exist in the original structures and became occupied by H.

(d) The RE–H and H–H interactions dominate the structural behaviour of these anisotropic hydrides. Their hydrogen sublattices contains H atoms with all interatomic H–H separations greater then 1.8 Å, which can be built as 12-, 7- or 15-vertex polyhedra formed by D around Ce or La.

(e) Since the behaviour of La- and Ce-containing hydrides is essentially very similar, the structural features of the anisotropic hydrides do not have roots in the valence decrease of Ce during the hydrogenation.

Acknowledgements

This work is a part of the activities within a joint laboratory "Advanced materials for hydrogen storage" between IFE and PhMI National AS, Ukraine. Financial support from the Norwegian Research Council and travel funds from the Visby Programme of the Swedish Institute is gratefully acknowledged. We thank Håkan Rundlöf and Anders Wannberg of NFL for skilled assistance with the collection of the neutron diffraction data and Marit Stange (IFE) for assistance in the XRD measurements. We are grateful to Prof. O. Isnard (Laboratory of Crystallography, CNRS, Grenoble) for the cooperation.

References

[1] V.A. Yartys, R.V. Denys, B.C. Hauback, H. Fjellvåg, I.I. Bulyk, A.B. Riabov, Ya.M. Kalychak, J. Alloys Compd. 330–332 (2002) 132.

[2] V.A. Yartys, O. Isnard, A.B. Riabov, L.G. Akselrud, J. Alloys Compd. 356–357 (2003) 109.

[3] A.C. Larson, R.B. von Dreele, General Structure Analysis System, LANL, 1994.

[4] K.H.J. Buschow, J. Magn. Magn. Mater. 40 (1983) 224.

Advanced Materials for Energy Conversion III: A Symposium in Honor of Drs. Gary Sandrock, Louis Schlapbach, and Seijirau Suda
Edited by D. Chandra, J.J. Petrovic, R. Bautista, and A. Imam ***TMS (The Minerals, Metals & Materials Society), 2006***

ALUMINUM TRIHYDRIDE STUDIED BY POWDER SYNCHROTRON X-RAY DIFFRACTION: CRYSTAL STRUCTURE AND THERMAL DECOMPOSITION

Jan Petter Maehlen and Volodymyr A. Yartys

Institute for Energy Technology (IFE), P.O. Box 40
NO-2027 Kjeller
Norway

Keywords: Hydrogen storage, Metal hydrides, Crystal structure

Abstract

Solid H-absorbing materials are in focus of ongoing R&D to offer viable solutions for the hydrogen storage and supply systems aimed on use of hydrogen as energy carrier for automotive transportation. Low operating pressures, combined with high gravimetric and volumetric efficiencies, together with fast kinetics of hydrogen release at ambient temperatures (providing conditions for a low energy loss due to decomposition), are the most important features of the "ideal" H storage material. Hydrides of the light elements are the only possible candidates to build systems with an overall efficiency similar to those accommodating liquid or compressed (700 bar) hydrogen. One promising material from this point of view is aluminium trihydride, alane AlH_3 with a gravimetric storage capacity of 10 wt.% H. This work was focused on studies of the crystal structure and thermal decomposition of alane by application of powder synchrotron X-Ray diffraction.

Introduction

Facing rapidly approaching limits of the resources of fossil fuels, one is hoping that renewables, including solar or wind energy, will increasingly contribute to solve the growing energy demand of the future society. To utilize these energy sources, hydrogen and electricity are considered as an ideal combination of energy carriers, providing versatile and environmental benign solutions. Every step in a complete hydrogen energy cycle, which includes hydrogen production from water by electrolysis, hydrogen storage and conversion into electricity in the fuel cell stack, needs to be sufficiently improved to increase the competitiveness of hydrogen energy with the available energy systems.

Hydrogen storage is considered as the most important issue to be solved. An efficient hydrogen storage solution should combine several key features including high hydrogen storage densities, volumetric and gravimetric, fast and easy reversible H loading/H release, together with affordable price and fulfillment of the safety requirements. A storage system satisfying all these beneficial features, unfortunately, is not developed yet. Even though solid state storage materials, first of all reversible metal hydrides, have been appreciated as an efficient way for reaching high volumetric efficiency of the storage system and fast rates of hydrogen exchange, reaching these advantages has always been paid by a price of having a rather poor gravimetric hydrogen storage capacity.

To reach the high gravimetric hydrogen densities required for commercially competitive hydrogen storage solutions for the transport sector, metal hydride systems containing light elements are needed. In the present work we have focused our studies on the binary metal-hydrogen system of such a type, namely on the aluminium trihydride alane.

Aluminium trihydride alane is considered as a prospective solid H storage material, having high gravimetric (10 wt.% H) and volumetric density of H (2 times higher compared to LH_2) and, also, because of its convenient range of thermal stability. AlH_3 forms several polymorphic modifications, which are often polymers $(AlH_3)_n$ [1]. α-Alane AlH_3 was first synthesized in 1947 by an exchange reaction between $AlCl_3$ and lithium hydride in ether solution [2]. This binary hydride has a covalent Al-H bonding and exhibits dielectric properties. α-AlH_3, the most stable modification of alane, has a rhombohedral unit cell (space group $R\bar{3}c$) [3]. Metastable alane does not release hydrogen at normal conditions and is stable in air. At atmospheric pressure AlH_3 desorbs hydrogen at rather moderate temperatures (350 – 400 K, depending on its preparation history). Achieving sufficiently rapid and controllable decomposition of AlH_3 and proposal of the efficient synthesis routes to make the system Al-AlH_3 reversible are focused in ongoing research (see, e.g., [4]); the first task is solved by doping alane with LiH. This work was aimed on studies of crystal structure of AlH_3 and phase-structural transformations in the system Al-AlH_3 during decomposition of the hydride by application of *in situ* synchrotron X-ray powder diffraction (SR-XRD).

Experimental Details

Several methods for the wet chemical synthesis of AlH_3 have been reported in the literature a few decades ago. A frequent problem is in getting AlH_3 free of solvent without decomposing the sample [1,2]. Aluminium hydride, α-AlH_3 was prepared using a method described by Brower *et al.* [1]. It was crystallised as a white, non containing solvent, powder from an ether-benzene solution containing a complex of AlH_3 with ether, $LiAlH_4$ and $LiBH_4$. It has been stored in an airtight container for the time between the synthesis and the measurements. Temperature desorption spectroscopy (TDS) study of the hydrogen release from the sample was performed by heating a small amount of the sample (less than 100 mg) in a stainless steel autoclave at a constant heating rate of 1 K/min. Dynamic secondary vacuum in the measurements setup was maintained by using a turbo-molecular pumping system, and the desorption pressure was monitored by the vacuum sensor.

SR-XRD studies of aluminum hydride were performed at the Swiss-Norwegian Beam Line (SNBL) at the European Synchrotron Radiation Facility (ESRF), Grenoble, France. A high-resolution data set at room temperature was first obtained, followed by an *in situ* measurement by heating with a constant heating rate while simultaneously maintaining secondary vacuum conditions. A setup designed for *in situ* studies of the chemical processes in hydrogen gas/vacuum [5] was used. A scheme of the setup used is shown in Figure 1. A small amount of the sample is contained in a 0.7 mm quartz glass capillary and fills approximately 1–2 mm in its bottom part. The capillary is hermetically connected to the gaseous system using a carbon ferrule mounted in a *T*-piece, which, in turn, is attached to the goniometer head. A two-stringed flow system makes it possible to switch between hydrogen gas and vacuum during the experiment. The fixed connection of the microreaction cell to the goniometer head makes a full rotation of the sample difficult. However, the averaging over the different orientations of the crystallites, resulting in the elimination of the preferred orientation effects in the collected diffraction data is achieved by applying wobbling of the setup around the axis of the capillary

using a flexible PEEK (Polyetheretherketon) tubing connection between the microreaction cell and the flow system. During the experiments, hydrogen gas is supplied from a portable metal hydride storage unit developed at IFE, Kjeller ($La_{1-x}Mm_xNi_5$ hydrogen storage alloy, plateau pressure 2.5 – 3 bar). Vacuum is created using a turbo molecular vacuum pump. Except for the PEEK tubing allowing the wobbling of the sample cell, stainless steel tubes are used for the connections to prevent oxygen diffusion through the tubes during the experiments.

The diffractometer is equipped with six counting chains, with an angular offset in 2θ of ~1.1°. For *in situ* measurements, in order to keep the counting time per scan as low as possible, the detector bank is moved by 1.2 º during one measurement and the data from the six different detectors are added using a data-binning program.

The wavelength λ selected for the measurements was accurately determined to be 0.37504(2) Å from separate calibration measurements of a standard Si sample. Two different measurement modes were applied. During the *in situ* measurements of the hydrogen desorption process of AlH_3, the data were obtained in steps of 0.01 ° (in 2θ). By applying the procedure described above, one data set (2θ = 6.07–12.67 °) was collected in 2 min during the heating of the sample under secondary vacuum conditions. Rietveld analysis of the powder diffraction data was performed using the Fullprof software [6]. The high-resolution measurement of AlH_3 was performed in steps of 0.005° in the 2θ range form 5.540 to 36.935 º. The Rietveld analysis of the powder diffraction data was carried out using the GSAS software [7].

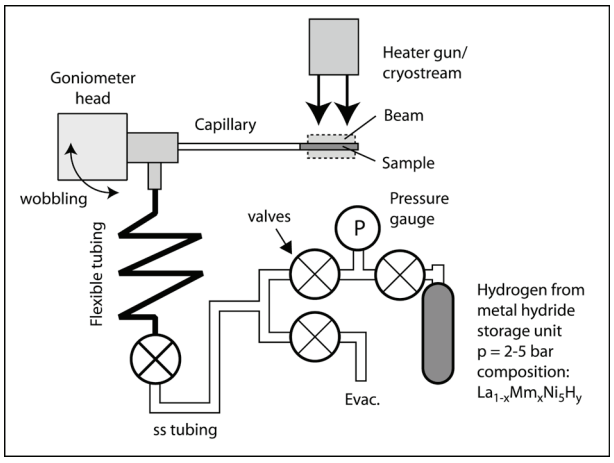

Figure 1. Scheme of the experimental set-up used for *in situ* SR-XRD experiments. The hydrogen and vacuum lines can be remotely operated.

Results and Discussion

During the study of AlH_3, at first a high-resolution data set at room temperature was measured. This study was then accompanied by collection of an *in situ* data of the thermal decomposition of the hydride. During that study the sample was heated with a constant rate of 1 K/min from 293 to 425 K.

The high-resolution SR-XRD pattern was indexed to the trigonal unit cell described in the space group $R\bar{3}c$ (No.167). The refinements yielded the unit cell parameters: a = 4.44994(5) Å, c = 11.8200(2) Å, and V = 202.701(4) $Å^3$ which agree well with the reference data: a = 4.449 Å; c = 11.804Å; V = 202.34 $Å^3$ [3].

The hydrogen sublattice was successfully located from the refinements of the powder XRD pattern, which have started with Al placed in a special position 6*a* [0,0,0]. Performing the refinements without including the H position gave the following best goodness-of-fit parameters: R_{wp} =14.2%, R_p = 11.7 %, and χ^2 = 6.0. Hydrogen atoms were located from the difference Fourier synthesis maps. Their involvement into the refinements of the SR diffraction pattern significantly improved quality of the fit; goodness-of-fit parameters became: R_{wp} =12.1%, R_p = 10.6 %, and χ^2 = 4.9.

The refinements yielded the Al-H bonding distance of 1.712(3) Å and an octahedral coordination of Al in the AlH_6 units. Furthermore, they indicated a small charge transfer from Al to H corresponding to the formation of $Al^{+0.15}$ and $H^{-0.05}$. This charge distribution can be observed in the Fourier transform of the observed XRD pattern as shown in Figure 4. We note a good correspondence between the data of the present powder XRD work and the results of the powder neutron diffraction study of AlD_3 [3], where an Al-D bond distance of 1.715 Å in the AlD_6 octahedra was reported. The crystal structure data for AlH_3 is summarised in Table I.

Table I: Crystal structure data (atomic site and coordinates, and isotropic temperature factors) derived from Rietveld refinement of SR-XRD data for α-AlH_3.

Space group $R\bar{3}c$ (No.167); a = 4.44994(5) Å, c = 11.8200(2) Å.

Calculated standard deviations in parentheses.

Atom	*Site*	*x*	*y*	*z*	U_{iso} *(10×Å²)*
Al	6*b*	0	0	0	3.14
H	18*e*	0.625(2)	0	1/4	4.96

Figure 2 shows the Rietveld-type plots of the high-resolution data while Figure 3 present the crystal structures of Al and AlH_3. Hydrogenation is accompanied by a volume increase of 103.5 (!) % equivalent to 5.73 $Å^3$/atom H. We note that these numbers are significantly higher compared to the traditional metal/intermetallic hydrides where both corresponding values are significantly lower, respectively, 20-30 % and 2.5-3.0 $Å^3$/at.H [8]. This dramatic increase of the unit cell volume is accompanied with an enlargement of the closest Al-Al distances of 13.3% (growing from 2.86 Å in the alloy to 3.24 Å in the hydride).

The *in situ* diffraction pattern of the decomposition of the hydride (Figure 5) collected in the temperature range 290 – 420 K showed that on heating a linear increase of the unit cell dimensions of AlH_3 takes place in an interval from RT to ~400 K (a= 4.46; c = 11.83 Å for T = 400 K; see Figure 6 and Figure 7). The volume expansion is pronouncedly anisotropic, as can be

seen from Figure 7. Indeed, the c-axis is almost constant in the temperature interval 300-400 K ($\Delta c/c$ ~0.02 %). This contrasts to a significant expansion along [100]: $\Delta a/a$ ~0.2 %. This expansion can mainly be attributed to the elongations of the bridge bonds Al-H-Al aligned along [1 $\bar{1}$ ½], which are expanding from 3.238 to 3.243 Å ($\Delta d/d$ ~ 0.17 %).

During the heating, a continuous decrease of the intensities of the pattern of AlH_3 was observed indicating a gradual decomposition of the crystalline hydride phase, probably forming amorphous aluminium. This decrease was not accompanied by any significant broadening of the peaks. The intensities of the diffraction peaks from Al firstly appeared at ~410 K and then gradually increased with raising temperature. At T~420 K, the hydride peaks completely vanished indicating a completeness of the transformation $AlH_3 \rightarrow Al$. The fraction of the hydride observed in the SR-XRD patterns as a function of the temperature is given in Figure 8. These *in situ* data agree well with the TDS measurements showing the onset of the peak of H desorption at ~ 400 K (see Figure 9).

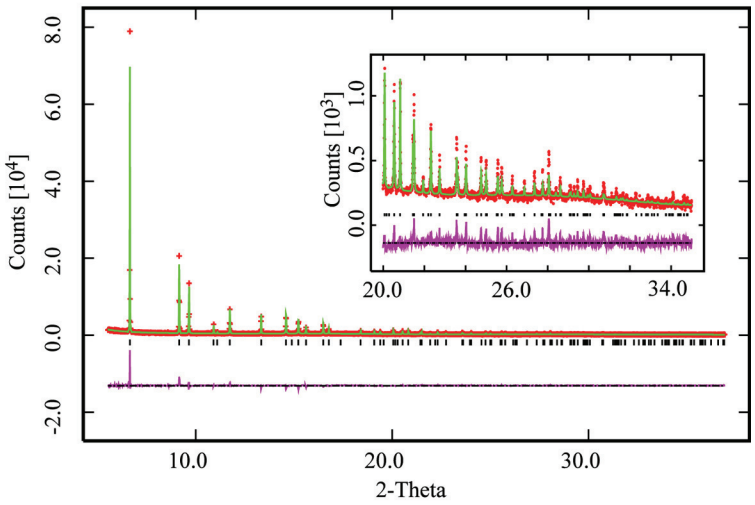

Figure 2. Rietveld-type plots of AlH_3 collected at 293 K showing observed (crosses), calculated (upper line) and difference (bottom line) plots. The positions of the Bragg peaks are shown as ticks. $\lambda = 0.37504$ Å.

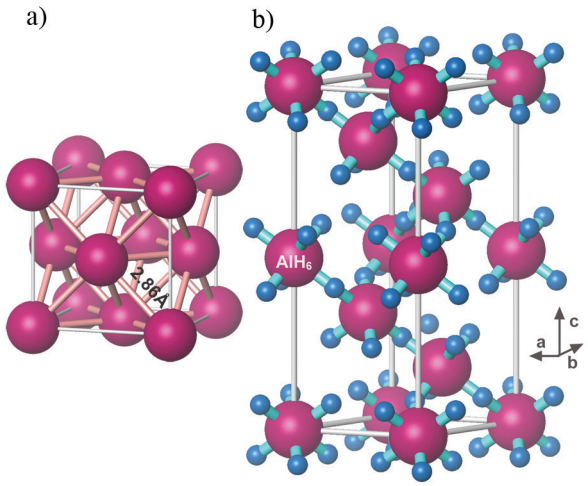

Figure 3. Crystal structures of the constituents:

a) FCC structure of aluminium metal showing Al-Al bonding distance of 2.86 Å;

b) structure of α-AlH_3 presented as a packing of the AlH_6 octahedra (the shortest Al-Al distance of 3.24 Å). The Al-H-Al bridge bonds are shown and have the following characteristics: ∠ Al-H-Al = 142.0(7) º; d_{Al-H} = 1.712(3) Å.

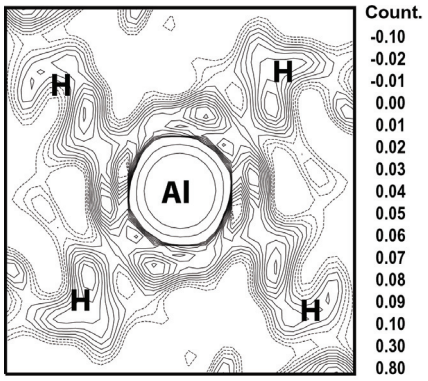

Figure 4. Fourier transform of the observed SR-XRD pattern (GSAS Rietveld refinements) showing the Al-H bonds (equatorial plane of the octahedron containing 4 H atoms is selected).

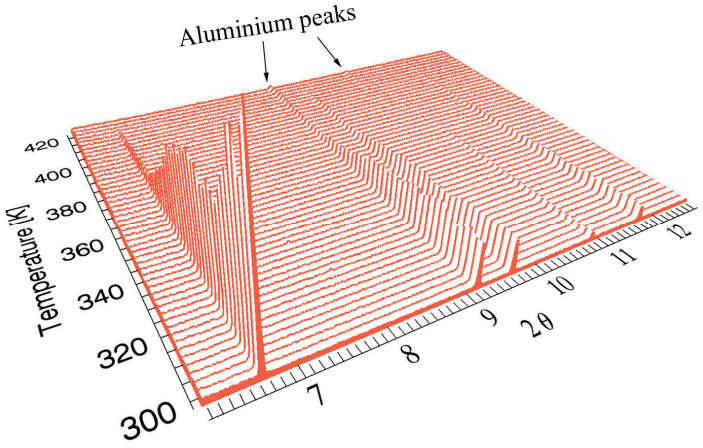

Figure 5. *In situ* SR-XRD patterns of the Al – AlH_3 system during heating of the sample. Heating rate was 1 K/min.

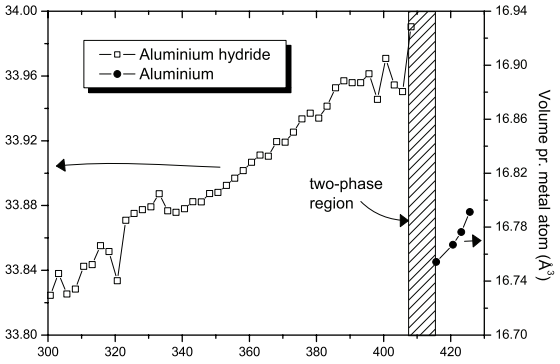

Figure 6. Volumes of the unit cells of the crystal structures of alane and Al metal (per one aluminium atom) *vs* the temperature as obtained from the refinements of the *in situ* SR-XRD patterns.

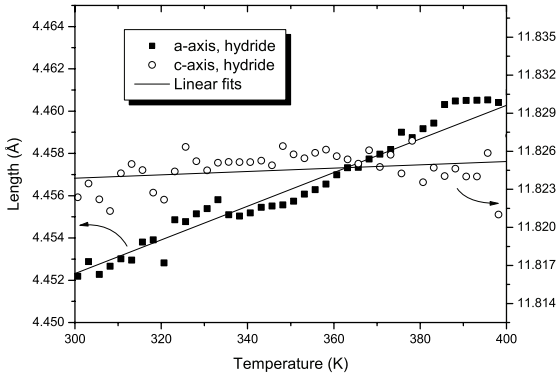

Figure 7. Evolution of the unit cell parameters of the hydride during the heating as obtained from the refinements of the *in situ* SR-XRD pattern.

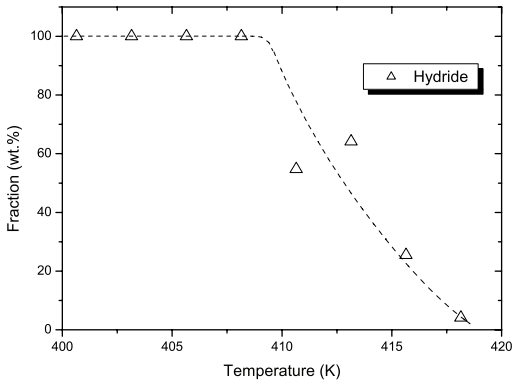

Figure 8. Temperature-dependent fraction of crystalline aluminium hydride (by mass) in the system as obtained from the refinements of the *in situ* SR-XRD patterns (the refinements included *crystalline* aluminium and *crystalline* aluminium hydride).

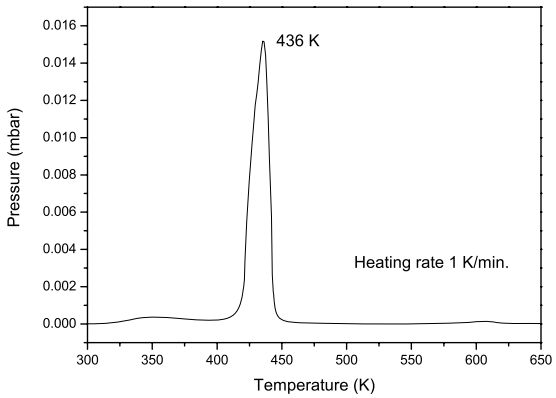

Figure 9. TDS traces of hydrogen desorption from the aluminium hydride.

Summary

In summary, in the present work X-ray synchrotron powder diffraction has been employed to study precise details of the crystal structure and thermal decomposition of aluminium trihydride alane. These studies allowed not only to locate hydrogen atoms by means of X-ray powder technique but also to identify a size of electron transfer occurring between aluminium and hydrogen.

The decomposition of the alane is firstly manifested by a decrease of the intensities of the diffraction peaks of AlH_3 accompanied by the formation of a non-crystalline phase (probably amorphous aluminium). At a temperature of about 410 K aluminium starts to crystallize and first appears in the SR diffraction pattern; the peaks from AlH_3 become weaker with a gradual change in relative amount of both constituents, until a complete transformation from AlH_3 to Al is reached at about 420 K.

The data from the SR-XRD study agree well with the results from the TDS study of thermal decomposition of alane.

Acknowledgments

We would like to thank H. Emerich and other members of the scientific staff at the Swiss-Norwegian Beam Line for their skilful assistance during the SR-XRD experiments.

Sincere thanks to Prof.B.M.Bulychev (Moscow State University), Prof.V.E. Antonov (Institute of Solid State Physics of the Russian Academy of Sciences) and Prof.V. Dmitriev (SNBL, ESRF) for kindly providing us with the sample of aluminium hydride used in this study.

We are grateful to Drs. A.B.Riabov, M.Sato and T.Førde for the help in the preparation of the samples and experimental measurements.

References

[1] F.M. Brower, N.E. Matzek, P.F. Reigler, H.W. Rinn, C.B. Roberts, D.L. Schmidt, J.A. Snover, and K. Terada, "Preparation and Properties of Aluminum Hydride", *Journal of the American Chemical Society*, 98 (1976), 2450-2453.

[2] A.E. Finholt., C. Bond, Jr , and H.I. Schlesinger, "Lithium aluminum hydride, aluminum hydride and lithium gallium hydride, and some of their applications in organic and inorganic chemistry", *Journal of the American Chemical Society*, 69 (1947), 1199-1203.

[3] J.W. Turley, and H.W. Rinn, "Crystal Structure of Aluminum Hydride", *Inorganic Chemistry*, 8 (1969), 18-22.

[4] G. Sandrock, J. Reilly, J. Graetz, W.-M. Zhou, J. Johnson, and J. Wegrzyn, "Accelerated thermal decomposition of AlH_3 for hydrogen-fueled vehicles", *Applied Physics A-Materials Science & Processing*, 80 (2005), 687-690.

[5] M. Stange, J.P. Maehlen, V.A. Yartys, P. Norby, W. van Beek, and H. Emerich, "In situ SR-XRD studies of hydrogen absorption-desorption in $LaNi_{4.7}Sn_{0.3}$", *Journal of Alloys Compounds*, 404-406 (2005) 604-608; and P. Norby, "Hydrothermal conversion of zeolites: An in situ synchrotron X-ray powder diffraction study", *Journal of the American Chemical Society*, 119 (1997) 5215-5221; and E. Krogh Andersen, I.G. Krogh Andersen, P. Norby, and J.C. Hanson, "Kinetics of oxidation of fuel cell cathode materials lanthanum strontium Manganates(III)(IV) at actual working conditions: In situ powder diffraction studies", *Journal of Solid State Chemistry*, 141 (1998), 235-240.

[6] J. Rodriguez-Carvajal, "FULLPROF: A Program for Rietveld Refinement and Pattern Matching Analysis", Abstracts of the Satellite Meeting on Powder Diffraction of the XV Congress of the IUCr, p. 127, Toulouse, France (1990).

[7] A.C. Larson, R.B.Von Dreele, Program GSAS, General Structure Analysis Program, LANCE, MS-H 805, Los Alamos National Laboratory, Los Alamos, NM, USA.

[8] V.A. Yartys, V.V. Burnasheva, N.V. Fadeeva, S.P. Solov'ev, and K.N. Semenenko, "Crystal chemistry of $RT_2H(D)_x$, $RT_5H(D)_x$ and $RT_3H(D)_x$ hydrides based on intermetallic compounds of $CaCu_5$, $MgCu_2$, $MgZn_2$ and $PuNi_3$ structure Types", *International Journal Hydrogen Energy*, 7 (1982), 957-965; and V.A.Yartys, V.V. Burnasheva, and K.N. Semenenko, "Structural chemistry of hydrides of intermetallic compounds", *Soviet Advances in Chemistry*, 52 (1983), 529-562.

Inorg. Chem. **2007**, *46*, 1051–1055

Double-Bridge Bonding of Aluminium and Hydrogen in the Crystal Structure of γ-AlH_3

Volodymyr A. Yartys,*,† Roman V. Denys,† Jan Petter Maehlen,† Christoph Frommen,‡ Maximilian Fichtner,‡ Boris M. Bulychev,§ and Hermann Emerich#

Institute for Energy Technology, Kjeller NO 2027, Norway, Institute of Nanotechnology, Forschungszentrum Karlsruhe GmbH, P.O. Box 30640, D-76021 Karlsruhe, Germany, Chemistry Department, Moscow State University, Leninskie Gori, Moscow 119992, Russia, and Swiss-Norwegian Beam Line, ESRF, BP 220, F-38043 Grenoble, France

Received September 14, 2006

Aluminum trihydride (alane) is one of the most promising among the prospective solid hydrogen-storage materials, with a high gravimetric and volumetric density of hydrogen. In the present work, the alane, crystallizing in the γ-AlH_3 polymorphic modification, was synthesized and then structurally characterized by means of synchrotron X-ray powder diffraction. This study revealed that γ-AlH_3 crystallizes with an orthorhombic unit cell (space group *Pnnm*, $a = 5.3806(1)$ Å, $b = 7.3555(2)$ Å, $c = 5.77509(5)$ Å). The crystal structure of γ-AlH_3 contains two types of AlH_6 octahedra as the building blocks. The Al–H bond distances in the structure vary in the range of 1.66–1.79 Å. A prominent feature of the crystal structure is the formation of the bifurcated *double-bridge* bonds, Al–2H–Al, in addition to the normal bridge bonds, Al–H–Al. This former feature has not been previously reported for Al-containing hydrides so far. The geometry of the double-bridge bond shows formation of short Al–Al (2.606 Å) and Al–H (1.68–1.70 Å) bonds compared to the Al–Al distances in Al metal (2.86 Å) and Al–H distances for Al atoms involved in the formation of normal bridge bonds (1.769–1.784 Å). The crystal structure of γ-AlH_3 contains large cavities between the AlH_6 octahedra. As a consequence, the density is 11% less than for α-AlH_3.

Introduction

Aluminum trihydride (alane), having a high gravimetric (10 wt %) and volumetric density of hydrogen (twice that of liquid H_2), is among the most promising materials for on-board hydrogen-storage applications.

An ethereal complex of solvated alane was first synthesized in 1947 by an exchange reaction between $AlCl_3$ and lithium hydride in ether solution.[1] Its synthesis in nonsolvated form was first described in ref 2. AlH_3 forms six polymorphic modifications, α, α', β, γ, δ, and ϵ, which are considered to be polymers $(AlH_3)_n$.[2] The measured thermodynamic properties of alane show that the equilibrium hydrogen pressure in the $Al-AlH_3$ system is extremely high at ambient temperatures exceeding 25 kBar; therefore, alane should easily decompose at normal conditions and can be only formed by application of extremely high hydrogen pressures.[3,4] However, AlH_3 does not release very much hydrogen even while storing for years because the decomposition is kinetically hindered, possibly because of the formation of a thin protective oxide layer.

At atmospheric pressure, AlH_3 desorbs hydrogen at rather moderate temperatures (350−400 K, depending on its preparation history). Sufficiently rapid and controllable decomposition of AlH_3 and efficient synthesis routes to make the $Al-AlH_3$ system reversible are focuses in ongoing research (see, for example, ref 5). The doping of alane with LiH assists in solving the first task. All other alane modifications, including γ-alane, are less stable than α-alane

* To whom correspondence should be addressed. E-mail: Volodymyr.Yartys@ife.no. Phone: +47 63 80 64 53. Fax: +47 63 81 29 05.
† Institute for Energy Technology.
‡ Institute of Nanotechnology, Forschungszentrum Karlsruhe GmbH.
§ Moscow State University.
# Swiss-Norwegian Beam Line.

(1) Finholt, A. E.; Bond, C., Jr.; Schlesinger, H. I. *J. Amer. Chem. Soc.* **1947**, *69*, 1199−1203.
(2) Brower, F. M.; Matzek, N. E.; Reigler, P. F.; Rinn, H. W.; Roberts, C. B.; Schmidt, D. L.; Snover, J. A.; Terada, K. *J. Amer. Chem. Soc.* **1976**, *98*, 2450−2453.
(3) (a) Tkacz, M.; Filipek, S.; Baranowski, B. *Pol. J. Chem.* **1983**, *57*, 651−653. (b) Baranowski, B.; Tkacz, M. *Z. Phys. Chem.* **1983**, *135*, 27.
(4) Konovalov, S. K.; Bulychev, B. M. *Inorg. Chem.* **1995**, *34*, 172.
(5) Sandrock, G.; Reilly, J. J.; Graetz, J.; Zhou, W.-M.; Johnson, J.; Wegrzyn, J. *Appl. Phys. A* **2005**, *80*, 687−690.

10.1021/ic0617487 CCC: $37.00
Published on Web 12/15/2006

and transform into the α-modification at temperatures slightly above ambient.[6]

α-AlH_3 is the best-studied modification of alane. These studies included its structural characterization.[7,8] The high-resolution synchrotron X-ray diffraction (SR-XRD) structural study[8] showed that a rhomobohedral lattice of α-AlH_3 (space group $R\bar{3}c$, a = 4.44994(5) Å, c = 11.8200(2) Å, V = 202.701(4) Å^3) is composed of vertex-sharing AlH_6 octahedra. The Al−H−Al bridge bonds are formed and have the following characteristics: ∠Al−H−Al = 142.0(7)°, d_{Al-H} = 1.712(3) Å. The refinements of the diffraction data indicated a small charge transfer from Al to H, corresponding to the formation of $Al^{+0.15}$ and $H^{-0.05}$.

However, the structures of the other allotropic modifications of the alane have not been reported yet. The present paper gives results of the studies of the crystal structure of γ-AlH_3 by means of SR-XRD.

Experimental Section

Synthesis of γ-alane was performed by two different groups, the Institute of Nanotechnology, FZK, in Germany (M.F. and C.F.) and Moscow State University in Russia (B.M.B.). Both synthesis techniques, despite differences in the synthesis processes, resulted in obtaining a nearly single-phase γ-AlH_3. For further studies, by SR-XRD, the sample prepared at FZK was used. However, both synthesis routes will be described below.

Synthesis at Institute of Nanotechnology, FZK. Reagents. Diethyl ether (Merck, certified ACS, 99% purity) was double-distilled over sodium/benzophenone and $LiAlH_4$ and stored under purified nitrogen. $AlCl_3$ (Merck, anhydrous, >98%) was used as received. $LiAlH_4$ (Merck, >97%) was purified prior to use by dissolution in DEE and filtration of a light gray residue. After the solvent was evaporated under a vacuum, a white powder was obtained. According to powder XRD measurements, the material was purely a single phase.

Chemical synthesis of γ-AlH_3 was carried out on the bench using Schlenk tube techniques. The glassware was evacuated down to a pressure of 10^{-3} mbar and flushed with dry oxygen-free nitrogen prior to use. Solids were handled in an argon-filled glove box equipped with a recirculation and regeneration system. Both the water and oxygen concentrations were kept below 1 ppm during operation. The synthesis procedure is a modification of a description given in the literature.[1]

Diethyl ether solutions of $LiAlH_4$ (2.4 g, 250 mL of Et_2O) and $AlCl_3$ (2.1 g, 70 mL of Et_2O) were prepared; both were precooled in an ice bath, and the $AlCl_3$ solution was quickly added to the $LiAlH_4$ solution with stirring. The reaction proceeded immediately, forming a fine, white precipitate. Stirring was continued for a period of 5 min; the precipitate was allowed to settle, and the solution was filtered through a fine grade glass filter frit into a round-bottom flask fitted with a nitrogen inlet. After filtration, the solvent was slowly removed at room temperature under vacuum (10^{-3} mbar), and the remaining white residue was ground and heated under vacuum at 60 °C in a rotating glass oven (Büchi B585) for 4 h.

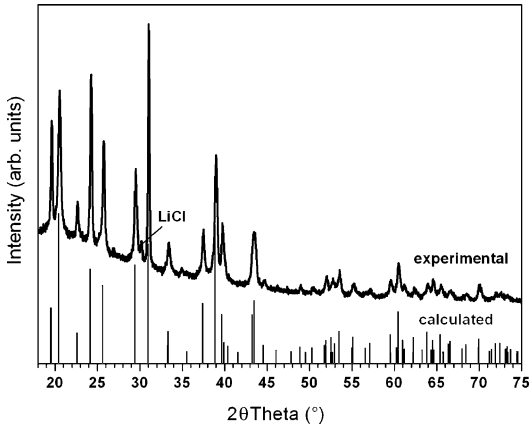

Figure 1. Experimental and calculated powder XRD pattern of γ-AlH_3 (Cu Kα). The calculation was performed on the basis of the structural data of this paper.

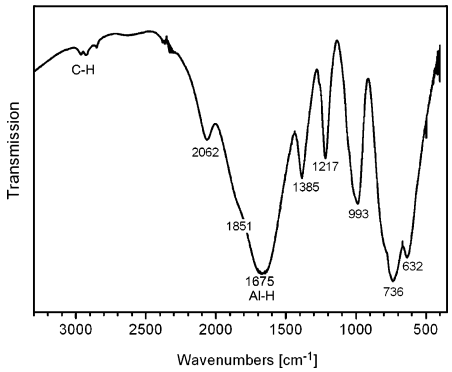

Figure 2. IR spectrum of γ-AlH_3.

The solid was finally transferred to a fine-grade glass filter frit, washed several times with small aliquots of Et_2O to remove excess $LiAlH_4$ and any remaining AlH_3-etherate, and dried under vacuum, yielding 1.5 g (75%) of aluminum hydride.

The material was a nearly pure single phase. The X-ray powder pattern resembled the reference pattern ICDD-PDF #38-0757 for γ-AlH_3 with only a trace amount of LiCl in the material (see Figure 1). The infrared spectra of the samples showed a broad band with a maximum at 1675 cm^{-1} in the Al−H stretch region, and only a residual amount of hydrocarbons was detected in the C−H stretch region at 3000 cm^{-1}, see Figure 2.

Instrumentation and Analyses. Solid-state infrared spectra of the product (as KBr pellets) were recorded in the range of 4000−370 cm^{-1} under a nitrogen atmosphere and ambient conditions by using a Perkin-Elmer Spectrum GX FTIR spectrometer. The evaluation was done with the Perkin-Elmer Spectrum, version 2.00, Software.

Powder X-ray diffraction patterns were obtained with a Philips X'PERT diffractometer (Cu Kα radiation, 2 kW, with X'Celerator RTMS detector, automatic divergence slit). The powder was measured on a single Si crystal and sealed in the glove box by an airtight hood made of Kapton foil, the foil being mounted out of the focus of the diffractometer. The software for data acquisition and evaluation was X'PERT HighScore 2.2.

Synthesis at Moscow State University. Commercial $LiAlH_4$ was purified by recrystallization from the ether−toluene solution to a purity of 99.3% (these data were obtained by quantitative element analysis, chromatography of the gaseous phase, IR spectroscopy, and XRD). Commercial $AlCl_3$ was additionally purified by sublimation in a glass ampule above aluminum metal to a purity of

(6) (a) Graetz, J.; Reilly, J. J. *J. Alloys Compd.* **2006**, *424* (1−2), 262−265. (b) Graetz, J.; Reilly, J. J. *J. Phys. Chem. B* **2005**, *109*, 22181−22185.
(7) Turley, J. W.; Rinn, H. W. *Inorg. Chem.* **1969**, *8*, 18−22.
(8) Maehlen, J. P.; Yartys, V. A. In *Advanced Materials for Energy Conversion III*; Chandra, D., Petrovic, J., Bautista, R. G., Imam, A., Eds.; The Minerals, Metals & Materials Society: Warrendale, PA, 2006; pp 77−85.

99.9%. Total content of the transition metals in both initial chemicals was less than 10^{-3}%. Ether and benzene were purified by boiling and distillation over $LiAlH_4$.

γ-AlH_3 was synthesized according to the technique described in ref 1 using the reaction $3LiAlH_4 + AlCl_3 \rightarrow 4AlH_3 + 3LiCl$ in ether−benzene solution at room temperature. A 12% excess of lithium alanate was used, compared to the stoichiometry. After the reaction was complete, the solution was heated for a distillation of the mixed solvent until the hydride started to crystallize at 75−76 °C. The residual suspension was cooled under Ar gas. Solid γ-AlH_3 was received as thin needles or plates with sizes of (1−2) × (3−5) × (20−30) μm. This product was separated, washed by ether, and dried in a vacuum under slight heating.

Synchrotron X-ray Diffraction. SR-XRD studies of γ-alane were performed at the Swiss-Norwegian Beam Line (SNBL, BM1) at the European Synchrotron Radiation Facility (Grenoble). The high-resolution powder diffraction data for γ-AlH_3 was collected at room temperature with the powder diffractometer (in Debye−Scherrer mode) in steps of 0.003° in the 2θ range from 4.020 to 50.001°. Monochromatic X-rays were obtained from a channel-cut Si (111) crystal. For the measurements, the sample was put into a 0.7 mm quartz capillary. The wavelength, λ, selected for the measurements was accurately determined to be $\lambda = 0.60008$ (2) Å from separate calibration measurements of a standard LaB_6 sample. The Rietveld analysis of the data was carried out using the GSAS software.[9]

Results and Discussion

The SR-XRD pattern was indexed as an orthorhombic cell with unit cell parameters of $a = 5.3806(1)$ Å, $b = 7.3555(2)$ Å, $c = 5.77509(5)$ Å, and volume, V, $= 228.561(7)$ Å^3. The use of the rhombohedral α-AlH_3 (space group $R\bar{3}c$ (No. 167) ($a = 4.44994(5)$ Å, $c = 11.8200(2)$ Å, $V = 202.701$ Å^3) with 33.78 Å^3/fu of AlH_3[8] for comparison leads to a proposal that the unit cell of γ-AlH_3 contains 6 fu of AlH_3, yielding a higher value of the molecular volume for γ-AlH_3 (38.10 Å^3/AlH_3) and a smaller value, by 11%, of the density of γ-AlH_3 (1.31 g/cm^3), compared to that of α-AlH_3 (1.48 g/cm^3).

Analysis of the powder diffraction pattern showed that the experimentally observed *hkl* indices obey the following extinction rules: *0kl*, $k + l = 2n$; *h0l*, $h + l = 2n$; *h00*, $h = 2n$; *0k0*, $k = 2n$; *00l*, $l = 2n$. The latter are consistent with the space group *Pnnm* (No. 58). The FOX software package[10] has been used for this space group to determine the structure of the aluminum sublattice. The calculations yielded the positions of Al atoms occupying 2 different sites: 2-fold 2*b* (0,0,1/2) and 4-fold 4*g* (x,y,0; $x \approx 0.78$, $y \approx 0.08$). Even without the locatation of the hydrogen atoms, the refinement, based on the introduction of 6 Al atoms per unit cell, resulted in a rather good fit: $R_p = 5.41\%$, $R_{wp} = 6.91\%$, and $\chi^2 = 2.63$.

Anisotropic line broadening of the diffraction pattern was observed and was accounted for in the refinements using the Thompson−Cox−Hastings pseudo-Voigt-type function as proposed in ref 11. Size broadening coefficients, P and X (describing the Gausian and Lorentzian contributions, respectively), the mixing coefficient, η, and six microstrain parameters for the orthorhombic system were refined. The values of U, V, and W, defining instrumental parameters of the measurements, obtained from refinements of a LaB_6 standard, were fixed.

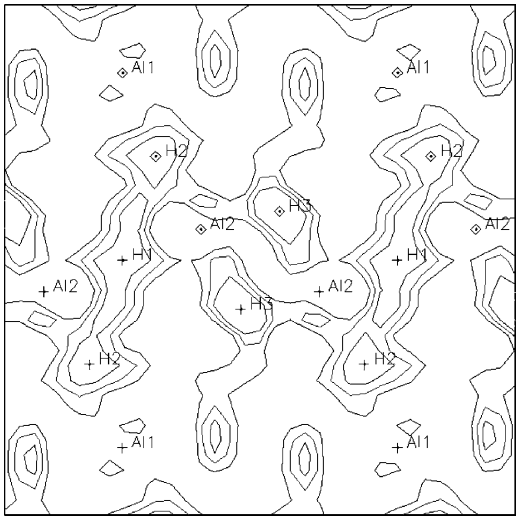

Figure 3. Difference Fourier map plotted in the x,y plane centered at x,y,z $= (1/2,1/2,1/2)$ for γ-AlH_3 showing peaks of electron density associated with the H1, H2, and H3 atoms in the vicinity of Al1 and Al2 (the width of the plot is 10 Å).

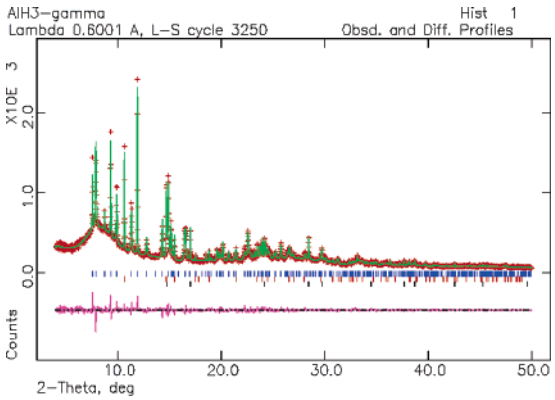

Figure 4. Observed (+), calculated (upper line), and difference (lower line) XRD profiles for γ-AlH_3. Positions of the peaks of the constituent phases are marked (from top to bottom): γ-AlH_3 (83.1(1) wt %), α-AlH_3 (10.7(1) wt %), and Al (6.2(1) wt %). The secondary phases, α-AlH_3 and Al, are formed during storage of the initial phase-pure γ-AlH_3 prior to the SR-XRD measurements.

An interesting feature of the Al sublattice is the formation of very short Al−Al distances of 2.606 Å between atoms Al2 and Al2. This feature will be further explained later in the paper, after description of the findings, associated with the most important features of the hydrogen sublattice and Al−H bonding in the structure.

Hydrogen atoms in the structure were located from the difference Fourier synthesis maps allowing identification of 4 different crystallographic sites occupied by 18 H atoms/unit cell. These included H1 (2d 0, 1/2, 1/2), H2 (4g x, y, 0), H3 (4g x, y, 0), and H4 (8h x, y, 0). Figure 3 shows a

(9) Larson, A. C.; van Dreele, R. B. General Structure Analysis System (GSAS), LANSCE, MS-H 805 (1994).
(10) Favre-Nicolin, V.; Černý, R. *J. Appl. Crystallogr.* **2002**, *35*, 734−743.
(11) Stephens, P. *J. Appl. Crystallogr.* **1999**, *32*, 281−289.

Table 1. Experimental Details and Crystallographic Data for γ-AlH_3

composition	AlH_3
fw	30.006
cryst syst	orthorhombic
space group	*Pnnm* (No. 58)
a (Å)	5.3806(1)
b (Å)	7.3555(2)
c (Å)	5.77509(5)
V (Å^3)	228.561(7)
Z	6
D (g cm^{-3})	1.308
color	white
temp (K)	293
wavelength (Å)	0.60008
diffractometer	Beamline BM01, SNBL, ESRF, France
data collection mode	Debye−Scherrer
2θ (deg)	4.020−50.001, increments of 0.003
no. of points refinement	15 327
R factors and GOF	$R_{wp} = 0.0614$, $R_p = 0.0488$, and $\chi^2 = 2.079$

Table 2. Atomic Coordinates and Thermal Parameters for γ-AlH_3

atom	site	*x*	*y*	*z*	U_{iso} (×100 Å^2)
Al1	*2b*	0	0	1/2	1.27(5)
Al2	*4g*	0.7875(2)	0.0849(2)	0	0.40(2)
H1	*2d*	0	1/2	1/2	2.0(−)
H2	*4g*	0.626(4)	0.278(2)	0	2.0(−)
H3	*4g*	0.094(2)	0.130(2)	0	2.0(−)
H4	*8h*	0.762(2)	0.078(2)	0.309(1)	2.0(−)

difference Fourier map in which the H1, H2, and H3 atoms are clearly seen in the neighborhood of the Al1 and Al2 atoms.

The introduction of hydrogen atoms into the calculations allowed further improvement of the refinement fits. The *R* values decreased to $R_p = 4.88\%$, $R_{wp} = 6.14\%$, and $\chi^2 = 2.08$. The good quality of the fit of the powder diffraction data is shown in Figure 4. Table 1 summarizes crystallographic data for γ-AlH_3, and Table 2 gives the atomic coordinates and thermal parameters for γ-AlH_3.

In γ-AlH_3, hydrogen atoms form octahedra around Al. Al1 is bonded with two H2 atoms and four H4 atoms, while Al2 is surrounded by H1, H2, two H3, and two H4 atoms (see Figure 5). The Al−H bonding distances in the structure are in the range of 1.66−1.79 Å (Table 3). Despite the rather large variation, they are all close to the only available Al−H binding distance in α-AlH_3 of 1.712 Å.[8]

The structure of γ-AlH_3 is composed of AlH_6 octahedra, as the building blocks (Figure 6), similar to α-AlH_3. However, these octahedra are connected differently, resulting in formation of hydrogen bridge bonds, Al−H−Al, in α-AlH_3 (Al−H = 1.712 Å, Al−Al = 3.24 Å, ∠142°) or two different types of bridges in γ-AlH_3 (Figure 5), where AlH_6 octahedra of two kinds share vertices and edges. In addition to a normal bridge bond (γ Al−H = 1.65−1.80 Å, Al−Al = 3.17 Å, ∠124.9°), a bifurcated bridge bond between two aluminum and two hydrogen atoms is formed. The geometry of this bond (Al−H = 1.68 and 1.70 Å, ∠100.7°) allows for a close proximity between aluminum atoms Al−Al = 2.606 Å. This appears to be even shorter than the Al−Al distances in Al metal (2.86 Å).

The formation of the bifurcated double-bridge bond, Al−2H−Al, is a prominent feature of the crystal structure of

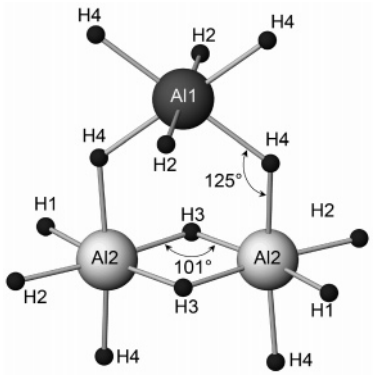

Figure 5. Two types of the available AlH_6 octahedra, $Al1H2_2H_4$ and $Al2H1H2H3_2H4_2$, and their interconnection in the crystal structure of γ-AlH_3. A double-bridge bond, Al2−2H3−Al2, and one type of the bridge bond Al1−H4−Al1 are shown. For Al1, all Al−H distances are large (1.78−1.79 Å). For Al2, the axial bonds, Al−H = 1.78 Å, are as long as the Al1−H distances. However, H atoms participating in the double-bridge bonds, H−2Al−H, form much shorter bonds with Al (1.68 and 1.72 Å). This proximity results in a short interatomic distance between two Al2 atoms of only 2.606 Å and a much lower bond angle (101°) than the normal bridge bond angle of 125°.

Table 3. Selected Interatomic Distances (Å) and Bond Angles (deg) in the Crystal Structure of γ-AlH_3[a]

atoms	distances	atoms	distances	atoms	angles
Al1−4Al2	3.1679(4)	Al2−H1	1.668(1)	Al1−H4−Al2	124.9(6)
Al1−4H4	1.784(6)	Al2−H2	1.664(8)	Al1−H2−Al2	171.0(2)
Al1−2H2	1.769(8)	Al2−H3	1.68(1)	Al2−H1−Al2	180.0(−)
Al2−2Al1	3.1679(4)	Al2−H3	1.70(1)	Al2−H3−Al2	100.7(7)
Al2−Al2	2.606(2)	Al2−2H4	1.790(8)		

[a] All H−H distances in the structure exceed 2.1 Å.

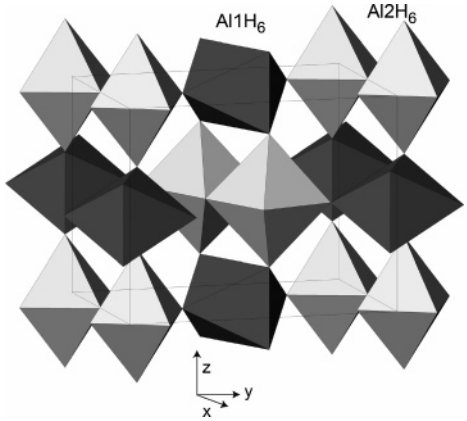

Figure 6. Framework of the AlH_6 octahedra in the crystal structure of γ-AlH_3 showing interconnection between two types of the available AlH_6 units, $Al1H_6$ and $Al2H_6$. Octahedra are connected by vertices ($Al1H_6$−$Al2H_6$) or by edges ($Al2H_6$−$Al2H_6$). This results in the formation of normal bridge bonds, H−Al−H, or double-bridge bonds, Al−2H−Al (latter).

γ-AlH_3. This feature is unique for the Al-containing hydrides and has not been previously reported for its hydrides.

Indeed, the AlH_6 octahedra are frequently found in the crystal structures of Al-containing hydrides. They exist either as AlH_6^{3-} ions or as covalently bound neutral AlH_6 polyhedra. The AlH_6^{3-} ions are present as isolated units in the structures of the R_3AlH_6 hexahydrides, for example, in Na_3AlH_6,[12] K_2LiAlH_6, and K_2NaAlH_6.[13]

(12) Ronnebro, E.; Noreus, D.; Kadir, K.; Reiser, A.; Bogdanovic, B. *J. Alloys Compd.* **2000**, *299*, 101 −106.

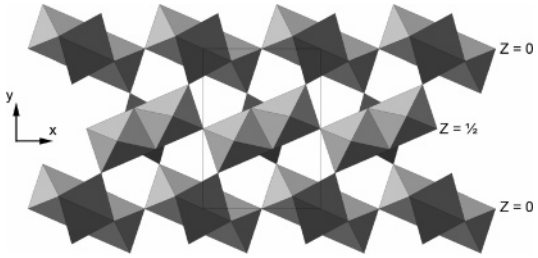

Figure 7. Projection of the crystal structure of γ-AlH_3 along [001] shown as a packing of the AlH_6 octahedra. Large cavities in the structure are clearly seen.

On the other hand, AlH_6 octahedra share vertices in the crystal structure of α-AlH_3,[8] thus, forming normal bridge bonds, Al−H−Al. Such bonds are a consequence of the electron deficiency of the elements of the third group, which may self-stabilize by the formation of 3-center 2-electron bridge bonds in the case of covalent compounds.

Finally, one additional feature of the crystal structure of γ-AlH_3 should be mentioned. This feature lies in the formation of large cavities between the AlH_6 octahedra. The cavities are clearly seen in the Figure 7. The vertices of a set of two edge-connected $Al2H_6$ octahedra are always connected to two other pairs of edge-connected $Al2H_6$ octahedra and to four single vertex-connected $Al1H_6$ octahedra. Hence, the strands of $Al2H_6$ are always separated by single $Al1H_6$ octahedra, which are differently oriented in space. As a result of such packing, the structure of γ-AlH_3 has a much smaller, by 11%, density than α-AlH_3.

(13) Graetz, J.; Lee, Y.; Reilly, J. J.; Park, S.; Vogt, T. Structures and thermodynamics of the mixed alkali alanate. *Phys. Rev. B*, **2005**, *71*, 184115.

The decomposition reaction enthalpy of γ-AlH_3 is 7.1 kJ/mol,[6] which is small, compared to that one of α-AlH_3 which is 11.4 kJ/mol.[6] In the case of AlH_3, the reaction enthalpy is the same as the enthalpy of formation because the products are elements; therefore, the average binding energy in γ-AlH_3 is lower than that in α-AlH_3. Since the (thermodynamic) decomposition temperature and the equilibrium pressure is related to the Gibbs free energy, this should make a contribution to lower the decomposition temperature of the γ-modification. A different contribution comes from the reaction entropy, which should be lower in the case of the γ-compound, if the assumption of a higher degree of disorder in the γ-phase is justified. At equilibrium ($\Delta G = 0$), the Gibbs equation can be written as

$$T_{eq} = \frac{\Delta H}{\Delta S} \quad (1)$$

Thus, both the numerator and denominator decrease in eq 1 when changing from the α- to γ-phase. However, because the equilibrium pressure of the γ-AlH_3 is higher and the decomposition temperature is lower, this indicates a dominating effect of the average binding energy, ΔH, over the entropy.

Acknowledgment. This work has received support from INTAS Project 05-1000005-7665 "New Alane. Novel Reversible Hydrogen Storage Materials Based on the Alloys of Al" and from the HGF initiative "FuncHy". We thank ESRF and SNBL for provision of beam time.

Supporting Information Available: Crystallographic data in CIF format. This material is available free of charge via the Internet at http://pubs.acs.org.

IC0617487

ELSEVIER

Journal of Alloys and Compounds 437 (2007) 140–145

Journal of ALLOYS AND COMPOUNDS

www.elsevier.com/locate/jallcom

Synchrotron X-ray diffraction study of $ErMn_2D_2$

J.P. Maehlen [a], V.A. Yartys [a,*], A.B. Riabov [b], A. Budziak [c], H. Figiel [d], J. Żukrowski [d]

[a] *Institute for Energy Technology, P.O. Box 40, Kjeller No-2027, Norway*
[b] *Physico-Mechanical Institute of the National Academy of Science of Ukraine, 5 Naukova Street, 79601 Lviv, Ukraine*
[c] *The H. Niewodniczanski Institute of Nuclear Physics, Radzikowskiego 152, 31-342 Krakow, Poland*
[d] *Department of Solid State Physics, Faculty of Physics and Applied Computer Science AGH, University of Science and Technology, 30 Mickiewicza av., 30-059 Krakow, Poland*

Received 29 June 2006; received in revised form 19 July 2006; accepted 20 July 2006
Available online 7 September 2006

Abstract

$ErMn_2D_2$ deuteride has been studied by high-resolution synchrotron X-ray powder diffraction at temperatures between 150 and 298 K. Below 210 K a transformation from the hexagonal C14 Laves phase type structure (space group $P6_3/mmc$; $a = 5.55357(3)$ Å; $c = 9.05368(7)$ Å; $T = 298$ K) into the monoclinic one crystallising in the space group $C2/m$ ($a = 9.61247(9)$ Å; $b = 5.57558(4)$ Å; $c = 9.07102(8)$ Å; $\beta = 90.5451(5)^\circ$; $T = 150$ K) takes place. A rather large two-phase region of coexistence of both structural modifications was observed between 185 and 205 K.

Keywords: Magnetically ordered materials; Hydrogen absorbing materials; Crystal structure; Phase transitions; Synchrotron radiation

1. Introduction

The $ErMn_2H_2$ ($ErMn_2D_2$) hydride has earlier been studied using standard X-ray diffraction technique [1,2]. At room temperature the hexagonal C14 Laves phase-related structure, space group (s.g.) $P6_3/mmc$, was found, while the pattern obtained below ~210 K was attributed to a triclinic distortion to s.g. $P1$ [1]. Because of rather low quality of the data, attempts to refine them with structures of higher symmetry did not give satisfactory results. In present work we have performed synchrotron X-ray powder diffraction (SR-XRD) studies to solve the structure of the low temperature $ErMn_2D_2$ deuteride unambiguously.

2. Experimental details

2.1. Sample preparation

The sample was prepared from high purity metals. Induction melting was followed by annealing of the sample placed into an evacuated quartz ampoule at 1070 K for 5 days and then quenching into a mixture of ice and water, yielding a nearly pure intermetallic alloy $ErMn_2$. The deuteration was performed using standard technique described, e.g. in [3]. Dideuteride $ErMn_2D_2$ was synthesised by absorbing the amount of deuterium gas necessary to reach stoichiometry $D/ErMn_2 = 2.0$. Synthesis was accompanied by annealing at 453 K for a few hours to improve the homogeneity of the material. The X-ray diffraction data collected using conventional technique showed a formation of close to single-phase deuteride. The sample contained small amounts of impurities, Er_2O_3 (approximately 2 wt.%, s.g. $Ia\bar{3}$, $a = 10.5480(7)$ Å) and $ErD_{2\pm x}$ (approximately 2 wt.%, s.g. $Fm\bar{3}m$, $a = 5.1158(8)$ Å), which were both introduced into the refinements of the X-ray powder diffraction data. At temperatures applied in present work (150–298 K), the studied deuteride is stable; no changes of the deuterium content in the sample take place.

2.2. The X-ray measurements

The preliminary X-ray diffraction measurements were performed on a SIEMENS D5000 diffractometer using Cu Kα radiation ($\lambda = 1.54056$ Å) with a continuous-flow cryostat supplied by Oxford Instruments.

SR-XRD data were collected at the Swiss-Norwegian Beam Line (BM01B) at ESRF, Grenoble (Si(1 1 1) channel-cut monochromator, $\lambda = 0.37504(2)$ Å, scintillation detectors) at temperatures 150, 185, 190, 195, 200, 205, 210, 215 and 298 K.

The sample was enclosed inside a quartz capillary of 0.3 mm in diameter. The experiment was performed in following steps:

1. Measurements were first done at 298 K for 2 h.
2. The sample was cooled down to 150 K and measured for 2 h.
3. A series of measurements (20 min each) with a stepwise increase in temperatures (185–215 K with a 5 K step) was performed. Prior to every measurement step, the sample was equilibrated at constant temperature for approximately 30 min.

* Corresponding author. Tel.: +47 63 80 64 53; fax: +47 63 81 29 05.
E-mail address: volodymyr.yartys@ife.no (V.A. Yartys).

0925-8388/$ – see front matter © 2006 Elsevier B.V. All rights reserved.
doi:10.1016/j.jallcom.2006.07.088

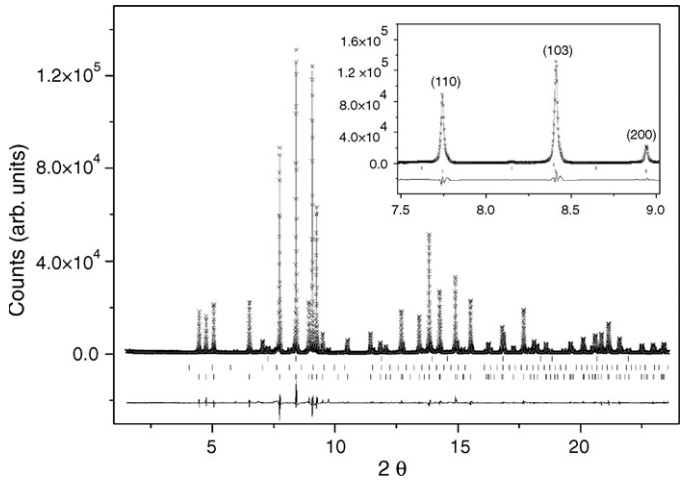

Fig. 1. Diffraction pattern of the hexagonal $ErMn_2D_2$ (s.g. $P6_3/mmc$) collected at 293 K showing observed (crosses), calculated (upper line) and difference (bottom line) plots. The positions of the Bragg peaks are shown as ticks (upper: $ErD_{2\pm x}$, middle: Er_2O_3, bottom: $ErMn_2D_2$). Inset: selected region of the diffraction pattern, 7.5–9.0°, with Bragg indexes of three peaks given.

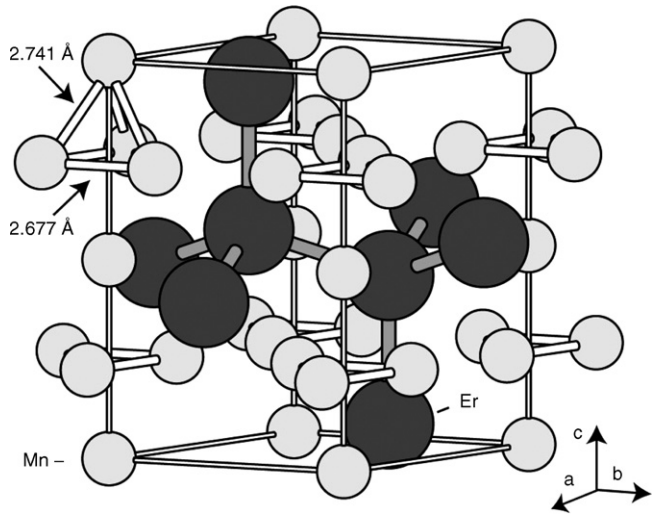

Fig. 2. The metal sublattice in the hexagonal crystal structure of $ErMn_2D_2$ at room temperature. The Mn_4 tetrahedra are slightly elongated along the c-axis (Mn–Mn interatomic distances in the (a, b) plane are 2.677 Å; distances out of the plane, along [0 0 1] are 2.741 Å).

3. Results

All powder diffraction data were analysed by the Rietveld whole-profile refinement method [4] using the General Structure Analysis System (GSAS) software [5]. Peak shapes were described by a multi-term Simpson's rule integration of the pseudo-Voigt function [6,7], which includes the asymmetry correction according to Finger et al. [8].

3.1. Crystal structure of $ErMn_2D_2$ at room temperature

The refinements of the room temperature data confirm the formation of the hexagonal C14 type Laves type hydride: s.g. $P6_3/mmc$; $a = 5.55357(3)$ Å; $c = 9.05368(7)$ Å and are shown in Fig. 1. The metal sublattice of the $ErMn_2D_2$ crystal structure is presented in Fig. 2 while Table 1 summarises the results obtained from the refinements of the diffraction data. The interatomic metal–metal distances change from ~3.24 Å (Er–Er), ~3.10 Å (Er–Mn), and ~2.65 Å (Mn–Mn) in the intermetallic compound $ErMn_2$ [$a = 5.294$ Å, $c = 8.664$ Å, s.g. $P6_3/mmc$] to 3.376(1)–3.4068(4) Å (Er–Er), 3.2500(3)–3.2890(8) Å (Er–Mn), and 2.677(3)–2.876(3) Å (Mn–Mn) in the deuteride. $ErMn_2$ belongs to the group of Laves phases RMn_2 (R = rare earth) compounds containing magnetic sublattices formed by 3d magnetic moments of the Mn atoms. The 3d shells lose their intrinsic magnetic moments when first-neighbour Mn–Mn distance d becomes smaller than some critical distance of $d_c \sim 2.7$ Å [9]. The shortest Mn–Mn distances present in the metal sublattice (2.678 Å) explain the absence of a long-range magnetic order of $ErMnD_2$ at room temperature.

3.2. Crystal structure of $ErMn_2D_2$ at low temperatures

Structural solution of the low temperature diffraction pattern (150 K) was achieved in the following manner. First, an individual peak fitting was performed for the selected reflections (40 peaks using the WinPLOTR software [10]) with the aim at obtaining as-accurate-as-possible peak positions. Then the unit cell was identified utilising indexing software packages (CRYSFIRE indexing suite [11]) yielding a monoclinic unit cell as the best choice. Systematic extinctions observed (for the hkl reflections a condition $h + k = 2n$ was the case) indicated that the unit cell was a C-centred cell with the possible groups among $C2$, Cm, and $C2/m$. The whole-profile Rietveld fitting was performed using starting atomic positions obtained through a general transformation from description of the crystal structure in s.g. $P6_3/mmc$ to s.g. $C2/m$ (no. 12). Lowering the symmetry (both space groups $C2$ (no.5) and Cm (no.8) were considered) did not give any improvements of the fit. The fitted pattern obtained at 150 K is presented in Fig. 3. Table 1 summarises the fitted parameters, while interatomic distances are presented in Table 2. The labelling of the sites presented in Tables 1 and 2 is chosen according to the following scheme (hexagonal → monoclinic): Er → Er1 and Er2; Mn1 → Mn1 and Mn2; Mn2 → Mn3 and Mn4. The scheme of the transformation from the room temperature to the low temperature structures is presented in Fig. 4. During this transformation, the irreducible number of atoms doubles (increasing from three in the hexagonal to six in the monoclinic cell).

During the transformation of the hexagonal modification into the monoclinic one it undergoes a deformation creating "enlarged" Mn–Mn interatomic distances. Even the shortest Mn–Mn distance in the monoclinic $ErMn_2D_2$ phase becomes quite long, being equal to ~2.71 Å. As a result, all $d_{Mn–Mn}$ distances become longer than the critical distance d_c of ~2.7 Å observed for the magnetically ordered RMn_2 (R = rare earth) compounds [9].

3.3. Region of coexistence of the hexagonal and monoclinic modifications

Within a certain temperature window, two structural modifications of $ErMnD_2$ coexist forming a two-phase region (see

Table 1
Crystal structure data (atomic coordinates, isotropic temperature factors ($U_{iso} \times 100$ Å^2), unit cell dimensions, phase fraction (by weight), and goodness-of-fit parameters) derived from the Rietveld refinements of the SR-XRD data for $ErMn_2D_2$ at selected temperatures

	T (K)								
	150	185	190	195	200	205	210	215	298
Low temperature phase, monoclinic cell[a]									
Er1 (x)	0.66341(13)	0.6641(5)	0.6650(5)	0.6642(5)	0.6656(6)	0.664(1)	–	–	–
Er1 (z)	0.93520(12)	0.9333(5)	0.9335(6)	0.9324(7)	0.9319(7)	0.933(2)	–	–	–
Er1 (U_{iso})	0.32(1)	0.1(1)	0.26	0.4	0.45	0.5	–	–	–
Er2 (x)	0.33296(13)	0.3327(5)	0.3319(5)	0.3325(6)	0.3321(7)	0.334(1)	–	–	–
Er2 (z)	0.43652(12)	0.4393(6)	0.4383(6)	0.4393(7)	0.4395(8)	0.439(2)	–	–	–
Er2 (U_{iso})	0.32(1)	0.1(1)	0.26	0.4	0.45	0.5	–	–	–
Mn1 (U_{iso})	0.24(3)	0.1(2)	0.09	0.16	0.2	0.6	–	–	–
Mn2 (U_{iso})	0.24(3)	0.1(2)	0.09	0.16	0.2	0.6	–	–	–
Mn3 (x)	0.1639(4)	0.1634(18)	0.1610(17)	0.1641(21)	0.1627(24)	0.169(4)	–	–	–
Mn3 (z)	0.7479(4)	0.7501(16)	0.7501(16)	0.7476(20)	0.7483(22)	0.749(4)	–	–	–
Mn3 (U_{iso})	0.24(3)	0.1(2)	0.09	0.16	0.2	0.6	–	–	–
Mn4 (x)	0.0818(3)	0.0804(12)	0.0835(11)	0.0823(13)	0.0819(15)	0.078(3)	–	–	–
Mn4 (y)	0.7569(4)	0.7531(16)	0.7580(17)	0.7575(19)	0.7580(21)	0.753(4)	–	–	–
Mn4 (z)	0.2520(3)	0.2551(15)	0.2514(17)	0.2528(18)	0.2520(20)	0.252(3)	–	–	–
Mn4 (U_{iso})	0.24(3)	0.1(2)	0.09	0.16	0.2	0.6	–	–	–
a (Å)	9.61247(9)	9.60364(32)	9.6034(3)	9.6017(4)	9.6001(4)	9.5965(6)	–	–	–
b (Å)	5.57558(4)	5.57279(14)	5.57240(15)	5.57189(17)	5.57122(18)	5.56972(25)	–	–	–
c (Å)	9.07102(8)	9.07047(25)	9.06965(27)	9.0685(3)	9.0674(3)	9.0639(5)	–	–	–
β	90.5451(5)	90.4231(18)	90.4206(19)	90.4059(23)	90.3922(28)	90.391(5)	–	–	–
V (Å^3)	486.140(7)	485.430(24)	485.341(26)	485.148(29)	484.95(3)	484.45(5)	–	–	–
Weight fraction	0.96(1)	0.65(5)	0.63(5)	0.57(5)	0.50(5)	0.26(5)	0	0	0
Ambient temperature phase, hexagonal cell[b]									
Er (z)	–	0.4354(4)	0.4357(4)	0.4360(4)	0.4358(4)	0.43616(19)	0.43594(15)	0.43595(16)	0.43642(6)
Er (U_{iso})	–	0.5(3)	0.5(3)	0.5(3)	0.5(3)	0.5(3)	0.29(8)	0.31(8)	0.713(18)
Mn1 (U_{iso})	–	0.5(3)	0.5(3)	0.5(3)	0.5(3)	0.5(3)	0.2(1)	0.03(12)	0.53(3)
Mn2 (x)	–	0.8408(12)	0.840371(13)	0.8401(11)	0.8403(9)	0.8403(4)	0.8403(3)	0.8395(3)	0.83931(15)
Mn2 (z)	–	0.6816(24)	0.680744(26)	0.6801(21)	0.6806(19)	0.6806(8)	0.6806(6)	0.6791(7)	0.67861(29)
Mn2 (U_{iso})	–	0.5(3)	0.5(3)	0.5(3)	0.5(3)	0.5(3)	0.2(1)	0.03(12)	0.53(3)
a (Å)	–	5.54891(15)	5.54831(15)	5.54823(16)	5.54829(16)	5.54848(12)	5.54833(22)	5.54820(10)	5.55357(3)
c (Å)	–	9.0492(3)	9.0492(3)	9.0492(3)	9.0495(3)	9.04943(24)	9.0489(4)	9.04840(18)	9.05368(7)
V (Å^3)	–	241.299(13)	241.247(13)	241.241(13)	241.254(13)	241.268(10)	241.241(16)	241.216(8)	241.8241(27)
Weight fraction	0	0.30(5)	0.33(5)	0.39(5)	0.47(5)	0.71(5)	0.97(5)	0.96(5)	0.96(2)
Goodness-of-fit parameters									
R_{wp} (%)	8.26	8.43	8.83	9.33	9.64	9.74	10.40	11.12	9.74
R_p (%)	6.04	6.36	6.68	7.00	7.42	7.37	7.45	8.13	6.74

Calculated/estimated standard deviations in parentheses. During the refinements the isotropic temperature factors for the atoms the same type, Er or Mn, were constrained to be equal. No other constraints were applied in the refinements.

[a] Atomic positions in the monoclinic cell, space group: $C2/m$ (no. 12): Er1, Er2, and Mn3 in 4i (x, 0, z), Mn1 in 2a (0, 0, 0), Mn2 in 2c (0, 0, 1/2), and Mn4 in 8j (x, y, z).

[b] Atomic positions in the hexagonal cell, space group: $P6_3/mmc$ (no. 194): Er in 4f (1/3, 2/3, z), Mn1 in 2a (0, 0, 0), and Mn2 in 6h (x, 2x, 1/4).

Table 2
Interatomic distances in the monoclinic phase ($T = 150$ K) and hexagonal phase ($T = 298$ K) derived from the Rietveld refinements of SR-XRD data for $ErMn_2D_2$

T = 150 K		T = 298 K	
Vector	Length	Vector	Length
(a) Mn–Mn interatomic distances (in Å, distance below $d_c = 2.7$ Å is shown in bold)			
Mn1–Mn3	2.789(4)	Mn1–Mn2	2.7409(8)
Mn1–Mn4	2.766(3)		
Mn2–Mn3	2.733(3)		
Mn2–Mn4	2.748(3)		
Mn3–Mn4	2.723(3)	**Mn2–Mn2**	**2.677(3)**
Mn3–Mn4	2.833(3)	Mn2–Mn2	2.876(3)
Mn4–Mn4	2.711(5)		
Mn4–Mn4	2.865(5)		
(b) Er–Er interatomic distances (in Å)			
Er1–Er1	3.364(3)	Er–Er	3.3756(11)
Er1–Er1	3.4479(12)		
Er1–Er2	3.3728(10)		
Er2–Er2	3.401(2)	Er–Er	3.4068(4)
Er2–Er2	3.417(2)		
(c) Er–Mn interatomic distances (in Å)			
Er1–Mn1	3.2559(7)	Er–Mn1	3.25761(10)
Er1–Mn1	3.2832(11)		
Er2–Mn2	3.2575(13)		
Er2–Mn2	3.2655(6)		
Er1–Mn3	3.265(2)	Er–Mn2	3.2500(3)
Er1–Mn3	3.306(3)	Er–Mn2	3.2890(8)
Er2–Mn3	3.2513(2)	Er–Mn2	3.2500(3)
Er2–Mn3	3.273(4)		
Er1–Mn4	3.228(3)		
Er1–Mn4	3.286(4)		
Er1–Mn4	3.311(3)		
Er2–Mn4	3.223(3)		
Er2–Mn4	3.264(4)		
Er2–Mn4	3.265(3)		

Calculated standard deviations are given in parentheses.

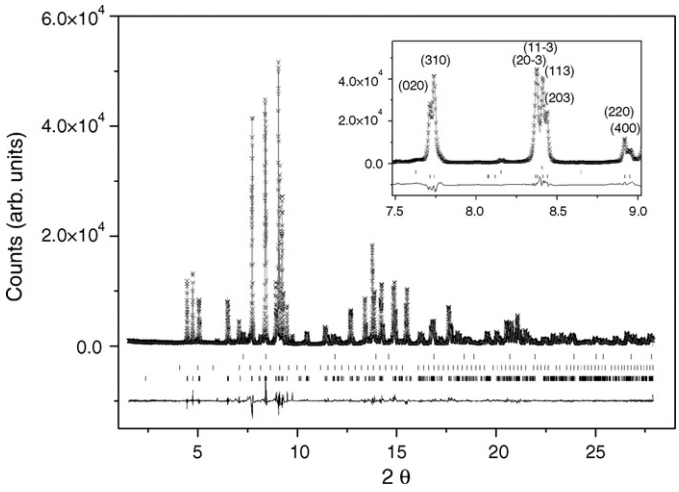

Fig. 3. Diffraction pattern of the monoclinic $ErMn_2D_2$ (s.g. *C2/m*) collected at 150 K showing observed (crosses), calculated (upper line) and difference (bottom line) plots. The positions of the Bragg peaks are shown as ticks (upper: $ErD_{2\pm x}$, middle: Er_2O_3, bottom: $ErMn_2D_2$). Inset: selected region of the diffraction pattern, 7.5–9.0°; splitting of three originally single peaks $(1\,1\,0)_{hex}$, $(1\,0\,3)_{hex}$ and $(2\,0\,0)_{hex}$ [compare with Fig. 1] is clearly seen. The Bragg indexes for the monoclinic cell are given.

Fig. 5). An example of a fitted pattern (collected at 200 K) is presented in Fig. 6, while the results from the refinements are summarised in Table 1. The two-phase region was experimentally observed at temperatures between 185 and 205 K. The appearance of the monoclinic phase at 205 K is clearly visible in the diffraction pattern (Fig. 7). The upper temperature limit of the existence of the monoclinic $ErMn_2D_2$ agrees rather well with the temperature of the magnetic ordering transition reported in [1] (∼214 K).

It cannot be ruled out that the two-phase region in the low temperature area extends to temperatures below 185 K before a complete transformation is achieved at 150 K. The weight fraction ratio of the two phases present in the mixture and the changes

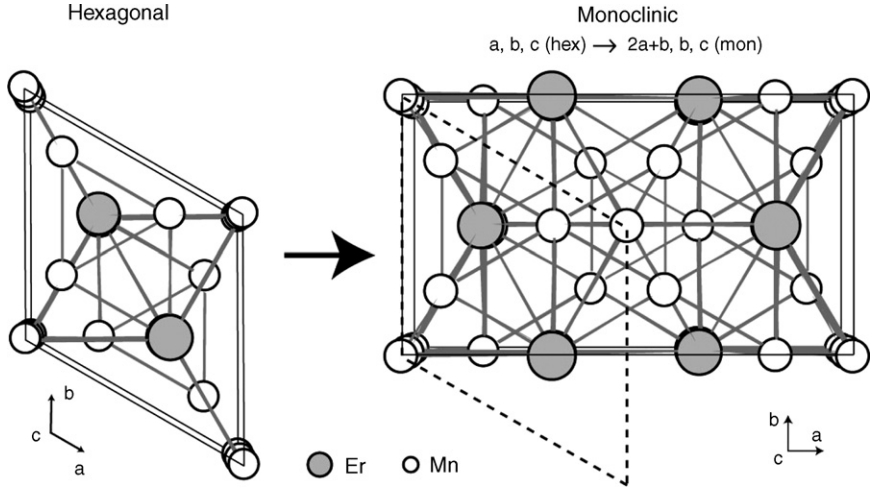

Fig. 4. Scheme of the transformation of the unit cell of the hexagonal phase of $ErMn_2D_2$ observed at room temperature (left) into the monoclinic low temperature one (right; the original hexagonal cell is shown with the dashed lines). During this transformation, the Er position splits into two positions (Er → Er1 and Er2), and the two Mn positions both split into two (Mn1 → Mn1 and Mn2; Mn2 → Mn3 and Mn4).

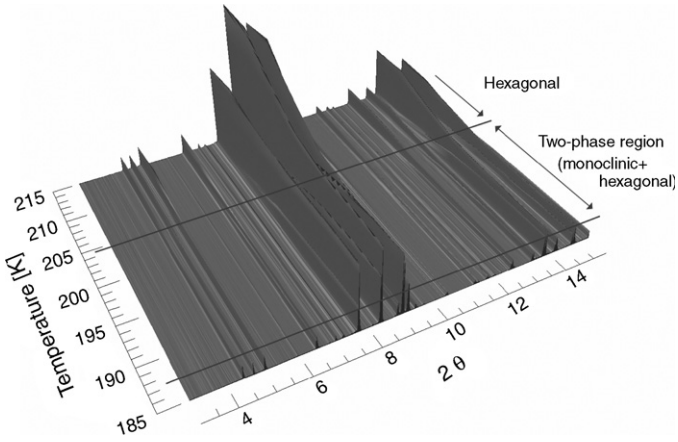

Fig. 5. Evolution of the in situ SR-XRD patterns of the $ErMn_2D_2$ as a function of temperature ($T = 185$–215 K in steps of $\Delta T = 5$ K; $\lambda = 0.3750$ Å). This plot contains a smoothened subset of the graphs to give an impression of the time development of the process.

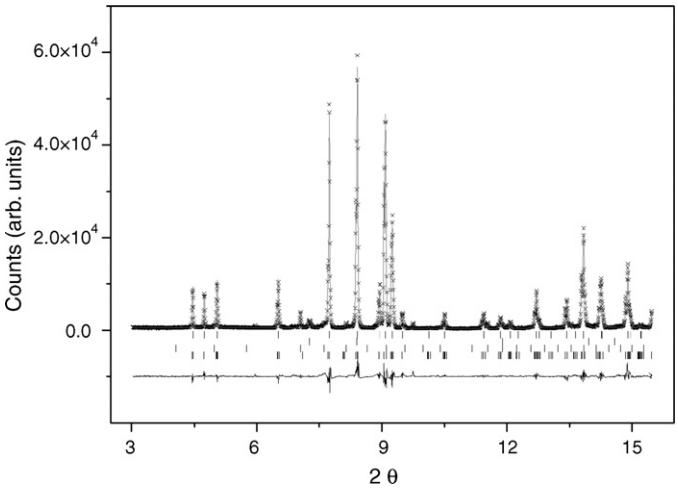

Fig. 6. Example of the refinements of the diffraction pattern of $ErMn_2D_2$ collected in the two-phase region. This plot shows the data obtained at $T = 200$ K showing observed (crosses), calculated (upper line) and difference (bottom line) plots. The positions of the Bragg peaks are shown as ticks (from top to bottom: hexagonal $ErMn_2D_2$, $ErD_{2\pm x}$, Er_2O_3, monoclinic $ErMn_2D_2$).

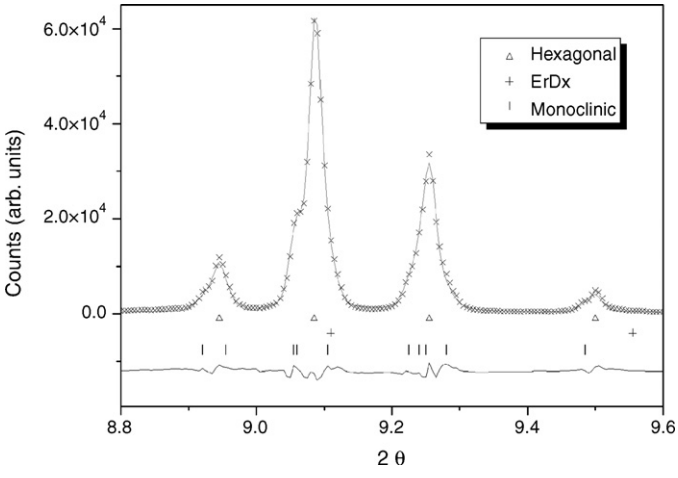

Fig. 7. Diffraction pattern of the $ErMn_2D_2$ sample collected at 205 K. The presence of the monoclinic phase is clearly visible. Observed intensities are represented as crosses, the calculated intensities (upper line) and difference (bottom line) as lines.

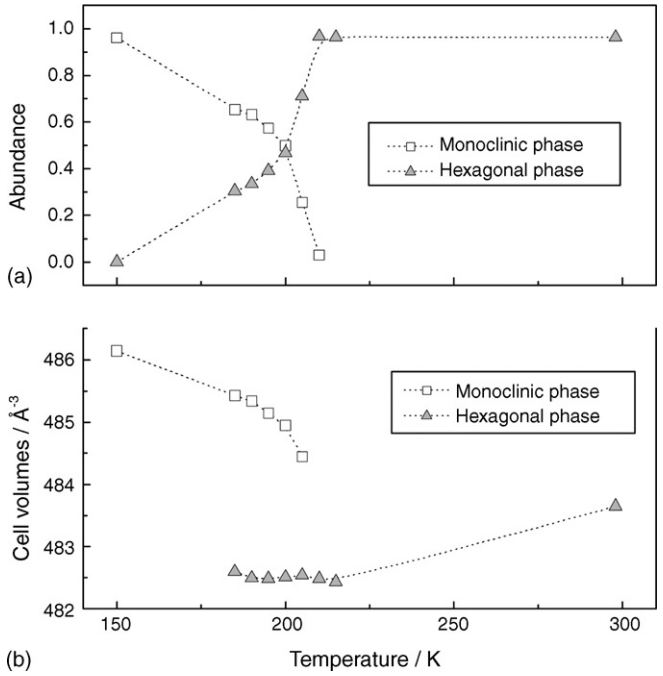

Fig. 8. Relative abundances of the hexagonal and monoclinic phases (a), and changes of unit cell volumes (b) as a function of temperature. For the hexagonal phase the doubled values of V are presented to have them in the same scale with the values for the monoclinic cell.

of the unit cell volumes as a function of temperature are shown in Fig. 8.

We note opposite trends observed in changes of the unit cell volumes on cooling. For the hexagonal phase, a contraction takes place ($\Delta V_{\text{hexagonal}}$ is -0.24% upon cooling from 298 down to 200 K). In contrast, for the monoclinic phase the cooling is associated with a rather pronounced expansion ($\Delta V_{\text{monoclinic}}$ equals to 0.35% upon cooling from 205 down to 150 K).

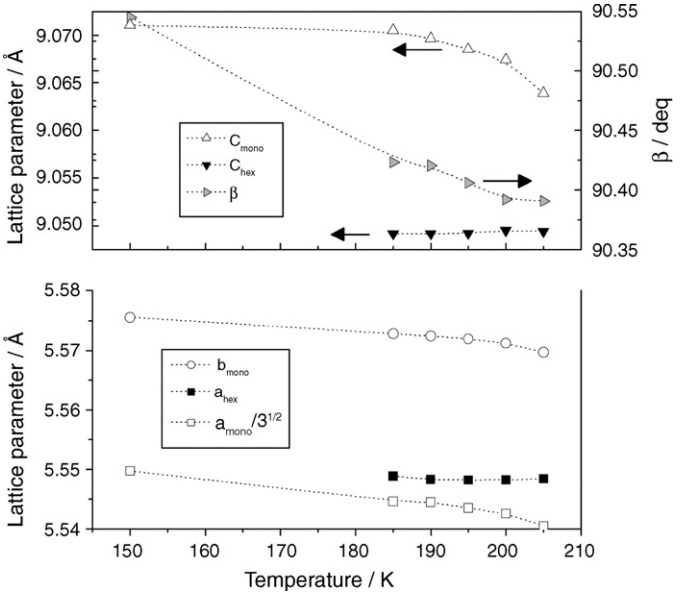

Fig. 9. Changes of the unit cell parameters and angle β of the monoclinic unit cell of $ErMn_2D_2$ as a function of temperature between 150 and 205 K.

Fig. 9 shows in detail the changes of the unit cell parameters of the monoclinic and hexagonal $ErMn_2D_2$ between 150 and 205 K. The driving force for this transformation is probably strongly related to the behaviour of hydrogen (deuterium) atoms in the structure. At high temperature, the hydrogen atoms freely diffuse between the most preferable for hydrogen accommodation interstitial sites in the hexagonal structure. Lowering of the temperature leads to hydrogen ordering in the lattice via "freezing" of hydrogen atoms in the specific interstitial sites, which, in turn, creates a distortion of the structure. It is not possible to find the ordering of hydrogen in the material using SR-XRD. Neutron diffraction measurements on this sample aiming to resolve the type of the ordering of deuterium in this compound are required.

Acknowledgements

This paper is in part supported by the Polish Research Council, Norwegian Research Council and Nordic Energy Research (project NORSTORE). We wish to thank H. Emerich and other members of the scientific staff at the Swiss-Norwegian Beam Line for their skilful assistance during the SR-XRD experiments. We are grateful to Dr. M. Sato (Tokai University, Japan and IFE) and T. Foerde (IFE) for their help in the experimental measurements.

References

[1] H. Figiel, A. Budziak, P. Zachariasz, J. Żukrowski, G. Fischer, E. Dormann, J. Alloys Compd. 368 (2004) 260.
[2] H. Figiel, A. Budziak, J. Żukrowski, G. Wiesinger, B. Ouladdiaf, J. Magn. Magn. Mater. 272–276 (2004) 585.
[3] H. Figiel, J. Przewoźnik, V. Paul-Boncour, A. Lindbaum, E. Gratz, M. Latroche, M. Escorne, A. Percheron-Guegan, P. Mietniowski, J. Alloys Compd. 274 (1998) 29.
[4] H.M. Rietveld, J. Appl. Crystallogr. 2 (1969) 65.
[5] A.C. Larson, R.B. von Dreel, General Structure Analysis System, LANL, Los Alamos, 1994.
[6] C.J. Howard, J. Appl. Crystallogr. 15 (1982) 615.
[7] S.P. Thompson, E.D. Cox, J.B. Hastings, J. Appl. Crystallogr. 20 (1987) 79.
[8] L.W. Finger, D.E. Cox, A.P. Jephcoat, J. Appl. Crystallogr. 27 (1994) 892.
[9] O.L. Makarova, I.N. Goncharenko, A.V. Irodova, I. Mirebeau, E. Suard, Phys. Rev. B 66 (2002) 104423.
[10] T. Roisnel, J. Rodriguez-Carvajal, WinPLOTR: a Windows tool for powder diffraction patterns analysis. Material Science Forum, Proceedings of the Seventh European Powder Diffraction Conference (EPDIC7), 2000, p. 118–123. Ed. R. Delhez and E. J. Mittenmeijer.
[11] R. Shirley, The CRYSFIRE System for Automatic Powder Indexing: User's Manual, The Lattice Press, Guildford, Surrey, England, 2000.

ELSEVIER

Journal of Alloys and Compounds 446–447 (2007) 280–289

Journal of ALLOYS AND COMPOUNDS

www.elsevier.com/locate/jallcom

Thermal decomposition of AlH_3 studied by *in situ* synchrotron X-ray diffraction and thermal desorption spectroscopy

J.P. Maehlen [a], V.A. Yartys [a,*], R.V. Denys [a,b], M. Fichtner [c], Ch. Frommen [c], B.M. Bulychev [d], P. Pattison [e], H. Emerich [e], Y.E. Filinchuk [e], D. Chernyshov [e]

[a] *Institute for Energy Technology, P.O. Box 40, Kjeller No-2027, Norway*
[b] *Physico-Mechanical Institute of the National Academy of Science of Ukraine, 5, Naukova Str., 79601 Lviv, Ukraine*
[c] *Institute of Nanotechnology, Forschungszentrum Karlsruhe GmbH, P.O. Box 30640, D-76021 Karlsruhe, Germany*
[d] *Chemistry Department, Moscow State University, Leninskie Gori, Moscow 119992, MSU, Chemistry Department, Russia*
[e] *Swiss-Norwegian Beam Line, ESRF, BP 220, F-38043 Grenoble, France*

Received 30 October 2006; received in revised form 28 November 2006; accepted 29 November 2006
Available online 12 January 2007

Abstract

The thermal decomposition of alane was investigated by application of synchrotron X-ray diffraction (SR-XRD) and thermal desorption spectroscopy (TDS). Two polymorphs were studied, α- and γ-AlH_3. Activation energies, anisotropic volume expansions, and phase transformation paths were found. In addition, the crystal structure data, including structure of hydrogen sublattice, and small charge transfer from the aluminium towards the hydrogen sites were observed during a high-resolution SR-XRD study of α-AlH_3.

Keywords: Hydrogen absorbing materials; Crystal structure; Phase transitions; Synchrotron radiation

1. Introduction

To utilize renewable energy sources, hydrogen and electricity are considered as an ideal combination of energy carriers, providing versatile and environmentally benign solutions. Every step in a complete hydrogen energy cycle, which includes hydrogen production from water by electrolysis, hydrogen storage and conversion into electricity in the fuel cell stack, needs to be sufficiently improved to increase the competitiveness of hydrogen energy with the available energy systems. Hydrogen storage is considered as the most important issue to be solved. An efficient hydrogen storage solution should combine several key features including high hydrogen storage densities, volumetric and gravimetric, fast and easy reversible H loading/H release, together with affordable price and fulfilment of the safety requirements. A storage system satisfying all these beneficial features, unfortunately, is not developed yet. Even though solid state storage materials, first of all reversible metal hydrides, have been appreciated as an efficient way for reaching high volumetric efficiency of the storage system and fast rates of hydrogen exchange, reaching these advantages has always been paid by a price of having a rather poor gravimetric hydrogen storage capacity.

To reach the high gravimetric hydrogen densities required for commercially competitive hydrogen storage solutions for the transport sector, metal hydride systems containing light elements are needed. In the present work we have focused our studies on the binary metal-hydrogen system of such a type, namely on the aluminium trihydride (alane). Aluminium trihydride alane is considered as a prospective solid H storage material, having high gravimetric (10 wt.% H) and volumetric density of H (2 times higher compared to LH_2) and, also, because of its convenient range of thermal stability. AlH_3 forms several polymorphic modifications, which are often polymers $(AlH_3)_n$ [1]. α-Alane AlH_3 was first synthesized in 1947 by an exchange reaction between $AlCl_3$ and lithium hydride in ether solution [2]. This binary hydride has a covalent Al–H bonding and exhibits dielectric properties. α-AlH_3, the most stable modification of alane, has a trigonal crystal structure (space group $R\bar{3}c$) [3,4] and is composed of the corner-sharing AlH_6 octahedra. The AlH_6 octahedra remain as the building elements of the crystal struc-

* Corresponding author. Tel.: +47 63 80 64 53; fax: +47 63 81 29 05.
E-mail address: volodymyr.yartys@ife.no (V.A. Yartys).

0925-8388/$ – see front matter © 2006 Elsevier B.V. All rights reserved.
doi:10.1016/j.jallcom.2006.11.199

tures of the other polymorphs of AlH_3. However, their packing densities decrease compared to α-AlH_3. This decrease is due to the formation of cavities in γ-AlH_3 [5] or from the large empty channels in between the octahedra in β-AlD_3 [6]. The double bridge Al–2 H–Al bonds were firstly experimentally observed for the Al-based hydrides [5] in γ-AlH_3 containing the edge-sharing AlH_6 octahedral units. NMR investigation of the γ-AlH_3 [7] showed formation of distorted coordination polyhedra of H around Al, in agreement with the data of the crystal structure studies [5].

Metastable alane does not release hydrogen at normal conditions and is stable in air, probably due to the formation of oxide layers at the surface. At atmospheric pressure AlH_3 desorbs hydrogen at rather moderate temperatures (350–400 K, depending on its preparation history). Achieving sufficiently rapid and controllable decomposition of AlH_3 and proposal for efficient synthesis routes to make the system Al–AlH_3 reversible are focused in ongoing research (see, e.g. [8–11]). Thermodynamic characterisation of the polymorphs of alane and studies of the kinetics of hydrogen release facilitated by alkali metal hydrides showed that during decomposition β- and γ-AlH_3 transform into the alpha modification and that significantly fast hydrogen release from alane starts at the temperatures well below 100 °C. However, detailed mechanism of the decomposition process and its kinetics at different temperatures requires further investigation in order to propose the most optimal way of utilizing AlH_3-based systems for hydrogen supply aimed for the use in automotive mobile applications.

This work was focused on studies of the thermal decomposition of alane by application of synchrotron X-ray diffraction (SR-XRD) and thermal desorption spectroscopy (TDS). Two polymorphs were studied, α- and γ-AlH_3.

2. Experimental details

Samples from three different alane batches were investigated in this work; two α-AlH_3 batches (aged α-AlH_3 and fresh α-AlH_3), and one γ-AlH_3. Several methods for the wet chemical synthesis of AlH_3 have been reported in the literature decades ago. The most difficult problem is to obtain AlH_3 free of solvent without decomposing the sample [1,2] as temperatures of solvent desorption and hydride decomposition are close to each other. Both α-AlH_3 samples were prepared using modifications of a method described by Brower et al. [1]. Preparation method of the γ-AlH_3 modification is described in [5]. All samples were stored under argon atmosphere, in airtight containers for the time between the synthesis and the measurements.

Temperature desorption spectroscopy (TDS) study of the hydrogen release from the samples were performed by heating a small amount of the selected sample (less than 100 mg) in a stainless steel autoclave at a constant heating

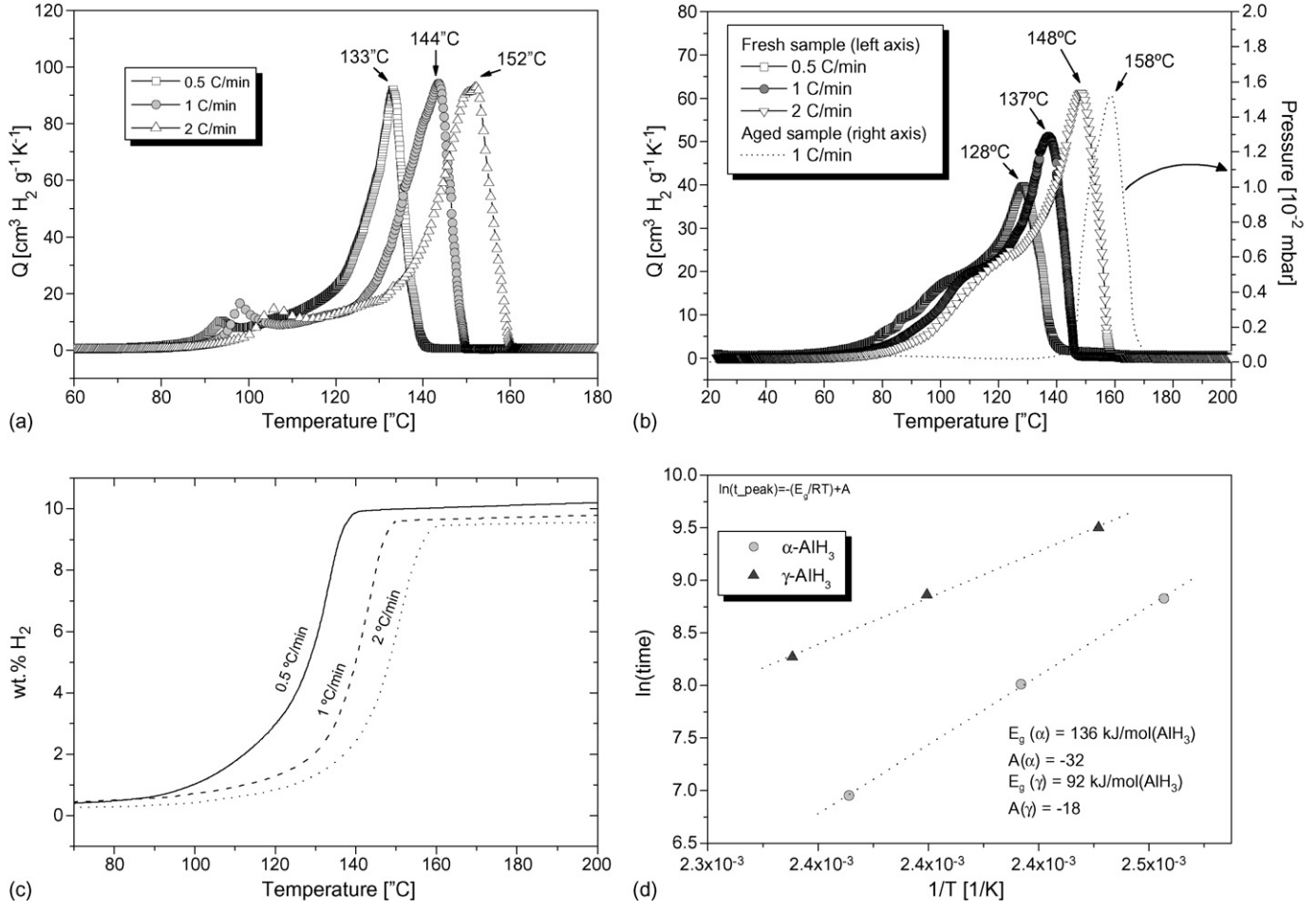

Fig. 1. Thermal desorption spectra of hydrogen desorption from AlH_3, (a) γ-AlH_3; (b) fresh and aged α-AlH_3; note that the aged sample shows higher desorption temperatures with more symmetric peak shape; probably due to thicker and more evenly distributed oxide layers; (c) integrated desorption traces for γ-AlH_3; (d) Arrhenius plots for α- and γ-AlH_3. The activation energy for the γ is lower than for the α.

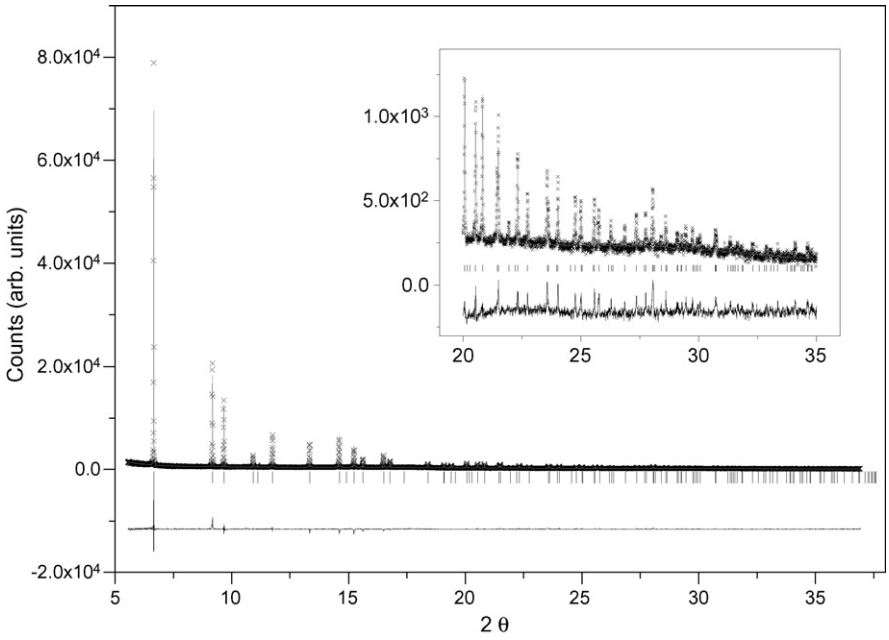

Fig. 2. Rietveld-type plots of the SR-XRD pattern for α-AlH_3 (λ = 0.37504 Å) collected at room temperature showing observed (crosses), calculated (upper line) and difference (bottom line) plots. The positions of the Bragg peaks are shown as ticks. An enlargement of the high-angle part is shown in the inset.

rate. Dynamic secondary vacuum in the measurements setup was maintained by using a turbo-molecular pumping system, while desorption pressure was continuously monitored by the vacuum sensor.

SR-XRD studies of AlH_3 were performed at the Swiss-Norwegian Beam Lines (SNBL) at the European Synchrotron Radiation Facility (ESRF), Grenoble, France. Three different experiments were performed:

1. High-resolution scan at room temperature of the aged α-AlH_3 sample (station BM01B).
2. *In situ* scan of the aged α-AlH_3 sample (station BM01B), heating rate 1 K/min.
3. *In situ* scan of the γ-AlH_3 sample (station BM01A), heating rate 1/2 K/min.

The *in situ* measurements were performed using a setup designed for *in situ* studies of the chemical processes occurring in hydrogen or gas/vacuum atmosphere [12–14]. In this setup, a small amount of the sample is put in a 0.7 mm quartz glass capillary filling approximately 1–2 mm of the capillary's bottom part. The capillary is hermetically connected to the gas system using a carbon ferrule mounted in a T-piece, which, in turn, is attached to the goniometer head. Averaging over the different orientations of the crystallites, resulting in the elimination of preferred orientation effects in the collected diffraction data, is achieved by oscillating the setup around the axis of the capillary. The required elasticity of the setup is made possible by using a flexible PEEK polymer tubing connection between the microreaction cell and the flow system. Vacuum is created using a turbo molecular vacuum pump. Except for the PEEK tubing allowing the oscillation of the sample cell, stainless steel tubes are used for the connections to prevent oxygen diffusion through the tubes during the experiments.

The diffractometer at station BM01B (Si(1 1 1) channel-cut monochromator, scintillation detectors) is equipped with six counting chains, with an angular offset in 2θ of ∼1.1°. For *in situ* measurements, in order to keep the counting time per scan as low as possible, the detector bank is moved by 1.2° during one measurement and the data from the six different detectors are added using a data-binning program. One data set (2θ = 6.07–12.67°) was collected in 2 min during the heating of the sample under secondary vacuum conditions. The high-resolution measurement of the aged α-AlH_3 was performed in steps of 0.005°

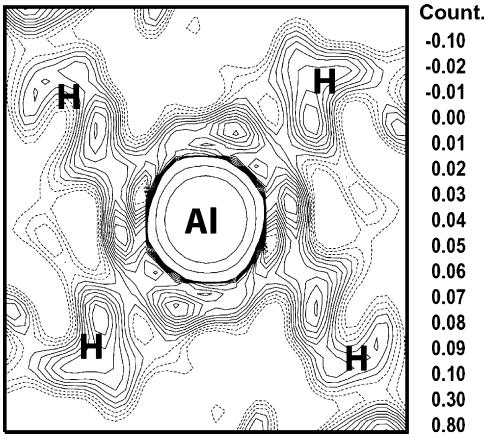

Fig. 3. Fourier transform of the observed SR-XRD pattern (GSAS Rietveld refinements) showing the Al–H bonds (equatorial plane of the octahedron containing 4 H atoms is selected).

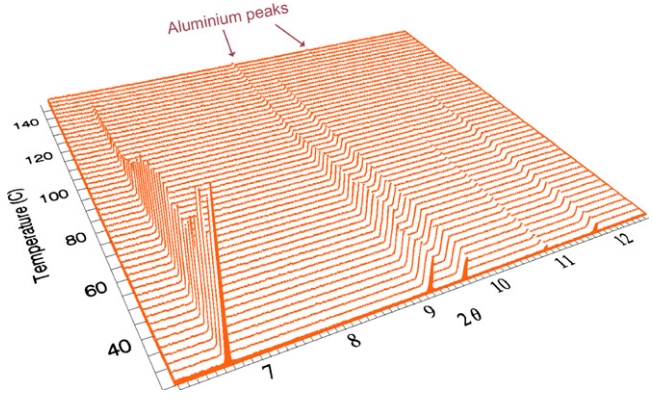

Fig. 4. *In situ* SR-XRD pattern of the thermal decomposition of α-AlH_3 (heating rate 1 °C/min). The α-AlH_3 peaks are diminishing during the heating, indicating amorphisation. At higher temperatures small aluminium peaks appear indicating a nucleation and growth process for the aluminium formation.

in the 2θ range from 5.540° to 36.935°. A wavelength of 0.37504(2) Å was used in both experiments.

Experimental data at BM01A were collected using a MAR2300 image plate detector and then integrated using the software Fit2D. The wavelength ($\lambda = 0.71118$ Å) and sample to detector distance ($d = 199.768$ mm, giving a usable 2θ range of about 1–40° for the 1D patterns) were calibrated from an individual run of a LaB_6.

All powder diffraction data were analysed by the Rietveld whole-profile refinement method [15] using the General Structure Analysis System (GSAS) software [16]. Peak shapes were described by a multi-term Simpson's rule integration of the pseudo-Voigt function [17,18], which includes the asymmetry correction according to Finger et al. [19]. Anisotropic line broadening of the diffraction pattern was observed for the γ-polymorph and was accounted for by refinements using the Thompson–Cox–Hastings pseudo-Voigt type function as proposed in [20].

3. Results and discussion

3.1. Thermal desorption spectroscopy

Fresh α-, and γ-AlH_3 samples were studied by TDS at three different constant heating rates ($\Delta T = 0.5$, 1, and 2 K/min). A two-peak desorption behaviour was observed for all runs (see Fig. 1a and b). Prior to the main desorption peak which appeared at around 130–160 °C, a smaller, low temperature desorption event was observed. It is well pronounced as a separate desorption peak in case γ-AlH_3 (Fig. 1a) and seen as a shoulder on a low-temperature side of the peak observed for the α-AlH_3 (Fig. 1b). For γ-AlH_3 it is reasonable to suggest that the low-temperature event corresponds to a direct decomposition process γ-$AlH_3 \rightarrow Al + 3/2\ H_2$; the second, main event, is associated with a decomposition of α-AlH_3, which is formed first during the heating of γ-AlH_3. In case of α-AlH_3, since hydrogen release from this modification should be a single step process, it is likely that the observed behaviour is due to non-uniform surface properties of the different parts of the sample because of the variations in the covering by the particles protective oxide layer.

Activation energies for the desorption process from AlH_3 were found from Arrhenius plots: $E_a = 136$ and 92 kJ/mol AlH_3, for α-AlH_3 and γ-AlH_3, respectively. Graetz and Reilly reported that the activation energy might vary with the age of the sample. They found between 102 and 150 kJ/mol for the α-phase [10].

A TDS run of the aged α-AlH_3 sample was also performed. Compared to fresh samples of α-AlH_3, a much higher desorption temperature was observed for the aged sample. Experimental data and the Arrhenius plots of the TDS experiments are presented in Fig. 1.

3.2. High-resolution SR-XRD investigation of α-AlH_3

The high-resolution SR-XRD pattern of α-AlH_3 was indexed in trigonal setting, space group $R\bar{3}c$ (No. 167). The refinements yielded unit cell parameters: $a = 4.44994(5)$ Å; $c = 11.8200(2)$ Å, and $V = 202.701(4)$ Å^3 which agree well with the reference data: $a = 4.449$ Å; $c = 11.804$ Å; $V = 202.34$ Å^3 [3]. Since Al has a relatively low atomic number, it was possible to locate the hydrogen sublattice during the refinements, starting with Al placed in a special position 6*a* [0, 0, 0] and performing difference Fourier analysis. Performing the refinements without including the H position gave the following best goodness-of-fit parameters: $R_{wp} = 14.2\%$, $R_p = 11.7\%$, and $\chi^2 = 6.0$. Including the hydrogen atom (at site 18*e* [0.625(2), 0, 1/4]), the quality of the fit significantly improved, giving goodness-of-fit parameters of $R_{wp} = 12.1\%$, $R_p = 10.6\%$, and $\chi^2 = 4.9$. Fig. 2 shows the Rietveld-type plots of the high-resolution data.

The refinements yielded an Al–H bonding distance of 1.712(3) Å and an octahedral coordination of Al into AlH_6 units where bridge bonds Al–H–Al are formed with a bond angle of 141°. Furthermore, they indicated a small charge transfer from Al to H corresponding to the formation of $Al^{+0.15}$ and $H^{-0.05}$. This charge distribution can be observed in the Fourier transform of the observed XRD pattern as shown in Fig. 3. We note a good

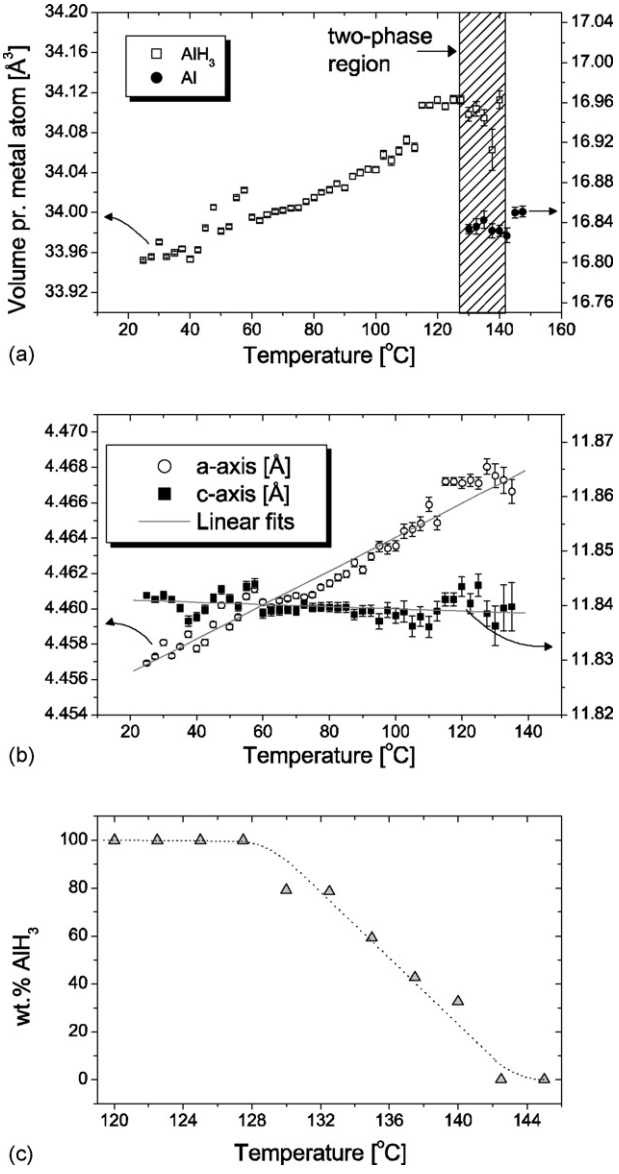

Fig. 5. Results from the refinements of the *in situ* SR-XRD patterns of the aged α-AlH_3 thermal decomposition *vs.* temperature; (a) volumes of the unit cells of the crystal structures of alane and Al metal (per one mole AlH_3/Al), (b) evolution of the unit cell parameters of the hydride during the heating, and (c) temperature-dependent fraction of the crystalline aluminium hydride (by mass) in the system (the refinements included crystalline aluminium and crystalline aluminium hydride).

correspondence between the data of the present powder XRD work and the results of the powder neutron diffraction study of AlD_3 [3], where an Al–D bond distance of 1.715 Å in the AlD_6 octahedra was reported.

Hydrogenation is accompanied by a volume increase of 103.5 (!)% equivalent to 5.73 Å^3/atom H. We note that these numbers are significantly higher compared to the conventional metal/intermetallic hydrides where both corresponding values are significantly lower, respectively, 20–30% and 2.5–3.0 Å^3/atom H [21,22]. This dramatic increase of the unit cell volume is accompanied with an enlargement of the closest Al–Al distances of 13.3% (growing from 2.86 Å in the alloy to 3.24 Å in the hydride).

3.3. *In situ* SR-XRD investigation of the α-AlH_3 to Al transformation

The *in situ* diffraction pattern of the decomposition of the hydride were collected in the temperature range 25–150 °C (see Fig. 4). Rietveld-type refinements of the data were performed (goodness-of-fit parameters for the refinements were all rather large, with R_{wp} in the range 13–28%) and showed that on heating a linear increase of the unit cell dimensions of AlH_3 takes place in an interval from RT to ∼125 °C (a = 4.46; c = 11.83 Å for T = 135 °C; see Fig. 5a and b). The volume expansion is pronouncedly anisotropic, as can be seen from Fig. 5b. Indeed, the c-axis is almost constant in the temperature interval 25–125 °C ($\Delta c/c \sim -0.02\%$). This contrasts to a significant expansion along [1 0 0]: $\Delta a/a \sim 0.28\%$. The latter expansion can mainly be attributed to the elongations of the bridge bonds Al–H–Al aligned along [1 $\bar{1}$ 1/2], which are expanding from 3.243 to 3.248 Å ($\Delta d/d \sim 0.17\%$).

During the heating, a continuous decrease of the intensities of the pattern of AlH_3 was observed indicating a gradual decomposition of the crystalline hydride phase, probably forming amorphous aluminium. This decrease was not accompanied by any significant broadening of the peaks. The intensities of the diffraction peaks from Al firstly appeared at ∼135 °C and then

Table 1
Selected parameters derived from Rietveld-type refinements of the *in situ* SR-XRD data of the thermal decomposition of AlH_3

Parameters						
In situ SR-XRD study of thermal decomposition of 'aged' α-AlH_3						
T (°C)[a]	30	80	100	115	127.5	137.5
α-AlH_3[b]						
a (Å)	4.4581(1)	4.4614(2)	4.4636(3)	4.4672(2)	4.4681(4)	4.468(2)
c (Å)	11.8420(7)	11.8497(9)	11.838(1)	11.841(1)	11.839(2)	11.82(1)
V (Å^3)	203.82(1)	204.09(1)	204.26(2)	204.64(1)	204.64(3)	204.4(1)
v (Å^3)[c]	33.970(2)	34.015(2)	34.043(3)	34.107(2)	34.113(4)	34.06(2)
wt.%	100	100	100	100	100	42.6
No. var.[d]	14	13	10	10	10	13
R_{wp} (%)	17.68	16.61	18.17	18.87	17.22	16.26
In situ SR-XRD study of thermal decomposition of γ-AlH_3						
T (°C)[a]	30	80	88	95	100	115
α-AlH_3[b]						
a (Å)	4.4438(3)	4.4493(3)	4.4524(1)	4.4530(1)	4.4534(1)	4.4525(6)
c (Å)	11.807(1)	11.810(1)	11.8110(6)	11.8111(4)	11.8110(5)	11.809(3)
V (Å^3)	201.92(3)	202.48(2)	202.77(1)	202.829(7)	202.858(8)	202.75(5)
v (Å^3)[c]	33.653(4)	33.746(4)	33.796(2)	33.805(1)	33.810(1)	33.791(8)
wt.%	15.97	16.354	32.49	44.00	38.91	6.65
γ-AlH_3[e]						
a (Å)	5.3762(4)	5.3757(6)	5.3758(5)	5.376(1)	5.375(4)	–
b (Å)	7.3431(6)	7.3447(7)	7.3450(8)	7.344(2)	7.343(7)	–
c (Å)	5.7684(3)	5.7708(4)	5.7711(4)	5.7707(8)	5.771(4)	–
V (Å^3)	227.72(2)	227.85(3)	227.87(3)	227.82(6)	227.8(2)	–
v (Å^3)[c]	37.954(4)	37.975(4)	37.979(5)	37.97(1)	37.97(4)	–
wt.%	70.62	68.83	50.56	19.50	3.32	<0.5
x_2	0.7886(5)	0.7882(6)	0.7873(7)	0.785(1)	0.725(8)	–
y_2	0.0830(4)	0.0831(5)	0.0829(6)	0.082(1)	0.087(6)	–
No. var.[d]	37	37	37	37	34	26
R_{wp} (%)	4.26	4.25	3.79	3.76	3.82	4.4

Standard deviations are given in parentheses.

[a] Estimated error in temperature is ∼±5 °C.

[b] Crystal structure data for α-AlH_3. Space group $R\bar{3}c$; 6 Al in 6a (0, 0, 0); 18 H in 18e (0.63, 0, 0).

[c] Molar volume (unit cell volume/6 f.u. AlH_3).

[d] No. of variables refined in the Rietveld-type refinements.

[e] Crystal structure data for γ-AlH_3 [5]. Space group *Pnnm*; 2 Al1 in 2b (0, 0, 1/2); 4 Al2 in 4g (x_2, y_2, 0); 2 H1 in 2d (0, 1/2, 1/2); 4 H2 in 4g (0.16, 0.24, 1/2); 4 H3 in 4g (0.43, 0.64, 1/2); 8 H4 in 8h (0.79, 0.08, 0.30).

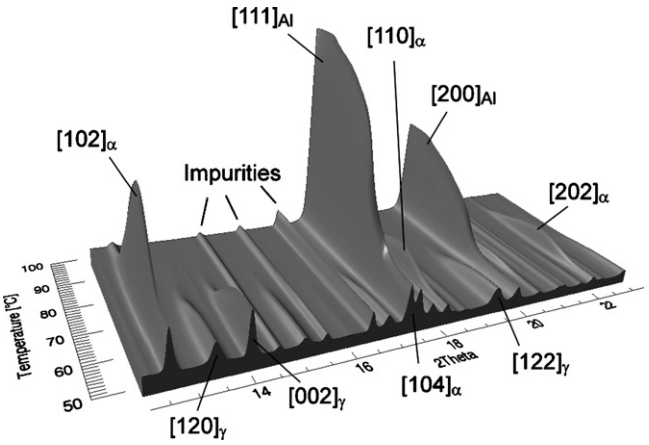

Fig. 6. *In situ* SR-XRD pattern of γ-AlH_3 thermal decomposition (in the temperature range 50–100 °C, heating rate 1/2 °C/min). The γ-AlH_3 peaks observed in the low temperature region diminish as α-AlH_3 starts to form. At higher temperatures, a relatively fast growth of the aluminium diffraction peaks is observed.

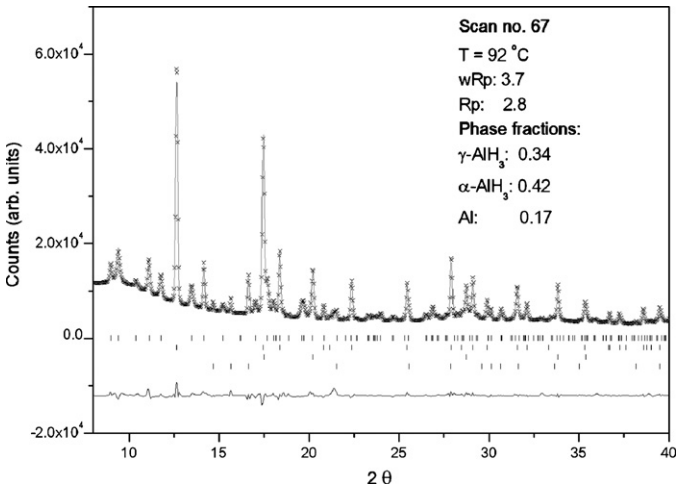

Fig. 7. Rietveld-type plots of the γ-AlH_3 sample from the *in situ* scan (λ = 0.71118 Å) collected at 92 °C showing observed (crosses), calculated (upper line) and difference (bottom line) plots. The positions of the Bragg peaks are shown as ticks (from top to bottom: γ-AlH_3, α-AlH_3, Al).

gradually increased with raising temperature. At $T \sim 145$ °C, the hydride peaks completely vanished indicating completeness of the transformation $AlH_3 \rightarrow Al$. The fraction of the hydride observed in the SR-XRD patterns as a function of the temperature is given in Fig. 5c. These *in situ* data agree well with the TDS measurements showing the onset of the peak of H desorption at ∼140 °C as can be seen in Fig. 1b. Crystallographic and Rietveld refinement parameters for selected scans are presented in Table 1.

3.4. *In situ* SR-XRD investigation of the thermal decomposition of γ-AlH_3

The initial sample used in the *in situ* SR-XRD experiment contained mainly γ-AlH_3 with minor additions of α-AlH_3 and aluminium. Goodness-of-fit parameters for the refinements were all satisfactory, with R_{wp} in the range 3.7–4.7%. A plot of a selected range of the experimental data is presented in Fig. 6. Crystallographic and Rietveld refinement parameters for selected scans are presented in Table 1 and an example of Rietveld-type plot (data collected at $T = 92$ °C) is presented in Fig. 7, where similar abundances of γ- (34%) and α- (42%) are observed, with 17% of the initial alane already decomposed into Al.

Fig. 8 presents the obtained phase fractions and calculated hydrogen concentrations as a function of temperature while Figs. 9 and 10 show the evolution of the unit cell volumes and unit cell parameters for the two alane polymorphs as a function of the temperature. The γ-AlH_3 starts to decompose

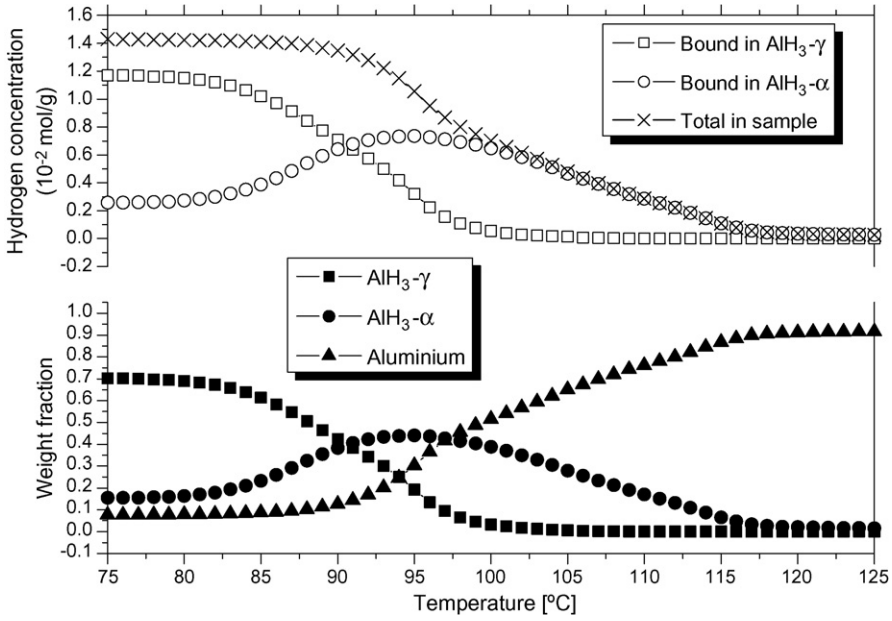

Fig. 8. Calculated phase percentages and hydrogen concentration from the *in situ* SR-XRD patterns of the γ-AlH_3 thermal decomposition.

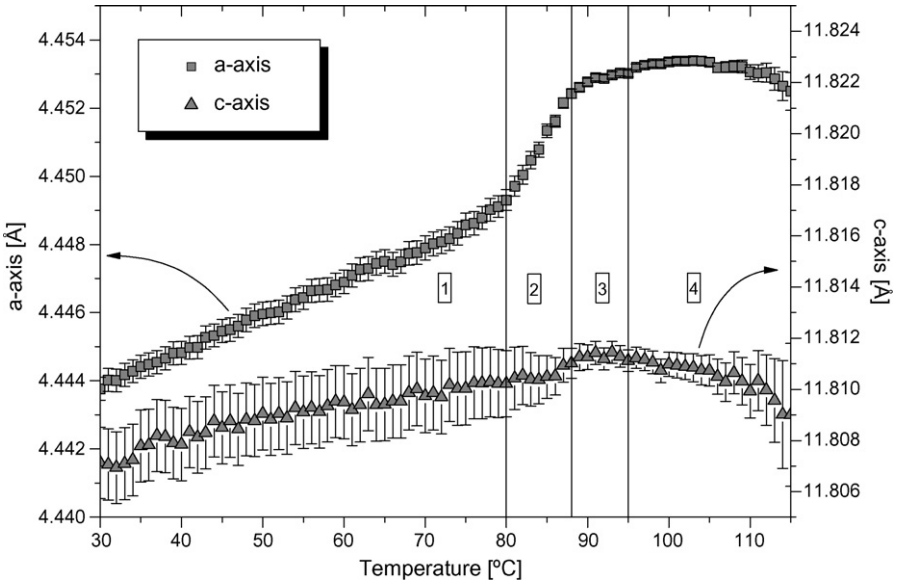

Fig. 9. Changes in unit cell dimensions for the α-AlH_3 phase *vs*. temperature from the *in situ* SR-XRD pattern of the γ-AlH_3 thermal decomposition. The numbers indicates the partition into temperature intervals with constant lattice changes: interval 1: (25–80 °C) constant phase fractions, mainly γ-AlH_3 present, 2: (80–88 °C) fast growth of α-AlH_3, growth of aluminium, γ-AlH_3 decreases, 3: (88–95 °C) slower growth of α-AlH_3, γ-AlH_3 decreases, fast growth of aluminium, 4: (95–115 °C) α-AlH_3 decreases to ∼0 at 115 °C, γ-AlH_3 decreases to ∼0 at 100 °C, steady growth of aluminium.

at $T \sim 80\,^{\circ}C$ and the content of aluminium and α-AlH_3 starts to increase. As this happens, the anisotropic expansion of the α-AlH_3 unit cell gets more pronounced, as can be seen from Fig. 9. The unit cell axes expand almost linearly within limited temperature regions. Relative changes per degree Celsius ($\Delta F/\Delta T$) were obtained by linear fits of the values obtained from the Rietveld-type refinements within four chosen temperature partitions and are presented in Table 2 and graphically for the α-modification in Fig. 11. In the first partition (25–80 °C) before the decomposition of γ-AlH_3 sets in, a change $\Delta F/\Delta T$ of $0.23 \times 10^{-2}\,^{\circ}C^{-1}$ is observed for the *a*-axis of α-AlH_3 while the *c*-axis is almost constant. In partition 2 (80–88 °C), during the fast growth-regime of α-AlH_3, $\Delta F/\Delta T$ for the *a*-axis increases almost four-fold to $0.89 \cdot 10^{-2}\,^{\circ}C^{-1}$. The maximum formation rate of α-AlH_3 appears at 88 °C, and after this, in partition 3 (88–95 °C), the axes expansion slows down to values similar as for the first partition. At higher temperatures (95–115 °C), partition 4, both the amount of α-AlH_3 and γ-AlH_3 decreases to ∼0 (at ∼115 and ∼100 °C, respectively) and a possible small nearly isotropic contraction of the α-AlH_3 unit cell is observed. Representative Rietveld-plots for the different temperature regions are presented in Figs. 7 and 12.

To get a more detailed view of how the phase transformations proceed, the changes of hydrogen concentrations in

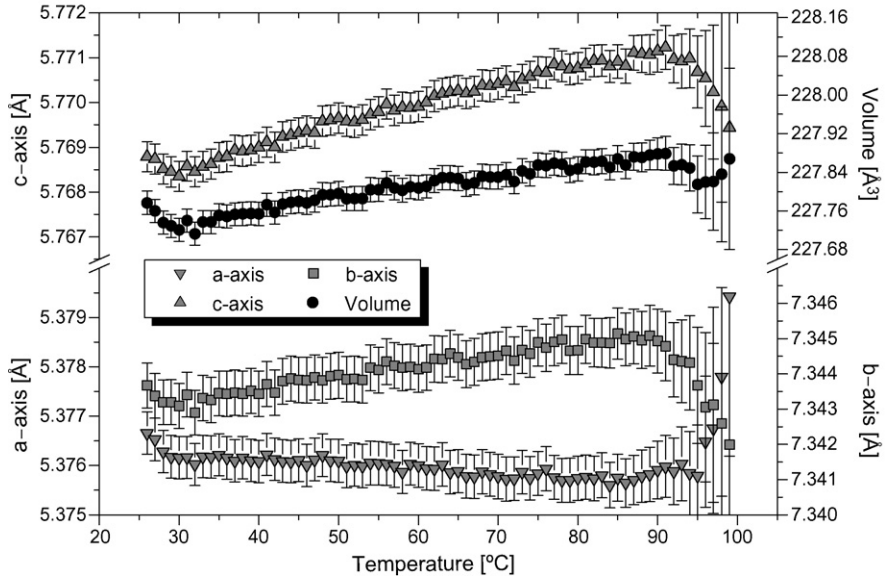

Fig. 10. Changes in unit cell dimensions for the γ-AlH_3 phase *vs*. temperature from the *in situ* SR-XRD patterns of the γ-AlH_3 thermal decomposition.

Table 2
Changes in lattice parameters as obtained from Rietveld-type fittings of *in situ* SR-XRD data of the thermal decomposition of AlH_3 samples

Phase	Variable (unit)	$T_{interval}$ (°C)	X_{start}[a]	X_{final}[a]	$\Delta F/\Delta T$[b] (10^{-2}%/°C)	Notes
α-AlH_3[c]	*a* (Å)	25–127.5	4.4567	4.4671	0.23	Only α-AlH_3 present AlH_3 (α-decomposition starts at ∼128 °C)
	c (Å)		11.8405	11.8392	−0.01	
	V (Å^3)		203.67	204.60	0.44	
α-AlH_3[d]	*a* (Å)	30–80	4.4438	4.4490	0.23	Mainly γ-phase present (constant phase fractions)
	c (Å)		11.8074	11.8105	0.05	
	V (Å^3)		201.93	202.46	0.52	
	a (Å)	80–88	4.4493	4.4525	0.89	γ-Phase starts to decompose, α-phase grows fast
	c (Å)		11.8103	11.8108	0.06	
	V (Å^3)		202.47	202.77	1.85	
	a (Å)	88–95	4.4525	4.4531	0.18	Slower α-phase growth (α formation peak ∼88 °C)
	c (Å)		11.8112	11.8113	0.01	
	V (Å^3)		202.79	202.84	0.38	
	a (Å)	95–115	4.4534	4.4529	−0.06	γ-Phase < 1 wt.% above 105 °C. α-phase decreases
	c (Å)		11.8114	11.8095	−0.08	
	V (Å^3)		202.87	202.79	−0.20	
γ-AlH_3[d]	*a* (Å)	30–75	5.37622	5.37579	−0.02	Mainly γ-phase present (constant phase fractions)
	b (Å)		7.34321	7.34474	0.05	
	c (Å)		5.76853	5.77069	0.08	
	V (Å^3)		227.73	227.85	0.11	

[a] Value of parameter obtained from linear fitting of lattice parameters in the range given in column '$T_{interval}$'. X_{start} is the first value in the temperature interval, X_{final}, the last. The lattice parameters used as data points in the fitting were obtained from Rietveld-type refinements of the experimental diffraction data.
[b] The fractional changes $\Delta F/\Delta T$ are defined as $100\cdot\Delta X/T$ where ΔX is $100\cdot(X_{final} - X_{start})/(X_{start})$.
[c] As obtained from the *in situ* SR-XRD study of thermal decomposition of 'aged' α-AlH_3.
[d] As obtained from the *in situ* SR-XRD study of thermal decomposition of γ-AlH_3.

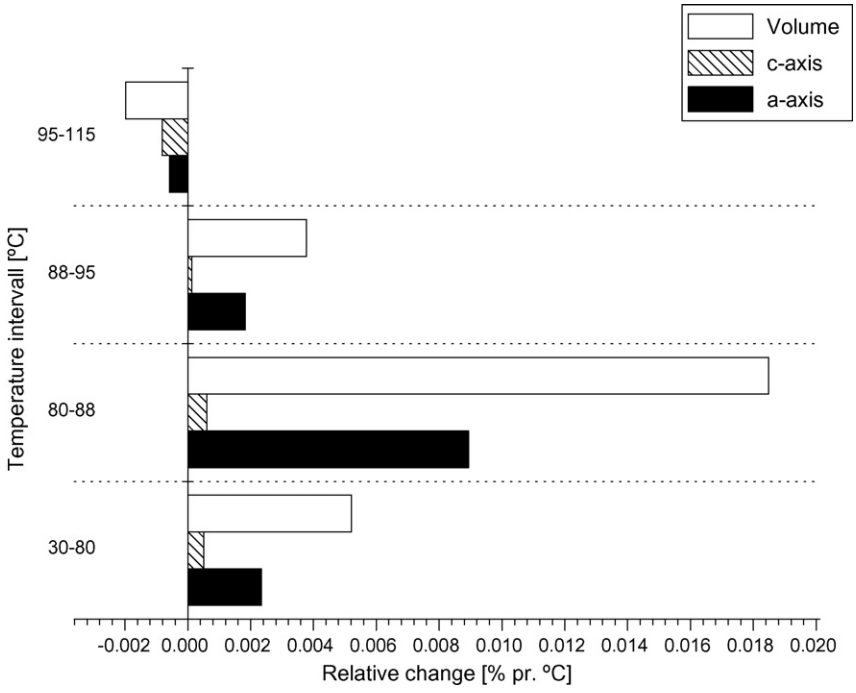

Fig. 11. Relative changes in unit cell dimensions for the α-AlH_3 phase *vs*. temperature from the *in situ* SR-XRD patterns of the γ-AlH_3 thermal decomposition.

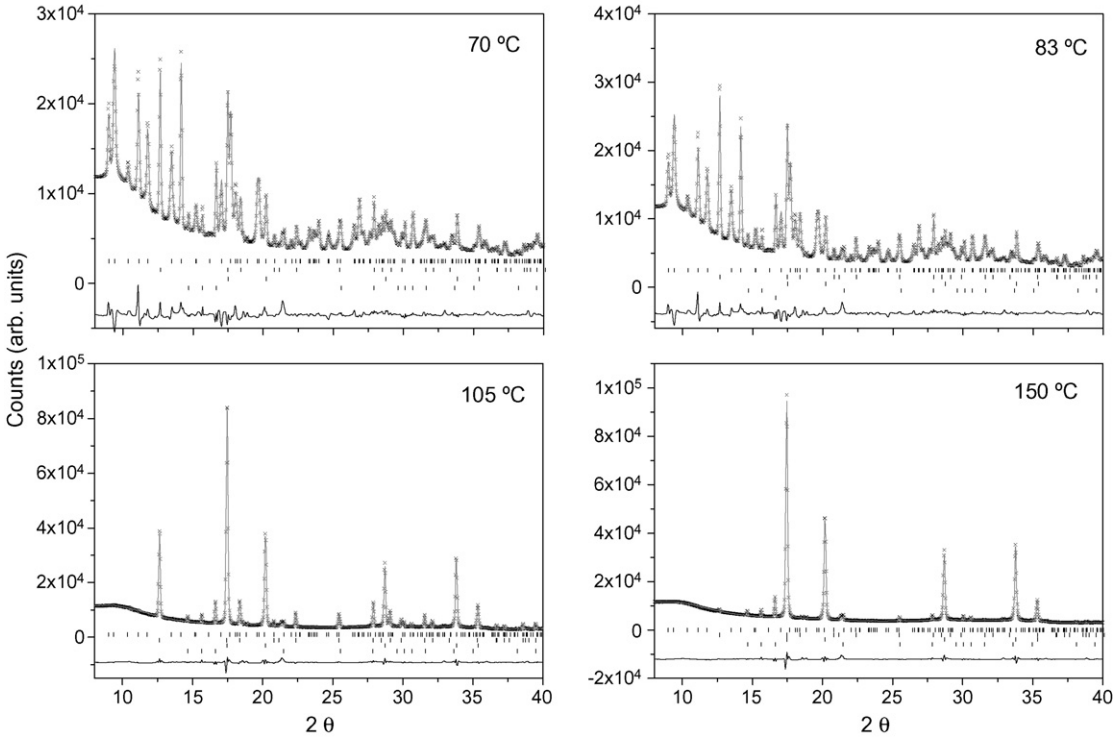

Fig. 12. Selected Rietveld-type plots of the *in situ* SR-XRD pattern of the γ-AlH_3 thermal decomposition showing observed (crosses), calculated (upper line) and difference (bottom line) plots. The positions of the Bragg peaks are shown as ticks (from top to bottom: γ-AlH_3, α-AlH_3, Al, impurity phases).

the hydride phases were calculated based on the weight fractions of the crystalline phases as obtained from the Rietveld refinements and assuming that hydrogen content decreases from 10 wt.% H to 0 during the decomposition process. The results are presented in Fig. 13 in the form of 'hydrogen desorption traces'. Formation of the α-phase consumes less hydrogen than the number of moles of hydrogen liberated by the decomposition of γ-AlH_3. Obviously, an excess of hydrogen is desorbed directly from the γ-AlH_3, *i.e.* due to direct transformation of γ-AlH_3 to aluminium. This provides an evidence of coexistence of two decomposition paths: γ-AlH_3 → Al, and γ-AlH_3 → α-AlH_3 → aluminium. From integrating the 'desorption traces', we arrive to a conclusion that direct decomposition of γ-AlH_3 is a prevailing process, yielding about 60% of the released hydrogen at the given heating rate (1/2 °C/min).

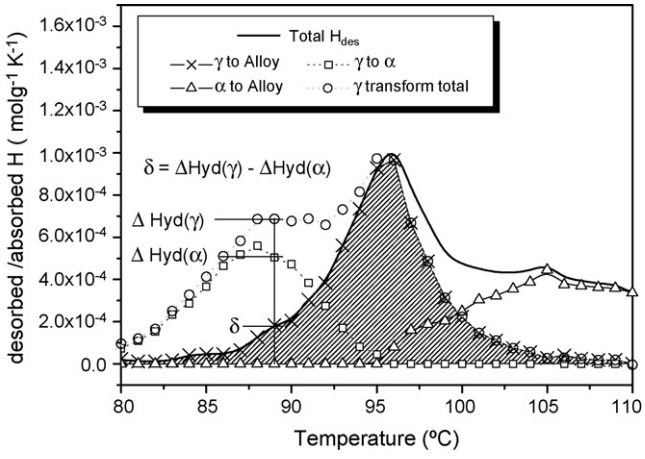

Fig. 13. Calculated hydrogen desorption and absorption traces from the *in situ* SR-XRD patterns of the γ-AlH_3 thermal decomposition. Subtracting the amount of hydrogen used during the formation of α-AlH_3 from the amount of hydrogen released by the decomposition of γ-AlH_3, a net hydrogen desorption trace is found (shaded area). This amount is attributed to direct γ-AlH_3 → Al phase transformation.

4. Summary

TDS studies and subsequent Arrhenius plots of fresh α-AlH_3 and γ-AlH_3 revealed that the activation energy of hydrogen desorption from γ-AlH_3, 92 kJ/mol AlH_3, is lower compared to α-AlH_3, 136 kJ/mol AlH_3. A TDS run of the aged α-AlH_3 sample showed a much higher desorption temperature compared to the freshly synthesized sample.

Crystal structure data for α-AlH_3, including the structure of hydrogen sublattice, was successfully obtained by Rietveld-type refinements and difference Fourier analysis of the high-resolution SR-XRD data. The refinements indicated a small charge transfer from Al to H atoms corresponding to the formation of $Al^{+0.15}$ and $H^{-0.05}$.

A significant anisotropic volume expansion of α-AlH_3 during its heating was observed with the main expansion proceeding along the *a*-axis and attributed to the elongations of the bridge bonds Al–H–Al aligned along [1 −1 1/2]. The expansion of the *a*-axis proceeds considerably faster during the fast "*in situ*" formation of the α-phase from the γ-hydride, as observed in the decomposition experiments of the γ-AlH_3. A small anisotropic expansion of the γ-AlH_3 was also observed.

In the decomposition experiment of the 'aged' α-AlH_3 sample, it seems that formation of an amorphous phase precedes the formation of aluminium and subsequently that the nucleation step limits the rate of aluminium formation. Aluminium forms easily in the γ-AlH_3 decomposition experiment. However, in this sample aluminium is already present of in the starting composition, providing already existing nuclei for the growth of aluminium. Thus, both experiments give complementary evidences that nucleation is the rate-limiting step in the growth of aluminium during the alane decomposition process. This observation agrees well with the findings of Graetz and Reilly [10].

From the analysis of the *in situ* SR-XRD pattern of the thermal decomposition of γ-AlH_3, evidence of two parallel decomposition processes of γ-hydride to aluminium were found (1) $\gamma \rightarrow Al$ and (2) $\gamma \rightarrow \alpha \rightarrow Al$. Direct decomposition process $\gamma \rightarrow Al$ was identified as a prevailing one.

Acknowledgements

This work received support from the Norwegian Research Council. We are grateful to Dr. M. Sato (Tokai University, Japan and IFE), T. Foerde (IFE) and Dr. A.B. Riabov (PhMI AS Ukraine) for their help.

References

[1] F.M. Brower, N.E. Matzek, P.F. Reigler, H.W. Rinn, C.B. Roberts, D.L. Schmidt, J.A. Snover, K. Terada, J. Am. Chem. Soc. 98 (1976) 2450–2453.
[2] A.E. Finholt, A.C. Bond, H.I. Schlesinger, J. Am. Chem. Soc. 69 (1947) 1199–1203.
[3] J.W. Turley, H.W. Rinn, Inorg. Chem. 8 (1969) 18.
[4] J.P. Maehlen, V.A. Yartys, in: D. Chandra, J. Petrovic, R.G. Bautista, A. Imam (Eds.), Symposium TMS 2006 Annual Meeting on Advanced Materials for Energy Conversion III, San Antonio, Texas, USA, March 12–16, 2006, pp. 77–85.
[5] V.A. Yartys, R.V. Denys, J.P. Maehlen, C. Frommen, M. Fichtner, B.M. Bulychev, H. Emerich, Inorg. Chem. 46 (2007) 1051–1055.
[6] H.W. Brinks, W. Langley, C.M. Jensen, J. Graetz, J.J. Reilly, B.C. Hauback, J. Alloys Compd., in press.
[7] S.-J. Hwang, R.C. Bowman, J. Graetz, J.J. Reilly, Mater. Res. Soc. Symp. Proc. 927 (2006), 0927-EE03-03 and S.-J. Hwang, R.C. Bowman, Jr., J. Graetz, J.J. Reilly, MH2006, O-071.
[8] G. Sandrock, J. Reilly, J. Graetz, W.M. Zhou, J. Johnson, J. Wegrzyn, Appl. Phys. A: Mater. Sci. Process. 80 (2005) 687–690.
[9] J. Graetz, J.J. Reilly, J. Alloys Compd. 424 (1/2) (2006) 262–265.
[10] J. Graetz, J.J. Reilly, J. Phys. Chem. B 109 (2005) 22181–22185.
[11] G. Sandrock, J. Reilly, J. Graetz, W.-M. Zhou, J. Johnson, J. Wegrzyn, J. Alloys Compd. 421 (1/2) (2006) 185–189.
[12] M. Stange, J.P. Maehlen, V.A. Yartys, P. Norby, W. van Beek, H. Emerich, J. Alloys Compd. 404 (2005) 604–608.
[13] P. Norby, J. Am. Chem. Soc. 119 (1997) 5215–5221.
[14] E.K. Andersen, I.G.K. Andersen, P. Norby, J.C. Hanson, J. Solid State Chem. 141 (1998) 235–240.
[15] H.M. Rietveld, J. Appl. Crystallogr. 2 (1969) 65–71.
[16] A.C. Larson, R.B.v. Dreele (LANL, Los Alamos, 1994).
[17] P. Thompson, D.E. Cox, J.B. Hastings, J. Appl. Crystallogr. 20 (1987) 79–83.
[18] C.J. Howard, J. Appl. Crystallogr. 15 (1982) 615–620.
[19] L.W. Finger, D.E. Cox, A.P. Jephcoat, J. Appl. Crystallogr. 27 (1994) 892–900.
[20] P.W. Stephens, J. Appl. Crystallogr. 32 (1999) 281–289.
[21] V.A. Yartys, V.V. Burnasheva, K.N. Semenenko, Usp. Khim. 52 (1983) 529–562.
[22] V.A. Yartys, V.V. Burnasheva, K.N. Semenenko, N.V. Fadeeva, S.P. Solovev, Int. J. Hydrogen Energy 7 (1982) 957–965.

ELSEVIER

Journal of Alloys and Compounds 446–447 (2007) 166–172

Journal of ALLOYS AND COMPOUNDS

www.elsevier.com/locate/jallcom

Hydrogen storage properties and structure of $La_{1-x}Mg_x(Ni_{1-y}Mn_y)_3$ intermetallics and their hydrides

R.V. Denys [a,b], B. Riabov [a,b], V.A. Yartys [a,*], R.G. Delaplane [c], M. Sato [d]

[a] *Institute for Energy Technology, Kjeller, Norway*
[b] *Physico-Mechanical Institute of the National Academy of Sciences of Ukraine, Lviv, Ukraine*
[c] *The Studsvik Neutron Research Laboratory, Uppsala University, Nyköping, Sweden*
[d] *Department of Applied Science, School of Engineering, Tokai University, Hiratsuka, Kanagawa, Japan*

Received 30 October 2006; received in revised form 22 December 2006; accepted 25 December 2006
Available online 11 January 2007

Abstract

'Hybrid' RNi_3 (R = rare earth metal) crystal structures are built of the slabs of simpler types, $CaCu_5$ and $MgZn_2$. Different affinities of these slabs to hydrogen result in unusual "anisotropic" expansion of the RNi_3 and R_2Ni_7 (R = La, Ce) structures upon hydrogenation. This work focuses on studies of the hydrogenation behaviour of $LaNi_3$ and on the properties of the hydrides of the modified by Mg and Mn La–Ni alloys. The crystal structure of $LaNi_3D_{2.8}$ and the crystal structure and hydrogen storage behaviours of the $La_{1.5}Mg_{0.5}Ni_7$ and $La(Ni_{1-x}Mn_x)_3$ ($x = 0$; 0.067; 0.133; 0.2; 0.267; 0.3; 0.333; 0.4) alloys were in focus. The deuteration of $LaNi_3$ with $PuNi_3$ type of structure leads to the formation of $LaNi_3D_{2.8}$ and is accompanied by a deformation of the metal matrix causing a change of the initial rhombohedral symmetry (space group $R\bar{3}m$) to a monoclinic one (space group $C2/m$; $a = 8.6408(7)$ Å, $b = 4.9281(4)$ Å, $c = 32.774(3)$ Å; $\beta = 90.850(8)^\circ$; $V = 1395.5(2)$ Å^3). Similar to the earlier studied $CeNi_3D_{2.8}$, preferential occupation by deuterium atoms of the AB_2 layers takes place, leading to the "anisotropic" expansion of the unit cell along [0 0 1] ($\Delta c/c = 30.6\%$). 14 occupied D crystallographic sites have 4 chemically different types of metal-atom surroundings, including Ni_4 (2), La_2Ni_2 (2), La_3Ni (6), and La_3Ni_3 (4). Modification of the La–Ni alloys by magnesium and manganese leads to the formation of intermetallic compounds crystallising with the $PuNi_3$, $CeNi_3$, and Ce_2Ni_7-type structures. An ordered substitution of La by Mg in the $MgZn_2$-type slabs was observed, causing a complete alteration of the hydrogenation behaviour of the original $LaNi_3$ alloy. $La_{1.5}Mg_{0.5}Ni_7D_9$ isotropically expands upon its formation and leads to a substantial increase of the stability against hydrogenation-induced amorphisation. On the other hand, replacement of Ni by Mn leads to the change in crystal-structure type from $PuNi_3$ to $CeNi_3$ in the $LaNi_{3-x}Mn_x$ alloys ($x > 0.1$). An ordered substitution of Ni by Mn proceeds inside the RNi_5 slabs only. This decreases the stability of the initial alloy against amorphisation on hydrogenation.

Keywords: Metal hydrides; Gas–solid reactions; Crystal structure; Neutron diffraction

1. Introduction

The hexagonal/trigonal AB_3 and A_2B_7 structures (A – atom of larger size, rare earth metal, Mg; B – atom of smaller size, Ni and Mn) are formed by stacking of AB_5 and A_2B_4 ($2 \times AB_2$) layers of, $CaCu_5$ and $MgZn_2$ types, *r* in different ratios yielding AB_3 ($AB_5 + 2 \times AB_2 = 2 \times AB_3$) and A_2B_7 ($AB_5 + AB_2 = A_2B_7$) stoichiometries. The alteration of the $CaCu_5$ and $MgZn_2$-type slabs proceeds along the [0 0 1] direction and gives either hexagonal $CeNi_3$ and Ce_2Ni_7 types or rhombohedral $PuNi_3$ and Er_2Co_7 structure types.

Hydrogen-absorbing AB_3 intermetallic compounds (A = La, Ce, Y) are known already for more than 30 years [1]. However, increased interest in these AB_3 "hybrid" compounds as hydrogen storage materials has appeared in recent years [2–6], mainly because of the prospects of their electrochemical applications.

The structures of intermetallic hydrides with filled $PuNi_3$-type alloy lattices have been studied for a rather large number of systems such as $HoNi_3H_{1.3–1.8}$ [7,8], $ErNi_3H_{1.2–3.75}$ [9], $ErCo_3H_{4.3}$ [10,11], and YCo_3D_4 [10]. Their hydrogenation is accompanied by different types of lattice expansion, including "anisotropic" enlargement of the unit cell mostly along the [001] direction and relatively modest $\Delta c/c$ values of 7–8%, and

* Corresponding author. Tel.: +47 63 80 64 53; fax: +47 63 81 29 05.
E-mail address: volodymyr.yartys@ife.no (V.A. Yartys).

0925-8388/$ – see front matter © 2007 Elsevier B.V. All rights reserved.
doi:10.1016/j.jallcom.2006.12.137

isotropic expansion, which was observed for $ErNi_3H_{3.75}$ [9]. The crystal structures of the hydrides retained the initial trigonal symmetry of the intermetallic compounds.

On the other hand, a number of "hybrid" compounds during the hydride formation reveal large expansions along the [0 0 1] axis, which reach 25–30% (the basal plane remains almost unchanged). Although this phenomenon has been known for a rather long time [12,13], the structures of such "anisotropic" hydrides have been determined in recent years for only $CeNi_3D_{2.8}$ [14], $La_2Ni_7D_{6.5}$ [15], and $CeY_2Ni_9D_{7.7}$ [16].

The aim of the present work was to study the unusual hydrogenation behaviour of $LaNi_3$, as well as the properties of the hydrogenated and virgin La–Ni alloys modified by Mg and Mn.

The choice of constituents was aimed at replacing the heavier and more expensive La by lighter and cheaper Mg and reaching higher hydrogenation capacities by replacement of Ni by Mn.

2. Experimental

$LaNi_3$ and $LaNi_{3-x}Mn_x$ alloys were prepared by arc-melting mixtures of the corresponding high-purity metals. The 1 at.% excess of La and 2 at.% of Mn were introduced into the alloy in order to compensate for their evaporation during melting. The alloys were sealed in evacuated quartz tubes and annealed for five weeks at 600 °C ($LaNi_3$) or 550 °C (Mn-series). The samples were quenched in ice water after the annealing.

The Mg-substituted material was prepared using the following procedure. A mixture of $LaNi_3$, Mg (with excess of 10 at.%) and Ni powders was compacted into a pellet, wrapped in a Ta foil, and sealed in a quartz tube under 0.5 bar Ar pressure. It was then sintered with the temperature increased in four steps (600, 700, 800, and 980 °C; holding time 4 h at each temperature; heating rate 1 °C/min) and subsequently annealed at 750 °C for 4 days followed with quenching.

Hydrides were synthesised by charging the vacuum-activated (at 300 °C) alloys with H_2 (D_2) gas using two different synthesis routes: (a) a very "mild" synthesis route (small aliquots of D_2 added into an autoclave cooled down to −20 °C) for $LaNi_3$ and Mn-containing samples or (b) constant application of hydrogen synthesis (5 bar H_2(D_2) at room temperature) for the Mg-containing intermetallics.

The prepared alloys and their hydrides have been characterised by means of X-ray diffraction (Siemens D 5000 diffractometer, Cu $K\alpha_1$ radiation, Bragg–Brentano geometry). Powder neutron diffraction (PND) data were collected at the R2 reactor at the Studsvik Neutron Research Laboratory using the high-resolution R2D2 instrument ($\lambda = 1.55134$ Å; 2Θ step 0.05°; 2Θ range 10–120°) [17]. Crystal structure data were derived by Rietveld profile refinements of the XRD and PND data using the GSAS software [18]. Neutron scattering lengths, $b_{La} = 8.24$, $b_{Ni} = 10.30$m, $b_{Mn} = -3.73$, and $b_D = 6.67$ fm, were taken from the GSAS library. The details of the monoclinic distortion of the crystal structure of $LaNi_3D_{2.8}$ deuteride were investigated using high-resolution SR XRD diffraction studies of the deuteride ($\lambda = 0.37504$ Å, at the BM1B instrument, SNBL, ESRF, Grenoble, France).

3. Results

3.1. Intermetallic alloys $LaNi_{3-x}Mn_x$ and $La_{2-x}Mg_xNi_7$

3.1.1. Structure of the $LaNi_3$ alloy

Phase-structural analysis of the prepared $LaNi_3$ material revealed the formation of a single-phase $LaNi_3$ intermetallic compound crystallising with rhombohedral structure and unit cell parameters $a = 5.0817(2)$ and $c = 25.092(1)$ Å [1]. Refinement of the structure indicated the formation of a $PuNi_3$-type structure with the following refined parameters: sp. gr. $R\bar{3}m$ (No. 166); La1 in 3*a*: 0, 0, 0; La2 in 6*c*: 0, 0, 0.1410(1); Ni1 in 3*b*: 0, 0, ½; Ni2 in 6*c*: 0, 0, 0.3327(3); Ni3 in 18*h* 0.500, 0.500, 0.796(2). These data agree well with the reference publication [19].

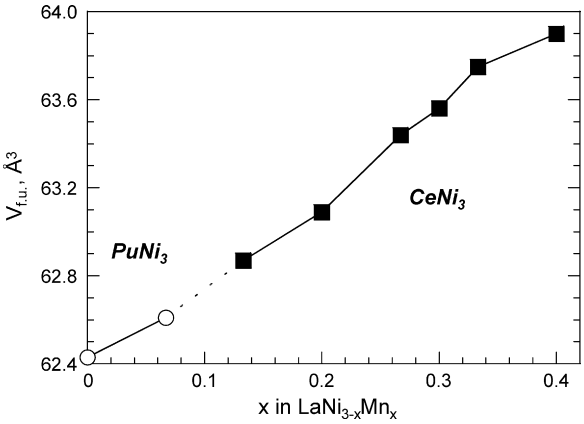

Fig. 1. Increase of the unit cell volumes upon Mn substitution for Ni in the structure of $LaNi_3$ showing area of existence of two types of the structures adopted by the alloys ($PuNi_3$ and $CeNi_3$).

3.1.2. Structure of the $LaNi_{3-x}Mn_x$ alloys

The substitution of smaller Ni atoms by larger Mn atoms results in a monotonic and almost linear increase of the unit cell volumes from 62.4 to 64.0 Å^3 per formula unit (Fig. 1). At a substitution level exceeding $x = 0.1$, the structures of the $LaNi_{3-x}Mn_x$ alloys adopt the hexagonal $CeNi_3$-type structure instead of the rhombohedral $PuNi_3$-type structure characteristic of the initial $LaNi_3$ compound.

In order to study the effect of Mn substitution, the $LaNi_{2.67}Mn_{0.33}$ compound has been investigated by PND (see Fig. 2). From the data presented in Table 1, it can be concluded that Mn substitutes mostly for Ni inside the $CaCu_5$-type layer with a very small amount of Mn replacing Ni atoms in the Kagome nets connecting the AB_5 and AB_2 slabs.

3.1.3. Structure of the $La_{2-x}Mg_xNi_7$

X-ray data indicated that the synthesis process described above did not yield an alloy with AB_3 ($La_{0.67}Mg_{0.33}Ni_3$) composition. A single-phase compound with A_2B_7 ($La_{1.5}Mg_{0.5}Ni_7$)

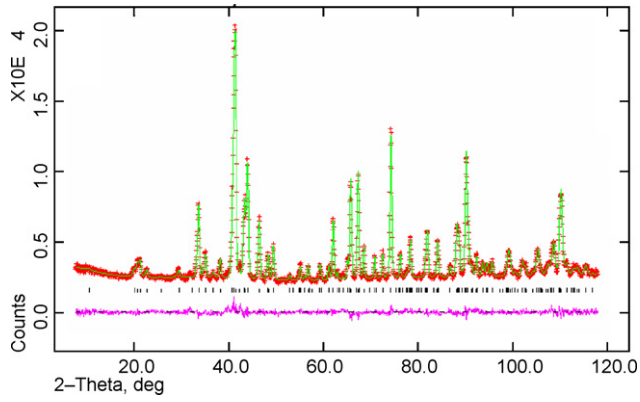

Fig. 2. Powder neutron diffraction pattern of the $LaNi_{2.67}Mn_{0.33}$ alloy (R2D2 instrument, $\lambda = 1.5514$ Å) showing observed (+), calculated (upper line) and difference (lower line) pattern. Positions of the peaks are marked.

Table 1
Crystal structure data for the $LaNi_{2.69}Mn_{0.31}$ alloy (ordered $CeNi_3$ type of structure) refined on the basis of the powder neutron diffraction data

Atom	Site	x	y	z	$U_{iso} \times 100$ (Å^2)	SOF
La1	2*c*	1/3	2/3	1/4	2.1(1)	1.0(−)
La2	4*f*	1/3	2/3	0.4585(2)	1.18(8)	1.0(−)
Ni1	2*a*	0	0	0	0.7(1)	1.0(−)
M2	2*b*	0	0	1/4	1.3(4)	0.472(8)Ni + 0.528(8)Mn
M3	2*d*	1/3	2/3	3/4	1.6(2)	0.728(9)Ni + 0.272(9)Mn
Ni4	12*k*	0.8338(2)	0.6676(4)	0.37166(6)	0.72(4)	0.981(6)Ni + 0.019(6)Mn

Space group $P6_3/mmc$ (No. 194); $a = 5.1404(1)$ Å, $c = 16.7547(6)$ Å; $V = 383.41(2)$ Å^3; composition: $3 \times LaNi_{2.69(2)}Mn_{0.31(2)} = LaNi_{4.14(1)}Mn_{0.86(1)} + 2 \times LaNi_{1.97(1)}Mn_{0.03(1)}$.
$R_p = 0.0300$; $R_{wp} = 0.0376$; $\chi^2 = 1.727$.

Table 2
Crystal structure data for $La_{1.5}Mg_{0.5}Ni_7$ alloy (ordered Ce_2Ni_7 type of structure) refined on the basis of the X-ray diffraction data

Atom	Site	x	y	z	SOF
La1	4*f*	1/3	2/3	0.0209(3)	0.49(1)
Mg1	4*f*	1/3	2/3	0.0209(3)	0.51(1)
La	4*f*	1/3	2/3	0.1728(2)	1.0(−)
Ni1	2*a*	0	0	0	1.0(−)
Ni2	4*e*	0	0	0.1650(4)	1.0(−)
Ni3	4*f*	1/3	2/3	0.8309(5)	1.0(−)
Ni4	6*h*	0.834(1)	0.668(2)	1/4	1.0(−)
Ni5	12*k*	0.8271(7)	0.6542(14)	0.0834(2)	1.0(−)

Space group $P6_3/mmc$ (No. 194); $a = 5.02822(7)$ Å, $c = 24.2032(6)$ Å; $V = 529.95(2)$ Å^3.
$R_p = 0.0284$; $R_{wp} = 0.0371$; $\chi^2 = 1.706$.

stoichiometry was obtained instead. This slight shift in stoichiometry is due to a significant evaporation of Mg during synthesis. Results of the X-ray diffraction data refinements for the $La_{1.5}Mg_{0.5}Ni_7$ alloy are given in Table 2 and Fig. 3. As can be seen from Table 2, magnesium substitutes for La exclusively within the AB_2 slabs of the structure.

3.2. Comparison of the structure of AB_2 and AB_5 slabs in studied intermetallics

Although all three studied intermetallic compounds crystallise with different types of structures, it is nevertheless possible to compare them by analysing the structures of the constituent AB_2 and AB_5 slabs. The relevant crystallographic parameters are provided in Table 3. As can be seen, substitutions of larger La by smaller Mg and smaller Ni by larger Mn have opposite effects on the structures of the intermetallic compounds. As expected, the most significant impact of substitution is observed within the slabs accommodating the "guest" atoms. As compared to the $LaNi_3$ intermetallic, the AB_2 slab shrinks by 9.6% upon substitution of La by Mg; in contrast, the AB_5 slab expands by 4.5% upon substitution of Ni by Mn. The other, "unmodified" slabs vary their parameters very marginally, by less than only 1.2%. Shrinking or expansion of the corresponding slabs of the unit cells leads to the corresponding shortening or elongation of the relevant interatomic distances. The La(Mg)–La(Mg) bonds become 4% shorter than the relevant La–La bonds in the structure of $LaNi_3$. As a result of

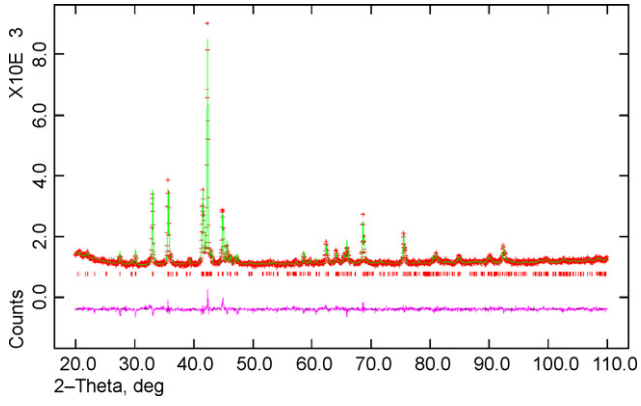

Fig. 3. Powder X-ray diffraction pattern of the $La_{1.5}Mg_{0.5}Ni_7$ alloy showing observed (+), calculated (line) and difference (lower line) pattern. Positions of the peaks are marked.

Table 3
Selected crystallographic parameters of the AB_2 and AB_5 slabs in the crystal structures of $LaNi_3$, $LaNi_{2.69}Mn_{0.31}$, and $La_{1.5}Mg_{0.5}Ni_7$

Compound	$LaNi_3$	$LaNi_{2.69}Mn_{0.31}$	$La_{1.5}Mg_{0.5}Ni_7$
Str. type	$PuNi_3$	$CeNi_3$	Ce_2Ni_7
a (Å)	5.0817(2)	5.1404(1)	5.02822(7)
$\Delta a/a_{LaNi_3}$	–	1.2%	−1.1%
c (Å)	25.092(1)	16.7547(6)	24.2032(6)
Data source	XRD	PND	XRD
AB_2 layer			
Composition	$2 \times LaNi_2$	$2 \times LaNi_{1.97}Mn_{0.03}$	$2 \times La_{0.5}Mg_{0.5}Ni_2$
c_{AB_2}	4.371	4.299	4.037
$\Delta c_{AB_2}/c_{AB_2}$	–	−1.6%	−7.6%
c/a	0.86	0.84	0.80
V	97.8	98.4	88.4
$\Delta V_{AB_2}/V_{AB_2}$	–	0.6%	−9.6%
La(Mg)–La(Mg)	3.204	3.277	3.074
La(Mg)–Ni	3.004–3.186	3.048–3.211	2.885–2.947
Ni–Ni	2.541–2.632	2.578–2.610	2.420–2.518
AB_5 layer			
Composition	$LaNi_5$	$LaNi_{4.14}Mn_{0.86}$	$LaNi_5$
c_{AB_5}	3.993	4.077	4.032
$\Delta c_{AB_5}/c_{AB_5}$	–	2.1%	1.0%
c/a	0.79	0.79	0.80
V	89.3	93.3	88.3
$\Delta V_{AB_5}/V_{AB_5}$	–	4.5%	−1.1%
La–Ni(Mn)	2.934–3.232	2.968–3.280	2.904–3.317
Ni(Mn)–Ni(Mn)	2.541–2.632	2.519–2.524	2.420–2.905
V_{AB_2}/V_{AB_5}	1.09	1.05	1.00

shrinking of the AB_2 slab in the Mg-substituted material, the volumes of the AB_2 and AB_5 slabs become equal (Table 3).

3.3. Hydrogenation properties

Only very low synthesis temperatures and starting pressures of hydrogenation allowed us to synthesise the crystalline $LaNi_3D_{2.8}$. Deuterium was introduced step-by-step in small portions starting from 0.01 to 0.05 bar D_2, in about 20 steps, before reaching a final pressure of 1 bar. This yielded a deuteride with the stoichiometry $LaNiD_{\sim 3}$. The hydrogenation of $LaNi_3$ by immediate injection of 1 bar D_2 into the autoclave resulted in almost complete amorphisation of the material, because of the high reaction rate and high heat of hydrogenation causing the temperature increase. For the Mn-substituted alloys the amorphisation occurred even at −20 °C. The volumetrically measured capacity of these amorphous hydrides were found to be approximately the same as those reported for $LaNi_3$ [4]: $LaNi_{2.8}Mn_{0.2}D_{4.3}$ and $LaNi_{2.6}Mn_{0.4}D_{4.5}$.

On the other hand, the magnesium compound was deuterated using a synthesis pressure of 5 bar D_2 with saturation reached in just 15 min. The synthesis led to a formation of crystalline $La_{1.5}Mg_{0.5}Ni_7D_9$. It is formed via an isotropic expansion of the unit cell ($\Delta a/a = 7.1\%$, $\Delta c/c = 9.3\%$, $\Delta V/V = 25.3\%$) [20]. The structural data for the deuteride $La_{1.5}Mg_{0.5}Ni_7D_9$ will be published elsewhere [20].

3.4. Crystal structure of the $LaNi_3D_{2.8}$ deuteride

The X-ray diffraction study of $LaNi_3D_{2.8}$ showed a pronounced linear expansion of the original trigonal unit cell along [0 0 1], $\Delta c/c = 27.8\%$ together with a slight contraction in the basal plane, $\Delta a/a \sim -2.5\%$. From the analysis of the synchrotron X-ray diffraction pattern, the splitting of the $h\,k\,l$, $h\,h\,l$, and $h\,k\,0$ peaks was evident with the $0\,0\,l$ reflections remaining unsplit (see inset in Fig. 4 as illustration). Thus, lowering of the symmetry of the original trigonal structure was concluded. From group–subgroup relations, the following transformation of the original trigonal unit cell into the monoclinic one for the hydride was deduced: $R\bar{3}m \rightarrow P\bar{3}m1 \rightarrow C2/m$ ($a_{mon} = (a + 2b)_{trig}$; $b_{mon} = -a_{trig}$; $C_{mon} = C_{trig}$; $V_{mon} = 2\ V_{trig}$). The monoclinic deformation of the structure was further confirmed by analysis of the PND profiles. Besides the broadening of the pattern due to the splitting of the peaks, extra peaks appeared in the diffraction profile in addition to those allowed by the trigonal symmetry; the most distinct of these peaks are marked in Fig. 4.

The refinement of the XRD data revealed a strong expansion of the AB_2 layers of the structure with the AB_5 layers remaining unchanged. This feature makes the structure of the monoclinically deformed $LaNi_3D_{2.8}$ deuteride similar to the previously studied, chemically related, "anisotropic", orthorhombic $CeNi_3D_{2.76}$ [14] and hexagonal $La_2Ni_7D_{6.1}$ [15] deuterides.

Starting from the known structure of the metal sublattice, obtained from a transformation from the trigonal unit cell to the monoclinic expanded one, the deuterium atoms were located using the difference Fourier synthesis process. Several steps of such a process were applied before all 14 D sites were located. All deuterium atoms in $LaNi_3D_{2.8}$ are located inside the $MgZn_2$-type layers or on the borders between the AB_5 and AB_2 slabs (D7 and D8 sites in the Table 4) with no D atoms inside the AB_5 slabs.

The results of the Rietveld refinements of PND data are presented in Table 4. The crystal structures of the initial intermetallic $LaNi_3$ compound and corresponding $LaNi_3D_{2.8}$ deuteride are shown in Fig. 5.

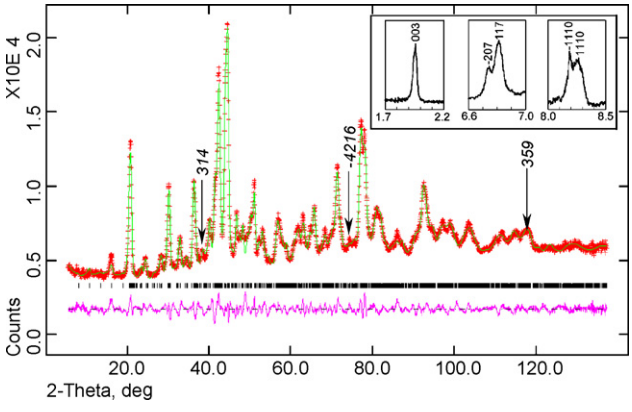

Fig. 4. Powder neutron diffraction pattern of the $LaNi_3D_{2.8}$ deuteride showing calculated (upper line), observed (+) and difference (lower line) pattern. Positions of the peaks are marked. Arrows indicate peaks, which are not allowed in the trigonal symmetry. Inlets show splitting of the peaks in the SR XRD pattern because of a monoclinic distortion of the metal matrix of the deuteride.

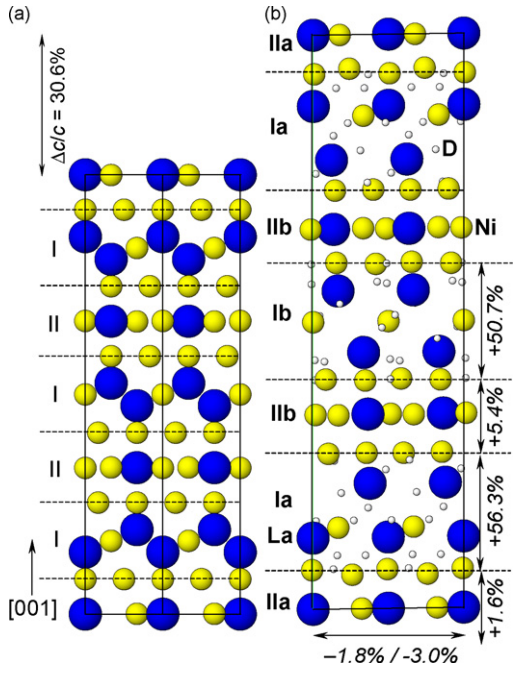

Fig. 5. Crystal structures of the $LaNi_3$ intermetallic compound (a) and the $LaNi_3D_{2.8}$ deuteride, (b) "anisotropic" expansion of the metal sublattice upon hydride formation is shown for two different types of the available structure slabs (I –$MgZn_2$ and II –$CaCu_5$). Due to monoclinic distortion, the AB_2 slabs in the structure of hydride become nonequivalent, having $LaNi_2D_{4.5}$ (I*a*) and $LaNi_2D_{3.2}$ (I*b*) compositions. Difference in deuterium content between the AB_5 layers (II*a* and II*b*) is less pronounced, $LaNi_5D_{0.25–0.28}$.

Table 4
Crystal structure data for $LaNi_3D_{2.8}$

Atom	Site	x/y[a]	z	Fraction		Occupied interstice[b] (corresponding site in the IMC)
La1	2*a*	0	0	1.0(−)		(La1)
La2	4*i*	0.636(2)	0.3387(6)	1.0(−)		
La3	4*i*	0.002(3)	0.8760(6)	1.0(−)		(La2)
La4	4*i*	0.378(2)	0.7823(6)	1.0(−)		
La5	4*i*	0.665(3)	0.4461(7)	1.0(−)		
Ni1	2*c*	0	½	1.0(−)		(Ni1)
Ni2	4*i*	0.667(2)	0.8586(5)	1.0(−)		
Ni3	4*i*	0.016(2)	0.6615(4)	1.0(−)		(Ni2)
Ni4	4*i*	0.676(3)	0.0002(6)	1.0(−)		
Ni5	4*i*	0.668(2)	0.6627(5)	1.0(−)		
Ni6	4*i*	0.493(2)	0.9319(6)	1.0(−)		(Ni3)
Ni7	8*j*	0.740(1)/0.749(3)	0.0592(3)	1.0(−)		
Ni8	4*i*	0.855(2)	0.7288(6)	1.0(−)		
Ni9	8*j*	0.899(2)/0.262(3)	0.2704(4)	1.0(−)		
Ni10	4*i*	0.154(2)	0.3972(6)	1.0(−)		
Ni11	8*j*	0.916(2)/0.261(3)	0.3999(4)	1.0(−)		
Layer I*a*						
D1	4*i*	0.4930(2)	0.1587(1)	1.0(−)	La_3Ni *c*	
D2	4*i*	0.134(3)	0.1804(4)	1.0(−)	La_3Ni *c*	
D3	4*i*	0.334(2)	0.1965(8)	1.0(−)	La_3Ni *c*	
D4	8*j*	0.240(2)/0.249(2)	0.1518(6)	1.0(−)	La_3Ni *c*	
D5	4*i*	0.8979(4)	0.06109(4)	0.57(7)	La_2Ni_2 *a*	
D6	4*i*	0.650(2)	0.092(1)	1.0(−)	La_3Ni_3 *d*	
D7	4*i*	0.017(3)	0.2387(9)	1.0(−)	La_3Ni_3 *d*	
D8	4*i*	0.326(7)	0.249(2)	0.75(4)	La_3Ni_3 *e*	
D9	4*i*	0.331(5)	0.09566(4)	1.0(−)	Ni_4 *b*	
Layer I*b*						
D10	4*i*	0.138(2)	0.4727(8)	0.70(7)	La_3Ni *c*	
D11	8*j*	0.435(5)/0.218(4)	0.5026(4)	0.5(−)	La_3Ni *c*	
D12	4*i*	0.5126(2)	0.39418(5)	0.25(6)	La_2Ni_2 *a*	
D13	4*i*	0.406(9)	0.4275(3)	0.54(5)	La_3Ni_3 *d*	
D14	4*i*	0.001(5)	0.4727(7)	0.80(4)	Ni_4 *b*	

Space group *C*2/*m* (No. 12): $a = 8.6392(2)$ Å; $b = 4.9265(5)$ Å; $c = 32.780(4)$ Å; $\beta = 90.85(1)^\circ$; $V = 1395.8(2)$ Å^3. U_{iso} was constrained to be equal for the chemically similar types of the atoms: La1–La2 (0.5(3)), La3–La5 (1.3(2)); Ni1–Ni2 (3.6(5)); Ni3–Ni5 (1.1(1)); Ni6–Ni11 (0.75(7)); D1–D14 (2.2(2) Å$^2 \times 10^{-2}$); $R_{wp} = 0.0397$; $R_p = 0.0310$.

[a] $y = 0$ if the other values are not stated.

[b] Letter after the type of interstice corresponds to the labeling in the Fig. 6.

4. Discussion

The study of the substitution of the constituent atoms in the structure of $LaNi_3$ by Mg and Mn revealed that it selectively proceeds in the different layers of the structure:

- In $La_{0.75}Mg_{0.25}Ni_{3.5}$ Mg substitutes for 50% of La within the Laves-type AB_2 slabs only: ($LaNi_2 \rightarrow La_{0.5}Mg_{0.5}Ni_2$). The AB_5 slab remains unchanged and has the $LaNi_5$ composition.
- An opposite behaviour is observed when Ni is substituted by Mn in $LaNi_3$ forming $LaNi_{2.69}Mn_{0.31}$: $LaNi_2$ slabs remain nonmodified while the Ni substitution by Mn proceeds inside the AB_5-type slabs until reaching the stoichiometry $LaNi_{4.14}Mn_{0.86}$. Such a substitution reveals an opposite trend to those observed in the structures of the AB_5 $LaNi_{4.1}Mn_{0.91}$ intermetallic, where Mn atoms mostly substitute for Ni atoms within the Kagome nets [21]. The unit cell of the latter AB_5 phase has smaller volume (91.6 Å^3 compared to 93.3 Å^3 for the AB_5 layer in $LaNi_{2.69}Mn_{0.31}$ (Table 4)).
- Substitution of Ni by Mn proceeds until reaching a Mn content of at least 0.4 at. Mn/f.u. Increase of the Mn content above 0.1 at. Mn/AB_3 leads to the change of the structure type from trigonal $PuNi_3$ to hexagonal $CeNi_3$. The substitution is accompanied by an approximately linear increase in the unit cell volumes with the rise in Mn content from 62.4 up to 63.9 Å^3/f.u. AB_3.

Similar ways of both types of substitution were observed in [22] during the synthesis of the hexagonal $La_4Mg(Ni,Co)_{19}$ (Pr_5Co_{19} structure type), where the 3d-element, cobalt, substitutes for Ni in the AB_5 layers only and Mg replaces La atoms exclusively in the AB_2 layer.

The hydrogenation of the $LaNi_3$ under mild conditions resulted in the synthesis of the $LaNi_3D_{2.8}$, whose formation is

accompanied by the monoclinic distortion of the metal matrix and leads to the insertion of the D atoms only into the AB_2 slabs of structure. This leads to a large elongation of the unit cell along the [0 0 1] direction by 30.6%, the AB_2 layers being expanded by 50.7–56.3%. The basal plane of the unit cell contracts during the hydride formation by −1.8/−3.0%. Such features of the $LaNi_3D_{2.8}$ deuteride structure are common to the other known structures of the "anisotropic" hydrides [14–16].

Monoclinic distortion of the unit cell reveals differences in the expansion of the metal sublattice caused by variations of H content of the initially equivalent in the trigonal structure layers of the AB_2 or AB_5 types. This distortion results in formation of stronger (I*a*: AB_2; II*b*: AB_5) and weaker (I*b*: AB_2; II*a*: AB_5) expanded layers, where a more pronounced expansion agrees well with higher hydrogen content in the corresponding AB_2-type I*a* layer–$LaNi_2D_{4.52}$ ($\Delta c/c = 56.3\%$) compared to the I*b* layer with lower D content, $LaNi_2D_{3.17}$, and smaller linear expansion, $\Delta c/c = 50.7\%$ (Fig. 5). Coordination numbers of La atoms in LaDx polyhedra withing the I*a* layer are 12 and 9. These coordination characteristics are similar to those observed in the crystal structure of $CeNi_3D_{2.8}$ (12 and 7 D atoms for Ce atoms) [14]. In case of the I*b* layer, formation of disordered LaD_{11} polyhedra takes place.

In the structure of $LaNi_3D_{2.8}$, hydrogen atoms occupy 14 types of interstices with 5 different types of surroundings (Fig. 6). These include 4 types already existing in the structure of $LaNi_3$ intermetallic alloy interstices (two types of La_2Ni_2 and two types of Ni_4 tetrahedra Fig. 6a–b) and ten new types of sites formed due to the distortion of the metal matrix within the AB_2 slab (Fig. 6c–e). The latter include 4 La_3Ni_3 and 6 La_3Ni interstices. These new types of sites are similar to those filled by H atoms in the "anisotropic" structures of $CeNi_3D_{2.8}$ [14] and $La_2Ni_7D_{6.5}$ [15].

We note that D3 and D8 atoms occupy neighbouring interstices with a common La_3 triangular face (upper and lower parts of the cluster shown in Fig. 6e. This results in a D3–D8 separation of 1.74 Å. Such a feature is similar to that observed for the hexagonal $RNiInD_{1.33-x}$ deuterides with short D. . .D distances (1.56–1.63 Å) formed because of a double filling by D atoms of the trigonal bipyramids R_3Ni_2 [23].

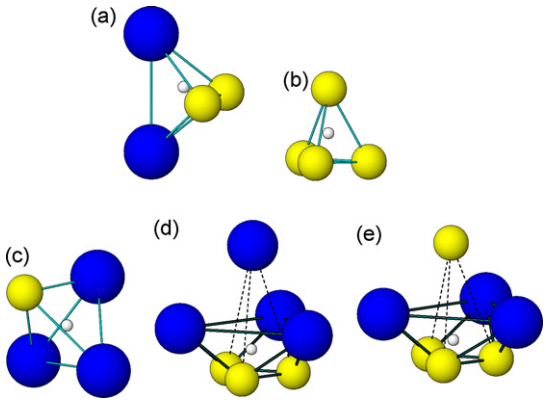

Fig. 6. Types of occupied interstices in the structure of $LaNi_3D_{2.8}$, both existing in the $LaNi_3$ structure (a, b) and, also, formed due to the deformation of the AB_2 layers (c–e).

The shortest interatomic distances observed in the structure of $LaNi_3D_{2.8}$ are: La–La 3.58 Å, La–Ni 2.67 Å, Ni–Ni 2.38 Å (within a contracted $LaNi_5$-layer), La–D 2.16 Å, Ni–D 1.47 Å, and D–D 1.74 Å. All other D–D distances except D3–D8 exceed 1.8 Å. The D sites distanced at 1.44 (D12–D13) and 1.13 Å (D11–D11), are never simultaneously occupied since their occupation numbers are low.

Maximum hydrogen capacity for the considered model of the deuterium sublattice corresponds to $LaNi_3D_{3.11}$. This means that at higher hydrogen content exceeding 3.11 at. H/$LaNi_3$, hydrogen atoms should also occupy the AB_5 slabs.

The formed crystalline $LaNi_3D_{2.8}$ deuteride has a much lower hydrogen storage capacity compared to the maximum capacity observed for the completely amorphous $LaNi_3H_{4.5}$ [4] which indicates that on amorphisation, the structure of the metal sublattice changes.

As it follows from the data of the Table 4 and Fig. 5, in the structure of the $LaNi_5D_{2.8}$ deuteride ~ 90% of deuterium atoms are located within the AB_2 slabs, and 10% are situated on the boundaries between the AB_2 and AB_5 slabs (sites D7–D8 in the Table 3). Such a distribution corresponds to the alternation of the $LaNi_2D_{3.17–4.52}$ and $LaNi_5D_{0.25–0.28}$ layers. Hydrogen contents of the AB_2 layers for both $LaNi_3D_{2.8}$ and $CeNi_3D_{2.76}$ are rather similar (4.0 and 3.0 at. H/f.u. in both cases). These values are also close to the hydrogen storage capacity of the amorphous Laves-type $LaNi_2$-based hydride $LaNi_2H_{>3.5}$ [24]. However, in the hybrid "anisotropic" structures, the hydrogenated AB_2 layer remains crystalline, possibly because of a stabilising effect of the nonhydrogen-absorbing AB_5 slabs. When the AB_5 slabs become expanded, the crystallinity of the hybrid hydride structure worsens before vanishing. The $LaNi_3D_{2.8}$ in this relation is less stable compared to the $CeNi_3D_{2.8}$, since the pressures of hydrogen uptake by the AB_5 phases $LaNi_5$ and $CeNi_5$ are 2 and 48 bar, respectively [14]. Since they are significantly lower for $LaNi_5$, this makes its hydrogenation inside the AB_3 alloy much more easily achievable.

Ni substitution by Mn in the structure of $LaNi_5$ is known to reduce the hydride formation pressures [21]. Increase of Mn content leads to the expansion of the AB_5^- slabs in the Mn-containing samples; thus, hydrogenation pressures for the AB_5 slabs should be at lower pressures compared to $LaNi_3$. Such easier hydrogenation, furthermore, explains why these alloys appear to be less stable against the hydrogen-induced amorphisation. This difference in hydrogen affinity of the different slabs of the structure can be concluded from the analysis of the structures of the initial intermetallics. As long as the volume of the AB_2 slab is larger than that of the AB_5 slab, the AB_2 slabs remain more active with respect to hydrogenation and, thus, the formation of the "anisotropic" hydrides can be expected. When the volumes of slabs in the initial compound become equal because of expansion of the AB_5 slabs caused by the doping elements (Mn), this reduces differences in the hydrogenation affinities of the AB_5 and AB_2 slabs. Similar H uptake by both layers causes alteration of the hydrogenation behaviour from an "anisotropic" (H in the AB_2 layers and no H uptake by the AB_5 layer) to an "isotropic" hydride with even distribution of the H atoms between these two types of slabs. Such changes can be reached

by a selective substitution of the constituent atoms within the AB_2 layer of the initial AB_3 intermetallic phase. The examples of such substitution are La replacement by Mg (this work) or Y in the structure of $LaY_2Ni_9D_{12.8}$ [16].

5. Conclusions

'Hybrid' crystal structures of the La–Ni intermetallics formed by the stacking of the AB_2 (Laves phase) and AB_5 ($CaCu_5$) type slabs were selectively modified by a partial substitution of La by Mg and of Ni by Mn. Mg atoms enter the AB_2 slabs only, whereas Mn atoms mostly replace Ni atoms inside the AB_5 slab, with just small amounts of Mn observed in the network joining the AB_5 and AB_2 slabs.

Because of the thermodynamically metastable character of the hydride formed, $LaNi_3$ easily becomes amorphous on hydrogenation. Its crystalline hydride was synthesised only during the synthesis at −20 °C and by using low hydrogenation pressures, below 1 bar. Mg increases the stability of the metal sublattice towards its disproportionation in hydrogen: the crystalline hydride was obtained at room temperature and a hydrogen charging pressure of 5 bar. In contrast, Mn reduces stability of the intermetallic alloy; only amorphous hydrides were obtained even when proceeding with synthesis of the hydride at subzero temperatures and at reduced H_2 pressures.

Upon hydrogenation, the rhombohedral $LaNi_3$ forms a monoclinically distorted $LaNi_3D_{2.8}$ deuteride. Hydrogen atoms occupy only AB_2 slabs in the structure. They fill interstices both existing in the original $LaNi_3$ and formed because of the H-induced deformation of the metal matrix. Such selective filling by H of the metal sublattice results in a very pronounced expansion of the AB_2 slabs and of the unit cells in total along the [0 0 1] direction (50.7–56.3% and 30.6%, respectively). Deuterium atoms occupy 14 different types of interstices with 4 different types of surroundings, La_2Ni_2, Ni_4 (both present already in the initial intermetallics), La_3Ni and La_3Ni_3 interstices (formed because of substantial shifts of the atoms within the AB_2 slabs). La atoms in the AB_2 slabs are surrounded by 12, 11, or 9 hydrogen atoms.

Acknowledgements

This work was supported by the Nordic Energy Research (Project 46-02 NORSTORE) and NEDO, Japan (Project "Novel Intermetallic Hydrides with High Volume Density and Advanced Surface Properties" between IFE and Tokai University).

References

[1] K.H.J. Buschow, H.H. van Mal, J. Less-Common Met. 29 (2) (1972) 203–210.
[2] R. Baddour-Hadjean, L. Meyer, J.P. Pereira-Ramos, M. Latroche, A. Percheron-Guégan, Electrochim. Acta 46 (15) (2001) 2385–2393.
[3] B. Liao, Y.Q. Lei, L.X. Chen, G.L. Lu, H.G. Pan, Q.D. Wang, J. Alloys Compd. 376 (2004) 186–195.
[4] J. Chen, H.T. Takeshita, H. Tanaka, N. Kuriyama, T. Sakai, I. Uehara, M. Haruta, J. Alloys Compd. 302 (2000) 304–313.
[5] K. Kadir, T. Sakai, I. Uehara, J. Alloys Compd. 302 (2000) 112–117.
[6] K. Kadir, T. Sakai, I. Uehara, J. Alloys Compd. 257 (1997) 115–121.
[7] S.P. Solov'ev, N.V. Fadeeva, V.A. Yartys, V.V. Burnasheva, K.N. Semenenko, Sov. Solid State Phys. 23 (1981) 1226 (in Russian).
[8] Y.E. Filinchuk, D. Sheptyakov, K. Yvon, J. Alloys Compd. 413 (2005) 106–113.
[9] Y.E. Filinchuk, K. Yvon, J. Alloys Compd. 404–406 (2005) 89–94.
[10] M.I. Bartashevich, A.N. Pirogov, V.I. Voronin, T. Goto, M. Yamaguchi, I. Yamamoto, J. Alloys Compd. 231 (1995) 104–107.
[11] Y.E. Filinchuk, K. Yvon, J. Solid State Chem. 179 (2006) 1041–1052.
[12] V.A. Yartys, V.V. Burnasheva, K.N. Semenenko, N.V. Fadeeva, S.P. Solov'ev, Int. J. Hydrogen Energy 7 (12) (1982) 957–965.
[13] R.H. Van Essen, K.H.J. Buschow, J. Less-Common Met. 70 (2) (1980) 189–198.
[14] V.A. Yartys, O. Isnard, A.B. Riabov, L.G. Akselrud, J. Alloys Compd. 356–357 (2003) 109–113.
[15] V.A. Yartys, A.B. Riabov, R.V. Denys, M. Sato, R.G. Delaplane, J. Alloys Compd. 408–412 (2006) 273–279.
[16] M. Latroche, V. Paul-Boncour, A. Percheron-Guégan, J. Solid State Chem. 177 (2004) 2542–2549.
[17] A. Wannberg, M. Gronros, A. Mellergard, L.-E. Karlsson, R.G. Delaplane, B. Lebech, Z. Kristallogr. Suppl. 23 (2006) 195.
[18] A.C. Larson, R.B. von Dreele, General Structure Analysis System, LANL, 1994.
[19] A.V. Virkar, A. Raman, J. Less-Common Met. 18 (1969) 59–66.
[20] R.V. Denys, V.A. Yartys, R.G. Delaplane, Unpublished results.
[21] C. Lartigue, A. Percheron-Guégan, J.C. Achard, F. Tasset, J. Less-Common Met. 75 (1) (1980) 23–29.
[22] E. Akiba, H. Hayakawa, T. Kohno, J. Alloys Compd. 408–412 (2006) 280–283.
[23] V.A. Yartys, R.V. Denys, B.C. Hauback, H. Fjellvåg, I.I. Bulyk, A.B. Riabov, Ya.M. Kalychak, J. Alloys Compd. 330–332 (2002) 132–140.
[24] V. Paul-Boncour, A. Percheron-Guégan, N. Diaf, J.C. Achard, J. Less-Common Met. 131 (1–2) (1987) 201–208.

Available online at www.sciencedirect.com
ScienceDirect
Journal of Solid State Chemistry 180 (2007) 2566–2576
JOURNAL OF SOLID STATE CHEMISTRY
www.elsevier.com/locate/jssc

Crystal chemistry and thermodynamic properties of anisotropic $Ce_2Ni_7H_{4.7}$ hydride

R.V. Denys[a,b], V.A. Yartys[a,*], Masashi Sato[c], A.B. Riabov[a,b], R.G. Delaplane[a,d,1]

[a]*Institute for Energy Technology, P.O. Box 40, Kjeller NO-2027, Norway*
[b]*Physico-Mechanical Institute of the National Academy of Science of Ukraine, 5 Naukova Street, Lviv 79601, Ukraine*
[c]*Department of Applied Chemistry, School of Engineering, Tokai University, 1117 Kita-Kaname, Hiratsuka, Kanagawa 259-1292, Japan*
[d]*The Studsvik Neutron Research Laboratory, Uppsala University, S-611 82 Nyköping, Sweden*

Received 26 April 2007; received in revised form 25 June 2007; accepted 2 July 2007
Available online 10 August 2007

Abstract

A new intermetallic deuteride $Ce_2Ni_7D_{4.7}$ with an anomalous volume expansion has been studied. Its structure was solved on the basis of *in situ* neutron diffraction data. Expansion proceeds along the *c*-axis and within the $CeNi_2$ slabs only. All D atoms are located inside these slabs and on the border between $CeNi_2$ and $CeNi_5$. Ordering of D atoms in the bulk of $CeNi_2$ is accompanied by substantial deformation of these slabs thus lowering the hexagonal symmetry to orthorhombic [space group *Pmcn* (No. 62); $a = 4.9251(3)$ Å, $b = 8.4933(4)$ Å, $c = 29.773(1)$ Å]. Inside the $CeNi_2$ layer the hydrogen sublattice is completely ordered; all D–D distances exceed 2.0 Å. Local coordination of Ni by D inside the $CeNi_2$ blocks is of "open", saddle-like type. Hydrogen ordering is mainly determined by Ce–H and H–H interactions. The pressure–composition–temperature measurements yielded the following thermodynamic parameters of the formation of the hydride: $\Delta H = -22.4\,kJ/mol_H$, $\Delta S = -59.9\,J/(K\,mol_H)$.

Keywords: Metal hydrides; Crystal structure and symmetry; Neutron diffraction; Pressure–composition–temperature relationships

1. Introduction

The hydrogenation of intermetallic alloys is utilised for the storage of atomic, interstitial H thus providing a high-volume density of stored hydrogen. The crystal chemistry of the corresponding hydrides can be related to their hydrogen storage characteristics that can be applied for the optimisation of H storage performance.

Typically, for intermetallic hydrides the metal lattice is modestly modified with the accommodation of hydrogen atoms into the available interstitial vacancies; the interatomic metal–metal distances change by only a few percent. However, recent studies have shown the existence of "anisotropic" RE–Ni-based hydrides (RE = rare-earth metal) where a large expansion occurs along a single crystallographic direction [1], and very small changes in directions normal to this expansion take place. Earlier, there were reported data on the crystal structures of $CeNi_3D_{2.8}$ [2], $LaNi_3D_{2.8}$ [3], $CeY_2Ni_9D_{7.7}$ [4] and $La_2Ni_7D_{6.5}$ [1] that are related to the $RENi_3$ and RE_2Ni_7 intermetallics [5]. The structures of the initial intermetallic alloys are built up from two types of metal slabs, $RENi_5$ ($CaCu_5$ type) and $RENi_2$ ($MgZn_2$ type) that are stacked along $[001]_{hex}$. The combination $1 \times RENi_5 + 2 \times RENi_2$ gives the overall stoichiometry $3 \times RENi_3$, and for the RE_2Ni_7 compounds the ratio of the $RENi_5$ to $RENi_2$ slabs is 1:1.

During the hydrogenation process to form $CeNi_3D_{2.8}$ [2], $LaNi_3D_{2.8}$ [3] and $La_2Ni_7D_{6.5}$ [1], common and unusual structural features are observed:

- The lattice expansion proceeds within the $RENi_2$ slabs only and is confined to [001]. Such expansion amounts to 58–63% and is associated with occupation by D atoms of the Laves-phase layers.
- The $RENi_5$ slabs remain unoccupied by D. This correlates with absence of the lattice expansion of these layers.

*Corresponding author. Fax: +47 63 81 29 05.
E-mail address: volodymyr.yartys@ife.no (V.A. Yartys).
[1]Present address: Borgdalsgången 36, SE-611 57 Nyköping, Sweden.

0022-4596/$ - see front matter © 2007 Elsevier Inc. All rights reserved.
doi:10.1016/j.jssc.2007.07.002

- New types of interstitial sites occupied by D are formed because of anisotropic expansion, namely RE_3Ni_3 octahedra and RE_3Ni tetrahedra. In addition to these sites, D enters RE_2Ni_2 tetrahedra belonging to both $RENi_5$ and $RENi_2$ layers.
- An ordered hydrogen sublattice is formed in $CeNi_3D_{2.8}$ and $La_2Ni_7D_{6.5}$. The structural behaviour of $CeNi_3D_{2.8}$ and $La_2Ni_7D_{6.5}$ is dominated by RE–H and H–H interactions.

The present work is focused on studies of the thermodynamics and crystal structure of $Ce_2Ni_7H(D)_{4.7}$, which is chemically related to $La_2Ni_7D_{6.5}$. The goal of this study is to gain a better understanding of the structural and physical–chemical properties of anisotropic hydrides. While writing this manuscript, we became aware that a similar orthorhombic Ce_2Ni_7-based hydride and deuteride have been independently studied by Filinchuk et al. [6]. They have confirmed the typical group behaviour for anisotropic hydrides [1–4] of the transformation of the metallic sublattice during hydrogenation (elongation along [001], with only the Laves-phase blocks becoming enlarged). As the main conclusion, a tetrahedral NiD_4 coordination of Ni atoms within the $CeNi_2$ blocks has been reported [6]. We will show later in this paper that formation of NiD_4 tetrahedra contradicts the findings of the present study, where a different, saddle-type ordering of four H atoms around Ni was found. A significantly different deuterium substructure and smaller deuterium content (4.1 at. D/Ce_2Ni_7) were reported [6] compared to the findings of the present study where deuterides with 4.4 and 4.7 at. D/f.u. have been investigated. Possible reasons for the disagreements between Ref. [6] and the present work could be in the experimental conditions employed in [6] (exposure of the studied hydrides to air leading to their partial oxidation) as compared to the present work (*in situ* diffraction experiment under the pressure of deuterium gas allowing to study the material at equilibrium conditions). These variations in the experimental conditions will be proposed to account for the differences between the results of the two studies.

2. Experimental

2.1. Sample synthesis and characterisation

The Ce_2Ni_7 alloy was prepared by arc melting of bulk metals Ce (99.9%) and Ni (99.95%) under argon atmosphere followed by annealing in evacuated quartz ampoules at 1073 K for 2 weeks and then quenching in cold water. XRD characterisation with a DRON 3.0 X-ray diffractometer (Cu$K\alpha$ radiation) showed the alloy to be single-phase containing no detectable impurities. From the X-ray diffraction profile, a hexagonal unit cell was derived with $a = 4.9419(9)$ Å, $c = 24.508(5)$ Å, $V = 518.36(17)$ Å^3 which agrees well with published values [5,7].

All handling of the sample was done in a glove box in an inert argon atmosphere. For the preparation of the deuteride the sample was crushed in an agate mortar, loaded in a stainless steel autoclave (tube wall thickness 0.1 mm, $d_{inner} = 4$ mm), and activated by heating in vacuum up to 673 K followed by cooling to room temperature. Then the autoclave was slowly filled with 0.1 MPa D_2 (99.8% purity). The deuteration process was rather fast, and after saturation, reached within 1 min, the pressure was increased up to 2 MPa. The final product was a single-phase deuteride of 4.70 ± 0.05 at. D/Ce_2Ni_7 that was already reached at 0.1 MPa of pressure.

After PND measurements described below, deuterium was completely desorbed from the material; the sample was filled into a 0.3 mm glass capillary for SXRD analysis. Measurement was carried out at the high-resolution powder diffraction station BM01B at the Swiss–Norwegian Beam Lines at ESRF ($\lambda = 0.37504(1)$ Å, Debye–Scherrer geometry, 2Θ step size 0.0025°). Refined unit cell parameters of Ce_2Ni_7 agree well with those determined for the initial alloy: $a = 4.94131(3)$ Å; $c = 24.5136(2)$ Å; $V = 518.349(6)$ Å^3.

2.2. Neutron powder diffraction

After synthesis, powder neutron diffraction (PND) data were immediately collected with the high-resolution R2D2 diffractometer ($\lambda = 1.551(1)$ Å, 2Θ step size 0.05°) at the Studsvik Neutron Research Laboratory, Uppsala University, Sweden [8]. The instrument calibration parameters and wavelength of the neutron beam were determined by a least-squares fit for diffraction data collected for the standard reference materials; Si, NIST 640c and Al_2O_3, NIST 676 [8]. The preparation laboratory was located in annex to the Studsvik R2 reactor hall that ensured a minimum delay from sample preparation to the diffraction measurements. After the PND *in situ* measurement (in the stainless steel autoclave under 2 MPa D_2) the deuteride was reloaded from the autoclave into a vanadium sample holder with an inner diameter of 5 mm. The reloading was done in a glove box under a purified argon atmosphere, and the vanadium container was sealed with indium wire. A new *ex situ* PND data set was then collected with R2D2.

The GSAS program [9] was used for the Rietveld profile refinements of the crystal structure parameters of the initial intermetallic alloy and the prepared deuteride. Reflections from the stainless steel autoclave (space group $Fm\bar{3}m$; $a = 3.597$ Å) were excluded from the *in situ* PND profile during refinements. Neutron scattering lengths of the elements were taken from GSAS library: $b_{Ce} = 4.84$ fm; $b_{Ni} = 10.3$ fm; $b_D = 6.67$ fm.

2.3. Measurement of pressure–composition–temperature relationships for Ce_2Ni_7–H_2

Pressure–composition–temperature (PCT) relationships for the Ce_2Ni_7–H_2 system were measured by the Sieverts'

method on the sample used for the PND experiments after complete desorption of the deuterium to reform again the intermetallic Ce_2Ni_7 alloy. The sample was activated in vacuum at 573 K for 1 h, cooled under vacuum to 298 K and then slowly charged with hydrogen gas ($P_{H_2} = 1$ MPa). To achieve reproducible kinetics of hydrogen uptake and release, several absorption–desorption cycles were performed before measuring the isotherms. The purity grade of hydrogen gas used was 99.999%. The cycling has been done at the low temperature of 273 K in order to avoid a possible disproportionation of the Ce_2Ni_7 alloy. The measurements of the isotherms were performed in the temperature range 293–333 K and with hydrogen pressures from 10^{-3} to 10^{-1} MPa. An equilibrium state was considered to have been reached when the pressure change became less than 10^{-5} MPa.

3. Results and discussion

3.1. Thermodynamics studied by PCT isotherms

Fig. 1a shows the measured pressure–composition–temperature diagrams for the Ce_2Ni_7–H systems at temperatures between 293 and 333 K. The presence of a rather flat plateau is clearly seen at approximately $0.2 < H/Ce_2Ni_7 < 4.4$, which agrees well with an earlier report described in [10]. The isotherms saturate in the vicinity of 4.4–4.6 H/Ce_2Ni_7; the hydrogen solid solution limit is about $H/Ce_2Ni_7 = 0.2$. The limiting maximum hydrogen content in the hydride is close to 4.7 at. H/f.u. at 293 K, the experimental conditions for the PND experiment. Hysteresis between the absorption and desorption measured ($P_{abs}/P_{des} = 1.2$ at 313 K) is relatively modest.

Based on the obtained isotherms, the van't Hoff plots in the plateau regions are shown for the H_2 absorption and desorption processes in Fig. 1b. The equilibrium pressure on the plateau region for the present work is slightly lower than the pressure reported by van Essen and Buschow [10]. The Ce_2Ni_7 alloy is relatively unstable with respect to the disproportionation process; therefore, to avoid decomposition, rather modest hydrogenation pressures below 1 MPa were applied (these pressures were much higher in [10], 4 MPa).

Changes of enthalpy ΔH_H and entropy ΔS_H as a function of H content are shown in Fig. 2a and b, respectively. The shape of the curves is very typical for the metal–hydrogen systems [11]. The ΔH_H and ΔS_H values are nearly constant: -22.4 ± 0.5 kJ/mol$_H$ and -59.9 ± 0.4 J/(K mol$_H$), respectively, for the range $0.5 < H/Ce_2Ni_7 < 3.2$; both values increase at H content exceeding 3.2.

Calculated thermodynamic properties of the Ce_2Ni_7–H_2 system in the pressure plateau area are summarised in Table 1. The reference data for the hydrides of the Ce–Ni and Ce–Co binary intermetallics are also included for comparison. It is interesting to note that, despite of significant differences in the Ce/Ni ratios, the heat of formation, ΔH_H, is very close for the $CeNi_3$- and Ce_2Ni_7-based hydrides, −22.4 and −22.6 kJ/mol$_H$, respectively. This feature, perhaps, has roots in preferential accommodation of hydrogen by the $CeNi_2$ layers in both structures, and will be discussed later in this paper. Furthermore, we note a very unusual alteration of the thermodynamics of hydrogen–metal interaction for the related Co- and Ni-containing binary intermetallics, respectively, $CeNi_3$ and $CeCo_3$, Ce_2Ni_7 and Ce_2Co_7. Indeed, for the conventional interstitial-type intermetallic hydrides, Co-containing systems are characterised by a higher thermal stability of the hydrides and, correspondingly lower values of

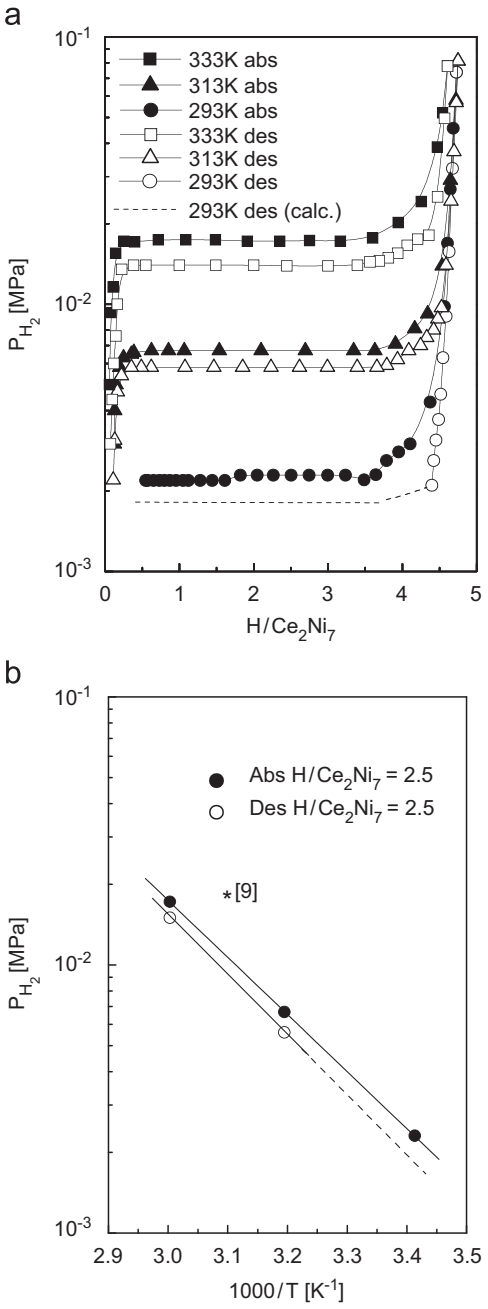

Fig. 1. (a) Absorption–desorption isotherms for the system Ce_2Ni_7–H_2. (b) van't Hoff plots lp P vs. $1/T$.

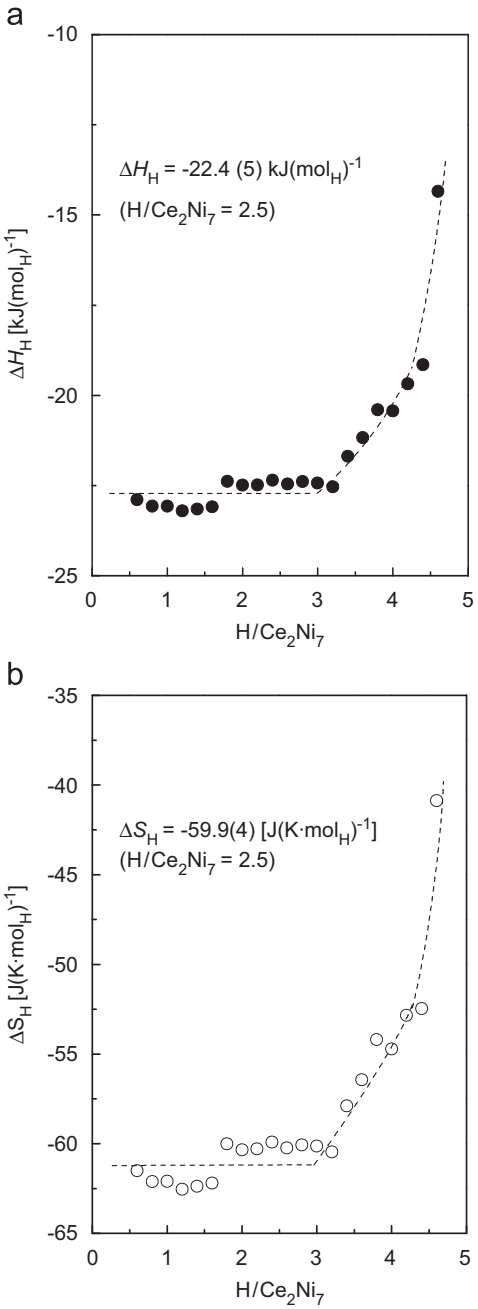

Fig. 2. Enthalpy (a) and entropy (b) changes with H content in the system Ce_2Ni_7–H_2.

enthalpies of the hydrogenation ΔH_H (see Table 1 where the data for such "conventional" $CeNi_5$- and $CeCo_5$-based hydrides are given). In contrast, an opposite trend is observed for the pairs of anisotropic hydrides, Ce_2Ni_7–Ce_2Co_7 and $CeNi_3$–$CeCo_3$. From the data given in Table 1, it is seen that (a) the ΔH_H values are similar for Ni and Co compounds with stoichiometries Ce/Ni(Co) = 1/3 or 2/7; (b) the Ni-based hydrides have slightly, yet significantly higher thermal stabilities. These observations clearly reflect the unusual behaviours of the anisotropic hydrides, which can be related to their crystal structure features.

Table 1
Thermodynamic properties of the Ce-based intermetallic hydrides

Hydride	Plateau pressure (MPa)	ΔH_H (kJ/mol$_H$)	Reference
$Ce_2Ni_7H_{4.7}$	0.017 (333 K)	-22.4 ± 0.5	Present work
$Ce_2Ni_7H_{4.4}$	0.02 (323 K)	-21.6[a]	[9]
$Ce_2Co_7H_{6.4}$	0.05 (323 K)	-20.3[a]	[9]
$CeNi_3H_3$	0.009 (323 K)	-22.6[a]	[9]
$CeCo_3H_{4.2}$	0.02 (323 K)	-21.5[a]	[9]
$CeNi_5H_6$	4.9 (298 K)	-7.1	[11]
$CeCo_5H_{2.6}$	0.13 (296 K)	-19.5	[11]
$CeNi_2H_4$	$<10^{-4}$ (298 K)	-27	[9,12]

[a]The partial molar enthalpy data were calculated based on the assumption that the partial molar entropy value is dominated by the dissociation from H_2 molecules to H atoms, -60 J/(K mol$_H$).

3.2. Crystal structure of the deuteride

In situ neutron diffraction data of the deuteride, indexed using a hexagonal unit cell (space group $P6_3/mmc$; $a = 4.9151(2)$ Å; $c = 29.776(2)$ Å), showed a pronounced (21.5%) expansion along [001] compared to the Ce_2Ni_7 intermetallic alloy ($\Delta V/V = 20.1\%$). Smaller unit cell parameters for the deuteride were obtained from *ex situ* PND data ($a = 4.9009(2)$ Å, $c = 29.633(2)$ Å), indicating a partial deuterium desorption from the sample.

Rietveld profile refinements of both *in situ* and *ex situ* PND data in the hexagonal setting revealed that unit cell expansion proceeds within the $CeNi_2$ slabs only (62–63%) with the $CeNi_5$ units remaining unchanged. Furthermore, such an uneven deformation of the metal sublattice is in agreement with deuterium occupancy of these structure fragments. Using difference Fourier analysis, we found D atoms distributed among six crystallographic sites with three chemically different metal atom surroundings, including Ce_3Ni_3, Ce_3Ni and Ce_2Ni_2. In general, the structures of $Ce_2Ni_7D_{4.4}$ and $Ce_2Ni_7D_{4.7}$ resemble that of the hexagonal $La_2Ni_7D_{6.5}$ [1]; as in other anisotropic hydrides, all D sites are located inside the $CeNi_2$ slabs or in the Ni nets connecting the $CeNi_2$ and $CeNi_5$ layers.

However, refinements in the hexagonal setting revealed the presence of significant features, which are impossible to explain unless the symmetry is assumed to be lowered from a hexagonal to an orthorhombic space group. These features included:

(a) The shift of a Ni1 atom located in the middle of $CeNi_2$ slab along hexagonal *c*-axis, described as splitting of the initial 2*a* site (0, 0, 0) into a 50% occupied 4*e* (0, 0, *z*) site with a distance of 1.4 Å between the sites.

An attempt to describe this feature as an anisotropic thermal displacement of Ni in the 2*a* site gave unreliably high U_{aniso} values along the hexagonal *c*-axis, $u_{33} = 0.80(8)$ Å^2 ($u_{11} = 0.011(6)$ Å^2, $u_{22} = 0.011(5)$ Å^2, $u_{12} = 0.005(3)$ Å^2).

(b) Unrealistically high isotropic displacement parameter for Ce1 atom located in the $CeNi_2$ slab ($U_{iso} = 0.066$ Å^2).

(c) 50% occupancy of the Ce_3Ni sites formed with a participation of a "split" Ni atom. These interstices do not exist in the parent intermetallic structure and are formed as a result of strong anisotropic expansion of the $CeNi_2$ slab. A 50% occupancy of this site together with a 50% occupancy of the split Ni1 site indicate possible ordering of D atoms.

From group–subgroup relations, $P6_3/mmc$–$Cmcm$, an orthorhombic unit cell with metrics $a_{orth} = a_{hex}$, $b_{orth} = a_{hex} + 2b_{hex}$, $c_{orth} = c_{hex}$ was first tested. However, it was rejected, as a description of the observed splitting of the Ni1 site was not possible. A completely ordered metal matrix substructure and successful description of the hydrogen sublattice were obtained when the symmetry of the structure was additionally lowered to the symmetry related to *Cmcm* orthorhombic space group *Pmcn*.

A model of the structure in the *Pmcn* space group contained 4 Ce sites, 11 Ni sites and 20 D sites. 11 from 20 D sites were rejected and the structure model with 9 occupied D sites and ordered D sublattice was found, giving an excellent fit to both *in situ* and *ex situ* PND data (see Fig. 3a and b).

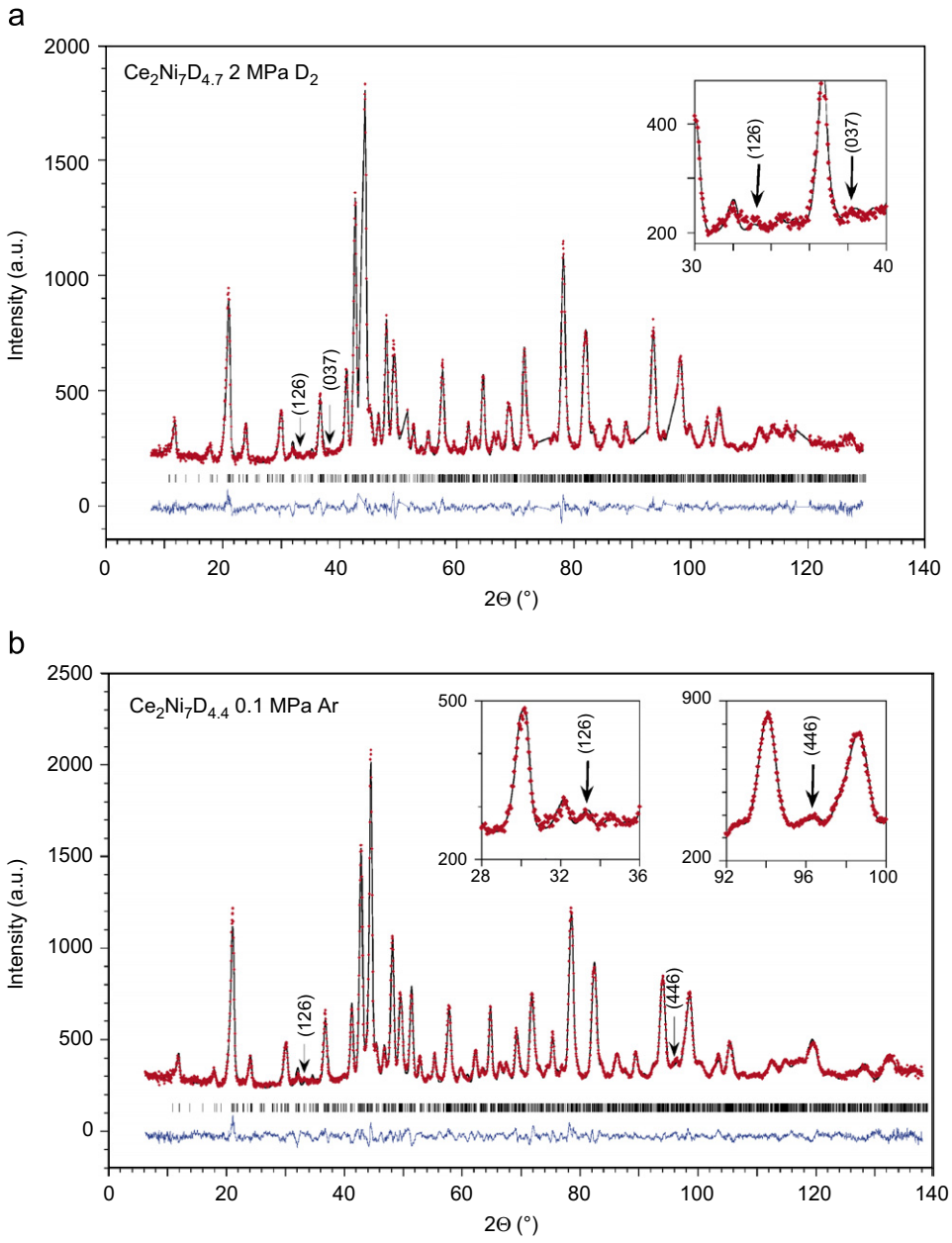

Fig. 3. Observed (dots), calculated (upper line) and difference (lower line) powder neutron diffraction profiles of the Ce_2Ni_7-based deuterides ($\lambda = 1.551(1)$ Å): (a) *in situ* measurement (2Θ angular ranges where contributions from the stainless steel autoclave were observed, 43.2–44.2; 50.35–51.55; 73.85–75.85; 90.35–92.5; 95.8–97.3 and 118.05–120.2, were excluded from the refinements); (b) *ex situ* measurement. Insets show the regions with superstructure peaks.

The final refinement showed a very small orthorhombic distortion of the deuteride structure for both data sets: $(b_{orth}/\sqrt{3}-a_{orth})/a_{orth} \approx -0.5\%$. Apparently, the peak splitting caused by such a small orthorhombic distortion cannot be clearly seen in the neutron diffraction pattern; however, a presence of weak reflections violating the hexagonal symmetry confirms the orthorhombic deformation of the structure. The most distinct of these peaks are marked in Fig. 3. The unit cell parameters for the orthorhombic structure are summarised in Table 2 and compared to those of parent Ce_2Ni_7 structure. Atomic parameters for the Ce_2Ni_7 structure (Table 3) were obtained from the Rietveld refinement of the SXRD pattern for the sample after complete deuterium desorption (confirmed by thermal desorption spectroscopy measurements of the studied sample).

A sample stoichiometry of $Ce_2Ni_7D_{4.65(9)}$ was obtained for *in situ* PND data and $Ce_2Ni_7D_{4.43(9)}$ for the *ex situ* experiments, respectively. Both values fit the stochiometric range obtained by PCT measurements where the limiting maximum hydrogen content is about 4.7 at. H/f.u. (see Section 3.1). Atomic positions in the structure of $Ce_2Ni_7D_{4.7-x}$ deuterides are presented in Table 4; selected interatomic distances are given in Table 5.

A complete rebuilding of the metal sublattice takes place within the $CeNi_2$ slabs. Fig. 4 illustrates the deformation of the metal sublattice that occurs inside these slabs during D uptake. Together with a huge expansion along the [001] direction, substantial shifts of both the central Ni1 atom and surrounding Ce atoms are observed. These shifts give rise to an orthorhombic distortion of the parent hexagonal structure. For Ni1, which is coordinated by the Ce_6 octahedron, the large unilateral expansion dramatically changes its coordination from 12 (Ce_6Ni_6) to 9 (Ce_6Ni_3).

The observed deformation of the metal sublattice is in agreement with the ordered deuterium locations in the structure as shown in Fig. 5. Deuterium atoms occupy six completely filled crystallographic sites, which are located inside the $CeNi_2$ slab, and three partially occupied sites lying on the boundary between $CeNi_2$ and $CeNi_5$ slabs. D atoms are almost evenly distributed among these three types of interstices: 1.5 at. D/f.u. in octahedra Ce_3Ni_3 (D1–D3), 1.5 at. D/f.u. in tetrahedra Ce_3Ni (D5, D6) and 1.65 at. D/f.u. in tetrahedra Ce_2Ni_2 (D4; D7–D9) (Fig. 6). Only the Ce_2Ni_2 interstitial sites exist in the structure of the original intermetallic compound; the Ce_3Ni and Ce_3Ni_3 interstices are formed via deformation of the metal sublattice induced by D atoms.

The D sublattice within the $CeNi_2$ slab is completely ordered; all D–D distances between completely filled D1–D6 sites D exceed 2.0 Å (1.9 Å in $Ce_2Ni_7D_{4.43}$). Local coordination of Ni by D atoms inside the $CeNi_2$ blocks is of an ''open'', saddle-like type within the layer formed from Ce_6 octahedra (Fig. 5 and Table 6). This shows a principal difference between $Ce_2Ni_7D_{4.7}$ and mixed

Table 3
Atomic parameters in the structure of the Ce_2Ni_7 intermetallic compound (space group: $P6_3/mmc$, $a = 4.94131(3)$ Å; $c = 24.5136(2)$ Å)

Atom	Site	x	y	z	U_{iso} (10^{-2} Å^2)
Ce1	4*f*	1/3	2/3	0.47021(4)	1.51(2)
Ce2	4*f*	1/3	2/3	0.32561(5)	0.97(2)
Ni1	2*a*	0	0	0	1.4(1)
Ni2	4*e*	0	0	0.3305(1)	0.33(5)
Ni3	4*f*	1/3	2/3	0.8182(7)	0.24(4)
Ni4	6*h*	0.8318(3)	2*x*	1/4	0.33(4)
Ni5	12*k*	0.8334(2)	2*x*	0.41529(5)	0.62(3)

Table 2
Crystallographic characteristics of the Ce_2Ni_7 compound and its deuterides

Compound	Ce_2Ni_7[a]	$Ce_2Ni_7D_{4.65(9)}$	$Ce_2Ni_7D_{4.43(9)}$
Space group	$P6_3/mmc$	$Pmcn$	$Pmcn$
Unit cell parameters (Å)	$a = 4.94131(3)$	$a = 4.9251(3)$	$a = 4.9146(3)$
	$c = 24.5136(2)$	$b = 8.4933(4)$	$b = 8.4651(5)$
		$c = 29.773(1)$	c = 29.629(1)
Unit cell volume (Å^3)	518.349(6)	1245.4(1)	1232.6(1)
Volume per formula unit (Å^3)	129.587(2)	155.68(1)	154.08(1)
H-induced deformation (%)			
$(b_{orth}/\sqrt{3}-a_{orth})/a_{orth}$	–	−0.44	−0.55
$\Delta c/c$	–	21.5	20.9
$\Delta V/V$	–	20.1	18.9
$\Delta c_{CeNi_2}/c_{CeNi_2}$	–	63.4	61.7
$\Delta V_{CeNi_2}/V_{CeNi_2}$	–	61.7	59.1
$\Delta c_{CeNi_5}/c_{CeNi_5}$	–	−0.02	−0.03
$\Delta V_{CeNi_5}/V_{CeNi_5}$	–	−1.11	−1.65
Source data	SXRD (293 K)	PND (2 MPa D_2, 293 K)	PND (0.1 MPa Ar, 293 K)
R-factors (%)			
R_{wp}	8.71	3.97	3.85
R_p	6.49	3.20	3.22
χ^2	9.46	2.90	4.44

[a]IMC after complete deuterium desorption from the deuteride.

Table 4
Atomic parameters in the structure of Ce_2Ni_7-based deuterides from Rietveld refinements of the powder neutron diffraction data

Atom[a]	Site	$Ce_2Ni_7D_{4.65(9)}$				$Ce_2Ni_7D_{4.43(9)}$			
		x	y	z	U_{iso}[b] (10^{-2} Å^2)	x	y	z	U_{iso}[b] (10^{-2} Å^2)
Ce1	4*c*	1/4	0.362(3)	0.0415(8)	2.8(3)	1/4	0.379(3)	0.0379(7)	2.8(3)
Ce2	4*c*	1/4	0.054(3)	0.9446(6)	2.8(3)	1/4	0.073(4)	0.9440(6)	2.8(3)
Ce3	4*c*	1/4	0.401(4)	0.1820(8)	0.9(2)	1/4	0.406(4)	0.1804(8)	1.5(2)
Ce4	4*c*	1/4	0.090(3)	0.8182(7)	0.9(2)	1/4	0.089(2)	0.8156(8)	1.5(2)
Ni1	4*c*	1/4	0.745(2)	0.0223(3)	1.0(2)	1/4	0.744(1)	0.0224(2)	0.5(1)
Ni2	4*c*	1/4	0.749(2)	0.1833(4)	1.2(1)	1/4	0.748(2)	0.1829(4)	1.1(1)
Ni3	4*c*	1/4	0.763(2)	0.8160(4)	1.2(1)	1/4	0.763(2)	0.8170(4)	1.1(1)
Ni4	4*c*	1/4	0.416(2)	0.8158(3)	0.7(1)	1/4	0.429(2)	0.8209(4)	0.3(1)
Ni5	4*c*	1/4	0.076(2)	0.1816(3)	0.7(1)	1/4	0.076(2)	0.1816(3)	0.3(1)
Ni6	4*c*	1/4	0.909(2)	0.2459(5)	1.2(1)	1/4	0.909(2)	0.2487(5)	1.20(8)
Ni7	8*d*	0.000(3)	0.833(2)	0.7463(3)	1.2(1)	0.006(3)	0.837(1)	0.7476(3)	1.20(8)
Ni8	4*c*	1/4	0.918(2)	0.3839(6)	1.18(6)	1/4	0.904(1)	0.3925(4)	0.90(5)
Ni9	4*c*	1/4	0.917(2)	0.1107(6)	1.18(6)	1/4	0.901(1)	0.1114(4)	0.90(5)
Ni10	8*d*	0.009(1)	0.840(1)	0.8856(4)	1.18(6)	−0.002(2)	0.847(1)	0.8838(3)	0.90(5)
Ni11	8*d*	0.501(2)	0.160(1)	0.3863(4)	1.18(6)	0.501(2)	0.164(1)	0.3861(3)	0.90(5)
D1	4*c*	1/4	0.103(3)	0.0808(7)	1.8(1)	1/4	0.088(3)	0.0768(6)	2.4(1)
D2	4*c*	1/4	0.779(3)	0.4215(5)	1.8(1)	1/4	0.746(3)	0.4184(5)	2.4(1)
D3	4*c*	1/4	0.080(4)	0.4196(6)	1.8(1)	1/4	0.079(4)	0.4176(5)	2.4(1)
D4	4*c*	1/4	0.606(2)	0.5507(6)	1.8(1)	1/4	0.628(2)	0.5588(6)	2.4(1)
D5	4*c*	1/4	0.580(3)	0.9990(6)	1.8(1)	1/4	0.584(3)	0.9969(5)	2.4(1)
D6	8*d*	0.529(3)	0.154(2)	0.0148(4)	1.8(1)	0.553(2)	0.146(2)	0.0152(4)	2.4(1)
D7[c]	8*d*	0.414(7) $n = 0.47(3)$	0.332(3)	0.111(1)	1.8(1)	0.433(8) $n = 0.34(3)$	0.357(7)	0.105(1)	2.4(1)
D8[c]	8*d*	0.422(8) $n = 0.33(3)$	0.493(5)	0.109(1)	1.8(1)	0.425(8) $n = 0.40(3)$	0.486(5)	0.108(1)	2.4(1)
D9[c]	8*d*	0.453(9) $n = 0.35(3)$	0.348(6)	0.391(1)	1.8(1)	–	–	–	–
D10[c]	4*c*	–	–	–	–	1/4 $n = 0.37(5)$	0.276(7)	0.382(2)	2.4(1)

$Ce_2Ni_7D_{4.65(9)}$. Space group: *Pmcn*; $a = 4.9251(3)$ Å; $b = 8.4933(4)$ Å; $c = 29.773(1)$ Å. $Ce_2Ni_7D_{4.43(9)}$. Space group: *Pmcn*; $a = 4.9146(3)$ Å; $b = 8.4651(5)$ Å; $c = 29.629(1)$ Å.

[a]Transformation from hexagonal to orthorhombic unit cell: (Ce1)→Ce1 and Ce2; (Ce2)→Ce3 and Ce4; (Ni1)→Ni1; (Ni2)→Ni2 and Ni3; (Ni3)→Ni4 and Ni5; (Ni4)→Ni6 and Ni7; (Ni5)→Ni8, Ni9, Ni10 and Ni11.

[b]U_{iso} parameters have been constrained to be equal for the chemically and structurally identical groups of atoms: Ce1 and Ce2; Ce3 and Ce4; Ni2 and Ni3; Ni4 and Ni5; Ni6 and Ni7; Ni8–Ni11; D1–D10.

[c]Partially occupied sites, *n*—site occupancy factor; when value of *n* is not stated, it equals to 1.

ionic-covalent-type hydrides having a partial negative charge on H, e.g. Mg_2NiH_4 [14], which contains tetrahedral $[NiH_4]^{4-}$ units.

Partially occupied D7, D8, D9 and D10 sites are located in the tetrahedral Ce_2Ni_2 sites between $MgZn_2$- and $CaCu_5$-type fragments. In total, the orthorhombic structure contains eight types of Ce_2Ni_2 tetrahedra connected into two types of Ce_2Ni_6 bipyramids. The occupancy/vacancy of these tetrahedral holes are dependent on the hole size. One type of Ce_2Ni_6 is built of Ce_2Ni_2 tetrahedra with radii of interstitial holes of 0.45–0.55 Å, whereas the other contains interstices with much smaller radii, 0.33–0.41 Å. Correspondingly, more deuterium atoms are located in the larger bipyramid, 0.80 D/f.u. (in D7 and D8 sites) compared to 0.35 D/f.u. (in D9) in the smaller one. In total, 6 of 8 types of Ce_2Ni_2 tetrahedra fulfil the size criterion (0.4 Å) to accommodate D atoms; however, due to short distances (blocking effect) between neighbouring sites, only 3 Ce_2Ni_2 sites are occupied in an ordered way. The size effect also explains the difference in Ce_2Ni_2 site occupation between $Ce_2Ni_7D_{4.65(9)}$ and $Ce_2Ni_7D_{4.43(9)}$ (see Table 4 for details). In the $Ce_2Ni_7D_{4.43(9)}$ structure the D9 site (8*f*) becomes too small (unit cell is smaller) to accommodate D atoms (less than 0.4 Å), and a sufficiently large neighbouring D10 site (0.40 Å) is occupied instead (0.18 D/f.u.). Thus, 1.65 D/f.u. are located in the Ce_2Ni_2 sites in the saturated $Ce_2Ni_7D_{4.65(9)}$ deuteride and 1.43 D/f.u. in $Ce_2Ni_7D_{4.43(9)}$.

The hydrogenation behaviour of the constituent parts of $CeNi_5$ and $CeNi_2$, reveals differences in comparison with the corresponding binary intermetallic compounds. The $CeNi_2$ cubic Laves-phase becomes amorphous on hydrogenation [15] while the $CeNi_5$-based hydride at room temperature decomposes at pressures below 48 bar [16]. In contrast, the $CeNi_5$ units stabilise the $CeNi_2$ layers in Ce_2Ni_7 and a well crystalline $Ce_2Ni_7D_{4.7}$ is formed. Instead of filling the existing interstitial sites, deuterium (hydrogen) induces structural transformations leading to the creation

Table 5
Selected interatomic distances (Å) in the crystal structures of the Ce_2Ni_7-based deuterides

Atoms	$Ce_2Ni_7D_{4.65(9)}$	$Ce_2Ni_7D_{4.43(9)}$
D1…Ce1	2.49(4)	2.72(3)
D1…Ce2 × 2	2.90(2)	2.88(2)
D1…Ni9	1.81(3)	1.89(3)
D1…Ni10 × 2	1.69(2)	1.77(2)
D2…Ce1 × 2	2.78(2)	2.99(2)
D2…Ce2	2.91(3)	2.80(4)
D2…Ni8	1.63(2)	1.55(2)
D2…Ni10 × 2	1.89(2)	1.79(1)
D3…Ce1 × 2	3.29(3)	3.26(2)
D3…Ce2	3.20(4)	3.05(5)
D3…Ni8	1.74(3)	1.65(3)
D3…Ni11 × 2	1.72(2)	1.71(2)
D4…Ce2 × 2	2.505(5)	2.501(7)
D4…Ni1	1.53(3)	1.53(1)
D4…Ni9	1.80(2)	1.58(2)
D5…Ce1	2.25(4)	2.18(2)
D5…Ce1 × 2	2.79(1)	2.68(1)
D5…Ni1	1.56(3)	1.55(2)
D6…Ce1	2.37(3)	2.56(3)
D6…Ce2	2.64(2)	2.66(2)
D6…Ce2	2.40(3)	2.41(3)
D6…Ni1	1.78(2)	1.75(1)
D7…Ce1	2.23(4)	2.20(3)
D7…Ce3	2.35(4)	2.44(4)
D7…Ni8	1.82(4)	1.61(4)
D7…Ni10	1.53(3)	1.79(5)
D8…Ce1	2.45(5)	2.42(5)
D8…Ce3	2.45(4)	2.41(4)
D8…Ni8	1.75(5)	1.74(3)
D8…Ni11	1.47(4)	1.56(4)
D9…Ce2	2.07(5)	–
D9…Ce4	2.43(5)	–
D9…Ni9	1.58(5)	–
D9…Ni11	1.62(5)	–
D10…Ce2	–	2.24(6)
D10…Ce4	–	2.28(6)
D10…Ni11 × 2	–	1.56(3)

of significantly different environments for hydrogen atoms in $Ce_2Ni_7D_{4.7}$ in comparison with the initial intermetallic alloys $CeNi_5$ and $CeNi_2$.

With deuteration, very similar changes were previously observed in the $CeNi_2$ slab of the orthorhombic $CeNi_3D_{2.8}$ structure [2]. However, $CeNi_3D_{2.8}$ is characterised by a much larger degree of orthorhombic distortion, $(b_{orth}/\sqrt{3}-a_{orth})/a_{orth} = 1.37\%$, compared to $Ce_2Ni_7D_{4.65}$ (−0.44%). This can be explained by different ratios of $CaCu_5$- and $MgZn_2$-type slabs in the $CeNi_3$ and Ce_2Ni_7 units (1:2 and 1:1, respectively). Twice as large and containing no hydrogen, $CeNi_5$ units make the metal matrix of Ce_2Ni_7 more rigid to orthorhombic deformation.

The D sublattice of the $Ce_2Ni_7D_{4.7}$ structure is similar to that of $CeNi_3D_{2.8}$. In both cases, there are six fully occupied D sites in the $CeNi_2$ slabs giving 3.5 at. D/$CeNi_2$. Five of these six sites are equivalent in both deuterides. One significant difference for $Ce_2Ni_7D_{4.7}$ is in occupancy of the D4 site (Ce_2Ni_2), which is adjacent to the octahedron Ce_2Ni_4 (D6 site) occupied by D in $CeNi_3D_{2.8}$ [2]. This difference changes the local coordination of Ni by D atoms inside the $CeNi_2$ blocks: a tetrahedral NiD_4 coordination which can be concluded for Ni1 in the crystal structure of $CeNi_3D_{2.8}$ [2] (Ni1D3D5$_2$D6; Ni–D = 1.55–1.56 Å) is changed to the saddle-like-type NiD_4 units in $Ce_2Ni_7D_{4.7}$. Interestingly, saddle-type coordination is not known for the Ni-based complex hydrides [17]; however, it has been reported for various transition metals including Co in $Mg_6Co_2D_{11}$ [18] and Ru in Mg_2RuH_4 [19]. However, a wide variation in the Ni–D distances in $Ce_2Ni_7D_{4.7}$, from 1.53 to 1.78 Å, contrasts to a rather narrow range of transition metal-to-hydrogen distances observed for the tetrahedral $[NiH_4]^{4-}$ in Mg_2NiH_4 (1.519–1.572 Å) [13], and for saddle-like CoH_4 in $Mg_6Co_2H_{11}$ (1.521–1.603 Å) [18], and RuH_4 in Mg_2RuH_4 (1.665–1.681 Å) [19]. This difference is an argument in favour of absence of the formation of NiH_n complexes in the studied $Ce_2Ni_7D_{4.7}$ deuteride.

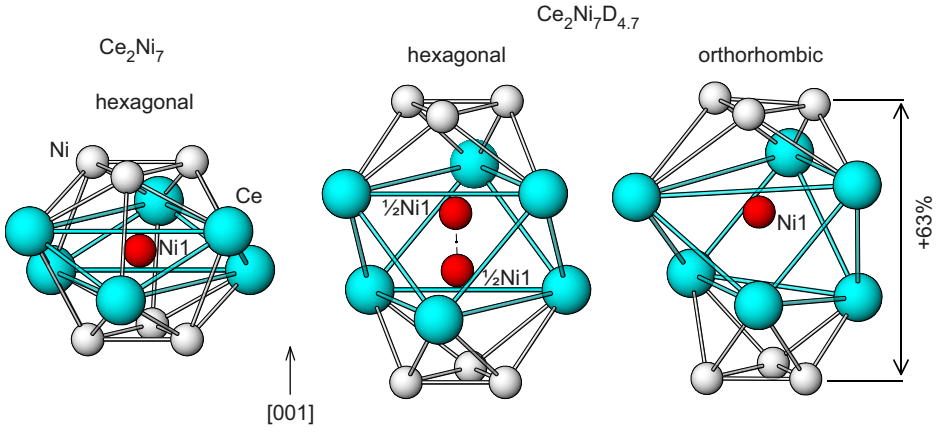

Fig. 4. Changes in coordination polyhedron of Ni1 during hydrogen absorption. The large unilateral expansion along the *c*-axis dramatically changes coordination from 12 (Ce_6Ni_6) to 9 (Ce_6Ni_3), and there is an extremely pronounced deformation of the layer formed by Ce_6 octahedra centred on Ni1. A hexagonal description of the structure allows for a split site with all Ni1 sites 50% occupied; the distance between those split sites is 1.4 Å. Note that for an orthorhombic unit cell the Ni1 atom shifts from the centre of the Ce_6 octahedra and fills one of the equivalent split sites in an ordered way; the other site is vacant.

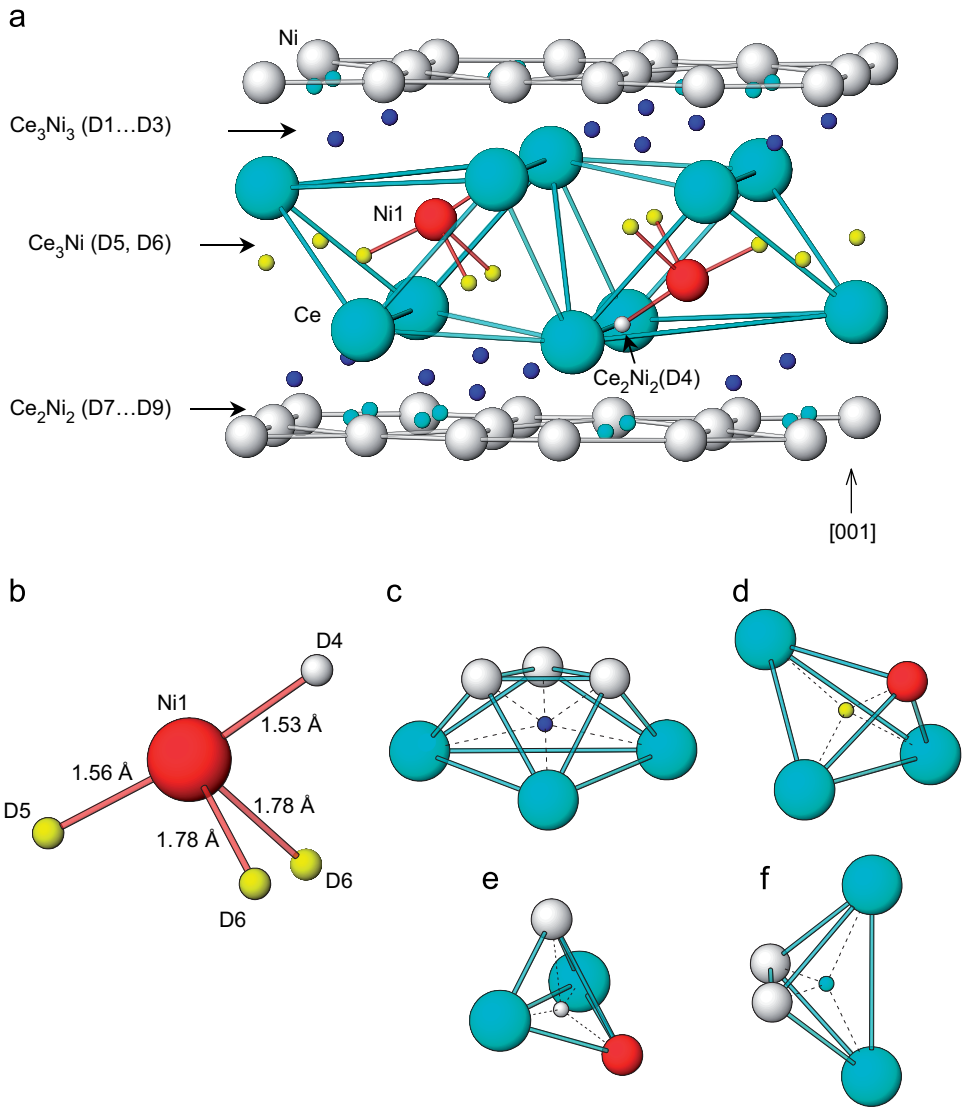

Fig. 5. $CeNi_2$ ($MgZn_2$-type) slab in the crystal structure of $Ce_2Ni_7D_{4.7}$: (a) showing the ordered D sublattice; (b) saddle-like coordination of Ni1 by 4 D atoms (within the layer formed from Ce_6 octahedra). Four types of D-occupied sites are shown: (c) deformed octahedra Ce_3Ni_3; (d) tetrahedra Ce_3Ni; (e) tetrahedra Ce_2Ni_2. These sites are occupied by D1–D6 and are completely filled. D7–D9 atoms partially fill the Ce_2Ni_2 sites (f) located on the interface between $CeNi_2$ ($MgZn_2$-type) and $CeNi_5$ ($CaCu_5$-type) slabs.

The existence of the specific MH_x coordination in structures of metal hydrides is necessary but far not sufficient criterion for considering a hydride as the complex one. Because of variety of Ni coordinations by H atoms, these anisotropic hydrides cannot be considered as genuine complex hydrides, which are formed in the systems of alkaline (alkaline earth or magnesium) and transition metals with hydrogen.

In the Kagome nets formed by Ni atoms, which are located on the border between $CeNi_2$ and $CeNi_5$, D content is very similar, 1.3 at. D/f.u. ($CeNi_3$) or 1.15 at. D/f.u. (Ce_2Ni_7). Different types of the Ce_2Ni_2 tetrahedral interstitial positions are occupied leading to differences in ordering of the hydrogen sublattice. Maximum possible H(D) content in these nets equals to 3.0 at. H/Ce_2Ni_7 leading to a possibility of reaching 6.5 at. H/f.u. Ce_2Ni_7 as a limiting value (3.5 at. H inside the $CeNi_2$ slab + 3.0 at. H on the border of $CeNi_2$ and $CeNi_5$; hydrogen sublattice will be different for the former layers from that experimentally observed in $Ce_2Ni_7D_{4.7}$).

Comparison of the results obtained in present work during studies of the Ce_2Ni_7-based hydrides and in the previous publication by Filinchuk et al. [6] shows similar features in the structure of the metal matrix of the hydrides. However, a smaller deuterium content (4.1D/Ce_2Ni_7) and a rather different deuterium substructure was reported [6]. These differences can be caused by the methods of preparation and handling of the sample in [6]. Indeed, exposure of the samples to air may lead to the chemical reaction of the hydride with O_2/N_2/water vapour causing hydrogen release, which would modify structural properties of the material. Such a reaction may result in the observed inhomogeneity of the material [6]; several coexisting Ce_2Ni_7-based hydride phases were identified.

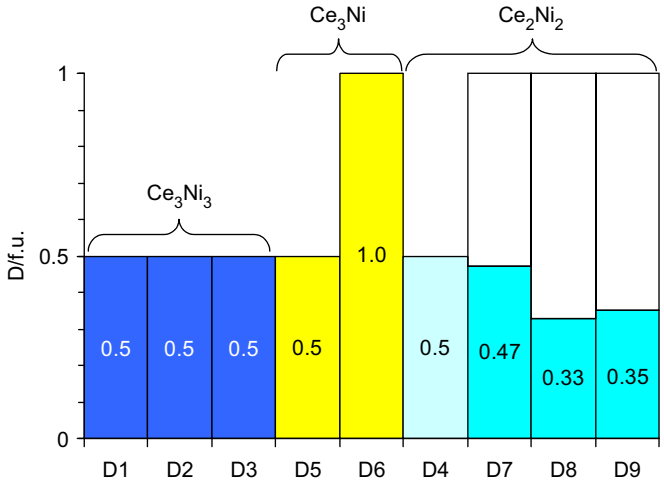

Fig. 6. Distribution of deuterium atoms in the structure of $Ce_2Ni_7D_{4.7}$ deuteride. Three different groups of sites are shown: octahedral D1–D3 and tetrahedral D4–D6 sites located inside the $CeNi_2$ slab, D7–D9 sites located in Ce_2Ni_2 tetrahedra on the interface between $CeNi_2$ and $CeNi_5$. The occupation of each D site is given in the fraction of atoms D/f.u.; the sum of these occupations is equal to the overall stoichiometry for each deuteride.

Table 6
Interatomic distances Ni1⋯D (Å) and angles D⋯Ni1⋯D (°)

Atoms	$Ce_2Ni_7D_{4.65(9)}$	$Ce_2Ni_7D_{4.43(9)}$
Ni1…D4	1.53(3)	1.53(1)
Ni1…D5	1.56(3)	1.55(2)
Ni1…D6 × 2	1.78(2)	1.75(1)
D4…Ni1…D5	173(1)	164(1)
D4…Ni1…D6 × 2	87(1)	94.1(9)
D5…Ni1…D6 × 2	99.1(8)	99.0(7)
D6…Ni1…D6	76(1)	67.3(7)

These phases also included a small quantity of the intermetallic alloy in the sample, which can be formed during completion of the H desorption from the hydride and which was indeed observed in the diffraction pattern. Possibly for these reasons, refinements of the structure of $Ce_2Ni_7D_{4.1}$ [6] yielded an unreliably short Ni–D distance of 1.38 Å and incomplete coordination of one of the D sites by the metal atoms (D7: with only two Ce atoms as closest neighbours, which form a nonlinear Ce–D–Ce unit) [6]. These features raise questions concerning the proposed hydrogen (deuterium) sublattice. Certainly, only *in situ* experiments under different selected pressures of $D_2(H_2)$ can confirm the proposed formation of the tetrahedral NiD_4 coordination [6].

Anomalous structural behaviour of anisotropic $RENi_3$- and RE_2Ni_7-based hydrides requires further studies to understand the mechanism of their formation. Such behaviour in all studied hydrides correlates with D ordering in the metallic matrix and preferential filling of interstitial sites coordinated mostly by RE atoms (RE_3Ni, RE_3Ni_3 and RE_2Ni_2). Obviously, the RE–H interactions play the most important role in hydrogen-induced structural transformation in the RE–Ni compounds. Theoretical first principal calculations will be of high value to probe the nature of the metal–hydrogen bonding in anisotropic hydrides and to address the question of hydrogen ordering and stabilisation of specific clusters containing RE, Ni and H atoms.

In conclusion, this study shows that anisotropic $Ce_2Ni_7D_{4.7}$ deuteride resembles structural features characteristic for the hydrogenation of the $RENi_3$ (RE = La, Ce) and RE_2Ni_7 (RE = La) intermetallic alloys. These include:

1. Expansion during H absorption proceeds exclusively within the $RENi_2$ layers and is caused by hydrogen atoms occupying these slabs.
2. The D atoms fill the sites where contribution from the active hydride-forming element La or Ce into their surrounding is high (octahedra RE_3Ni_3, tetrahedra RE_3Ni and tetrahedra RE_2Ni_2), not less than 50%.
3. Hydrogen sublattice within the $RENi_2$ slabs is completely ordered. However, types of the D ordering vary depending on the compound; $Ce_2Ni_7D_{4.7}$: saddle-type coordination NiD_4; $CeNi_3D_{2.8}$: tetrahedron NiD_4; $La_2Ni_7D_{6.5}$ and $LaNi_3D_{2.8}$: octahedra NiD_6. Thus, coordination of Ni by D has a variety of forms with Ni–D distances changing in a broad range indicating that formation of Ni–H complexes is rather unlikely.
4. Unusual thermodynamic behaviour of the Ce_2Ni_7-based hydride reflects its association with a group of anisotropic hydrides where metal–hydrogen bonding is expected to be significantly different from the traditional insertion-type intermetallic hydrides.

Acknowledgements

This work was supported by the Nordic Energy Research (Project 46-02 NORSTORE) and NEDO, Japan (Project "Novel Intermetallic Hydrides with High Volume Density and Advanced Surface Properties" between IFE and Tokai University). We wish to thank H. Emerich and W. van Beek for their skilful assistance during the SR-XRD experiments at the Swiss–Norwegian Beam Lines.

References

[1] V.A. Yartys, A.B. Riabov, R.V. Denys, M. Sato, R.G. Delaplane, J. Alloys Compds. 408–412 (2006) 273–279.
[2] V.A. Yartys, O. Isnard, A.B. Riabov, L.G. Akselrud, J. Alloys Compds. 356/357 (2003) 109–113.
[3] R.V. Denys, A.B. Riabov, V.A. Yartys, R.G. Delaplane, M. Sato, J. Alloys Compd. (2006), in press, doi:10.1016/j.jallcom.
[4] M. Latroche, V. Paul-Boncour, A. Percheron-Guegan, J. Solid State Chem. 177 (7) (2004) 2542–2549.
[5] K.H.J. Buschow, A.S. van der Goot, J. Less-Common Met. 22 (1970) 419–428.
[6] Y.E. Filinchuk, K. Yvon, H. Emerich, Inorg. Chem. 46 (7) (2007) 2914–2920.

[7] D.T. Cromer, A.C. Larson, Acta Crystallogr. 12 (1959) 855–859.
[8] A. Wannberg, M. Gronros, A. Mellergard, L.-E. Karlson, R.G. Delaplane, B. Lebech, Z. Kristallogr. Suppl. 23 (2006) 195–198.
[9] A.C. Larson, R.B. von Dreele, General Structure Analysis System (GSAS), LANSCE, MS-H, vol. 805, 1994.
[10] R.H. van Essen, K.H.J. Buschow, J. Less-Common Met. 70 (1980) 189–198.
[11] M. Sato, V.A. Yartys, J. Alloys Compds. 373 (2004) 161–166.
[12] C.E. Lundin, F.E. Lynch, C.B. Magee, J. Less Common Met. 56 (1977) 19–37.
[13] M.D. Chio, S. Livraghi, M. Baricco, J. Alloys Compds. 426 (2006) 180–185.
[14] P. Zolliker, K. Yvon, J.D. Jorgensen, F.J. Rotella, Inorg. Chem. 25 (20) (1986) 3590–3593.
[15] V. Paul-Boncour, C. Lartigue, A. Percheron-Guegan, J.C. Achard, J. Pannetier, J. Less-Common Met. 143 (1988) 301–313.
[16] F. Pourarian, W.E. Wallace, Int. J. Hydr. Energy 10 (1) (1985) 49–58.
[17] R. Bau, M.H. Drabnis, Inorg. Chim. Acta 259 (1997) 27–50.
[18] R. Cerny, F. Bornhomme, K. Yvon, P. Fischer, P. Zolliker, D.E. Cox, A. Hewat, J. Alloys Compds. 187 (1992) 233–241.
[19] F. Bornhomme, K. Yvon, G. Triscone, K. Jansen, G. Auffermann, P. Muller, W. Bronger, J. Alloys Compds. 178 (1992) 161–166.

Available online at www.sciencedirect.com
ScienceDirect
Journal of Solid State Chemistry 181 (2008) 812–821
JOURNAL OF SOLID STATE CHEMISTRY
www.elsevier.com/locate/jssc

Mg substitution effect on the hydrogenation behaviour, thermodynamic and structural properties of the La_2Ni_7–$H(D)_2$ system

R.V. Denys[a,b], A.B. Riabov[a,b], V.A. Yartys[a,*], Masashi Sato[c], R.G. Delaplane[a,d,1]

[a]*Institute for Energy Technology, P.O. Box 40, Kjeller NO 2027, Norway*
[b]*Physico-Mechanical Institute of the National Academy of Science of Ukraine, 5 Naukova St., Lviv 79601, Ukraine*
[c]*Department of Applied Chemistry, School of Engineering, Tokai University, 1117 Kita-Kaname, Hiratsuka, Kanagawa 259-1292, Japan*
[d]*The Studsvik Neutron Research Laboratory, Uppsala University, S-611 82 Nyköping, Sweden*

Received 9 October 2007; received in revised form 15 December 2007; accepted 30 December 2007
Available online 12 January 2008

Abstract

The present work is focused on studies of the influence of magnesium on the hydrogenation behaviour of the $(La,Mg)_2Ni_7$ alloys. Substitution of La in La_2Ni_7 by Mg to form $La_{1.5}Mg_{0.5}Ni_7$ preserves the initial Ce_2Ni_7 type of the hexagonal $P6_3/mmc$ structure and leads to contraction of the unit cell. The system $La_{1.5}Mg_{0.5}Ni_7$–H_2 (D_2) was studied using *in situ* synchrotron X-ray and neutron powder diffraction in H_2/D_2 gas and pressure–composition–temperature measurements. La replacement by Mg was found to proceed in an ordered way, only within the Laves-type parts of the hybrid crystal structure, yielding formation of $LaMgNi_4$ slabs with statistic and equal occupation of one site by La and Mg atoms. Mg alters structural features of the hydrogenation process. Instead of a strong unilateral anisotropic expansion which takes place on hydrogenation of La_2Ni_7, the unit cell of $La_{1.5}Mg_{0.5}Ni_7D_{9.1}$ is formed by nearly equal hydrogen-induced expansions proceeding in the basal plane ($\Delta a/a = 7.37\%$) and along [001] ($\Delta c/c = 9.67\%$). In contrast with $La_2Ni_7D_{6.5}$ where only $LaNi_2$ layers absorb hydrogen atoms, in $La_{1.5}Mg_{0.5}Ni_7D_{9.1}$ both $LaNi_5$ and $LaMgNi_4$ layers become occupied. Nine types of sites were found to be filled by D in total, including tetrahedral $(La,Mg)_2Ni_2$, $(La,Mg)Ni_3$, Ni_4, tetragonal pyramidal La_2Ni_3 and trigonal bipyramidal $(La,Mg)_3Ni_2$ interstices. The hydrogen sublattice around the La/Mg site shows formation of two co-ordination spheres of D atoms: an octahedron MgD_6 and a 16-vertex polyhedron LaD_{16} around La. The interatomic distances are in the following ranges: La–D (2.28–2.71), Mg–D (2.02–2.08), Ni–D (1.48–1.86 Å). All D–D distances exceed 1.9 Å. Thermodynamic PCT studies yielded the following values for the ΔH and ΔS of hydrogenation/decomposition; $\Delta H_H = -15.7 \pm 0.9\,kJ\,(mol_H)^{-1}$ and $\Delta S_H = -46.0 \pm 3.7\,J\,(K\,mol_H)^{-1}$ for H_2 absorption, and $\Delta H_H = 16.8 \pm 0.4\,kJ\,(mol_H)^{-1}$ and $\Delta S_H = 48.1 \pm 1.5\,J\,(K\,mol_H)^{-1}$ for H_2 desorption.

Keywords: Metal hydrides; Crystal structure and symmetry; Neutron diffraction; Pressure-composition-temperature relationships

1. Introduction

The crystal structures of the intermetallic alloys formed in the systems of rare-earth metals (A) with Ni or Co (B), have numerous representatives formed between compositions AB_2 (Laves compounds) and AB_5 (Haucke phases). Their composition AB_a ($2<a<5$) can be presented as a combination of n AB_5 and m A_2B_4 units. These include, for example, $A_2B_4 + AB_5 = 3 \times AB_3$ [1]; $A_2B_4 + 2 \times AB_5 = 2 \times A_2B_7$; and $2 \times A_2B_4 + 3 \times AB_5 = A_7B_{23}$ [2]. These compounds adopt several types of structures, which are built from the slabs of Laves and Haucke types stacking along the hexagonal/trigonal c-axis.

As the A/B ratio is in the range between 1/5 and 1/2, the corresponding intermetallic hydrides exhibit intermediate properties compared to the hydrogenated AB_5 and AB_2 alloys. The structures of the hydrides of the hybrid intermetallic compounds have been studied in detail for representatives belonging to different structure types, including $PuNi_3$ ([3] and references therein), $CeNi_3$ [1], and Ce_2Ni_7 [4–6]. The formation of the hydrides is accompanied by either isotropic or anisotropic expansion of the unit

*Corresponding author. Fax: +47 63 81 29 05.
E-mail address: volodymyr.yartys@ife.no (V.A. Yartys).
[1]Present address: Borgdalsgången 36, SE-611 57 Nyköping, Sweden.

0022-4596/$ - see front matter © 2008 Elsevier Inc. All rights reserved.
doi:10.1016/j.jssc.2007.12.041

cells. This expansion reaches $\Delta a/a = 7.2$, $\Delta c/c = 9.7\%$ ($LaY_2Ni_9D_{12.8}$ [7]) for isotropic and $\Delta a/a = -1.2$, $\Delta c/c = 30.7\%$ ($CeNi_3D_{2.8}$ [1]) for anisotropic hydrides.

Recently, it has been found that Mg-substituted $La_{1-x}Mg_xNi_3$ alloys ($x<0.7$) [8,9] possess higher H discharge capacities compared to the AB_5-based hydrides [10] which makes these alloys promising metal hydride electrode materials for Ni-MH rechargeable batteries. Studies of the isothermal cross-section of the La–Mg–Ni ternary system [11] revealed that, similar to $LaNi_3$, Mg also can substitute for La in La_2Ni_7. The solubility range of Mg in La_2Ni_7 at 500 °C is rather low (up to a composition of $La_{1.75}Mg_{0.25}Ni_7$ [11]) compared to $LaNi_3$, where 2/3 of La can be replaced by Mg to reach a composition of $La_{0.33}Mg_{0.67}Ni_3$. However, Mg solubility dramatically increases at higher temperatures. The formation of a single-phase $La_{1.5}Mg_{0.5}Ni_7$ compound was achieved by a stepwise sintering complemented by annealing at 750 °C [3] or by the annealing at 900 °C of the alloy obtained by induction melting [12].

The magnesium-substituted AB_3/A_2B_7-related alloys have been studied in detail; however, information on the thermodynamics and crystal structures of their corresponding hydrides is still not available. This work is focused on the synchrotron X-ray diffraction (SR XRD) and powder neutron diffraction (PND) study of the crystal structure of $La_{1.5}Mg_{0.5}Ni_7D_9$ and thermodynamic properties of the $La_{1.5}Mg_{0.5}Ni_7$–H_2 system.

2. Experimental

2.1. Preparation of the alloy and its hydride and deuteride

The $La_{1.5}Mg_{0.5}Ni_7$ alloy was prepared by a stepwise sintering (in the temperature range 600–980 °C) of a pellet prepared from the crushed $LaNi_{4.67}$ intermetallic alloy and Mg powder (purity grade 99.9%; mesh size 100). In order to compensate for loss by evaporation during the sintering, an excess of 10 at% Mg was added. Afterwards the sintered $LaNi_{4.67}$ + Mg pellet was annealed at 750 °C for 4 days with subsequent quenching into a mixture of ice and water. The details of the preparation of the alloy are given in [3].

The prepared alloy has been characterised by the synchrotron XRD (BM01A, $\lambda = 0.7243(1)$ Å, SNBL/ESRF) and high-flux PND (SLAD instrument, $\lambda = 1.116(1)$ Å, NFL, Studsvik), which showed no detectable amounts of impurity phases present in the sample.

The hydride/deuteride of the $La_{1.5}Mg_{0.5}Ni_7$ single-phase alloy has been synthesised by gas-charging of the alloy with hydrogen (99.999% purity grade) or with deuterium (98%). The sample had been previously activated by heating in vacuum up to 350 °C. The sample for SR XRD measurements of the hydride was synthesised *in situ* in a silica capillary by applying 1.2 MPa hydrogen gas. The deuteride was synthesised *in situ* in the stainless steel tube (wall thickness 0.2 mm, $d_{inner} = 6$ mm) which was used for the PND measurements. The sample, crushed in the inert atmosphere glove box, was placed into the tube, activated by heating in vacuum to 350 °C and then deuterated by adding 0.5 MPa deuterium.

2.2. Neutron powder diffraction

PND data for the deuterides were collected at the R2 reactor at the Studsvik Neutron Research Laboratory using the high-resolution R2D2 instrument ($\lambda = 1.551(1)$ Å, 2Θ step 0.05°) [13]. After the measurements, the deuteride was reloaded into a vanadium can ($d_{inner} = 5$ mm), sealed with indium wire; handling of the sample was performed in the glove box filled with purified argon. Subsequently, PND data were collected again for the "*ex situ*" sample.

The crystal structure of $La_{1.5}Mg_{0.5}Ni_7D_{9.1}$ was derived from Rietveld profile refinements of the SR XRD and PND data using the GSAS software [14]. Neutron scattering lengths ($b_{La} = 8.24$ fm; $b_{Ni} = 10.30$ fm; $b_{Mg} = 5.38$ fm; $b_D = 6.67$ fm) are taken from the GSAS library.

2.3. Measurements of the pressure–composition–temperature (PCT) relationships

The deuteride after the PND experiments has been decomposed by thermodesorption in vacuum and was used for measurements of the PCT relationships for the $La_{1.5}Mg_{0.5}Ni_7$–H_2 system by application of Sieverts' method. The sample was activated in vacuum at 350 °C for 1 h, cooled under vacuum to 25 °C and then slowly charged with hydrogen gas ($P_{H_2} = 1$ MPa). To achieve reproducible kinetics of hydrogen uptake and release, several absorption–desorption cycles were performed before measuring the isotherms. The purity grade of the hydrogen gas used was 99.999%. The measurements of the isotherms were performed in the temperature range 25–75 °C and at hydrogen pressures from 2×10^{-3} to 2 MPa. The equilibrium state was considered to be reached when the pressure changes became less than 10^{-5} MPa.

3. Results and discussion

3.1. Crystal structure of the $La_{1.5}Mg_{0.5}Ni_7$ alloy

A combined refinement of PND and SR XRD data for the initial $La_{1.5}Mg_{0.5}Ni_7$ intermetallic alloy concluded that it crystallises with the Ce_2Ni_7-type of hexagonal structure (space group $P6_3/mmc$). Substitution of La by Mg leads to a significant contraction of the unit cell from $a = 5.058$ Å, $c = 24.71$ Å; $V = 547.47$ Å^3 for La_2Ni_7 [15] to $a = 5.0285(2)$ Å, $c = 24.222(2)$ Å; $V = 530.42(4)$ Å^3 for $La_{1.5}Mg_{0.5}Ni_7$. The crystallographic data are provided in Table 1; SR XRD and NPD patterns are given in Fig. 1.

La substitution by Mg proceeds exclusively inside the Laves-type AB_2 slabs (site $4f_1$). After Mg substitution, the Laves-type slab has the composition $LaMgNi_4$. Because of the large difference in the atomic radii of La (1.877 Å) and Mg (1.602 Å), the Mg-containing $LaMgNi_4$ layer strongly

Table 1
Crystal structure data for metal matrix in the $La_{1.5}Mg_{0.5}Ni_7$ intermetallic compound and $La_{1.5}Mg_{0.5}Ni_7H_{9.3}$ hydride

Atom	Site	$La_{1.5}Mg_{0.5}Ni_7$					$La_{1.5}Mg_{0.5}Ni_7H_{9.3}$ (1.2 MPa H_2)				
		x	y	z	U_{iso} (10^{-2} Å^2)	Occupancy	x	y	z	U_{iso} (10^{-2} Å^2)	Occupancy
La1	$4f_1$	$\frac{1}{3}$	$\frac{2}{3}$	0.0246(2)	0.53(7)	0.498(17)	$\frac{1}{3}$	$\frac{2}{3}$	0.0166(3)	3.0(3)	0.516(11)
Mg1	$4f_1$	$\frac{1}{3}$	$\frac{2}{3}$	0.0246(2)	0.53(7)	0.502(17)	$\frac{1}{3}$	$\frac{2}{3}$	0.0166(3)	3.0(3)	0.484(11)
La2	$4f_2$	$\frac{1}{3}$	$\frac{2}{3}$	0.1701(2)	0.88(5)	1.0(–)	$\frac{1}{3}$	$\frac{2}{3}$	0.1751(2)	4.3(1)	1.0(–)
Ni1	$2a$	0	0	0	0.7(1)	1.0(–)	0	0	0	1.85(6)	1.0(–)
Ni2	$4e$	0	0	0.1656(2)	1.80(9)	1.0(–)	0	0	0.1619(3)	1.85(6)	1.0(–)
Ni3	$4f$	$\frac{1}{3}$	$\frac{2}{3}$	0.8335(2)	0.07(4)	1.0(–)	$\frac{1}{3}$	$\frac{2}{3}$	0.8275(3)	1.85(6)	1.0(–)
Ni4	$6h$	0.8337(5)	0.6675(10)	$\frac{1}{4}$	0.47(5)	1.0(–)	0.8285(9)	0.6570(18)	$\frac{1}{4}$	1.85(6)	1.0(–)
Ni5	$12k$	0.8336(4)	0.6673(7)	0.08391(6)	1.37(5)	1.0(–)	0.8331(6)	0.6662(12)	0.0858(1)	1.85(6)	1.0(–)

The data are based on combined Rietveld refinements of the SR XRD and PND data ($La_{1.5}Mg_{0.5}Ni_7$) and SR XRD ($La_{1.5}Mg_{0.5}Ni_7H_{9.3}$).
$La_{1.5}Mg_{0.5}Ni_7$: Space group $P6_3/mmc$; $a = 5.0285(2)$ Å, $c = 24.222(2)$ Å; $V = 530.42(4)$ Å^3.
$La_{1.5}Mg_{0.5}Ni_7H_{9.3}$: Space group $P6_3/mmc$; $a = 5.4121(1)$ Å, $c = 26.589(1)$ Å; $V = 674.48(4)$ Å^3.
R-factors: Alloy. SR XRD: $R_{wp} = 5.46\%$; $R_p = 4.56\%$; PND: $R_{wp} = 5.08\%$; $R_p = 3.44\%$; Combined: $R_{wp} = 5.11\%$; $R_p = 4.13\%$; $\chi^2 = 2.98$.
Hydride. SR XRD: $R_{wp} = 4.03\%$; $R_p = 2.99\%$; $\chi^2 = 2.32$.

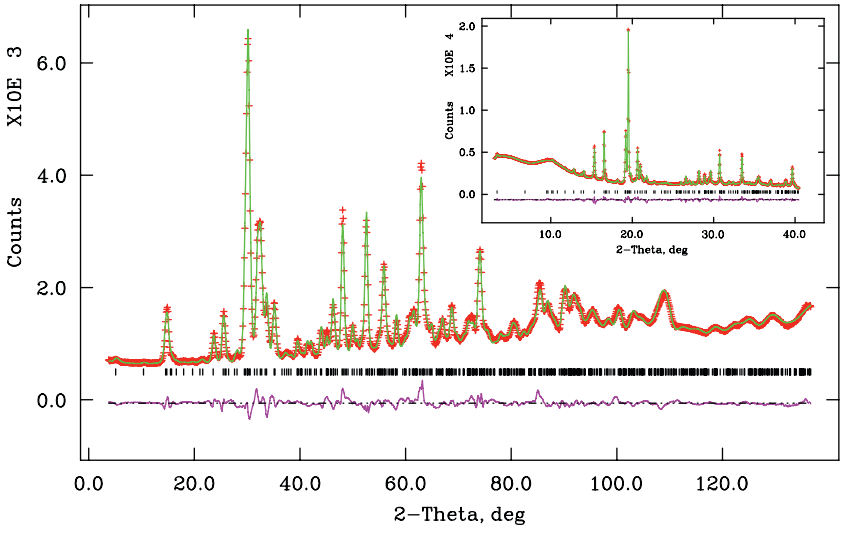

Fig. 1. Observed (+), calculated (upper line) and difference (lower line) profiles of the $La_{1.5}Mg_{0.5}Ni_7$ alloy: powder neutron diffraction (SLAD instrument, $\lambda = 1.116(1)$ Å). Inset: synchrotron X-ray diffraction (SNBL, BM01A, $\lambda = 0.7243(1)$ Å).

contracts (see Table 2) compared to the initial La_2Ni_4 slab. Due to the contraction of the basal plane of the unit cell, the adjacent $LaNi_5$ layer contracts as well but by less than 1%. The stacking of the slabs to form the crystal structure is shown in Fig. 2.

The structure of the $LaNi_5$ layer may be described as composed of two kinds of slabs with the $LaNi_5$ stoichiometry: the "outer" $LaNi_5$ slab connected to the $LaMgNi_4$ slab, and an "inner" $LaNi_5$ slab sandwiched in between two "outer" $LaNi_5$ ones. The combination $LaMgNi_4 + 2 \times LaNi_5$ gives an overall stoichiometry La_3MgNi_{14} ($2 \times La_{1.5}Mg_{0.5}Ni_7$). The "inner" AB_5-type layer is bordered above and below by the nets containing the La2 atoms; two identical "outer" parts are located above and below this "inner" part. The "outer" layers have a larger volume compared to the "inner" ones (see Table 2). The significant difference between the $LaNi_5$ layers is introduced by ordered Mg substitution for La. The external, "outer", $LaNi_5$ layer contains a number of interstitial sites formed with participation of Mg from the adjacent Laves-type $LaMgNi_4$ layer. With Mg substitution the volume of the $LaMgNi_4$ slab has decreased the most (−7.62%) compared with La_2Ni_7. The bordering "outer" $LaNi_5$ layer becomes contracted by −0.95%, whereas the central "inner" $LaNi_5$ slab is the least contracted compared to La_2Ni_7 (−0.38%) as this slab is the most distant from the Mg sites.

3.2. Thermodynamic (PCT) measurements

The single plateau behaviour is clearly seen in the absorption and desorption isotherms (Fig. 3). The two-phase

Table 2
Comparison of crystallographic parameters of La–Ni A_2B_7 compounds and their hydrides

Compound	La_2Ni_7 [15]	$La_2Ni_7D_{6.5}$ [4]	$La_{1.5}Mg_{0.5}Ni_7$	$La_{1.5}Mg_{0.5}Ni_7D_{9.1}$	$La_{1.5}Mg_{0.5}Ni_7D_{8.9}$
a (Å)	5.058	4.9534	5.0285	5.3991	5.3854
c (Å)	24.71	29.579	24.222	26.543	26.437
V (Å^3)	547.47	628.52	530.42	670.07	664.01
d_{AB_5} (inner) (Å)[a]	3.970	3.861	4.001	4.396	4.381
d_{AB_5} (outer) (Å)[a]	4.036	4.232	4.045	4.300	4.237
$d_{A_2B_4}$ (Å)	4.349	6.697	4.065	4.576	4.600
V_{AB_5} (inner) (Å^3)	87.96	82.04	87.62	110.96	110.05
V_{AB_5} (outer) (Å^3)	89.42	89.92	88.57	108.55	106.42
$V_{A_2B_4}$ (Å^3)	96.35	142.30	89.01	115.52	115.54
$\Delta a/a$ (%)[b]	–	−2.07	**−0.58**	7.37	7.10
$\Delta c/c$ (%)[a]	–	19.70	**−1.97**	9.58	9.14
$\Delta V/V$ (%)	–	14.8	**−3.1**	26.3	25.2
ΔV_{AB_5}(inner) (%)	–	−6.73	**−0.38**	26.64	25.59
ΔV_{AB_5} (outer) (%)	–	0.56	**−0.95**	22.56	20.15
$\Delta V_{A_2B_4}$ (%)	–	47.68	**−7.62**	29.78	29.80

[a]The separation between two types of the AB_5 layers is made along the buckled net containing the La2, Ni2 and Ni3 atoms.
[b]The changes of the crystallographic parameters due to partial Mg substitution for La are shown in bold type.

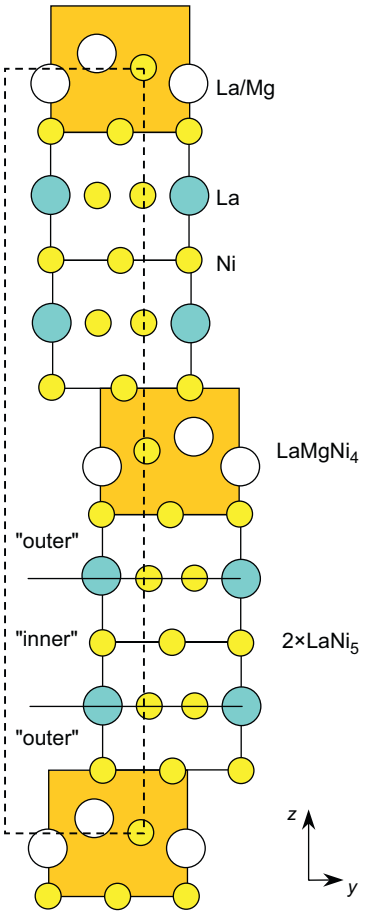

Fig. 2. Structure of $La_{1.5}Mg_{0.5}Ni_7$ intermetallic compound as a stacking of $MgZn_2$-type (shaded) and $CaCu_5$-type slabs.

region is observed at H content $1<[H]/[La_{1.5}Mg_{0.5}Ni_7]<8$. The isotherms are not horizontal; their slope becomes higher with an increase of temperature. The observed hysteresis P_{abs}/P_{des} is typical; its value of 1.4 is higher than that for the chemically similar $Ce_2Ni_7H_{4.7}$ [5]. Based on the measured PCT diagrams, the changes in the relative partial molar enthalpy ΔH_H and entropy ΔS_H were calculated for H_2 absorption and desorption at $[H]/[La_{1.5}Mg_{0.5}Ni_7]=5$ from the van't Hoff relation. The values obtained are $\Delta H_H=-15.7\pm0.9\,kJ(mol_H)^{-1}$ and $\Delta S_H=-46.0\pm3.7\,J\,(K\,mol_H)^{-1}$ for H_2 absorption, and $\Delta H_H=16.8\pm0.4\,kJ(mol_H)^{-1}$ and $\Delta S_H=48.1\pm1.5\,J\,(K\,mol_H)^{-1}$ for H_2 desorption.

The increase in Mg content in $La_{1-x}Mg_xNi_3$ ($x\leqslant0.67$) leads to a gradual decrease in the hydrogenation capacity [16]. In this work, the observed hydrogenation capacity of $H/La_{1.5}Mg_{0.5}Ni_7=9$ at 298 K is just slightly lower than that observed for the La_2Ni_7–H_2 system ($H/La_2Ni_7=10$ at 263 K). However, we note the dramatic increase of the reversible hydrogenation capacity (>7 at.H/f.u.; about 90% of capacity). In La_2Ni_7–H_2 system the reversible capacity is lower, being limited to 5 H/La_2Ni_7; hydrogen absorption–desorption cycling in this system seems to be accompanied by hydrogen-induced disproportionation. Similar observations have been made by Oesterreicher et al. [17], who noticed that $La_2Ni_7H_{10}$ decomposes with hydrogen desorption. Such disproportionation also made impossible measurements of the thermodynamic data for the chemically related $LaNi_3$–H and $LaNi_2$–H systems, where hydrides easily become amorphous and, later, disproportionate.

The comparison of the present results with the available data for hydrides of AB_3, A_2B_7 and AB_2 intermetallic compounds supports the conclusion that in all anisotropic hydrides, ΔH is in a rather narrow range of values, −22 to $-23\,kJ(mol_H)^{-1}$ neglecting the chemical nature of the constituent elements (see Table 2 in [5]), whereas the value for the hydride formation enthalpy, $-15.7\pm0.9\,kJ(mol_H)^{-1}$ obtained in this work is close to that obtained for the $LaNi_5$–H system, $-15.8\,kJ(mol_H)^{-1}$ [18]. Such a similarity

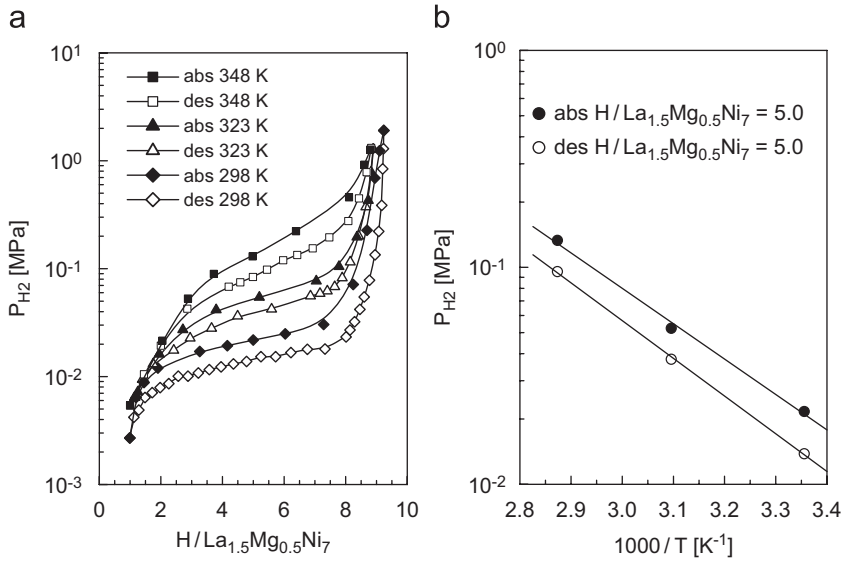

Fig. 3. PCT measurements for the $La_{1.5}Mg_{-0.5}Ni_7$–H_2 system: H_2 absorption–desorption isotherms (a) and vant' Hoff dependences $\log P_{H2}$ vs. $1/T$ (b).

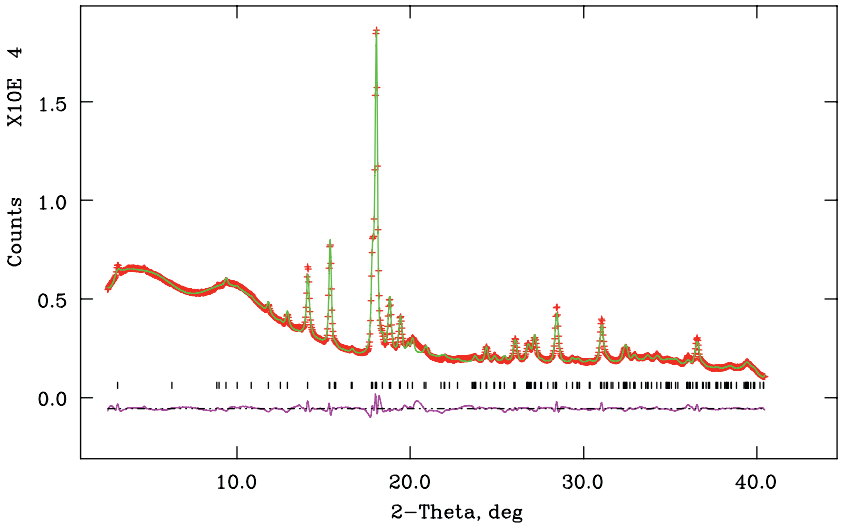

Fig. 4. Observed (+), calculated (upper line) and difference (lower line) profiles during *in situ* SR XRD experiment (1.2 MPa H_2) of the $La_{1.5}Mg_{0.5}Ni_7H_{9.3}$ hydride.

supports the conclusion that $La_{1.5}Mg_{0.5}Ni_7$ hydride belongs to conventional, interstitial type hydrides, represented by $LaNi_5H_{\sim 6}$.

3.3. SR XRD study of the hydride

The *in situ* hydrogenation of the $La_{1.5}Mg_{0.5}Ni_7$ alloy under 1.2 MPa hydrogen gas resulted in the formation of the hydride with the composition of $La_{1.5}Mg_{0.5}Ni_7H_{9.3}$, as follows from the PCT isotherm at 298 K (Fig. 3). The hydrogenation is accompanied by isotropic expansion of the unit cell, $\Delta a/a = 7.63\%$, $\Delta c/c = 9.77\%$. These values are close to those observed for the formation of the $LaY_2Ni_9D_{12.8}$ deuteride of the filled $PuNi_3$ type of structure [7] and are in sharp contrast with the values for the hydride of the isostructural non-substituted La_2Ni_7 alloy, which expands anisotropically [4] (see Table 2). The isotropic expansion of the unit cell of $La_{1.5}Mg_{0.5}Ni_7$ indicates that the hydrogenation leads to an even distribution of hydrogen through all the slabs of the structure, similarly as it has been observed for $LaY_2Ni_9D_{12.8}$ [7]. This is in contrast to anisotropic hydrides, where only Laves phase-type slabs accommodate hydrogen, leaving the $CaCu_5$-type layers unexpanded.

Refinements of the SR XRD data (Fig. 4 and Table 1) showed that Mg ordering within two types of the available 4*f* R-sites did not change with hydrogenation; only one type of sites (1/3, 2/3, 0.0166(3)) located inside the Laves-type slab was statistically and equally filled by La or Mg. The structure of the metal matrix as refined on the basis of

SR XRD data have been used as a starting point in the course of refinement of the PND data.

3.4. PND of deuterides

The Rietveld plots of the calculated and observed PND intensity data for the *in situ* and *ex situ* samples are shown in Fig. 5. The refinement results are given in Table 3; selected interatomic distances in the structures of $La_{1.5}Mg_{0.5}Ni_7D_{9.1}$ and $La_{1.5}Mg_{0.5}Ni_7D_{8.9}$ are provided in Table 4. Similar to the structure of the hydride described above, the formation of the deuteride is accompanied by an isotropic expansion of the unit cell, reaching values of $\Delta a/a = 7.37\%$, $\Delta c/c = 9.58\%$ for *in situ* and $\Delta a/a = 7.10\%$, $\Delta c/c = 9.14\%$ for the *ex situ* measurements. The positions of the deuterium have been determined by the use of Fourier synthesis after introduction of positions of the metallic atoms taken from the refinement of the SR XRD data for the hydride. The deuterium positions are situated inside the $(La,Mg)_2Ni_2$, $(La,Mg)Ni_3$ and Ni_4 tetrahedra; La_2Ni_3 tetragonal pyramids and $(La,Mg)_3Ni_2$ trigonal bipyramids (for details see Table 4 and Fig. 6). As follows from the comparison of refinement results for the *in situ* and *ex situ* data sets, the release of deuterium pressure leads to the slight decrease of deuterium content from 9.1 to 8.9 D/f.u. and is accompanied with a small contraction of the unit cell from ~670 to ~664 Å^3. The hydrogenation capacities of both *in situ* and *ex situ* samples agree well with the hydrogen desorption isotherm at 298 K in the $La_{1.5}Mg_{0.5}Ni_7$–H_2 system.

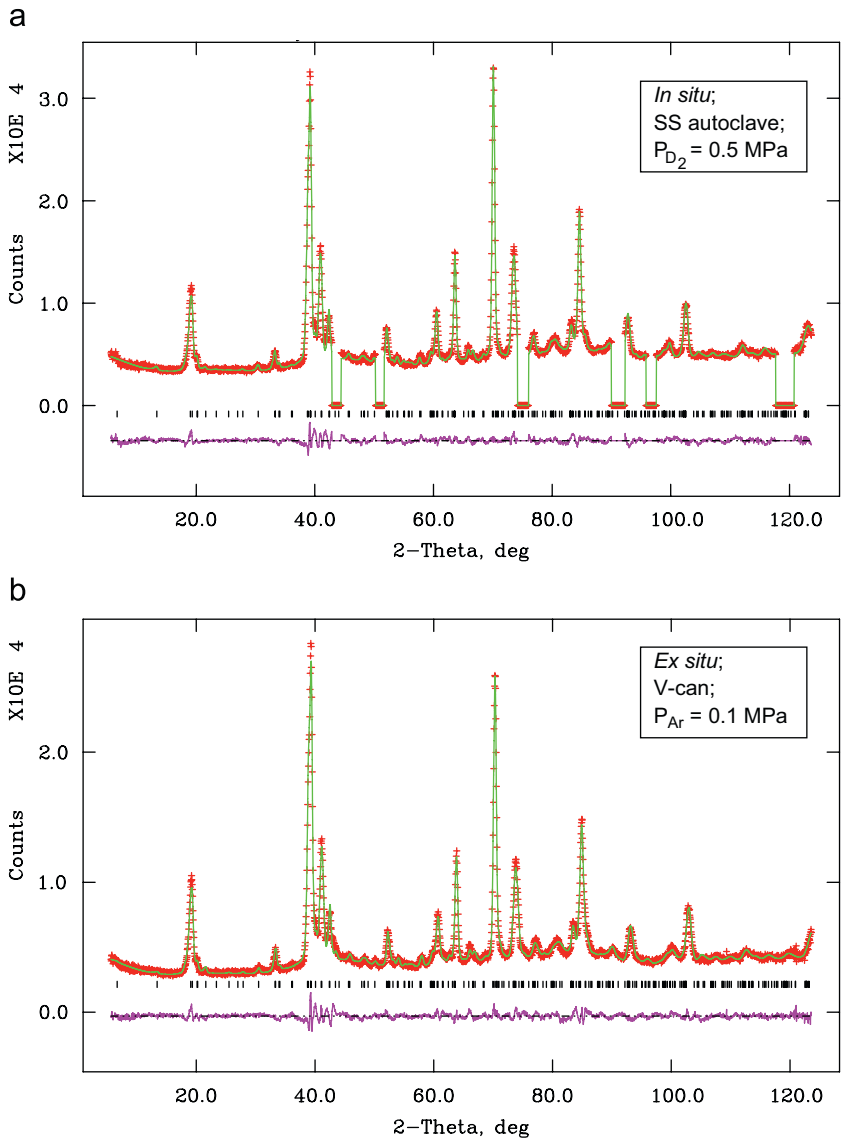

Fig. 5. Observed (+), calculated (upper line) and difference (lower line) PND profiles of the $La_{1.5}Mg_{0.5}Ni_7$-based deuterides ($\lambda = 1.551(1)$ Å): (a) *in situ* data collected for $La_{1.5}Mg_{0.5}Ni_7D_{9.1}$ at applied pressure of 0.5 MPa D_2 (2Θ ranges where contributions from the stainless steel autoclave were observed, 43.2–44.2; 50.35–51.55; 73.85–75.85; 90.35–92.5; 95.8–97.3 and 118.05–120.2, were excluded from the refinements); (b) *ex situ* data collected for $La_{1.5}Mg_{0.5}Ni_7D_{8.9}$.

Table 3
Atomic parameters in the structure of $La_{1.5}Mg_{0.5}Ni_7$-based deuterides from Rietveld refinements of the powder neutron diffraction data

Lattice parameters (Å)		$La_{1.5}Mg_{0.5}Ni_7D_{9.1}$ $a = 5.3991(1)$ $c = 26.543(2)$				$La_{1.5}Mg_{0.5}Ni_7D_{8.9}$ $a = 5.3854(1)$ $c = 26.437(2)$			
Atom	Site	x	y	z	Occ.	x	y	z	Occ.
La1	4*f*	$\frac{1}{3}$	$\frac{2}{3}$	0.0169(5)	0.50(–)	$\frac{1}{3}$	$\frac{2}{3}$	0.0160(5)	0.50(–)
Mg1	4*f*	$\frac{1}{3}$	$\frac{2}{3}$	0.0169(5)	0.50(–)	$\frac{1}{3}$	$\frac{2}{3}$	0.0160(5)	0.50(–)
La2	4*f*	$\frac{1}{3}$	$\frac{2}{3}$	0.1723(6)	1.0(–)	$\frac{1}{3}$	$\frac{2}{3}$	0.1735(5)	1.0(–)
Ni1	2*a*	0	0	0	1.0(–)	0	0	0	1.0(–)
Ni2	4*e*	0	0	0.1603(4)	1.0(–)	0	0	0.1603(4)	1.0(–)
Ni3	4*f*	$\frac{1}{3}$	$\frac{2}{3}$	0.8314(4)	1.0(–)	$\frac{1}{3}$	$\frac{2}{3}$	0.8323(4)	1.0(–)
Ni4	6*h*	0.843(1)	0.686(2)	$\frac{1}{4}$	1.0(–)	0.841(1)	0.682(2)	$\frac{1}{4}$	1.0(–)
Ni5	12*k*	0.8350(6)	0.670(1)	0.0863(2)	1.0(–)	0.8366(6)	0.673(1)	0.0869(2)	1.0(–)
D1	12*k*	0.310(3)	0.155(1)	0.1800(5)	0.40(1)	0.306(3)	0.153(1)	0.1809(5)	0.371(9)
D2	6*h*	0.512(1)	0.488(1)	$\frac{1}{4}$	0.77(3)	0.509(1)	0.491(1)	$\frac{1}{4}$	0.82(2)
D3	4*e*	0	0	0.2186(7)	0.50(–)	0	0	0.2176(6)	0.50(–)
D4	12*k*	0.342(4)	0.171(2)	0.1419(4)	0.46(1)	0.346(4)	0.173(2)	0.1438(4)	0.492(9)
D5	12*k*	0.174(3)	0.348(6)	0.0892(6)	0.32(1)	0.166(3)	0.332(6)	0.0942(7)	0.28(1)
D6	12*k*	0.484(2)	0.516(2)	0.0885(7)	0.40(2)	0.480(2)	0.520(2)	0.0878(7)	0.39(2)
D7	12*k*	0.306(2)	0.153(1)	0.0250(4)	0.50(2)	0.292(2)	0.146(1)	0.0240(4)	0.46(2)
D8	12*k*	0.527(2)	0.473(2)	0.4461(9)	0.31(2)	0.533(1)	0.467(1)	0.4494(8)	0.29(2)
D9	4*f*	$\frac{2}{3}$	$\frac{1}{3}$	0.068(1)	0.27(2)	$\frac{2}{3}$	$\frac{1}{3}$	0.073(1)	0.27(2)
		U_{iso} (10^{-2} Å^2)[a]				U_{iso} (10^{-2} Å^2)[a]			
La(Mg)		3.1(2)				2.3(2)			
Ni		2.59(6)				2.87(6)			
D		1.0(2)				1.1(1)			
R-factors		$R_{wp} = 3.88\%$; $R_p = 3.23\%$; $\chi^2 = 4.95$				$R_{wp} = 4.02\%$; $R_p = 3.43\%$; $\chi^2 = 4.33$			

[a] U_{iso} parameters have been constrained to be equal for the chemically and structurally identical groups of atoms: La1, Mg1 and La2; Ni1–Ni5; D1–D9.

3.5. Structure analysis of $La_{1.5}Mg_{0.5}Ni_7D_{9.1}$

We will present here the detailed analysis of the structure of the deuteride based on refinement results of the *in situ* data ($La_{1.5}Mg_{0.5}Ni_7D_{9.1}$).

The hydrogenation/deuteration leads to the expansion of all three types of slabs, which, however, varies from a minimum 22.56% for the "outer" $LaNi_5$ sub-slab to maximum 29.78% for the $LaMgNi_4$ slab (Table 2). In agreement with larger expansion (26.64% for the "inner" $LaNi_5$ slab), a much higher hydrogen content (5.71 at.D/f.u.) is observed for this internal layer.

3.5.1. $LaNi_5$ slabs

The hydrogen sublattice in the "inner" layer $LaNi_5D_{5.71}$ is formed by hydrogen occupation of the following sites (to simplify the comparison we use notation of sites as that for the $CaCu_5$-type Haucke structure; space group *P*6/*mmm*): 1.0 D in Ni_4/4*e*; 2.30 D in La_2Ni_2/6*m*; and 2.41 D in $LaNi_3$/12*n*. This sublattice is essentially the same as reported for $LaNi_5D_{6.37}$ [19] (0.95 D in 4*e*; 3.00 D in 6*m*; 2.42 D in 12*n*).

Due to the proximity of the "outer" $LaNi_5$ slab to the Mg-containing $LaMgNi_4$ layer, the former expands less than the "inner" $LaNi_5$ slab and accommodates 4.92 at.D/$LaNi_5$ (2.12 D in 6*m* + 2.76 D in 12*n*); the Ni_4 4*e* site remains unoccupied. The hydrogen sublattice in this layer is similar to that of the structure of the $LaNi_5D_{5.52}$ deuteride [20]. The introduction of Mg decreases the overall D content in the AB_5 layer from 5.71 to 4.92 at.D/f.u.; however, the occupancy of the interstitial sites formed by Mg replacement increases as compared to the original La-neighbouring sites. In contrast, the Ni_4 sites become completely unoccupied by D. No D-ordering is observed in neither the "inner" nor "outer" $LaNi_5$ slabs. The La atoms inside the $LaNi_5$ layer are surrounded by a 21-vertex polyhedron of D-sites, of which only 12 can be occupied simultaneously when considering the limitations imposed by D···D blocking for very short D interatomic distances (Fig. 7c).

3.5.2. $LaMgNi_4$ slab

The main feature of the $MgZn_2$-type $LaMgNi_4$ slab is the occupancy of all four available types of the R_2Ni_2 sites that are $6h_1$, $6h_2$, $12k_1$ and 24*l* sites according to the notation adopted for the $MgZn_2$-type hydrides [21]. D occupies simultaneously these four types of sites in the structures of $ZrMn_2D_{2.76}$ [22], $ScFe_2D_{2.53}$ [23], and $Ti_{1.2}Mn_{1.8}D_{3.1}$ [24]. In addition to $(La,Mg)_2Ni_2$, one of the RNi_3 sites, 4*f*, is also occupied also as is observed in the structure of $ZrVFeD_{3.6}$ [21]. The $(La,Mg)_2Ni_2$ sites are preferably filled

Table 4
Selected interatomic distances (Å) in the crystal structures of $La_{1.5}Mg_{0.5}Ni_7$-based deuterides

Atoms	Interstitial site	$La_{1.5}Mg_{0.5}Ni_7D_{9.1}$	$La_{1.5}Mg_{0.5}Ni_7D_{8.9}$
D1⋯2 La2	Tetragonal pyramid $La2_2Ni2Ni3Ni4$	2.709(2)	2.703(2)
D1⋯Ni2		1.54(1)	1.52(1)
D1⋯Ni3		1.70(1)	1.72(1)
D1⋯Ni4		1.86(1)	1.83(1)
D1⋯D3		1.77(2)	1.72(2)
D1⋯D4		1.02(1)	1.00(1)
D2⋯2 La2	Tetrahedron $La2_2Ni4_2$	2.65(1)	2.61(1)
D2⋯2 Ni4		1.556(6)	1.551(5)
D3⋯Ni2	Tetrahedron $Ni2Ni4_3$	1.55(2)	1.52(2)
D3⋯3 Ni4		1.69(1)	1.72(1)
D3⋯3 D1		1.77(2)	1.72(2)
D3⋯D3		1.67(4)	1.71(3)
D4⋯2 La2	Tetragonal pyramid $La2_2Ni2Ni3Ni5$	2.818(5)	2.805(4)
D4⋯Ni2		1.67(2)	1.67(2)
D4⋯Ni3		1.68(2)	1.63(2)
D4⋯Ni5		1.48(1)	1.51(1)
D4⋯D1		1.02(1)	1.00(1)
D5⋯(La,Mg)1	Tetrahedron $(La,Mg)1La2Ni5_2$	2.43(2)	2.59(2)
D5⋯La2		2.66(2)	2.62(3)
D5⋯2 Ni5		1.59(1)	1.55(1)
D5⋯D6		1.45(1)	1.49(1)
D6⋯(La,Mg)1	Tetrahedron $(La,Mg)1La2Ni5_2$	2.36(2)	2.34(2)
D6⋯La2		2.63(2)	2.65(2)
D6⋯2 Ni5		1.65(1)	1.667(8)
D6⋯D5		1.45(1)	1.49(1)
D6⋯D8		1.01(2)	1.10(3)
D6⋯D9		1.79(2)	1.78(2)
D7⋯2 (La,Mg)1	Trigonal bypyramid $(La,Mg)1_3Ni1Ni5$	2.711(2)	2.708(2)
D7⋯(La,Mg)1		2.02(1)	2.041(9)
D7⋯Ni1		1.58(1)	1.50(1)
D7⋯Ni5		1.63(1)	1.67(1)
D7⋯2 D7		1.96(2)	1.86(2)
D7⋯2 D8		1.71(1)	1.71(1)
D8⋯(La,Mg)1	Tetrahedron $(La,Mg)1_2Ni5_2$	2.29(3)	2.16(3)
D8⋯(La,Mg)1		2.06(1)	2.08(1)
D8⋯2 Ni5		1.69(1)	1.74(1)
D8⋯D6		1.00(2)	1.10(3)
D8⋯2 D7		1.71(1)	1.71(1)
D8⋯D9		1.36(2)	1.38(2)
D9⋯(La,Mg)1	Tetrahedron $(La,Mg)1Ni5_3$	2.26(3)	2.34(4)
D9⋯3 Ni5		1.65(1)	1.63(1)
D9⋯3 D6		1.79(2)	1.78(2)
D9⋯3 D8		1.36(2)	1.38(2)

Table provides the values of the "blocking" distances between neighbouring D positions (1.0–1.9 Å). Due to partial occupancy of D sites the "blocked" sites are never simultaneously filled; minimum distance between neighbouring D atoms in the structure exceeds 1.9 Å.

(93% from overall hydrogenation capacity of 7.56 at.D/$LaMgNi_4$). For the 24*l* sites, the D atoms are shifted into a common triangular $(Mg/La)Ni_2$ face, which makes this deuterium position co-ordinated by a trigonal bipyramid $(Mg/La)_3Ni_2$.

Similar to the structures of the hydrides of $MgZn_2$-type intermetallics the hydrogen sublattice within the $LaMgNi_4$ slab is not ordered. This is in contrast with the structure of $La_2Ni_7D_{6.5}$ where all D⋯D distances are larger than 1.8 Å, and the deuterium sublattice is completely ordered. In the latter case the capacity of the $MgZn_2$-type layer corresponds to $LaNi_2D_5$, which is significantly higher than the capacity of the $LaMgNi_4$ slab. This agrees with the values of the expansion of the layers, which are 47.68% and 29.78%, respectively (Table 2).

3.5.3. Deuterium sublattice

The R-site inside the $LaMgNi_4$ slab has an equal probability to be occupied by Mg or La. There are 22 partly occupied D-sites around the R-site; of these six are at distances of 2.02–2.06 Å and 16—at 2.25–2.71 Å. Accounting for the substantial difference in atomic radii of Mg and La, we can consider that the distances of 2.02–2.06 Å correspond to an octahedron around the Mg atom, whereas a 16-vertex external polyhedron surrounds the La atom (Figs. 7a and b). In total, D atoms fill nine types of interstitial sites (Fig. 6 and Table 4). In contrast to the previously studied anisotropic $La_2Ni_7D_{6.5}$ hydride, where the hydrogen sublattice is layered and limited only to Laves-type layers, the spatial framework of hydrogen atoms extended throughout all the structure of $La_{1.5}Mg_{0.5}Ni_7D_9$ is observed. This framework is formed by polyhedra of three types: an octahedron around each Mg atom as well as 16-vertex polyhedra around the La atoms (Fig. 7). The MgD_6 octahedra sites are completely occupied by H; thus, these octahedra are completely ordered. The $La1D_{16}$ polyhedron within the $LaMgNi_4$ slab is partially ordered and could have a maximum of 12 simultaneously occupied vertices—six D7, three D8 and three either D5 or D6 sites, on the boundary between $LaMgNi_4$ and the "outer" $LaNi_5$ slabs. For the case of complete ordering of La and Mg atoms inside the $LaMgNi_4$ slab, the D9 position will remain empty, since it is blocked by three D8 atoms surrounding the Mg atoms. The previously mentioned 21-vertex $La2D_{21}$ polyhedron inside the $LaNi_5$ slab also can not have more than 12 simultaneously occupied vertices—half of twelve mutually blocking D1 and D4 sites, three D2 sites and the same type of the occupancy of the D5 and D6 sites as described for the $La1D_{16}$ polyhedron. The maximum H storage capacity based on the structure thus described is $La_{1.5}Mg_{0.5}Ni_7D_{11}$ and can be presented as $\frac{1}{2}$ ($LaNi_5D_7$ (inner) + $LaNi_5D_6$ (outer) + $LaMgNi_4D_9$). Obviously, the isotropic expansion of the unit cell is caused by the fact that all the layers, Laves-type, and both Haucke types, reach a high content of H compared to their maximum theoretical capacities.

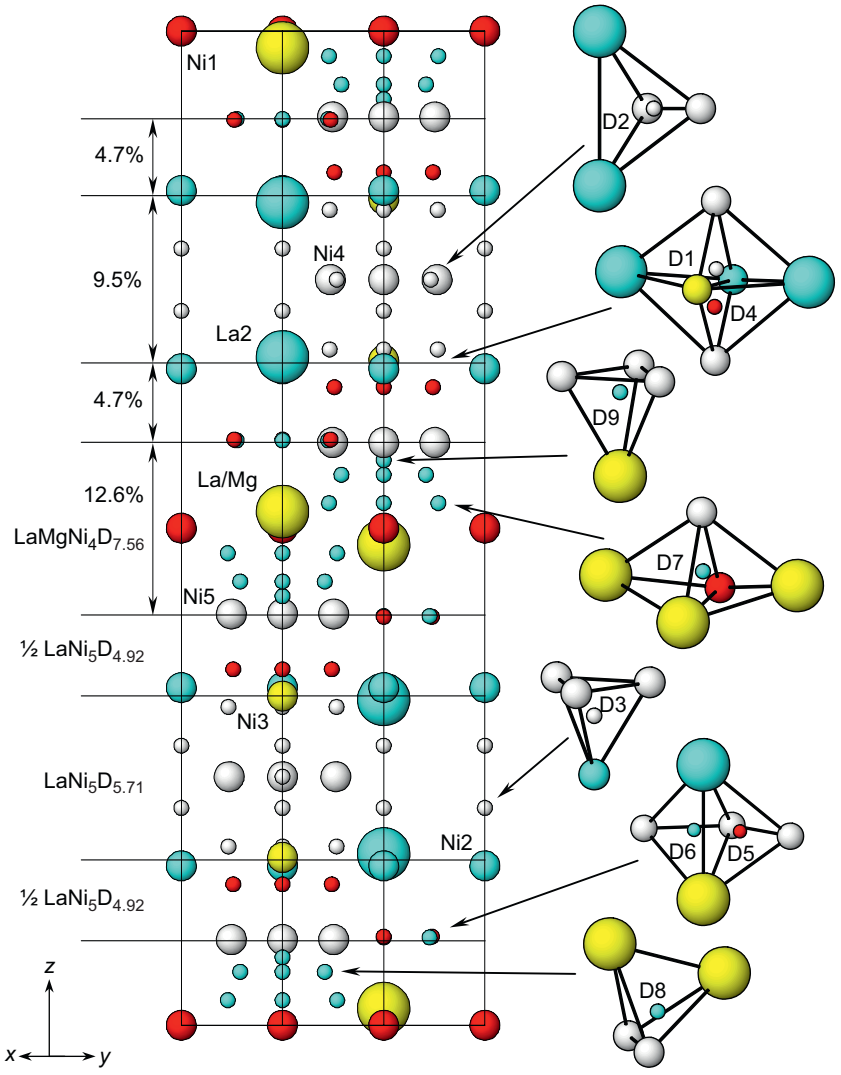

Fig. 6. Crystal structure of $La_{1.5}Mg_{0.5}Ni_7D_{9.1}$ showing the stacking of the $LaNi_5$ and $LaMgNi_4$ slabs with their relative expansion during deuteration. The coordination of each D site is shown and each site location is indicated.

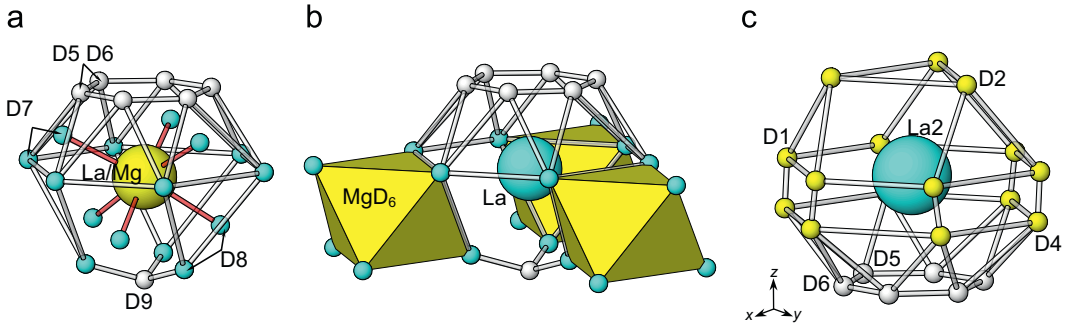

Fig. 7. (a) Hydrogen sublattice inside the $LaMgNi_4D_{7.56}$ layer. The central position is jointly occupied by La and Mg. Hydrogen sites form two different coordination spheres—an internal one, with $d_{Me-D} = 2.02–2.06$ Å, and an external sphere with much larger Me–D distances, 2.25–2.71 Å. The internal D sphere forms an octahedron around the metal atom; because of much smaller Me–D distances, this atom can only be Mg. The external sphere forms a 16-vertex polyhedron centred on La atom, LaD_{16}. (b) Assuming local ordering of Mg and La in the layer, gives packing of the MgD_6 octahedra and LaD_{16} polyhedra as shown. (c) Hydrogen sublattice inside the $LaNi_5$ layer formed by a 21-vertex polyhedron of D sites of which only 12 can be occupied simultaneously when considering the limitations imposed by D···D blocking for very short D interatomic distances.

The decrease of hydrogen content with the decrease of pressure from 0.5 to 0.1 MPa is not very substantial, only 0.25 $H/La_{1.5}Mg_{0.5}Ni_7$ as these pressures exceed the desorption plateau pressure at room temperature. The slight decrease in H content is accompanied by a moderate reduction of the unit cell volume. However, the desorption

in such a case occurs mostly from the $LaMgNi_4$ layer, which indicates that Mg reduces the affinity of this layer to hydrogen compared to that of the $LaNi_5$ layers. Interestingly, the partial release of hydrogen from the $LaMgNi_4$ layer is not accompanied by contraction of this layer (see Table 2); instead both the "inner" and "outer" $LaNi_5$ slabs slightly contract.

4. Conclusions

Our results show that Mg has an important influence on different aspects of hydrogen interaction with the $(La,Mg)_2Ni_7$ alloy.

These changes are caused by partial replacement of La by Mg inside the Laves type slabs and include:

- Increase of the reversible hydrogen storage capacity;
- Change of the mechanism of hydrogenation from an "anisotropic" hydride to an "isotropic" one;
- Absence of amorphisation and disproportionation of the metal matrix on cycling of hydrogenation and decomposition because of the stabilisation of the metal sublattice by Mg;
- Change of the thermodynamics of the metal-hydrogen interaction where smaller values of enthalpy of hydrogenation indicate formation of the interstitial type hydride.

Theoretical studies will be invaluable in gaining knowledge of the nature of the metal-hydrogen interactions in these structures. Successful synthesis of new materials will depend on the Mg-assisted ability to create new additional sites for hosting hydrogen. The present work contributes to the design of new Mg-containing materials with higher hydrogen discharge capacities for technological applications such as electrode materials in rechargeable Ni/MH batteries.

Acknowledgments

This project was supported by the Nordic Energy Research (Project 46-02 NORSTORE), Norwegian Research Council and NEDO, Japan (Project "Novel Intermetallic Hydrides with High Volume Density and Advanced Surface Properties" between IFE and Tokai University). We are grateful to Dr. J.P. Maehlen (IFE) for his help. We wish to thank Drs. Y. Filinchuk (SNBL) and D. Chernyshov (SNBL) for their skillful assistance during the SR-XRD experiments at the Swiss-Norwegian Beam Lines, ESRF.

References

[1] V.A. Yartys, O. Isnard, A.B. Riabov, L.G. Akselrud, J. Alloys Compd. 356–357 (2003) 109–113.
[2] T. Kohno, H. Yoshida, F. Kawashima, T. Inaba, I. Sakai, M. Yamamoto, M. Kanda, J. Alloys Compd. 311 (2) (2000) L5–L7.
[3] R.V. Denys, A.B. Riabov, V.A. Yartys, R.G. Delaplane, M. Sato, J. Alloys Compd. 446–447 (2007) 166–172.
[4] V.A. Yartys, A.B. Riabov, R.V. Denys, M. Sato, R.G. Delaplane, J. Alloys Compd. 408–412 (2006) 273–279.
[5] R.V. Denys, V.A. Yartys, M. Sato, A.B. Riabov, R.G. Delaplane, J. Solid State Chem. 180 (9) (2007) 2566–2576.
[6] Y.E. Filinchuk, K. Yvon, H. Emerich, Inorg. Chem. 46 (7) (2007) 2914–2920.
[7] M. Latroche, V. Paul-Boncour, A. Percheron-Guégan, J. Solid State Chem. 177 (2004) 2542–2549.
[8] K. Kadir, T. Sakai, I. Uehara, J. Alloys Compd. 257 (1997) 115–121.
[9] K. Kadir, T. Sakai, I. Uehara, J. Alloys Compd. 302 (2000) 112–117.
[10] Y.J. Chai, K. Sakaki, K. Asano, H. Enoki, E. Akiba, T. Kohno, Scripta Mater. 57 (2007) 545–548.
[11] S. De Negri, M. Giovannini, A. Saccone, J. Alloys Compd. 439 (2007) 109–113.
[12] F.-L. Zhang, Y.-C. Luo, J.-P. Chen, R.-X. Yan, J.-H. Chen, J. Alloys Compd. 430 (2007) 302–307.
[13] A. Wannberg, M. Gronros, A. Mellergard, L.-E. Karlson, R.G. Delaplane, B. Lebech, Z. Kristallogr. Suppl. 23 (2006) 195–198.
[14] C. Larson, R.B. von Dreele, General structure analysis system (GSAS), LANSCE, MS-H 805, 1994.
[15] K.H.J. Buschow, A.S. van der Goot, J. Less-Common Met. 22 (4) (1970) 419–428.
[16] B. Liao, Y.Q. Ley, G.L. Lu, L.X. Chen, H.G. Pan, Q.D. Wang, J. Alloys Compd. 356–357 (2003) 476–749.
[17] H. Oesterreicher, J. Clinton, H. Bittner, Mater. Res. Bull. 11 (1976) 1241–1248.
[18] W.N. Hubbard, P.L. Rawlins, P.A. Connick, R.E. Stedwell Jr., P.A.G. O'Hare, J. Chem. Thermodyn. 15 (8) (1983) 785–798.
[19] C. Lartigue, A. Percheron-Guegan, J.C. Achard, J.L. Soubeyroux, J. Less-Common Met. 113 (1985) 127–148.
[20] D. Noréus, L.G. Olsson, P.-E. Werner, J. Phys. F: Met. Phys. 13F (1983) 715–727.
[21] V.A. Yartys, V.V. Burnasheva, N.V. Fadeeva, S.P. Solov'ev, K.N. Semenenko, Int. J. Hydrogen Energy 7 (12) (1982) 957–965.
[22] J.-J. Didisheim, K. Yvon, D. Shaltiel, P. Fischer, Solid State Commun. 31 (1979) 47–50.
[23] V.A. Yartys, V.V. Burnasheva, N.V. Fadeeva, Sov. J. Inorg. Chem. 31 (10) (1986) 2500–2503.
[24] D. Fruchart, J.L. Soubeyroux, R. Hempelmann, J. Less-Common Met. 99 (1984) 307–319.